

REPORT DOCUMENTATION PAGE

AFRL-SR-AR-TR-04-

Public reporting burden for this collection of information is estimated to average 1 hour per response, including the time for reviewing instructions, maintaining the data needed, and completing and reviewing this collection of information. Send comments regarding this burden estimate and suggestions for reducing this burden to Department of Defense, Washington Headquarters Services, Directorate for Information Operations and Distribution, 1204, Arlington, VA 22202-4302. Respondents should be aware that notwithstanding any other provision of law, no person shall be subject to a civil fine or penalty for failing to comply with a requirement in a form that does not display a currently valid OMB control number. PLEASE DO NOT RETURN YOUR FORM TO THE ABOVE ADDRESS.

0246

1. REPORT DATE (DD-MM-YYYY) 20/04/2004		2. REPORT TYPE Final Technical Report		3. DATES COVERED (From - To) 01/01/01 - 12/1/03
4. TITLE AND SUBTITLE Stagnation point flow and heat transfer under free-stream turbulence				5a. CONTRACT NUMBER
				5b. GRANT NUMBER F49620-01-1-0138
				5c. PROGRAM ELEMENT NUMBER
				5d. PROJECT NUMBER
				5e. TASK NUMBER
				5f. WORK UNIT NUMBER
7. PERFORMING ORGANIZATION NAME(S) AND ADDRESS(ES) Department of Mechanical Engineering, Stanford University				8. PERFORMING ORGANIZATION REPORT
9. SPONSORING / MONITORING AGENCY NAME(S) AND ADDRESS(ES) Dr. Tom Beutner Air Force Office for Scientific Research				10. SPONSOR/MONITOR'S ACRONYM(S) AFOSR
				11. SPONSOR/MONITOR'S REPORT NUMBER(S)
12. DISTRIBUTION / AVAILABILITY STATEMENT Approved for public release, distribution unlimited				
<i>20040520 039</i>				
13. SUPPLEMENTARY NOTES				
14. ABSTRACT Stagnation point flow and heat transfer in the presence of free-stream turbulence is investigated through both numerical simulation and theoretical analysis. Large eddy simulations (LES) results for different free-stream turbulent intensity, length scale, and Mach number are reported. The Reynolds stress statistics and budgets are obtained and presented. The numerical results show good agreement with experimental measurements on elevated heat transfer coefficient, and reveals the characteristic vortical flow structures responsible for the observed heat transfer enhancement. The theoretical analysis shows that the vorticity amplification, and hence the heat transfer enhancement, increases with decreasing length scale and reaches a maximum value at about five times the boundary layer thickness. A new correlation for heat transfer enhancement which incorporates turbulence intensity, integral length scale and mean flow Reynolds number is derived and shown to reasonably collapse the recent experimental data.				
15. SUBJECT TERMS Stagnation point flow, free-stream turbulence, turbine blade heat transfer, large eddy simulation, vorticity dynamics, turbulence modelling.				
16. SECURITY CLASSIFICATION OF:		17. LIMITATION OF ABSTRACT	18. NUMBER OF PAGES	19a. NAME OF RESPONSIBLE PERSON Prof. Sanjiva K. Lele
a. REPORT non-classified	b. ABSTRACT non-classified	c. THIS PAGE non-classified	Unlimited	228
		19b. TELEPHONE NUMBER (include area code) 650-7237721		

RECEIVED APR 21 2004

Stagnation Point Flow and Heat Transfer Under Free-Stream Turbulence

Zhongmin Xiong Sanjiva K. Lele

Department of Mechanical Engineering
Stanford University, Stanford, California 94305

April 20, 2004

Abstract

Stagnation point flow and heat transfer in the presence of free-stream turbulence is investigated through both numerical simulation and theoretical analysis. Large eddy simulations (LES), using fourth order finite difference in curvilinear coordinates and an efficient dual time linearized sub-iteration scheme, are performed to investigate free-stream turbulence impingement upon an elliptical leading edge and the resulting heat transfer enhancement. A new blending procedure is developed through which independent, statistically identical realizations of homogeneous isotropic turbulence are combined to provide realistic representations of free-stream turbulence.

Results for different free-stream turbulent intensity, length scale, and Mach number are reported. Strong anisotropy of the turbulence due to the mean flow strain is observed as the stagnation point is approached. The Reynolds stress statistics and budgets are obtained and presented. These results are expected to provide unique data for turbulence modelling of strain dominated flows. The numerical results show good agreement with the experimental measurements on elevated heat transfer coefficient. It also reveals that small scale, intense vortical flow structures generated at the leading edge by vortex stretching induces significant changes in local thermal boundary layer, causing the observed heat transfer enhancement.

In the theoretical study, the distortion of three dimensional unsteady disturbance in an incompressible Hiemenz boundary layer and its effect on the wall heat transfer is analyzed based on linear vortex dynamics. An asymptotic solution for disturbance vorticity is obtained with explicit dependence on the disturbance length scale and frequency. It is shown that the vorticity amplification, and hence the heat transfer enhancement, increases with decreasing length scale and the maximum value is found around five times the boundary layer thickness. The unsteadiness of the disturbance reduces the disturbance amplification but is of second order at low frequency. By extending the analysis to free-stream turbulence, a new scaling correlation for the relative heat transfer enhancement is derived which incorporates turbulence intensity, integral length scale and mean flow Reynolds number. This correlation is shown to reasonably collapse the recent experimental data.

Keywords: Stagnation point flow, free-stream turbulence, turbine blade heat transfer, large eddy simulation, vorticity dynamics, turbulence modelling.

Contents

1	Introduction	3
1.1	Motivation and Background	3
1.2	Experimental Studies	5
1.3	Theoretical Analysis	8
1.4	Numerical Predication	10
1.5	Overview and accomplishments	12
2	Governing Equations	14
2.1	Governing Equations for Compressible Flow	14
2.2	Filtered Governing Equations	16
2.3	Dynamic Model for SGS Transport	18
3	Numerical Method	21
3.1	Implicit Scheme with Linearized Subiterations	21
3.2	Approximate Factorization	24
3.3	Spatial Discretization	26
3.4	Boundary Conditions	28
3.5	Numerical damping	30
3.6	Potential Flow solution	31
3.7	Similarity Solutions	31
3.8	Leading Edge Receptivity to Sound	32
4	Generation of Free Stream Turbulence	46
4.1	Inflow Turbulence	46
4.2	LES of homogeneous isotropic turbulence	47
4.3	Blending Procedure	48

5 Numerical Simulation Results	58
5.1 Experimental Setup	58
5.2 Simulation procedure	60
5.3 Inflow turbulence	64
5.4 Turbulent mean flow and heat transfer	65
5.5 Reynolds stress and turbulent transport	66
5.6 High intensity and High Mach Number cases	70
6 Theoretical Analysis	144
6.1 Introduction	144
6.2 Governing equations	147
6.3 Numerical Results	152
6.4 Linear Vortex Dynamics	156
6.4.1 Series expansion	156
6.4.2 Outside the boundary layer	158
6.4.3 Composite solution	160
6.4.4 Boundary conditions for the vorticity	162
6.5 Asymptotic Behavior	164
6.5.1 Vorticity asymptotes	164
6.5.2 Heat transfer scaling	165
6.6 Discussion of Free-Stream Turbulence	167
7 Summary and Conclusion	187
A Incompressible Potential Flow	191
B On the Coefficient of Numerical Dissipation	195
C Compressible Boundary Layer Over a Leading Edge	205
C.1 Introduction	205
C.2 Boundary Layer Approximation	205
C.3 Stewartson Transformation	209
C.4 Similar Solutions	213
D Vorticity boundary conditions	215
E Vorticity asymptotes	218

Chapter 1

Introduction

1.1 Motivation and Background

Stagnation point flow, where fluid approaching a solid surface divides into diverging streams, is a ubiquitous and important flow phenomenon. Hiemenz's pioneering work at the beginning of last century showed that the incompressible stagnation point flow is one of those very few fundamental types that admit exact solutions to the Navier-Stokes equations. However, this seemingly simple flow, when disturbed, exhibits surprisingly rich phenomena and intriguing dynamics. This can be, at least partially, attributed to the fact that in the stagnation region the upstream disturbance typically reaches its maximum by the effect of mean flow strain while the mean flow velocity itself, on the other hand, approaches zero — perturbed stagnation point flow is inherently nonlinear. This peculiar feature contributes to many difficulties in our understanding of the nature of the perturbed stagnation point flow. The correct account for the linear instability, for instance, did not appear until late 1970's.

In addition to the substantial theoretical interests, the practical reason why stagnation point flow continue to remain as an active research subject after more than a century's study lies in its ubiquity: almost all the interactions between fluid flow and solid structures involve some kinds of stagnation points or lines. Many flow and heat transfer problems encountered in various important engineering applications are of stagnation point nature. Gas turbine cooling and micro electronics design are among the most noticeable examples.

As one of the major energy conversion devices of our times, gas turbine is used both for aircraft propulsion and in land-based power generation. Up to now, it is widely recognized that the key technology to design and manufacture more efficient and powerful gas turbines is to increase the turbine inlet temperature, for the power output and thermal efficiency of gas turbine increases with the increasing inlet temperature. For this reason, the temperature of combustion gas at turbine inlet at present far exceeds the melting point of turbine blade superalloy, and very sophisticated measures (e.g. film cooling, internal cooling) must be applied to cool the turbine blades. To design effective cooling systems, accurate heat transfer prediction between the gas and the turbine blades is crucial. Overestimating heat transfer would cost excessive amount of cooling air bled from the compressor, hence incur severe penalties in the engine performance and efficiency. Underestimating heat transfer, on the other hand, could result in component failure. It has been reported that a ten degree underestimation of turbine blade temperature would reduce the blade life time by half. Accurate prediction of turbine heat transfer, however, has proven to be rather difficult. One of the key difficulties stems from the large scale and high intensity turbulence generated in the combustor through its intricate swirling, mixing and combustion processes. The turbulence contained in the free stream greatly enhances the heat transfer between the combustion gas and turbine blades. This augmentation effect becomes most salient in the stagnation region of blade leading edge, where the largest heat transfer occurs. Because the physical mechanism which leads to this significant heat transfer enhancement is not well understood, the prediction of heat transfer in the presence of free-stream turbulence remains empirical in gas turbine design.

Similar heat transfer problems related to stagnation point flow also arise in micro-electronics cooling. As the number of transistors on a standard-sized microprocessor continues to increase, the power density is expected to exceed 100 W/cm^2 in the near future. The thermal management of the power dissipation has become one of the major limiting factors in building more powerful, compact and reliable computers. With the development of MEMS technology, microjet (or jet array) impingement, capable of producing heat transfer coefficient one order of magnitude higher than that of the traditional fan-driven convection, has emerged as a promising new technology. Active experimental researches are conducted to explore various methods for increasing the heat removal rate as well as enhancing the controllability. Obviously, a detailed knowledge of the impinging jet flow and surface heat

transfer is essential to achieving a optimized cooling design which ensures both the performance and reliability for future microprocessors.

Many other engineering applications, such as combustion spray, fluidized bed, paper drying, wind-building interaction, need to deal with problems involving stagnation point flow and heat transfer. In all these practical cases, disturbances exist in the free stream and in fact, are often the major concerns of the problem. Hence, a better understanding of the dynamics of the stagnation flow and heat transfer under various disturbances is at the heart of the fluid mechanics research which aims at improving the existing technologies, and is also the primary goal of the present study.

In what follows, past studies through experimental measurements, theoretical analysis and numerical computations on the stagnation point flow and heat transfer are reviewed.

1.2 Experimental Studies

The experimental studies of stagnation point flow in the presence of disturbances started in later 1920s when the unexpectedly high velocity fluctuations were first observed in the stagnation region of a blunt body placed in the wind tunnels with uniform streams (Piercy and Richardson, 1928, 1930). Later, large disparities in the related heat transfer measurements among different researchers led to the discovery that much of the difference can be attributed to the different levels of the free-stream turbulence in the wind tunnels. Further systematic experimental studies confirmed that the free-stream turbulence causes significant heat transfer enhancement in the stagnation point region (Giedt, 1949; Hegge-Zijnen, 1957; Kestin et al., 1961).

To understand and model the effect of the free-stream turbulence in stagnation point flows, Smith and Kuethe (1966) used eddy viscosity which was assumed to be proportional to the product of free-stream turbulence intensity Tu and the distance from the wall. Upon applying the Hiemenz transformation, the combination of $\frac{Tu}{\sqrt{Re}}$ emerges as a parameter that controls the shape of the turbulent mean velocity and thermal profiles. This parameter later forms the basis of many empirical correlations, including Smith and Kuethe (1966); Kestin and Wood (1971); Lowery and Vachon (1975); Mehendale et al. (1991). These correlations fit the Frössling number $Fr = \frac{Nu}{\sqrt{Re_D}}$ (Frössling, 1940) all using a second order polynomial of $\frac{Tu}{\sqrt{Re_D}}$ but with slightly different coefficients by different investigators.

Correlations based on the parameter $\frac{T_u}{\sqrt{Re}}$ achieved some success in data reduction and some of them are still used today. But they generally have a rather narrow applicable range in terms of Reynolds number and turbulence intensity, which indicates that a potentially important role of turbulence scale has been missing in the formulation. The reason that in early experiments the length scale of turbulence did not receive much attention — most of the investigators did not measure the length scale except Hegge-Zijnen (1957), are probably twofold. In the first place, it is not very easy to achieve experimentally a large enough turbulence scale range so that a definite conclusion of its effect can be drawn. Secondly, it was expected that the turbulence length scale only plays a subordinate role (Kestin and Wood, 1971). As was then understood, the small velocity fluctuations in the free stream triggers the instability of the mean flow, but the resulting structures, presumably responsible for the heat transfer enhancement, are determined by the intrinsic instability features rather than by the free-stream turbulence *per se*.

Presently, the importance of turbulence length scales has been well recognized. Intuitively, very small scale disturbances are quickly damped by the viscosity, whereas very large scale disturbances only exert a quasi-steady effect. Hence there exists a certain length scales range in which the disturbances are most effective. However, it is not clear what is the precise role of the turbulence length scales in determining the overall turbulence effect, and different opinions exist on even which turbulence scale is relevant and should be incorporated into the formulation.

Yardi and Sukhatme (1978) measured the effect of the turbulence integral length scale L on the stagnation point heat transfer using a circular cylinder in a cross-flow, and showed that, at both very large and very small scales, the heat transfer enhancement is reduced. The maximum effect of turbulence length scale appeared somewhere between $5 < \frac{L Re_D^{1/2}}{D} < 15$, where D is the diameter of the cylinder, or roughly 4–12 times of boundary layer thickness.

Ames and Moffat (1990) studied the effect of free-stream turbulence with relative large scales ($\frac{L}{D} > 1.0$) on stagnation point heat transfer. The eddy viscosity formulation in Smith and Kuethe (1966) was generalized by taking into account the change of the turbulence intensity as the stagnation point is approached. Based on a model turbulence energy spectrum and rapid distortion theory (Hunt, 1973; Hunt and Graham, 1978), a new correlation parameter is developed incorporating the turbulence intensity, Reynolds number and turbulence energy scale (the dissipation scale of Hancock and

Bradshaw (1983)) in the form of $\frac{TuRe_D^{5/12}}{(Lu/D)^{1/3}}$. The energy scale represents the energy-containing eddies and is estimated by $Lu = 1.5u_{rms}^3/\epsilon$, where ϵ is the turbulence energy dissipation rate. This parameter appears to well correlate their experimental data. Data from other groups are also correlated but with more scatter. Further experiments have been reported recently (Ames et al., 2002) with a larger Reynolds number range and different turbulence conditions.

Van Fossen et al. (1995) made a systematic study on the influence of various flow parameters on stagnation point heat transfer, focusing on the relatively short turbulence length scale ($\frac{L}{D} = 0.05 - 0.3$). The turbulence intensity Tu varies from 1.1 to 15.9 percent, and Reynolds number Re_D from 37000 to 228000. They showed that the heat transfer enhancement increases as turbulence length scale decreases, but no peak was found within their range of length scale. The measured heat transfer enhancements are found to be best fitted using an empirical parameter of $\frac{TuRe_D^{0.8}}{(L/D)^{0.574}}$. Different mean flow strain rates are also studied but no significant influence was observed on the heat transfer enhancement. Further experiments concerning the effect of anisotropy of the turbulence (Oo and Ching, 2001), and for even higher (upto 28.5 percent) turbulence intensities (VanFossen and Bunker, 2000) have also been reported.

Dullenkopf and Mayle (1995) argued that across the entire turbulence energy spectrum, only a rather selective frequency band contributes significantly to the heat transfer enhancement. Thus, instead of using the total turbulence intensity, they proposed to use an effective turbulence intensity obtained by integrating the von Karman's model spectrum over a narrow frequency range. Based on their own and some previous data, they found that the heat transfer enhancement appears to vary linearly with this length scale weighted turbulence intensity, reminiscent to the earlier prediction by Smith and Kuethe (1966).

It should be pointed out that, in most cases, correlations developed through specific experiments are not applicable to data from other researchers. Moreover, of particular interest to the gas turbine applications is the stagnation point flow and heat transfer with turbulence present in a transonic free-stream, but experimentally this has proven very challenging and few measurements are available. Difficulties also arise when the correlations developed using simplified geometry are to fit the heat transfer data in a turbine blade leading edge region (Yeh et al., 1993; Thole et al., 2002). On one hand,

this may be attributed to the sensitivity of the stagnation point flow to various free stream disturbances. On the other hand, the empirical nature of these experimental correlations is the inherent reason for their limited applicability. From this perspective, theoretical analysis should shed more light on the underlying physical mechanism, and lead to a better understanding of the precise roles of the various flow parameters used in the experimental correlations.

1.3 Theoretical Analysis

In an attempt to explain the sensitivity of the stagnation point flow and heat transfer to the upstream disturbances, theoretical analysis has been carried out from various perspectives, mainly: unsteady mean flow effect, linear and nonlinear instability and vortex stretching and amplification.

The unsteadiness of the mean flow caused by upstream disturbances was first considered by Lighthill (1954), who examined the effect of pulsating upstream mean velocity about a cylindrical body and obtained the Stokes-layer correction, but no significant change in heat transfer was found. Similarly modulated stagnation point flows were also studied by Ishigaki (1970) and Pedley (1972), but with an emphasis on the surface skin friction. Merchant and Davis (1989) examined the steady streaming driven by large amplitude and high frequency temporal free stream modulation. The results show that the streaming, when it exists, is always confined within the Hiemenz boundary layer thickness. These unsteady analyses are limited to two dimensional case, thus do not explain the large three dimensional structures often observed in the perturbed stagnation point flow. These structures, presumably the reason of the heat transfer enhancement, often take the form of an array of secondary streamwise vortices separated by a distances of the order of boundary layer thickness.

From the point of view of flow instability, these structures are hypothesized as the result of a selective amplification process, i.e. the three dimensional disturbances originating from the viscous stagnation region of one particular spanwise wavelength is preferentially amplified. The wavelength may potentially correspond to the distance of vortex spacing observed in the experiments. Early linear stability analysis by Görtler (1955) and Häammerlin (1955), however, showed that the resulting eigenvalue problem yields a continuous spectrum of spanwise wavenumbers for the neutral time

dependent disturbance as opposed to a unique most amplified wave number. Later, Kestin and Wood (1970) pointed out that the lack of unique eigenvalue is the result of the over simplification of the boundary conditions at far upstream. The mathematical formulation was considerably clarified by Wilson and Gladwell (1978), who showed that the correct behavior of the disturbances originating from the stagnation region should be exponentially decaying far upstream. The resulting stability analysis in this case led to an unique eigenvalue problem, but the disturbances are all found to decay, i.e. the plane stagnation point flow is always linearly stable to the three dimensional disturbances. The nonlinear instability of finite amplitude disturbances was further considered by Lyell and Huerre (1985) using Galerkin method, and they showed that the flow can be destabilized if the level of the external two- or three dimensional disturbances exceeds certain threshold value.

In a comprehensive review, Morkovin (1979) argued that the enhancement of heat transfer is more likely a result of forced response to the upstream disturbances as opposed to the internal flow instability. The flow visualizations by Nagib and Hodson (1978) and Botcher and Wedemeyer (1989) strongly support this argument. The same point of view was advocated earlier by Sutera (1965) who analyzed the amplification effect of the mean flow straining on the incoming organized disturbances, indicating the sensitivity of the heat transfer to vortical disturbances. Hunt (1973) used rapid distortion theory to investigate the asymptotic behavior of free-stream turbulence as it approaches a bluff body; considerable insight was gained into the distortion process of the turbulence of different length scales. But the mean flow was assumed potential, therefore no heat transfer between the fluid and wall was considered. To explain the formation of the secondary vortices, Kerr and Dold (1994) showed that an inviscid two dimensional stagnation flow can possess periodic streamwise vortices. The characteristics of these vortices are also studied in the experiments of Andreotti et al. (2001). To connect the disturbances in the free stream with the vortices found in the stagnation region, Dhanak and Stuart (1995) showed that the weak external cross-stream vorticity with small length scales follows an algebraic structure in the wall normal direction, under which the corresponding inner viscous boundary layer can support a substructure of counter-rotating streamwise eddies. Regarding the effect of the three dimensional flow structures on the heat transfer, the numerical simulation of Rigby and VanFossen (1992) showed that the small spanwise nonuniformity can result in large increase of heat transfer in the

stagnation point region of a cylinder. Bae et al. (2000) also found that different length scales generate quite different flow patterns and in turn different heat transfer responses in a plane stagnation point flow.

Despite the significant progress made in the past, the precise mechanism governing the disturbance evolution and heat transfer augmentation is still not fully understood, and particularly elusive is its dependence on the various disturbance parameters.

1.4 Numerical Predication

To represent the turbulence effect on the flow and heat transfer for most of the practical applications, the Reynolds averaged Navier-Stokes equations based on various turbulence models are at present still the major predication tools. However, stagnating turbulence presents a serious challenge for turbulence modelling. This is chiefly because the formulation of turbulence models is in most cases based on the shear dominated flows such as boundary layer rather than the strain dominated flows like those found in a stagnation point.

One equation model of Spalart and Allmaras (1992) has been widely used and shown particularly successful in aerodynamic flows (Bardina et al., 1997; Wilcox, 2001). In this model the eddy viscosity is obtained algebraically through an effective eddy viscosity which satisfies a proposed transport equation. The model, however, does not explicitly account for the effect of free-stream turbulence. In order to predict the effect of free-stream turbulence, e.g. heat transfer enhancement, bypass transition, modifications must be introduced into the formulation (Tsourakis et al., 2002). Those modifications are often of rather ad hoc nature, and it is not clear how in general that the effect of free-stream turbulence may be incorporated.

Standard two equation models, e.g. $k - \epsilon$ or $k - \omega$ model, when used in the stagnation point turbulent flows, badly over predict the turbulent kinetic energy and heat transfer — “stagnation anomaly” has been termed to describe this phenomenon (Durbin, 1996) although it happens wherever the mean strain rate is large in the flow field, such as in a gas turbine passage (Medic and Durbin, 2002). For uniform mean flow strain, rapid distortion theory shows that the production of the turbulent kinetic energy is proportional to the mean flow strain rate. But in the two equation models, the normal stresses are expressed by eddy viscosity and mean flow gradients, thus the production terms becomes proportional to the square of the

strain rate. Moreover, turbulence effect in two equation models is represented chiefly by its kinetic energy, implying the turbulence is isotropic. But in stagnation point flows, the free-stream turbulence quickly becomes very anisotropic, because different components of the velocity fluctuation respond differently to the mean flow strain rate when the wall is approached. These two factors essentially render the standard two equation model inapplicable in the stagnation point type of flows. Various remedies have been proposed to cure the problem, ranging from modifying the standard model coefficients (Champion and Libby, 1991), changing the upstream boundary condition (Abid and Speziale, 1994), reformulating the turbulence production term (Kato and Launder, 1993) to zonal matching (Traci and Wilcox, 1975; Wang and Yeh, 1987) and using second order Reynolds stress model for the normal stresses (Taulbee and Tran, 1988). One recent development is to use time-scale limiters (Durbin, 1996), where an additional bound for the turbulent characteristic time scale is derived from the realizability considerations. When implemented into standard two equation models, it shows promising results in predicting the correct turbulence behavior and heat transfer coefficient (Medic and Durbin, 2002; Behnia et al., 1999; Parneix et al., 1999).

The Reynolds stress models are the most complicated turbulence models. They are used less often than the two equation models because not only more equations are involved, but also the coupling among different Reynolds stress terms makes the numerical problem difficult. Nevertheless, in Reynolds stress models, the anisotropy of the turbulence is explicitly accounted, so better predicative capability may be expected. However, though better than $k - \epsilon$ type models, Reynolds stress models are still far from satisfactory when applied to stagnating turbulent flows such as an impinging jet. Im et al. (2003) used three variants of Reynolds stress model, GL model (Gibson and Launder, 1978), GL-CL model (Craft et al., 1993) and SSG model (Speziale et al., 1991), to compute both the impinging and counter-current stagnation flows. All the models give severe over-predictions in turbulence kinetic energy and large discrepancies in other Reynolds stress components when compared with experimental measurements. The problem stems from, on one hand the over-prediction of the energy production, while on the other hand the under prediction of the redistribution due to the troublesome terms modelling the pressure strain correlations.

In summary, from the aforementioned studies using experimental, theoretical and numerical approaches, it is clear that despite the effort and progress made over the years, many important questions regarding to the

perturbed stagnation point flow remain to be answered. A closer and more detailed investigation, combining both numerical simulation and theoretical analysis, is thus of great interest. Not only will it shed much light into the physical mechanism but also can potentially provide valuable guidance towards developing and calibrating new turbulence models. The insight gained from the study may improve the design of experiments and help developing new technologies in a wide range of related industrial fields.

1.5 Overview and accomplishments

In this study, we adopt both numerical and theoretical approaches to investigate the turbulent flow and heat transfer at a two dimensional elliptical leading edge. The principal contributions and findings of this work are listed below.

- High order fully implicit numerical method, with a linearized dual time sub-iteration scheme offering a 4–5 times speed-up over the usual sub-iteration schemes, is developed and validated to study the stagnation point flow and heat transfer in the presence of free-stream turbulence.
- A new blending procedure is developed for generating realistic free stream turbulence. By blending a series of independent but statistically identical realizations of homogeneous isotropic turbulence, this simple yet effective method preserves the first order and most of the second order turbulence statistics.
- For low Mach number case, free-stream turbulence conditions with different length scales and turbulence intensities matching experimental conditions are computed using large eddy simulation. Very good agreement between the numerical simulation and experimental measurement on the heat transfer enhancement (Van Fossen et al., 1995) is obtained.
- Three different stages characterizing the interaction between free-stream turbulence and stagnation point are identified and examined in detail. Turbulence statistics are obtained and analyzed in the light of rapid distortion theory.
- The impinging and lateral movement of stretched free stream turbulent eddies are found to be directly responsible for the heat transfer

enhancement. The wall blockage effect are shown to be the cause of rapid lateral movement of the eddies, and the magnitude of the translating velocity is characterized.

- Large eddy simulation at high Mach number is performed, and the turbulence statistics are obtained and compared with the low Mach number case.
- The length scale effect on the disturbance evolution is analyzed using matched asymptotic expansion. A new uniformly valid analytic expression is obtained which describes evolution of three dimensional unsteady upstream disturbances being convected towards the stagnation point. The effect of mean flow straining and viscous dissipation as well as its implication on heat transfer are explicitly shown.
- The analysis for organized disturbances is generalized to the free stream turbulence. A new correlation parameter is developed which correlates the heat transfer enhancement to the turbulence intensity, integral length scale and Reynolds number. The new parameter is shown to reasonably collapse both the recent experimental data and the results of the present numerical simulations.

This report documents the primary computation and analysis methods as well as the results and findings at the time of writing. More detailed technical information will be available in the Stanford University Ph.D thesis (Xiong, 2004).

Chapter 2

Governing Equations

2.1 Governing Equations for Compressible Flow

The physical laws governing the motion of a compressible fluid are expressed through the continuity, momentum and energy equations. Using Cartesian tensor notation and dimensional primitive variables, they can be written as

$$\rho_{,t}^* + (\rho^* u_i^*)_{,i} = 0 \quad (2.1)$$

$$\rho^* u_{i,t}^* + \rho^* u_j^* u_{i,j}^* = -p_{,i}^* + \tau_{ij,j}^* \quad (2.2)$$

$$\rho^* h_{,t}^* + \rho^* u_j^* h_{,j}^* = (p_{,t}^* + u_j^* p_{,j}^*) + q_{j,j}^* + \tau_{ij}^* u_{i,j}^* \quad (2.3)$$

where ρ^* is the density, u_i^* is the velocity vector, p^* is the thermodynamic pressure, τ_{ij}^* is the viscous stress tensor, q_j^* is the heat flux, and h^* is the fluid enthalpy defined by

$$h^* = e^* + p^*/\rho^* \quad (2.4)$$

where e^* is the internal energy per unit mass. In the above equations, subscripts following a comma denote partial differentiation with respect to the subscript, and the Einstein summation convention is used.

We assume Newtonian fluid such that the viscous stress tensor and the heat flux are given by

$$\tau_{ij}^* = \lambda^* u_{k,k}^* \delta_{ij} + 2\mu^* S_{ij}^* \quad (2.5)$$

$$q_j^* = -\kappa^* T_{,j}^* \quad (2.6)$$

where μ^* and λ^* are the first and second coefficient of viscosity. κ^* is the thermal conductivity, $S_{ij}^* = \frac{1}{2}(u_{i,j}^* + u_{j,i}^*)$ is the rate-of-strain tensor, T^* is the absolute temperature, and δ_{ij} is the Kronecker delta.

To close the system of equations (2.1) - (2.3), an equation of state which links the thermodynamical variables and additional equations which relate the fluid properties to the thermodynamical variables are needed. We assume an ideal, calorically perfect gas with constant specific heats, so the equation of state is

$$p^* = \rho^* \mathcal{R}^* T^* \quad (2.7)$$

were $\mathcal{R}^* = c_p^* - c_v^*$ is the gas constant, c_p^* is the specific heat at constant pressure, and c_v^* is the specific heat at constant volume. Both c_p^* and c_v^* are constant as is the ratio $\gamma = c_p^*/c_v^*$. Under these conditions, the internal energy and the enthalpy are related to the absolute temperature by

$$e^* = c_v^* T^* \quad (2.8)$$

$$h^* = c_p^* T^* \quad (2.9)$$

The fluid properties, for a calorically perfect gas, are functions of temperature only. For low speed flows with small temperature variations, the viscosity μ^* and conductivity κ^* can be treated as constants. When the temperature dependence becomes important, μ^* and κ^* are often expressed in empirical relations in a nondimensional form involving reference states. So before describing them, we first nondimensionalize (2.1) - (2.9) using the following expressions,

$$\begin{aligned} \rho &= \frac{\rho^*}{\rho_r^*}, & u_i &= \frac{u_i^*}{u_r^*}, & T &= \frac{T^*}{T_r^*}, \\ p &= \frac{p^*}{\rho_r^* u_r^{*2}}, & \mu &= \frac{\mu^*}{\mu_r^*}, & \lambda &= \frac{\lambda^*}{\mu_r^*}, \\ \kappa &= \frac{\kappa^*}{\kappa_r^*}, & x_i &= \frac{x_i^*}{L_r^*}, & t &= \frac{t^*}{L_r^*/u_r^*} \end{aligned} \quad (2.10)$$

where subscript r denotes the reference variables, whose particular values are defined for each problem considered. Using (2.10) in (2.1) - (2.7), the nondimensional governing equations take the form

$$\rho_{,t} + (\rho u_i)_{,i} = 0 \quad (2.11)$$

$$\rho u_{i,t} + \rho u_j u_{i,j} = -p_{,i} + \frac{1}{Re} [(\lambda u_{j,j})_{,i} + (2\mu S_{ij})_{,j}] \quad (2.12)$$

$$\begin{aligned} \rho T_{,t} + \rho u_j T_{,j} + (\gamma - 1) \rho T u_{j,j} &= \frac{\gamma}{Pr Re} [\kappa T_{,i}]_{,i} + \\ \frac{\gamma(\gamma - 1) M^2}{Re} [\lambda S_{ii} S_{jj} + 2\mu S_{ij} S_{ij}] \end{aligned} \quad (2.13)$$

$$p = \frac{\rho T}{\gamma M^2} \quad (2.14)$$

where

$$M = \frac{u_r^*}{c_r^*}, \quad Re = \frac{\rho_r^* u_r^* L_r^*}{\mu_r^*}, \quad Pr = \frac{\mu_r^* c_r^*}{\kappa_r^*} \quad (2.15)$$

are the Mach number, Reynolds number and Prandtl number. In deriving the nondimensional energy equation (2.13), (2.9) is used to convert enthalpy to temperature. The continuity equation (2.1) along with the equation of state (2.7) are used to remove the explicit pressure dependence. The nondimensional viscosity $\mu = 1$ when it is independent of temperature, and otherwise a power law is used

$$\mu = T^n \quad (2.16)$$

where n is taken as $n = 0.70$. The second coefficient of viscosity is computed using Stokes hypothesis, $\lambda = -\frac{2}{3}\mu$ (giving zero bulk viscosity), and the thermal conductivity is determined by assuming constant Prandtl number, so that $\kappa = \mu$. Unless otherwise specified, the fluid is assumed to be air with a Prandtl number of 0.71 and a ratio of specific heats $\gamma = 1.4$.

2.2 Filtered Governing Equations

The governing equations for large eddy simulation (LES) are obtained by filtering equations (2.11)-(2.14). Let a filtered or large-scale flow quantity be denoted by an overbar

$$\bar{f}(x) = \int_D G(x - x') f(x') dx' \quad (2.17)$$

where G is some spatial filter and the integral is over the flow domain D . The velocity u_i , density ρ and temperature T can be decomposed as

$$u_i = \bar{u}_i + u'_i, \quad \rho = \bar{\rho} + \rho', \quad T = \bar{T} + T' \quad (2.18)$$

Applying the spatial filter G to equation (2.11)-(2.14) leads to

$$\bar{\rho}_{,t} + \overline{(\rho u_i)_{,i}} = 0 \quad (2.19)$$

$$\overline{\rho u_{i,t}} + \overline{\rho u_j u_{i,j}} = -\overline{p_{,i}} + \frac{1}{Re} [(\overline{\lambda u_{j,j}})_{,i} + \overline{(2\mu S_{ij})_{,j}}] \quad (2.20)$$

$$\overline{\rho T_{,t}} + \overline{\rho u_i T_{,i}} + (\gamma - 1) \overline{\rho T u_{j,j}} = \frac{\gamma}{Pr Re} \overline{[\kappa T_{,i}]_{,i}} + \frac{\gamma(\gamma - 1) M^2}{Re} [\lambda S_{ii} S_{jj} + 2\mu S_{ij} S_{ij}] \quad (2.21)$$

$$\bar{p} = \frac{\overline{\rho T}}{\gamma M^2} \quad (2.22)$$

The large-scale field equations (2.19)-(2.22) can be operationally simplified when the variables are recast in terms of Favre-filtered quantities. A Farve-filtered variable is defined as

$$\tilde{f} = \overline{\rho f} / \bar{\rho} \quad (2.23)$$

Note that

$$\overline{\rho u_i} = \overline{\rho \tilde{u}_i}, \quad \overline{\rho u_j u_{i,j}} = \overline{\rho \tilde{u}_j \tilde{u}_{i,j}}, \quad \overline{\rho u_j T_{,j}} = \overline{\rho \tilde{u}_j \tilde{T}_{,j}} \quad (2.24)$$

The stress tensor and the heat flux can be decomposed into resolved and sub-grid scale (SGS) components as follows:

$$\widetilde{\rho u_i u_j} = \overline{\rho \tilde{u}_i \tilde{u}_j} + \underbrace{\overline{\rho} (\widetilde{u_i u_j} - \tilde{u}_i \tilde{u}_j)}_{\tau'_{ij}} \quad (2.25)$$

$$\widetilde{\rho u_i T} = \overline{\rho \tilde{u}_i \tilde{T}} + \underbrace{\overline{\rho} (\widetilde{u_i T} - \tilde{u}_i \tilde{T})}_{q'_i} \quad (2.26)$$

Similar decompositions are made for the viscous terms in the momentum and energy equations and the pressure dilatation and conduction terms in energy equation. But their small scale subgrid components were neglected. When the filtering operation (2.17) is applied to homogenous directions of the flow, it commutes with the differentiation operator. In this case, the governing equations for the large-scale field become

$$\overline{\rho}_{,t} + (\overline{\rho \tilde{u}_i})_{,i} = 0 \quad (2.27)$$

$$\overline{\rho \tilde{u}_{i,t}} + \overline{\rho \tilde{u}_j \tilde{u}_{i,j}} = -\overline{p}_{,i} + \frac{1}{Re} [(\lambda \tilde{u}_{j,j})_{,i} + (2\tilde{\mu} \tilde{S}_{ij})_{,j}] - \tau'_{ij,j} \quad (2.28)$$

$$\overline{\rho \tilde{T}_{,t}} + \overline{\rho \tilde{u}_i \tilde{T}_{,i}} + (\gamma - 1) \overline{\rho \tilde{T} \tilde{u}_{j,j}} = \frac{\gamma}{Pr Re} [\tilde{\kappa} \tilde{T}_{,i}]_{,i} + \frac{\gamma(\gamma - 1) M^2}{Re} [\tilde{\lambda} \tilde{S}_{ii} \tilde{S}_{jj} + 2\tilde{\mu} \tilde{S}_{ij} \tilde{S}_{ij}] - q'_{i,i} \quad (2.29)$$

$$\bar{p} = \frac{\bar{\rho}\tilde{T}}{\gamma M^2} \quad (2.30)$$

where $\tilde{\mu}$ is the same as in (2.16) except the T is replaced by \tilde{T} . The second viscous coefficient $\tilde{\lambda}$ is still given by $\tilde{\lambda} = -\frac{2}{3}\tilde{\mu}$ and thermal conductivity $\tilde{\kappa} = \kappa$.

2.3 Dynamic Model for SGS Transport

To close the momentum and energy equation, τ'_{ij} and q'_i must be modelled. For notational convenience, the ' will be omitted in what follows. For τ_{ij} , the trace-free Smagorinsky eddy viscosity model is used

$$\tau_{ij} = \frac{1}{3}q^2\delta_{ij} - 2C\bar{\rho}\Delta^2|\tilde{S}|(\tilde{S}_{ij} - \frac{1}{3}\tilde{S}_{kk}\delta_{ij}) \quad (2.31)$$

where $q^2 = \tau_{ii}$ is the isotropic part of the SGS Reynolds stress tensor, $\tilde{S}_{ij} = \frac{1}{2}(\tilde{u}_{i,j} + \tilde{u}_{j,i})$ and $|\tilde{S}| = (2\tilde{S}_{ij}\tilde{S}_{ij})^{1/2}$. The SGS energy q^2 is parametrized using Yoshizawa's expression:

$$q^2 = 2C_I\bar{\rho}\Delta^2|\tilde{S}|^2 \quad (2.32)$$

For the q_i , the eddy diffusivity model is used

$$q_i = -\frac{C\bar{\rho}\Delta^2|\tilde{S}|}{Pr_t}T_i, \quad (2.33)$$

where the Pr_t is the SGS turbulent Prandtl number and C is the same as in (2.31). We will use dynamic procedure to compute the eddy coefficients C , C_I and SGS turbulent Prandtl number Pr_t (Moin et al., 1991). For this purpose, first define a test filter, denoted by a caret, with a width $\hat{\Delta}$ larger than that of the resolved grid filter. The test-filtered stresses \mathcal{F}_{ij} is defined by direct analogy to the stresses τ_{ij} :

$$\mathcal{F}_{ij} = \widehat{\rho u_i u_j} - (\widehat{\rho u_i})(\widehat{\rho u_j}) / \widehat{\rho} \quad (2.34)$$

By Germano's identity (Germano, 1990), the Leonard stresses \mathcal{L}_{ij} can be expressed in terms of \mathcal{F}_{ij} and $\hat{\tau}_{ij}$ as

$$\mathcal{L}_{ij} \equiv \mathcal{F}_{ij} - \hat{\tau}_{ij} = \widehat{(\rho \tilde{u}_i \tilde{u}_j)} - (\widehat{\rho \tilde{u}_i})(\widehat{\rho \tilde{u}_j}) / \widehat{\rho} \quad (2.35)$$

Since the test filter is always applied to the resolved field, all the quantities with $\hat{\cdot}$ are obtained from the computed field. So the right-hand side of (2.35) is computable from the solved variables. To determine coefficient C_I , the trace of (2.35) is used in conjunction with the model of (2.31) for \mathcal{F}_{ii} and τ_{ii} :

$$\widehat{\rho \tilde{u}_i \tilde{u}_i} - (\widehat{\rho \tilde{u}_i}) (\widehat{\rho \tilde{u}_i}) / \hat{\rho} = 2C_I (\hat{\rho} \hat{\Delta}^2 |\hat{\tilde{S}}|^2 - \Delta^2 \widehat{\rho} |\hat{\tilde{S}}|^2) \quad (2.36)$$

Hence C_I can be written as

$$C_I = \frac{\langle \widehat{\rho \tilde{u}_i \tilde{u}_i} - (\widehat{\rho \tilde{u}_i}) (\widehat{\rho \tilde{u}_i}) / \hat{\rho} \rangle}{\langle 2(\hat{\rho} \hat{\Delta}^2 |\hat{\tilde{S}}|^2 - \Delta^2 \widehat{\rho} |\hat{\tilde{S}}|^2) \rangle} \quad (2.37)$$

where $\langle \rangle$ indicates some kind of volume averaging procedure which is needed to make the determination of C_I and the other SGS coefficients well conditioned. In this LES study, $C_I = 0$ has been chosen following most of the previous studies for numerical stability.

To obtain C , we also use Smagorinsky model(2.31) for the test field stresses, i.e.

$$\mathcal{F}_{ij} - \frac{1}{3} \mathcal{F}_{kk} \delta_{ij} = -2C \hat{\rho} \hat{\Delta}^2 |\hat{\tilde{S}}| (\hat{\tilde{S}}_{ij} - \frac{1}{3} \hat{\tilde{S}}_{kk} \delta_{ij}) \quad (2.38)$$

Substituting \mathcal{F}_{ij} and τ_{ij} into (2.35), after contracting with $\hat{\tilde{S}}_{ij}$ and appropriate spatial averaging, we obtain

$$C = \frac{\langle [\widehat{\rho \tilde{u}_i \tilde{u}_j} - (\widehat{\rho \tilde{u}_i}) (\widehat{\rho \tilde{u}_j}) / \hat{\rho}] \hat{\tilde{S}}_{ij} - \frac{1}{3} \hat{\tilde{S}}_{kk} (\mathcal{F}_{mm} - \tilde{\tau}_{mm}) \rangle}{\langle -2\hat{\rho} \hat{\Delta}^2 |\hat{\tilde{S}}| (\hat{\tilde{S}}_{ij} \hat{\tilde{S}}_{ij} - \frac{1}{3} \hat{\tilde{S}}_{kk} \hat{\tilde{S}}_{mm}) + 2\Delta^2 (\widehat{\rho} |\hat{\tilde{S}}| \hat{\tilde{S}}_{ij} \hat{\tilde{S}}_{ij} - \frac{1}{3} \widehat{\rho} |\hat{\tilde{S}}| \hat{\tilde{S}}_{kk} \hat{\tilde{S}}_{mm}) \rangle} \quad (2.39)$$

where

$$\mathcal{F}_{mm} - \tilde{\tau}_{mm} = \widehat{\rho \tilde{u}_m \tilde{u}_m} - (\widehat{\rho \tilde{u}_m}) (\widehat{\rho \tilde{u}_m}) / \hat{\rho} \quad (2.40)$$

To determine Pr_t , let Q_i denote the the heat flux at the test filter scale and use the same eddy diffusivity model, it follows that

$$Q_i = \widehat{\rho \tilde{u}_i \tilde{T}} - (\widehat{\rho \tilde{u}_i}) (\widehat{\rho \tilde{T}}) / \hat{\rho} = -\frac{C \hat{\rho} \hat{\Delta}^2 |\hat{\tilde{S}}|}{Pr_t} \hat{\tilde{T}}_i \quad (2.41)$$

Substituting Q_i and q_i into(2.35), contracting with $\hat{\tilde{T}}_i$ and performing the appropriate spatial averaging, we obtain:

$$Pr_t = \frac{C \langle \hat{\Delta}^2 \hat{\rho} \hat{\tilde{T}}_i \hat{\tilde{T}}_i - \Delta^2 \widehat{\rho} |\hat{\tilde{S}}| \hat{\tilde{T}}_i \hat{\tilde{T}}_i \rangle}{\langle (\widehat{\rho \tilde{u}_i \tilde{T}} / \hat{\rho} - \widehat{\rho \tilde{u}_i \tilde{T}}) \hat{\tilde{T}}_i \rangle} \quad (2.42)$$

where C is given by (2.39).

With the dynamic SGS model, the equations for the filtered quantities now take the form

$$\bar{\rho}_{,t} + (\bar{\rho}\tilde{u}_i)_{,i} = 0 \quad (2.43)$$

$$\bar{\rho}\tilde{u}_{i,t} + \bar{\rho}\tilde{u}_j\tilde{u}_{i,j} = -\bar{p}_{T,i} + \frac{1}{Re}[(\tilde{\lambda}_T\tilde{u}_{j,j})_{,i} + (2\tilde{\mu}_T\tilde{S}_{ij})_{,j}] \quad (2.44)$$

$$\begin{aligned} \bar{\rho}\tilde{T}_{,t} + \bar{\rho}\tilde{u}_i\tilde{T}_{,i} + (\gamma - 1)\bar{\rho}\tilde{T}\tilde{u}_{j,j} &= \frac{\gamma}{PrRe}[\tilde{\kappa}_T\tilde{T}_{,i}]_{,i} + \\ &\quad \frac{\gamma(\gamma - 1)M^2}{Re}[\tilde{\lambda}\tilde{S}_{ii}\tilde{S}_{jj} + 2\tilde{\mu}\tilde{S}_{ij}\tilde{S}_{ij}] \end{aligned} \quad (2.45)$$

where

$$\bar{p}_T = \frac{\bar{\rho}\tilde{T}}{\gamma M^2} + \frac{2}{3}C_I\bar{\rho}\Delta^2|\tilde{S}|^2 \quad (2.46)$$

$$\tilde{\mu}_T = \tilde{\mu} + C\bar{\rho}\Delta^2|\tilde{S}|Re \quad (2.47)$$

$$\tilde{\lambda}_T = -\frac{2}{3}\tilde{\mu}_T \quad (2.48)$$

$$\tilde{\kappa}_T = \tilde{\kappa} + C\bar{\rho}\Delta^2|\tilde{S}|\frac{PrRe}{\gamma Pr_t} \quad (2.49)$$

This system of equations constitutes the governing equations for the large eddy simulation of compressible turbulence in the present study.

Chapter 3

Numerical Method

We describe in this chapter the numerical method of solving the compressible flow governing equations (2.43) - (2.49). The equations are discretized using a fully implicit, approximately-factorized (AF) time marching scheme in conjunction with fourth order spatial center differencing in a curvilinear coordinate. A linearized dual time sub-iteration scheme, which offers a 4 – 5 times speed-up over the usual subiteration scheme, is developed. The details of the finite difference scheme, implicit boundary conditions and other aspects such as numerical dissipation are also discussed. The numerical code is validated against the analytical, self-similar solution of stagnation point compressible boundary layer, and the computation of leading edge receptivity to sound of a flat plate compressible boundary layer.

3.1 Implicit Scheme with Linearized Subiterations

Implicit methods have been traditionally developed to compute steady state or slowly varying unsteady flows, whereas explicit methods like R-K schemes were typically the choices for time accurate computations in the past. With the growing demand for detailed flow simulations with complicated geometry particularly in the presence of solid surfaces, the high grid resolution inside boundary layers often makes the unsteady implicit method more preferable, because larger time steps can be taken than would be permitted by explicit stability limits.

For the implicit time marching scheme, we first recast the compressible

flow governing equations into a general form:

$$U_{,t} + F(U) = 0 \quad (3.1)$$

where $U = \{\rho, u, v, w, T\}^T$ is the vector of flow variables and $F(U)$ represents the nonlinear and viscous terms. With the second order backward Euler scheme, (3.1) can be written in a semi-discretized form as

$$\frac{3U^{n+1} - 4U^n + U^{n-1}}{2\Delta t} + F(U^{n+1}) = 0 \quad (3.2)$$

In the dual time formulation, a new pseudo time-derivative $U_{,\tau}$ is introduced into (3.2), i.e.

$$U_{,\tau} + \frac{3U^{n+1} - 4U^n + U^{n-1}}{2\Delta t} + F(U^{n+1}) = 0 \quad (3.3)$$

where τ is the pseudo time variable. Hence when (3.3) reach a steady state, i.e. $U_{,\tau}$, it recovers (3.2). To this purpose, we first linearize $F(U^{n+1})$ with respect to U^n

$$F(U^{n+1}) = F(U^n) + \mathcal{A}(U^n)\Delta U^n + O(\Delta U^2) \quad (3.4)$$

where $\mathcal{A}(U) = F_{,U}$ is the Jacobian of $F(U)$ and $\Delta U^n = U^{n+1} - U^n$. Typically, in a multi-dimension system, the size of the coefficient matrix \mathcal{A} , resulting from spatial discretizations, is of the the order $\sim (N_x N_y N_z)^2$, and often prohibitively expensive to be inverted directly, where N_x, N_y, N_z are number of grid points in x, y, z directions. In standard factorization (AF) method, the matrix \mathcal{A} is replaced by a sequence easily invertable matrices (Briley and McDonald, 1975; Beam and Warming, 1978) whose product recovers approximately to \mathcal{A} with factorization errors on the order of $(\Delta t)^2$. To ensure the factorization error is negligible and not to corrupt the solution, a time step far smaller than is required by time accuracy has to be used in unsteady computation.

To alleviate this problem, an inner iteration called subiteration is introduced for each physical time step of an unsteady computation (Rai, 1987; Pulliam, 1993). If the subiteration converges, the factorization error will be eliminated. For the steady state computation, subiteration enhances the stability and robustness of the AF method, whereas for unsteady computation, it will recover the desirable time accuracy. But the efficiency of the AF method now strongly depends on the convergence rate of the subiteration.

So introduce a subiteration index k and approximate $U_{,\tau}$ by first order backward Euler scheme,

$$U_{,\tau} = \frac{U^{k+1} - U^k}{\Delta\tau} \quad (3.5)$$

(3.3) becomes

$$\begin{aligned} \Delta U^k + \frac{\Delta\tau}{2\Delta t} (3U^{n+1} - 4U^n + U^{n-1}) + \\ \Delta\tau\mathcal{A}(U^n)\Delta U^n = -\Delta\tau F(U^n) \end{aligned} \quad (3.6)$$

where the $\Delta\tau$ is an appropriately chosen pseudo time step for subiteration and $\Delta U^k = U^{k+1} - U^k$. Furthermore, replacing $n+1$ by $k+1$ and subtract $\frac{3\Delta\tau}{2\Delta t}U^k$ from both sides of the 3.6, we obtain

$$\begin{aligned} \left(I + \frac{3\Delta\tau}{2\Delta t}\right)\Delta U^k + \Delta\tau\mathcal{A}(U^n)(U^{k+1} - U^n) = \\ -\frac{\Delta\tau}{2\Delta t}(3U^k - 4U^n + U^{n-1}) - \Delta\tau F(U^n) \end{aligned} \quad (3.7)$$

Finally, notice that

$$U^{k+1} - U^n = \Delta U^k + (U^k - U^n) \quad (3.8)$$

and expand $F(U^k)$ at U^n , the subiteration scheme for ΔU^k can be expressed as

$$\left[I + \frac{3\Delta\tau}{2\Delta t}I + \Delta\tau\mathcal{A}(U^n)\right]\Delta U^k = -\Delta\tau\mathcal{R}^k \quad (3.9)$$

where

$$\mathcal{R}^k = \frac{3U^k - 4U^n + U^{n-1}}{2\Delta t} + F(U^k) \quad (3.10)$$

For each physical time step, take U^n as the initial value for U^k where $k=0$ to start the subiteration. When the subiteration converges, we have $\Delta U^k \rightarrow 0$, $U^{k+1} = U^k$. The final value of U^{k+1} can be taken as U^{n+1} and $\mathcal{R}^{n+1} = 0$ recovers the second order fully implicit scheme in (3.2).

Notice that the left hand side operator in (3.9) is only a function of U^n , whereas in the standard subiteration schemes, it is a function of U^k . So (3.9) is actually linear for the subiteration variable ΔU^k (Venkateswaran et al., 1997); we can first perform the LU decomposition of the coefficient matrices and store the factored matrices in the first step and use them throughout

until the subiteration converges. This obviates the need of computing Jacobians and inverting the coefficient matrices at each subiteration step, therefore significantly improves the subiteration efficiency. Moreover, the present subiteration formulation is general in that it depends on neither the spatial discretization schemes nor the specific factorization form. Other implicit schemes than second order backward Euler can also be incorporated readily. A disadvantage of this linearized scheme is the requirement of large memory storage of the L and U . But when the algorithm is implemented on the modern parallel computers, the demand for memory is usually satisfied without major difficulties.

3.2 Approximate Factorization

As mentioned earlier, approximate factorization is needed to reduce a multi-dimension problem to a sequence of one dimension problems in terms of matrix inversion. For simplicity, we consider the governing equations in three dimensional Cartesian coordinates, where the Jacobian $\mathcal{A}(U)$ in (3.9) can be generally expressed as

$$\begin{aligned}\mathcal{A}(U) = & AU_{,x} + BU_{,y} + CU_{,z} + DU \\ & - V_{xx}U_{,xx} - V_{xy}U_{,xy} - V_{xz}U_{,xz} \\ & - V_{yy}U_{,yy} - V_{yz}U_{,yz} - V_{zz}U_{,zz}\end{aligned}\quad (3.11)$$

here the matrices (A, B, C, D, V_{ij}) are functions of U and its gradients, (see for example Collis (1997)). Substitute (3.11) into the left hand side of (3.9) and factorize it into three spatial directions, we obtain the factorized iteration scheme as follows

$$[S + \Delta\tau(A\Delta_x + D - V_{xx}\Delta_{xx})]\mathcal{P} = -\Delta\tau\mathcal{R}^k \quad (3.12)$$

$$[S + \Delta\tau(B\Delta_y - V_{yy}\Delta_{yy})]\mathcal{Q} = S\mathcal{P} \quad (3.13)$$

$$[S + \Delta\tau(C\Delta_z - V_{zz}\Delta_{zz})]\Delta U^k = S\mathcal{Q} \quad (3.14)$$

where

$$S \equiv I + \frac{3\Delta\tau}{2\Delta t} \quad (3.15)$$

and $\Delta_x, \Delta_{xx} \dots$ are the spatial differencing operators.

We can further examine the effectiveness of the factorization by rewriting (3.12 - 3.14) as a general implicit operator $\mathcal{L}(U^n)$

$$\begin{aligned}\mathcal{L}(U^n)\Delta U^k &= -\frac{\Delta\tau}{2\Delta t}(3U^k - 4U^n + U^{n-1}) \\ &\quad - \Delta\tau F(U^k)\end{aligned}\tag{3.16}$$

where

$$\begin{aligned}\mathcal{L}(U^n) &= [S + \Delta\tau(A\Delta_x + D - V_{xx}\Delta_{xx})]S^{-1} \\ &\times [S + \Delta\tau(B\Delta_y - V_{yy}\Delta_{yy})]S^{-1} \\ &\times [S + \Delta\tau(C\Delta_z - V_{zz}\Delta_{zz})]\end{aligned}\tag{3.17}$$

is a function of U^n only. Introducing the subiteration residual $e^k = U^k - \bar{U}$ where \bar{U} denotes the converged solution of subiteration, e^k satisfies the following equation:

$$\begin{aligned}\mathcal{L}(U^n)(e^{k+1} - e^k) &= -\frac{\Delta\tau}{2\Delta t}(3\bar{U} - 4U^n + U^{n-1}) \\ &\quad - \Delta\tau[F(\bar{U}) + A(\bar{U})e^k] - \frac{3\Delta\tau}{2\Delta t}e^k\end{aligned}\tag{3.18}$$

Since \bar{U} is the converged solution, the above equation is simplified as

$$\mathcal{L}(U^n)(e^{k+1} - e^k) = -[\frac{3\Delta\tau}{2\Delta t} + \Delta\tau A(\bar{U})]e^k\tag{3.19}$$

It follows that

$$e^{k+1} = \mathcal{L}^{-1}(U^n)[\mathcal{L}(U^n) - \frac{3\Delta\tau}{2\Delta t} - \Delta\tau A(\bar{U})]e^k\tag{3.20}$$

Thus the requirement for stability and convergence of the subiteration scheme is that

$$\|\mathcal{L}^{-1}(U^n)[\mathcal{L}(U^n) - \frac{3\Delta\tau}{2\Delta t} - \Delta\tau A(\bar{U})]\| \leq 1\tag{3.21}$$

which implies that

$$\mathcal{L}(U^n) \approx \frac{3\Delta\tau}{2\Delta t} + \Delta\tau A(\bar{U})\tag{3.22}$$

Therefore, in order to achieve rapid convergence, the factorized formulation \mathcal{L} needs to resemble the original unfactorized form as accurately as possible, i.e. keeping the factorization error minimum. On the other hand, as long as the subiteration converges, we obtain the second order temporal accuracy by (3.2); the particular form of the left hand matrix is only important in the sense that subiteration convergence can be achieved.

3.3 Spatial Discretization

In all the present computations, the spanwise direction z is assumed to be homogeneous. So to compute the spatial derivatives, the physical domain (x, y, z) is first transformed into a computational domain (ξ, η, z) by a two dimensional mapping $(x, y) \mapsto (\xi, \eta)$ with both ξ and η belong to $[0, 1]$. Consider derivative operators in the uniform computational space (ξ, η) , where ξ_i, η_j represent the nodal locations with $\xi_i = \Delta\xi(i - 1)$ for $1 \leq i \leq N_\xi$ and $\eta_j = \Delta\eta(j - 1)$ for $1 \leq j \leq N_\eta$. we need only to present the differencing schemes in ξ direction as it is completely analogous in the η direction.

At interior nodes, the fourth order central difference scheme is used for first and second derivatives.

$$\left(\frac{\partial f}{\partial \xi} \right)_i = \frac{1}{12\Delta\xi} [(f_{i-2} - f_{i+2}) - 8(f_{i-1} - f_{i+1})] \quad (3.23)$$

$$\left(\frac{\partial^2 f}{\partial \xi^2} \right)_i = \frac{1}{12(\Delta\xi)^2} [-(f_{i-2} - 2f_i + f_{i+2}) + 16(f_{i-1} - 2f_i + f_{i+1})] \quad (3.24)$$

Near the computational boundaries, the finite difference stencil need to be biased toward the interior. As in the interior points, a five point stencil is used at the boundary grid point ξ_1 . The resulting difference schemes are fourth and third order accurate for the first and second derivatives respectively. Hence, At the first grid point ξ_1 , the first and second derivative are expressed as :

$$\left(\frac{\partial f}{\partial \xi} \right)_1 = \frac{1}{12\Delta\xi} [-25f_1 + 48f_2 - 36f_3 + 16f_4 - 3f_5] \quad (3.25)$$

$$\left(\frac{\partial^2 f}{\partial \xi^2} \right)_1 = \frac{1}{12(\Delta\xi)^2} [11f_1 - 20f_2 + 6f_3 + 4f_4 - f_5] \quad (3.26)$$

$$(3.27)$$

while at the second point ξ_2 , they are

$$\left(\frac{\partial f}{\partial \xi} \right)_2 = \frac{1}{12\Delta\xi} [-3f_1 - 10f_2 + 18f_3 - 6f_4 + f_5] \quad (3.28)$$

$$\left(\frac{\partial^2 f}{\partial \xi^2} \right)_2 = \frac{1}{12(\Delta\xi)^2} [35f_1 - 104f_2 + 11f_3 - 56f_4 + 11f_5] \quad (3.29)$$

Similar expressions hold for the derivatives at nodes of $N_\xi - 1$ and N_ξ but with the stencils reversed and the signs switched on the coefficients for the

first derivatives. With the above fourth order discretization scheme, the left hand side in each of the (3.12) - (3.14) is a block penta-diagonal matrix, see the structures in figure 3.2 and 3.3, with additional blocks at the boundary nodes to account for high order boundary treatment. Each block is a 5×5 matrix for the five flow variables. The resulting coefficient matrix can be solved efficiently using direct Gaussian elimination method.

After the derivative is obtained in the computational space, they are converted to the physical space through the metrics of the mapping function. For first order derivative, it follows

$$\left\{ \begin{array}{c} \frac{\partial}{\partial x} \\ \frac{\partial}{\partial y} \end{array} \right\} = \left[\begin{array}{cc} \xi_x & \eta_x \\ \xi_y & \eta_y \end{array} \right] \left\{ \begin{array}{c} \frac{\partial}{\partial \xi} \\ \frac{\partial}{\partial \eta} \end{array} \right\} \quad (3.30)$$

and similarly for second derivative

$$\left\{ \begin{array}{c} \frac{\partial^2}{\partial x^2} \\ \frac{\partial^2}{\partial x \partial y} \\ \frac{\partial^2}{\partial y^2} \end{array} \right\} = \left[\begin{array}{ccc} (\xi_x)^2 & 2\xi_x \eta_x & (\eta_x)^2 \\ \xi_x \xi_y & \xi_x \eta_y + \xi_y \eta_x & \eta_x \eta_y \\ (\xi_y)^2 & 2\xi_y \eta_y & (\eta_y)^2 \end{array} \right] \left\{ \begin{array}{c} \frac{\partial^2}{\partial \xi^2} \\ \frac{\partial^2}{\partial \xi \partial \eta} \\ \frac{\partial^2}{\partial \eta^2} \end{array} \right\} + \left[\begin{array}{cc} \xi_{xx} & \eta_{xx} \\ \xi_{xy} & \eta_{xy} \\ \xi_{yy} & \eta_{yy} \end{array} \right] \left\{ \begin{array}{c} \frac{\partial}{\partial \xi} \\ \frac{\partial}{\partial \eta} \end{array} \right\} \quad (3.31)$$

where (ξ_x, η_x, \dots) are metrics of the mapping transformation. Most of mapping functions are given in an explicit form of $x = x(\xi, \eta)$, $y = y(\xi, \eta)$ instead of $\xi = \xi(x, y)$, $\eta = \eta(x, y)$. In such cases, the metrics terms (ξ_x, η_x, \dots) can be obtained by solving the linear system of equations resulting simply by substituting the coordinates x, y into the operators (3.30) and (3.31). Computational experience also shows that the x_ξ, y_η, \dots in the metrics expression should be computed using the same differencing scheme as those for the flow variables to achieve improved accuracy (Fletcher, 1991)

Since the subiteration is in fact a steady state problem, to accelerate the subiteration convergence, the pseudo time step size $\Delta\tau$ can be allowed to vary spatially. In a general curvilinear coordinates, taking into account the physical domain of dependence within a computation cell, the $\Delta\tau$ are chosen by

$$\Delta\tau = CFL \frac{\Delta\xi \Delta\eta}{\Lambda} \quad (3.32)$$

where

$$\begin{aligned} \Lambda &= |J_{1i}\bar{u}_i|\Delta\eta + |J_{2i}\bar{u}_i|\Delta\xi + \bar{c} \\ &\times [(J_{11}^2 + J_{12}^2)\Delta\eta^2 + (J_{21}^2 + J_{22}^2)\Delta\xi^2]^{1/2} \end{aligned} \quad (3.33)$$

$\Delta\xi, \Delta\eta$ are the cell size in the computational domain; \bar{c} is the mean speed of sound. This definition of λ includes the convective and acoustic phenomena but ignores viscous diffusion. The *CFL* in (3.32) is specified by a uniform physical time step Δt for unsteady computations which is independent of $\Delta\tau$ and should reflect the time resolution requirements for the physical process of interest.

Figure 3.4 shows a typical comparison of the convergence history between the present and standard subiteration schemes. After first subiteration step, the present scheme store the LU decomposition of the block penta diagonal matrix and use them in the subsequent steps. For a four order of magnitude of residual reduction, a factor of 4 – 5 speed-up is achieved in comparison with the standard subiteration scheme. Note the jump of residual at last points of the two curves correspond to the beginning of the next physical step.

3.4 Boundary Conditions

Boundary conditions are introduced to replace the governing equations at the inflow, outflow and the wall boundary of the computational domain, see figure 3.1.

Consider an arbitrary boundary constraint at time level $n+1$ on the flow variable $U = \{\rho, u, v, w, T\}$

$$\mathcal{B}(U^{n+1}) = 0 \quad (3.34)$$

The general implicit treatment of boundary conditions in terms of $\delta U = U^{n+1} - U^n$ can be written as

$$\left(\frac{\partial \mathcal{B}}{\partial U} \right)^n \delta U = -\mathcal{B}(U^n) \quad (3.35)$$

For example, the no-slip and isothermal boundary conditions are always enforce at the wall, for which (3.35) becomes

$$\delta u_i^n = -u_i^n = 0, \quad \delta T^n = -T^n = -T_w \quad (3.36)$$

. The density at the wall is obtained by solving the continuity equation.

The boundary conditions at inflow are needed to provide both the far field mean flow and to introduce disturbances or free stream turbulence in to the computational domain. According to characteristic analysis, for a subsonic

flow, four incoming quantities must be specified with one outgoing quantities computed from the interior domain. The specific choice of these quantities depends on the formulation of each problem. Here we constrain the entropy, spanwise and tangential velocity, and the incoming Riemann invariant. The outgoing Riemann invariant are computed by first order extrapolation from the neighboring points inside the boundary. The locally one-dimensional Riemann invariants are defined in the direction normal to the inflow boundary as

$$R_1 = v_n - \frac{2c}{\gamma - 1}, \quad R_2 = v_n + \frac{2c}{\gamma - 1} \quad (3.37)$$

where c is the local speed of sound and v_n is the velocity normal to the boundary. So at the inflow boundary,

$$\begin{aligned} s &= s_\infty, \quad w = w', \quad v_t = \bar{v}_t + v'_t, \\ R_1 &= \bar{R}_1 + R'_1, \quad R_2 = R_{2int} \end{aligned} \quad (3.38)$$

here the overline quantities denote the base flow in the absence of inflow disturbance; primed quantities represent the disturbance to be introduced into the domain, and the subscript t denotes the tangential velocity along the inflow boundary in the $x-y$ plane. In the present configuration, the inflow is place close to the body to reduce computational cost, and the flow passage is chosen to have significant blockage to mimic the wind tunnel experiments, so the potential solution should not be used directly to form the incoming Riemann invariant because of the development of the boundary layer on the body. Therefore, we first compute the two dimensional steady base flow using the same set of the inflow conditions but in the absence of disturbance. The velocities \bar{v}_t and \bar{v}_n are determined by

$$\bar{\omega} = 0, \quad \bar{v}_n = v_{np} \quad (3.39)$$

Here ω is the vorticity at the inflow and v_{np} denote the normal velocity obtained from the potential solution. These overline quantities are used to form the \bar{R}_1 and the primed quantities are interpolated from the precomputed disturbance flow field. The interpolation is implemented using fourth order B-spline. The R_{2int} are computed from the interior domain by first order extrapolation $R_{2int} = 2R_{2N-1} - R_{2N-2}$. When the Riemann invariants are obtained, the values of v_n and c are obtained as follows.

$$v_n = \frac{1}{2}(R_{1n} + R_{2i}), \quad c = \frac{\gamma - 1}{2}(R_{1n} - R_{2i}) \quad (3.40)$$

At the outflow, we follow Collis (1997) and use the parabolized Navier-Stokes equations, i.e. the streamwise second order derivatives in the equations are neglected. In addition, the streamwise pressure gradient is provided by the corresponding potential solution at the exit. This treatment is found to yield a adequate and stable outflow boundary conditions for the laminar mean flow and turbulence computations.

In the spanwise direction, periodic boundary condition is always imposed in the present study.

3.5 Numerical damping

The function of numerical dissipation, either implicitly contained in the differencing scheme like upwind scheme, or explicitly added to the discretized equations, is to damp the unresolved high wave number components generated by nonlinear flow interaction. Because of the symmetric stencil, the center finite differencing scheme in the present spatial discretization is by itself nondissipative. In large eddy simulation of turbulence, these high wave number components are constantly generated and, if left uncontrolled, leads to numerical instability. To overcome the problem and prevent the unresolved components from corrupting the numerical solution, the following numerical dissipation terms are added to the right hand side of the equation:

$$D = -\epsilon_d \sigma_d(\xi, \eta) \left(\Delta \xi^4 \frac{\partial^4 U}{\partial \xi^4} + \Delta \eta^4 \frac{\partial^4 U}{\partial \eta^4} + \Delta_z^4 \frac{\partial^4 U}{\partial z^4} \right) \quad (3.41)$$

where ϵ_d is the amplitude of the added dissipation, and $0 \leq \sigma_d \leq 1$ control and range of the dissipation. Typically in laminar computation, such numerical dissipation is not needed because the spatial scales of the flow is to some extent known *a priori*; grid can usually be generated with enough resolution. But numerical dissipation is generally needed in turbulence simulations to ensure numerical stability. But care must be taken to ensure the added numerical dissipation is minimum and it does not deteriorate the resolved solution. For this purpose, we choose ϵ_d in such way that the magnitude of the added D_n terms is significantly smaller than the that of the truncation error of the underlying spatial difference scheme. Based on modified wave number analysis, this is achieved by choosing

$$\epsilon \leq 0.01 N_g \quad (3.42)$$

where $N_g = (N_\xi + N_\eta + N_z)/3$ is the averaged number of grid points in one spatial direction. A more detailed discussion on this matter can be found in the appendix B.

3.6 Potential Flow solution

Two dimensional potential solution is needed in the present computation to provide necessary initial and boundary conditions for corresponding viscous computations. Let ϕ be the velocity potential such that

$$u = \phi_{,x}, \quad v = \phi_{,y} \quad (3.43)$$

the potential equation in a nonconservative form may be written as

$$(1 - M_x^2)\phi_{,xx} + (1 - M_y^2)\phi_{,yy} - 2M_x M_y \phi_{,xy} = 0 \quad (3.44)$$

where $M_x = u/c$, $M_y = v/c$ and $c = \sqrt{T}/M$ with T computed from the isentropic relation

$$T = 1 + \frac{(\gamma - 1)M^2}{2}(1 - u^2 - v^2) \quad (3.45)$$

and $M = u_\infty/c_\infty$ is the free stream Mach number. The no-penetration condition.

$$\frac{\partial \phi}{\partial n} = 0 \quad (3.46)$$

At inflow and outflow, the potential function is set to the values corresponding to the free stream values. The solution of the potential flow equation are obtained using the same approximately factorized implicit method with the fourth order finite difference scheme for spatial discretization.

3.7 Similarity Solutions

We choose the self-similarity analytic solutions of compressible boundary layer with heat transfer near a blunt leading edge (Reshotko and Beckwith, 1957) to validate the present numerical method in steady computations. The detailed derivations of the self-similar equations based on Stewartson-Illingworth transformation are given in the appendix. The boundary layer

velocity and enthalpy profiles at a circular leading edge is computed numerically with different Mach numbers, Prandtl number and different temperature ratio between the wall and incoming flow used. As required to possess a similarity solution, the viscosity is assumed to be a linear function of temperature. The computational grid in the x-y plane is generated by using an algebraic multi-surface method (Fletcher, 1991) which gives desirable orthogonality at the body surface and at the inflow/outflow boundaries. The grid is clustered towards the wall and the leading edge.

Figure 3.5 to figure 3.8 show the velocity and enthalpy profiles of the stagnation point boundary layer for $Pr = 1$. The wall temperature is set twice of the total temperature of the incoming flow, i.e. $T_w/T_0 = 2$. It can be seen that for both Mach numbers, $Ma = 0.1$ and $Ma = 0.8$, excellent agreement of the velocity and enthalpy profiles are obtained between the numerical and analytic solution. When $Pr \neq 1$, similarity solution exists in a strict sense only when the external velocity is zero, i.e. $u_e = 0$. This corresponds to the stagnation plane $y = 0$. So figure 3.9 and 3.10 show the enthalpy profiles for both Mach numbers at $Pr = 0.7$ and $T_w/T_0 = 0.5$, and again excellent agreement is reached between the numerical and analytic solutions.

3.8 Leading Edge Receptivity to Sound

Receptivity is defined as a process by which external flow disturbances are converted into instability waves (Morkovin, 1969). For flat plate boundary layer flow, the sound receptivity refers the generation of instability T-S waves inside the boundary layer by ambient acoustic waves. In low Mach number case, this process represents a change in characteristic flow length scale — from an acoustic, fast travelling, long-wavelength mode in free stream to a convective, slow-travelling and short wavelength T-S wave mode in the boundary layer. This conversion can be effectively realized when the leading edge of the flat plate is blunt.

The numerical solution of sound receptivity in a compressible boundary layer on a flat plate with a super ellipse leading edge (Lin, 1992; Collis, 1997) is presented here. Unlike the usual numerical approach for receptivity study in which the computation is based on linearized governing equations about a base flow, here the full nonlinear N-S equations are used both for the base flow and the disturbance computations. The evolution of the disturbance

is obtained by subtracting the base solution from the instantaneous solution. By comparing with results obtained through linear approaches, this computation provides a validation case for the present numerical method in unsteady flow simulations.

The flow configuration and the computational domain, including the surrounding inflow and outflow sponges, are shown schematically in figure 3.11. The inflow sponge is used to introduce acoustic waves with specified frequency and amplitude, whereas the outflow sponge damps spurious waves reflected from the outflow boundary. The geometry of the leading edge is defined by a super ellipse:

$$\left(\frac{x}{a}\right)^m + \left(\frac{y}{b}\right)^2 = 1 \quad (3.47)$$

where the a and b are the half major and minor axes of the super-ellipse. The junction between the leading edge and the flat plate is chosen to be $x = 0$, and the parameter m , controlling the smoothness of the junction, is taken as $m = 4$. The reference length scale is chosen to be a and the aspect ratio of the super ellipse is 6. The stagnation point is therefore at $x = -1$ and the surface of the plate is $y = b = 1/6$. Based on the free-stream velocity u_∞ and a , the Reynolds number $Re = u_\infty a / \nu$ is 14400. The free stream Mach number is $M = 0.1$. The Prandtl number is chosen as $Pr = 0.71$ and a power law $\mu = T^{0.70}$ is used for the viscosity. The wall is isothermal and the temperature equals to the free stream stagnation temperature. The number of grid points in streamwise direction is 481 and in wall normal direction 129. The grid is clustered near the wall and towards the leading edge with about 35 points across the boundary layer and 20 points per T-S wavelength.

To obtain the correct disturbance field, the base flow must first be a well converged solution to the N-S equations. In other words, the evolution of the full solution must be dominantly due to the evolution of the disturbance. Any changes of the mean flow part in the unsteady computation should be negligible compared to the disturbance itself. In the present computation, the mean flow is judged steady after the residue has dropped 8 orders of magnitude from its initial value. The mean flow wall vorticity ω_w and the streamwise pressure gradient $\partial p / \partial s$ at the wall are shown in figure 3.12 and 3.13, here s is the arc length of the surface from the stagnation point. The results are compared with those from Collis (1997) and the agreements are very good. In figure 3.14, the streamwise velocity profile at $x = 2.783$ is shown as a function of the Blasius variable η_b , defined as $\eta_b = y \sqrt{Re/(x+1)}$.

Again, the present result agrees well with Collis (1997).

After the base flow is obtained, acoustic wave is introduced through the inflow sponge at a frequency $\omega = 3.312$ and amplitude $A = 0.001$. With the mean flow Mach number $M = 0.1$, the downstream acoustic wave length is $\lambda_a = 20.833$. In the the sponge region, the following term is added to the right hand side of the N-S equations,

$$S = \sigma(\xi, \eta) [U(x, y, z, t) - U_{ref}(x, y, z, t)] \quad (3.48)$$

where the U_{ref} is an arbitrary reference state. For the inflow sponge U_{ref} is the base flow plus the acoustic wave, whereas for the outflow sponge, only the base flow itself. σ controls the distribution and strength of the sponges. Following Collis (1997), for the inflow sponge in η direction

$$\sigma(\eta) = A_s \left(\frac{\eta - \eta_s}{\eta_t - \eta_s} \right)^{N_s} \quad (3.49)$$

where η_s and η_t are the locations where the sponge starts and ends. $\sigma(\eta) \equiv 0$ for η outside (η_s, η_t) . The outflow sponge in ξ direction is constructed similarly. In the present computation, N_s is chosen to be 3; A_s is 50 for the inflow sponge and 100 for the outflow sponge. The time marching scheme is the second order backward Euler scheme with linearized sub-iterations. For the unsteady computation, Δt is chosen to be around 1000 time steps per acoustic period and four sub-iterations are used in each time step.

The overall disturbance flow fields in the boundary layer contains not only the excited T-S wave, but also the incoming and scattered acoustic waves. To extract the T-S wave, we need first remove the the acoustic component from the total solution. In low mach number flows, such a procedure was introduced by Wlezien (1994). The basic idea is that, in low Mach number flows the effect of the acoustic wave can be considered, due to its long wave length compared with the T-S wave, as to change the center of the circular orbit in the velocity phase plane for the T-S wave. By tracking and subtracting this center movement, the correct amplitude of the T-S wave can be recovered. This procedure works well for the T-S waves on the flat portion when vertical velocity is used to denote the T-S wave signal, but does not work in the curved leading edge region, or in high Mach number flows where the wave lengthes for the acoustic and T-S waves are comparable.

An instantaneous disturbance field is shown in figure 3.15 (excluding the sponge region) after the flow has reached a periodic state driven by the acoustic wave. The incident acoustic wave are clearly shown from ρ and u contours

away from the plate. The v contours show the generation and downstream development of the T-S wave inside the boundary layer. Generated at the leading edge, the T-S wave pattern becomes clearly visible on the flat portion of the wall, where the vertical component of the acoustic velocity is negligible. In the leading edge region itself, however, the scattered acoustic wave is of the same or greater order of magnitude than the T-S wave; the two velocity components can not be cleanly separated.

Figure 3.16 shows the local maximum of the amplitude of vertical component of total disturbance velocity and the extracted acoustic component as functions of x . The solutions from Collis (1997) are also plotted for comparison. The total disturbance amplitudes follow almost identical shape along x , with the present solution slightly lower. The acoustic wave components compares very well throughout out the domain.

By subtracting the acoustic components from the total disturbance solution, the amplitude of the T-S wave is shown in figure 3.17. The results from Lin (1992) for incompressible flow and from Collis (1997) are also plotted. Again, we can see that three computations follow similar shapes with some small quantitative differences. Given the great sensitivity of the growth rate of the T-S wave, the difference is considered to be acceptable, and the overall agreement is satisfactory.

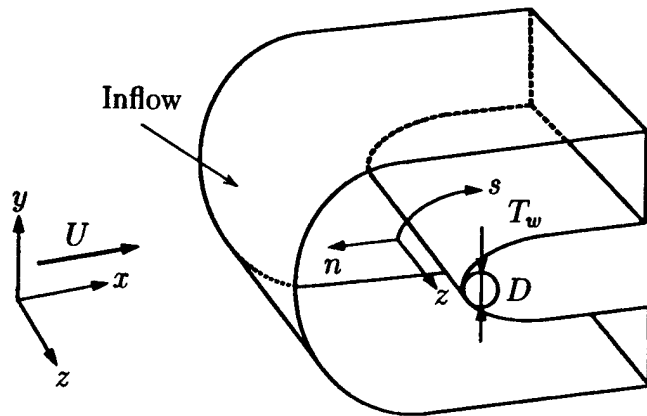


Figure 3.1: Flow configuration and inflow, outflow and wall boundary

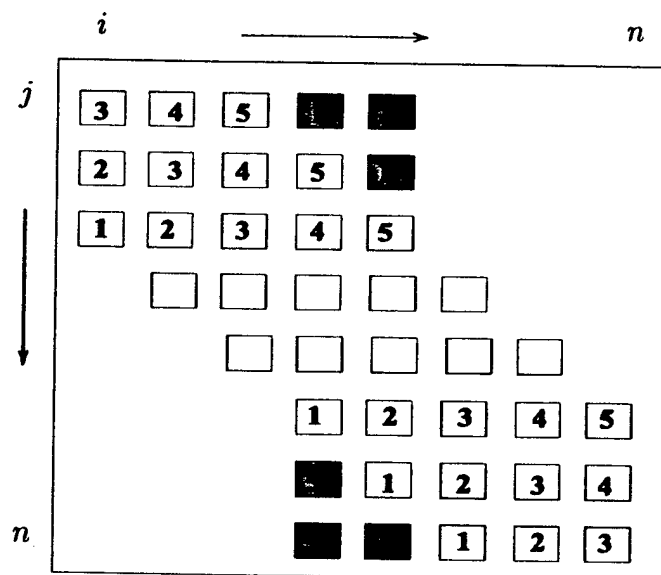


Figure 3.2: The structure of block penta-diagonal coefficient matrix resulting from implicit fourth order finite difference scheme. Each block is a 5×5 matrix.

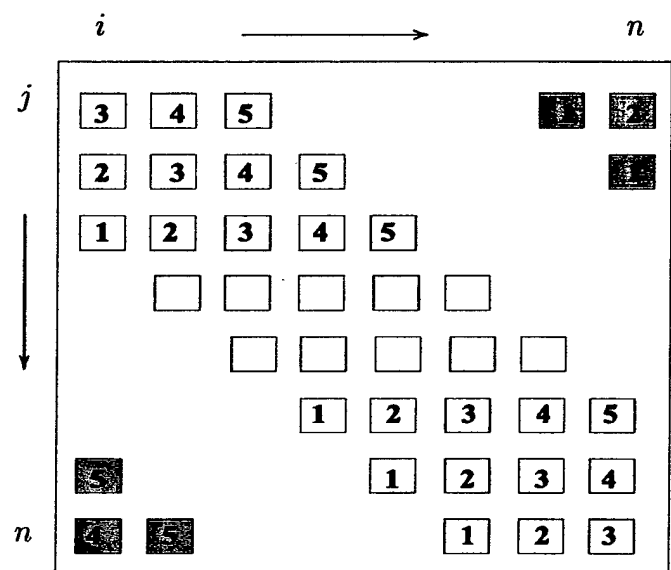


Figure 3.3: The structure of periodic block penta-diagonal coefficient matrix resulting from implicit fourth order finite difference scheme. Each block is a 5×5 matrix.

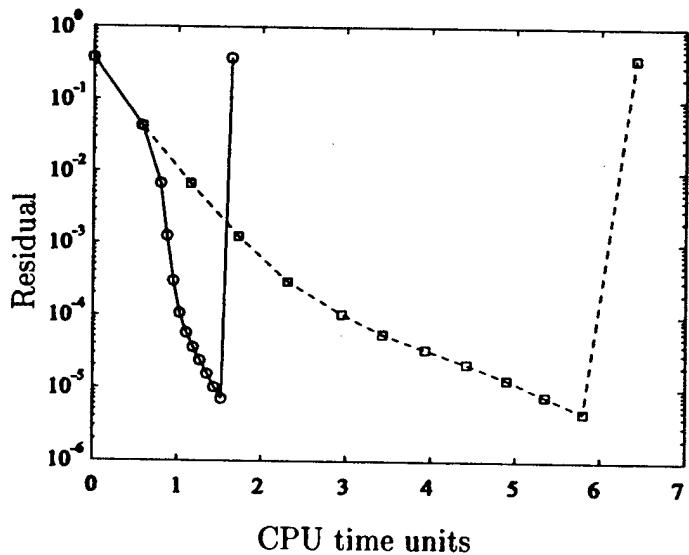


Figure 3.4: Comparison of the convergence history between the present and standard subiteration schemes. —: present linearized subiteration. - - -: standard subiteration, symbols stand for each subiteration step.

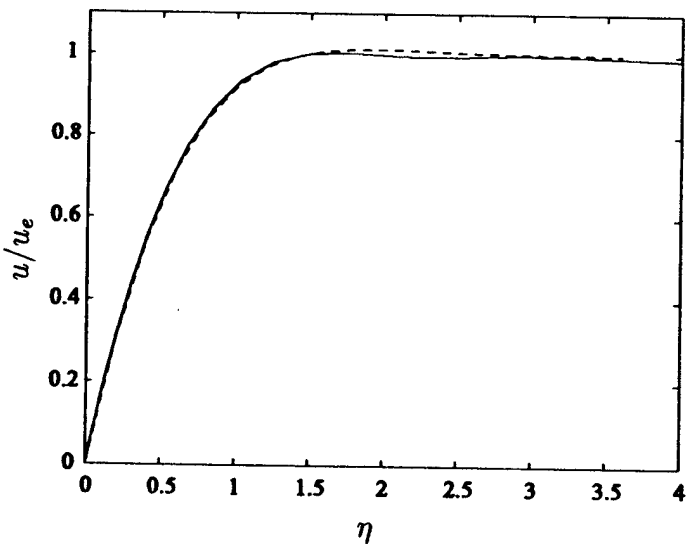


Figure 3.5: Comparison of boundary layer velocity profile at the leading edge. $Re = 10^5$, $M = 0.15$, $T_w/T_0 = 2.0$, $Pr = 1.0$. —: computation, - - -: similarity solution

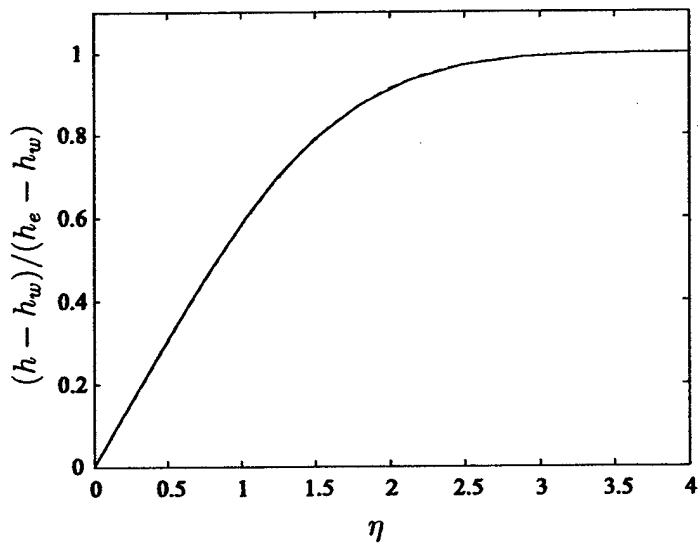


Figure 3.6: Comparison of boundary layer enthalpy profile at the leading edge. $Re = 10^5$, $M = 0.15$, $T_w/T_0 = 2.0$, $Pr = 1.0$. —: computation, - - -: similarity solution

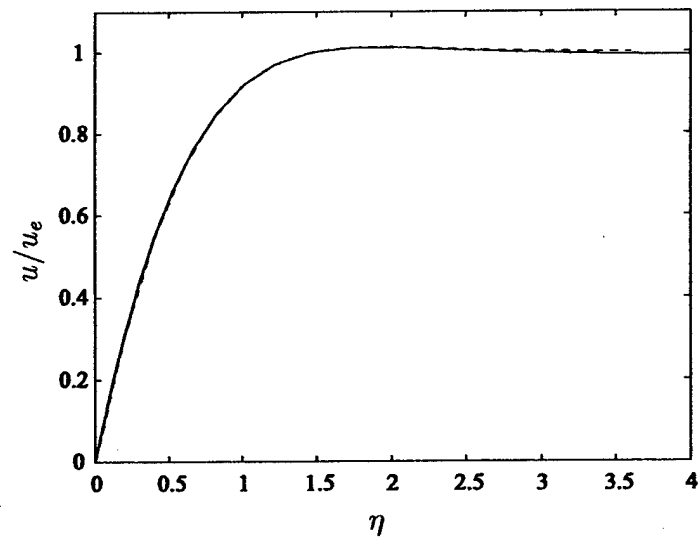


Figure 3.7: Comparison of boundary layer velocity profile at the leading edge. $Re = 10^5$, $M = 0.8$, $T_w/T_0 = 2.0$, $Pr = 1.0$. —: computation, - - -: similarity solution

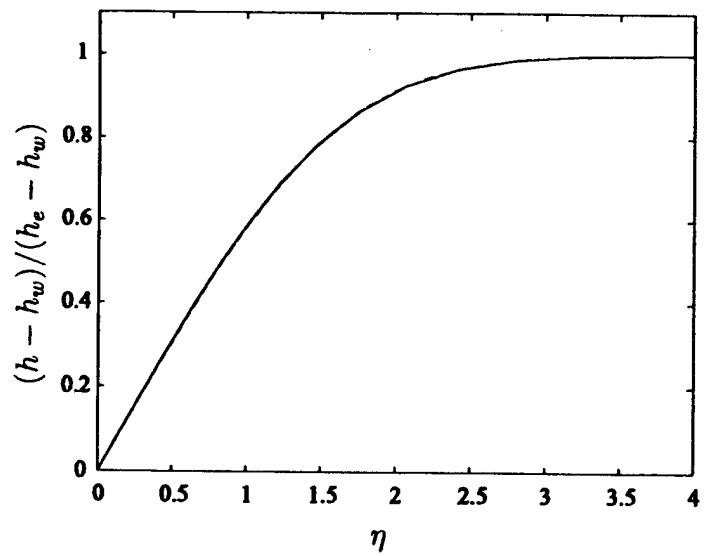


Figure 3.8: Comparison of boundary layer enthalpy profile at the leading edge. $Re = 10^5$, $M = 0.8$, $T_w/T_0=2.0$, $Pr = 1.0$.——: computation,
----: similarity solution

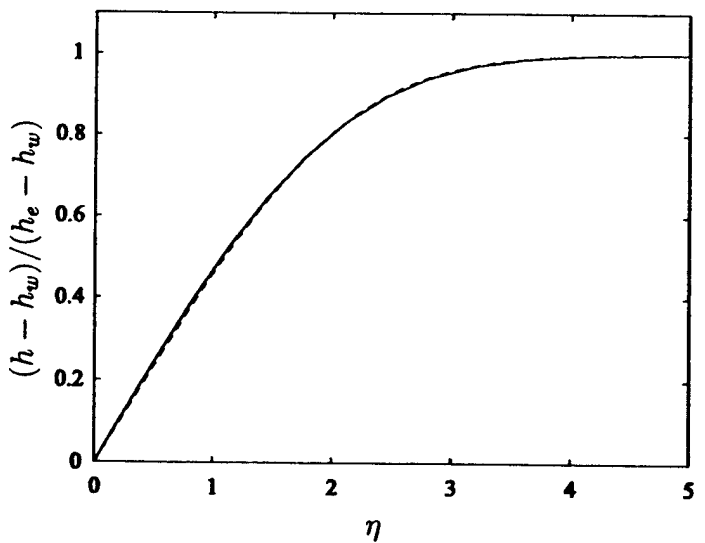


Figure 3.9: Comparison of boundary layer enthalpy profile at the leading edge. $Re = 10^5$, $M = 0.15$, $T_w/T_0=0.5$, $Pr = 0.7$.——: computation,
----: similarity solution

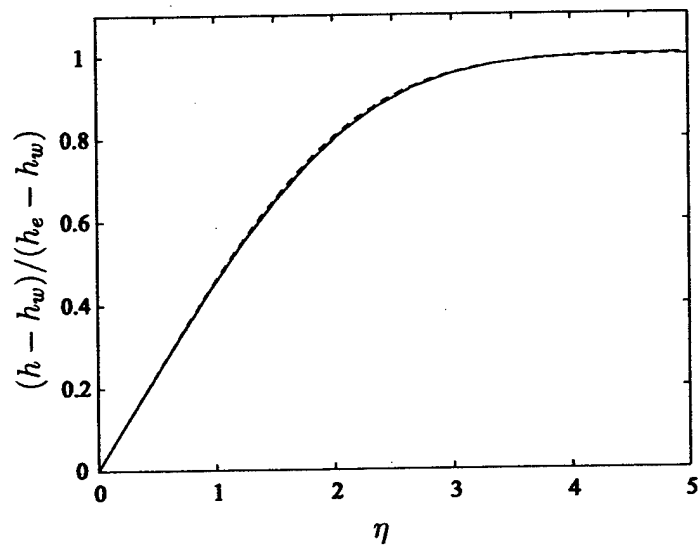


Figure 3.10: Comparison of boundary layer enthalpy profile at the leading edge. $Re = 10^5$, $M = 0.8$, $T_w/T_0 = 0.5$, $Pr = 0.7$. —: computation, - - -: similarity solution

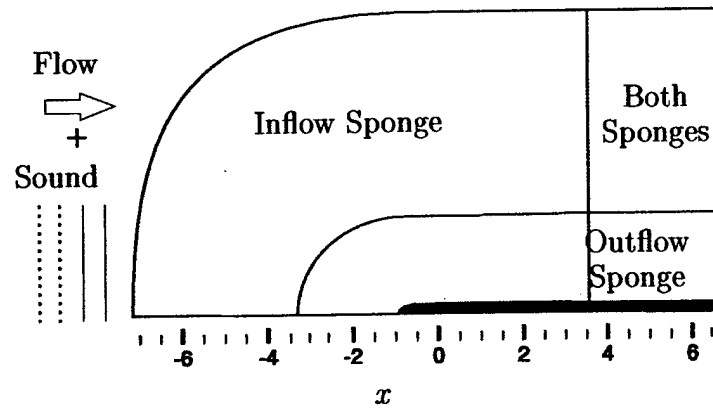


Figure 3.11: Schematic of computational domain and the inflow and outflow sponges.

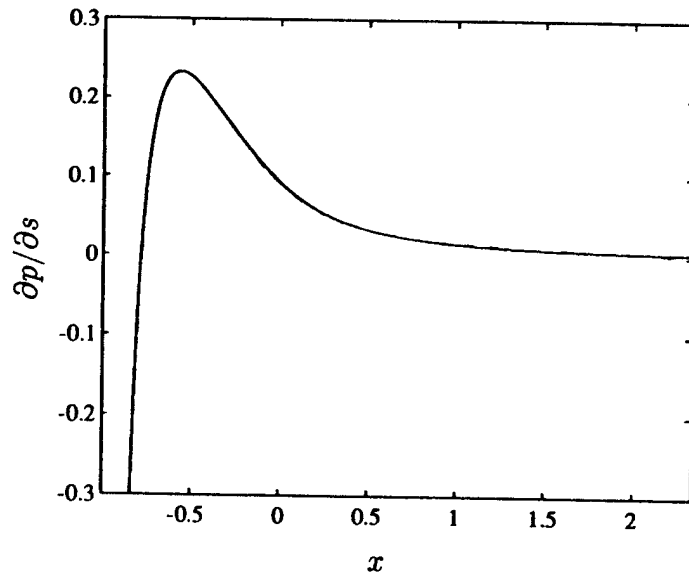


Figure 3.12: Pressure gradient $\partial p / \partial s$ along the plate. —, present computation, -----, result of Collis (1997).

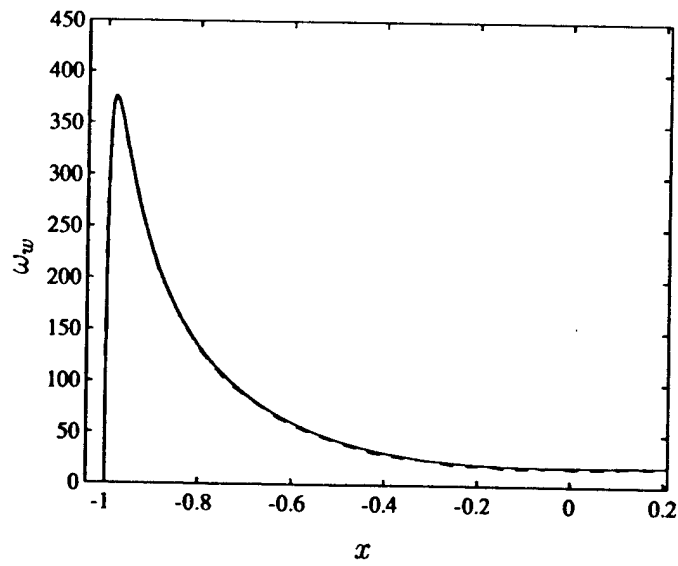


Figure 3.13: Comparison of the wall vorticity ω_{wall} . —, present computation, -----, result of Collis (1997).

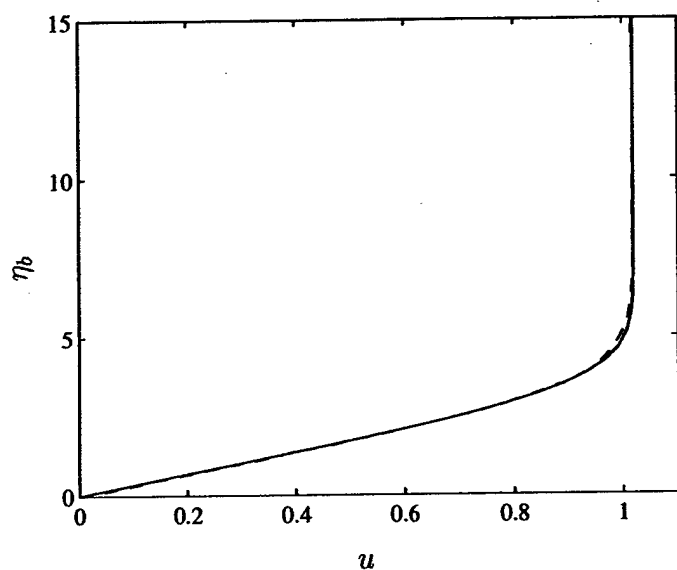


Figure 3.14: Streamwise velocity profile at $x = 2.783$. —, present computation, - - -, result of Collis (1997).

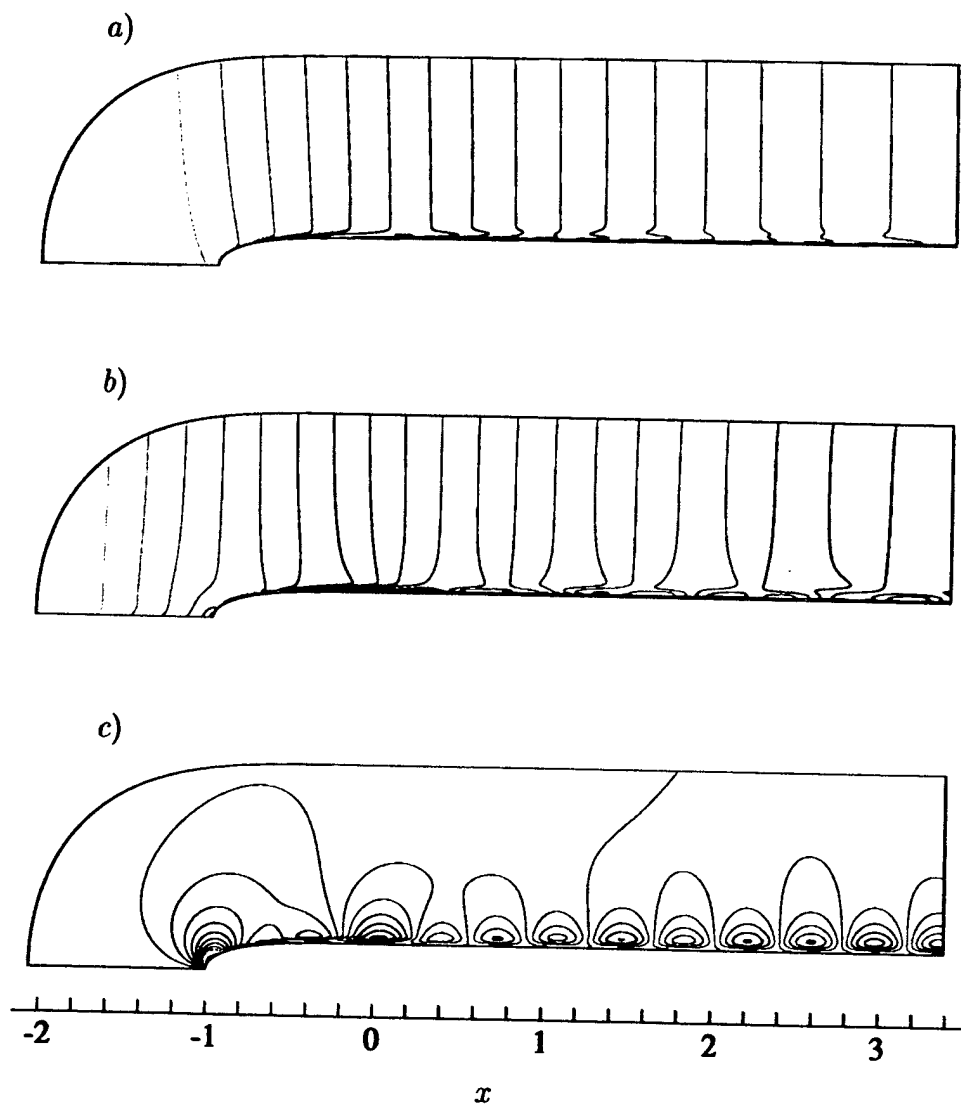


Figure 3.15: Disturbance flow fields of sound receptivity on a flat plate with a super-ellipse leading edge. a) density ρ , b) streamwise velocity u , c) vertical velocity v . Contour levels: $\rho_{max} = 5.07 \times 10^{-5}$, $\rho_{min} = -9.32 \times 10^{-5}$, $\Delta\rho = 7.59 \times 10^{-6}$. $u_{max} = 4.80 \times 10^{-4}$, $u_{min} = -9.20 \times 10^{-4}$, $\Delta u = 6.55 \times 10^{-5}$. $v_{max} = 1.17 \times 10^{-4}$, $v_{min} = -3.90 \times 10^{-4}$, $\Delta v = 8.16 \times 10^{-6}$.

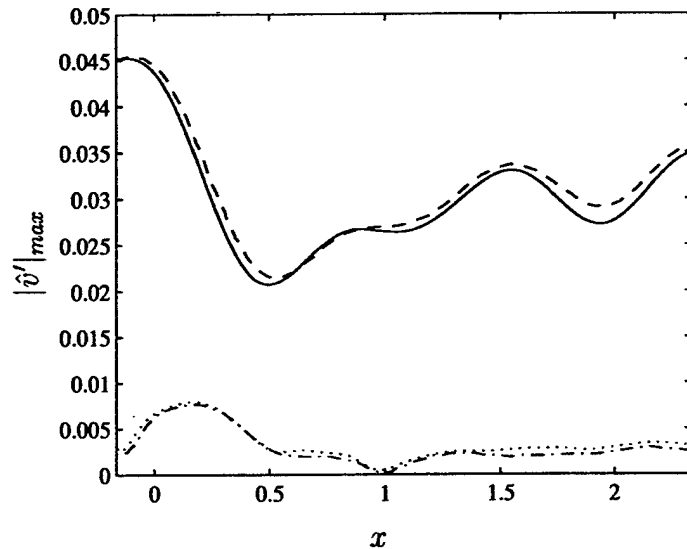


Figure 3.16: Local maximum of the amplitude of vertical component of disturbance velocity and the acoustic components. —: total disturbance. ——: acoustic component. -----and ·····: results of Collis (1997).

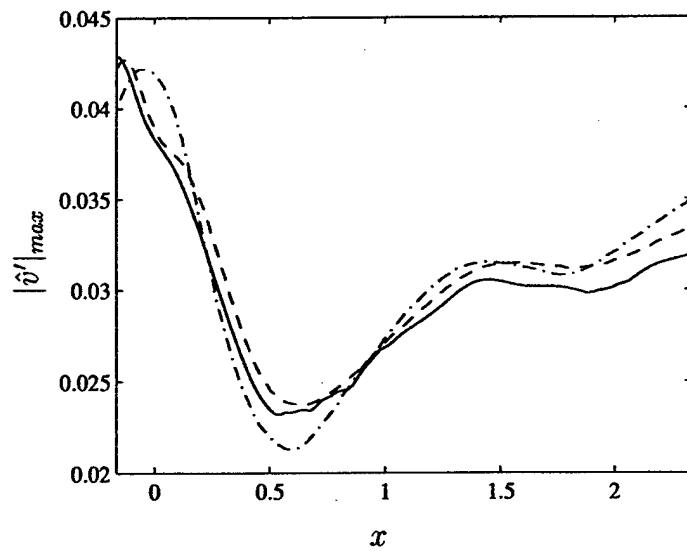


Figure 3.17: Local maximum of the amplitude of the T-S wave based on the vertical disturbance velocity. —: present computation. -----: result of Collis (1997). ——: result of Lin (1992).

Chapter 4

Generation of Free Stream Turbulence

In this chapter, we describe the methodology of generating free stream turbulence for the main large eddy simulations. In order to avoid the artificial periodicity of recycling the same free stream turbulence data, a series of independent but statistically identical, homogeneous and isotropic turbulence data sets are first computed. With the same specified length scale and intensity, they are concatenated by a blending procedure to form a sufficiently long time record for the main LES. Turbulence statistics before and after the blending shows that the blending procedure is a simple yet effective way of generating free stream turbulence.

4.1 Inflow Turbulence

Consider compressible turbulent flow in an arbitrary domain Ω (as shown in figure 4.1) with a nominally uniform mean flow outside Ω . The coordinate system (x, y, z) is such that the mean stream is aligned with the x -axis. The boundary $\partial\Omega$ of the domain Ω may be split into three parts: a) an inflow boundary $\partial\Omega_i$, b) an outflow boundary $\partial\Omega_o$, and c) the wall boundary $\partial\Omega_w$. These parts satisfy the requirement $\partial\Omega = \partial\Omega_i \cup \partial\Omega_o \cup \partial\Omega_w$. Turbulence is convected into the domain Ω by the mean velocity \mathbf{U} across the inflow boundary $\partial\Omega_i$.

The incoming stream is assumed to consist of a “frozen” turbulent field being carried by the mean. The time varying boundary condition on $\partial\Omega_i$

may then be obtained from the frozen field by converting, through Taylor's hypothesis, the x -coordinate to time (Lee et al., 1993). The problem then reduces to accurate description of the "frozen" field. The simplest approach is to obtain a realistic turbulence field by a separate calculation of homogenous isotropic turbulence with desired characteristics (Reynolds number, length scale, intensity etc.). However, this approach may turn out to be very expensive. For example, in the free-stream turbulence(FST)-induced bypass transition of a boundary layer, statistical convergence requires at least six flow through times; the domain for inflow turbulence simulation is thus $\sim 6L_x \times L_y \times L_z$ in size. If the resolution for the isotropic turbulence is the same as the main simulation, the inflow turbulence calculation becomes six times larger than the problem of interest, making this approach impractical.

This limitation may be overcome by catenating, in random order, isotropic turbulence in smaller boxes provided that the catenation is carried out without significant modification of turbulence characteristics. By exploiting isotropy and reusing individual boxes, a long time record can be generated with a limited number of realizations. Compared to the brute force method, this procedure is not only cheaper, but also capable of generating inflow turbulence with time varying characteristics. We first describe the large eddy simulation of the individual realizations, and then develop the the blending procedure to concatenate these realizations and form the long time record.

4.2 LES of homogeneous isotropic turbulence

The individual isotropic homogeneous turbulence data are computed by separate large eddy simulations. The numerical LES code is adapted from an existing DNS code (Lui and Lele, 2001) by incorporating the same dynamic SGS model described in Chapter 2. The temporal and spatial discretization is fourth order Runge-Kutta method and sixth order compact finite difference scheme (Lele, 1992). Periodic boundary conditions are applied in all spatial directions. The initial condition is a solenoidal velocity field with uniform density and temperature field. The initial three dimensional energy spectrum is of the form

$$E(\kappa) \propto \kappa^4 \exp[-2(\kappa/\kappa_p)^2] \quad (4.1)$$

where the peak wave number κ_p is equal to 4. After first validating the LES code against both the DNS of Lee et al. (1991) and the experiment of Comte-Bellot and Corrsin (1971), we apply the simulation to a rectangular

box of the size $1.6D$, $1.6D$ and $0.4D$ in x , y and z direction, where D is the diameter of the elliptic leading edge to be placed in the domain of the primary simulation. Note that the spanwise box size $0.4D$ is chosen to be the same as in the primary simulation. To preserve the isotropy of the turbulence, the grid size is chosen to be $128 \times 128 \times 32$, i.e. $\Delta x = \Delta y = \Delta z$. A few small wave numbers which represent the long waves permissible in the x and y directions but not in z are zeroed out initially to preserve the turbulence isotropy. After the turbulence statistics such as intensity and length scale reach predetermined values, snapshots of instantaneous flow fields are taken as one turbulence realization.

To compare directly with experimental measurements, throughout this report the turbulence integral scale L is determined by a least-squares curve-fitting to the autocorrelation data using an exponential function (Van Fossen et al., 1995)

$$R(r) = e^{-r/L} \quad (4.2)$$

Data between $0.33 \leq R(r) \leq 1.0$ were used for curve fitting. The exponential function does not have the correct limiting behavior for very small values of r , but the fit is satisfactory over the main portion and the fitted $R(r)$ can be integrated from 0 to ∞ to give the turbulence integral length scale. Figure 4.2 shows the initial and final three dimensional energy spectrum, where the small scale turbulence has filled the high wave number space. figure 4.3 shows the velocity skewness reaches the typical value $-0.4 - 0.5$ for the realistic turbulence at Re_L about 80. The time development of turbulence kinetic energy is shown in figure 4.4. Notice that w^2 is slightly larger than u^2 and v^2 in the time series, which may be caused by the different size of the computational domain in the z direction compared to the x and y directions. Since this lack of isotropy is small, it is not expected to have any major effect. As we started with the uniform density field, Figure 4.5 shows the time development of the RMS value of density fluctuation. The time development of the dynamic model coefficient C is shown in figure 4.6.

4.3 Blending Procedure

Before we introduce the blending zone, in which the two date set transition smoothly from one data to another, consider first two independent, statistically identical random velocity fields $\mathbf{u}^{(1)}$ and $\mathbf{u}^{(2)}$ that are homogeneous and

isotropic. Let \mathbf{u} be a linear combination of the form

$$\mathbf{u} = \alpha \mathbf{u}^{(1)} + \beta \mathbf{u}^{(2)} \quad (4.3)$$

where α and β are scalar constants. If $\mathbf{u}^{(1)}$ and $\mathbf{u}^{(2)}$ are velocity fields corresponding to homogeneous isotropic turbulence, their mean is zero, as is that of the new field \mathbf{u} . Furthermore, the two point correlation $R_{ij}(\mathbf{r})$ for the new field \mathbf{u} ,

$$\begin{aligned} R_{ij}(\mathbf{r}) = \langle u_i(\mathbf{x}) u_j(\mathbf{x+r}) \rangle &= \alpha^2 \left\langle u_i^{(1)}(\mathbf{x}) u_j^{(1)}(\mathbf{x+r}) \right\rangle + \beta^2 \left\langle u_i^{(2)}(\mathbf{x}) u_j^{(2)}(\mathbf{x+r}) \right\rangle \\ &\quad + \alpha \beta \left(\left\langle u_i^{(1)}(\mathbf{x}) u_j^{(2)}(\mathbf{x+r}) \right\rangle + \left\langle u_i^{(2)}(\mathbf{x}) u_j^{(1)}(\mathbf{x+r}) \right\rangle \right) \end{aligned}$$

reduces to,

$$R_{ij}(\mathbf{r}) = (\alpha^2 + \beta^2) R_{ij}^{(1)} \quad (4.5)$$

by virtue of $\mathbf{u}^{(1)}$ and $\mathbf{u}^{(2)}$ being independent, where the angled brackets $\langle \cdot \rangle$ indicate an averaging (volume average suffices for the homogeneous fields under consideration). To retain the second order statistics of the original fields $\mathbf{u}^{(1)}$ and $\mathbf{u}^{(2)}$, an appropriate rescaling of the definition in (4.3) is required. This renormalization yields

$$\mathbf{u} = \frac{\alpha}{\sqrt{\alpha^2 + \beta^2}} \mathbf{u}^{(1)} + \frac{\beta}{\sqrt{\alpha^2 + \beta^2}} \mathbf{u}^{(2)} \quad (4.6)$$

Using trigonometric identities, this may be rewritten as

$$\mathbf{u} = \cos \theta \mathbf{u}^{(1)} + \sin \theta \mathbf{u}^{(2)} \quad (4.7)$$

The new field so obtained retains the mean values and second order statistics of the original fields.

This linear combination may be generalized by varying θ , allowing smooth transition from one field to another over a blending zone within which θ varies from 0 to $\frac{\pi}{2}$ as illustrated in figure 4.7. With $\theta = \theta(x)$ and $\langle \cdot \rangle$ restricted to averaging in $y-z$ plane, the single point statistics are preserved, as are two point correlations in the $y - z$ plane. The two point correlation in the x direction, by (4.7), can be expressed as

$$\langle u_i(\mathbf{x}) u_j(\mathbf{x} + r_x) \rangle = \cos [\phi(\mathbf{x}, r_x)] R_{ij}(r_x) \quad (4.8)$$

where $\phi(\mathbf{x}, r) = \theta(\mathbf{x} + r) - \theta(\mathbf{x})$, and R_{ij} is the original two point correlation in x . Let us consider the case where $r < L$, where L is the correlation length of the original field, then in the blending zone, $\phi(x, r)$ can be estimated as

$$\phi(\mathbf{x}, r_x) \sim \left(\frac{d\theta}{dx} \right)_{max} L \sim \frac{\pi L}{2L_b} \quad (4.9)$$

where $L_b = (\pi/2)/(\partial\theta/\partial x)_{max}$ is defined as a characteristic length of the blending zone. From (4.8), the difference of the two point correlation in x between the blended and the original field is proportional to $\frac{1}{2}\phi^2$ when $\phi \ll 1$, so we have

$$| \langle u_i(\mathbf{x})u_j(\mathbf{x} + r_x) \rangle - R_{ij}(r_x) | \sim \left(\frac{L}{L_b} \right)^2 R_{ij}(r_x) \quad (4.10)$$

which means the longer the blending zone, the less error will result in the two point correlation in x direction.

The dependence of θ on x within the blending zone, however, also introduces an extra term \mathcal{D}_e in the dilatation field:

$$\begin{aligned} \nabla \cdot \mathbf{u} &= \cos \theta (\nabla \cdot \mathbf{u}^{(1)}) + \sin \theta (\nabla \cdot \mathbf{u}^{(2)}) + \mathcal{D}_e \\ \mathcal{D}_e &= (-\sin \theta \mathbf{u}^{(1)} + \cos \theta \mathbf{u}^{(2)}) \theta_x \end{aligned} \quad (4.11)$$

In incompressible flows, \mathcal{D}_e violates mass conservation, whereas in compressible flows it can cause large artificial pressure fluctuations. This undesired dilatation may be removed by a projection method based on the Helmholtz decomposition theorem for the velocity vector \mathbf{u}

$$\mathbf{u} = \nabla \times \mathbf{A} + \nabla \varphi \quad (4.12)$$

where \mathbf{A} and φ are the vector and scalar potential of \mathbf{u} . The scalar potential φ_e corresponding to the extra dilatation \mathcal{D}_e satisfies a Poisson equation obtained by taking the divergence of (4.7),

$$\nabla^2 \varphi_e = \mathcal{D}_e \quad (4.13)$$

This equation is solved with homogeneous boundary conditions in x direction and periodic in the other two directions. Subtracting $\nabla \varphi_e$ from \mathbf{u} yields the final expression of the blended velocity $\tilde{\mathbf{u}}$ as

$$\tilde{\mathbf{u}} = \mathbf{u} - \nabla \varphi_e \quad (4.14)$$

Two sample data sets of homogeneous isotropic turbulence are used to demonstrate the blending procedure. The two data sets may be regarded as different realizations of the same turbulent statistical state, to which the above blending procedure is applied. In the present case, the size of the blending zone is taken as 1/8 of the box length. The results for blending over 1/16 of the box length are found to be similar.

The energy spectra of the original and blended turbulence fields are shown in figure 4.8. The energy spectrum of the blended field is very close to the original. Because of the increased length in the x -direction, a lower wave number with very small amount of energy is present. The effect of the projection procedure is shown in figure 4.9, where dilatation, averaged over y - z plane, is plotted as a function of x . Simple blending using equation (4.7) produces a dilatation spike inside the blending zone which is removed by (4.14). Notice that outside the blending region, the flow field remains intact. Numerically, the velocity associated with the extra dilatation $\nabla\varphi_e$ is at least one order of magnitude smaller compared to \mathbf{u} . The effect of removing extra dilatation on the overall second order statistics is therefore negligible. The velocity gradient skewness averaged in y - z plane is plotted in figure 4.10 as a function of x . For clarity, the second half of the first data set and the first half of the second data set are shown together on top. The blended data of the corresponding range is shown at the bottom. All three components of the skewness maintain similar magnitude in the blending zone without excessively large fluctuations. The corresponding vorticity distribution, shown in figure 4.11 before and after blending, is also well behaved.

In this Chapter, a blending procedure is described for combining realizations of homogeneous isotropic turbulence into a unified field that serves as a realistic representation of free-stream turbulence. Different realizations are catenated by a smooth blending function, and extra dilatation is removed using Helmholtz vector decomposition theorem. By construction, the combined field preserves the turbulence intensity, and the change to other statistical quantities are shown to be minimal. Examples will be given from the LES of free-stream turbulence effect on leading edge heat transfer in the subsequent chapters. This simple yet effective method could be useful in other direct or large eddy simulations in which effects of sustained free-stream turbulence are important.

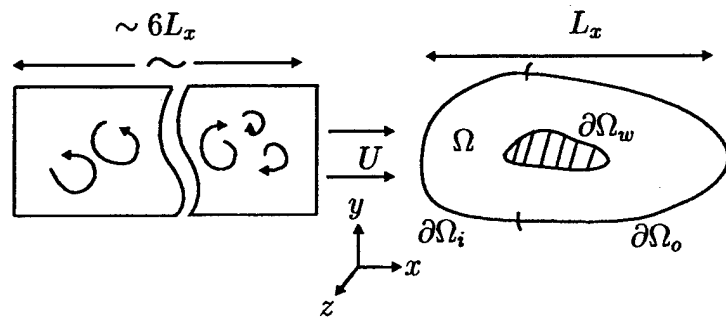


Figure 4.1: Length of free-stream turbulence field needed for typical spatial numerical simulations.

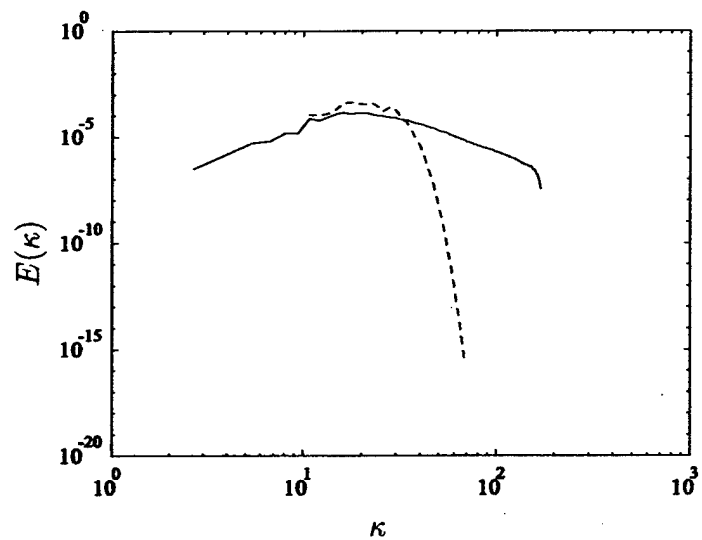


Figure 4.2: Initial and final three dimensional energy spectrum for isotropic homogeneous turbulence in a rectangular box.

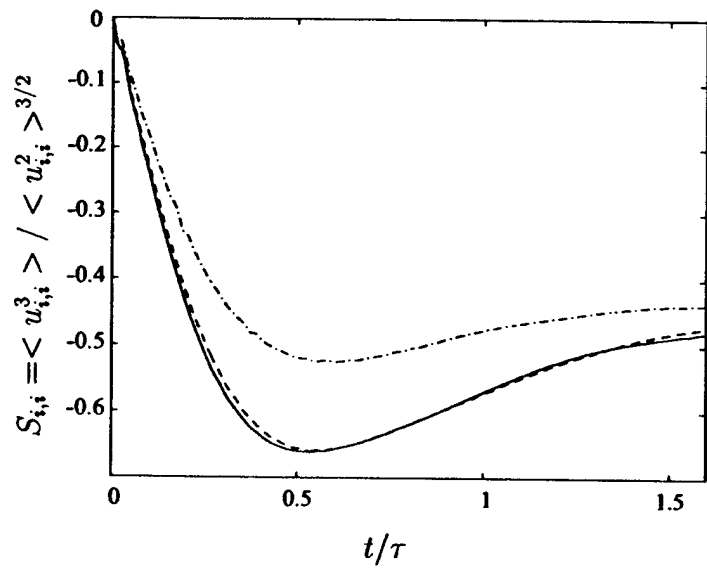


Figure 4.3: Time development of the velocity gradient skewness. $\tau = L/u_{rms}$, where L is the turbulence integral length scale.

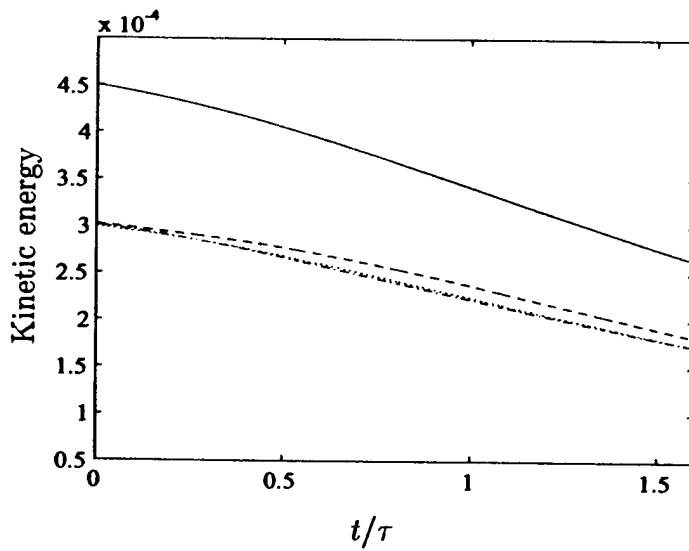


Figure 4.4: Time development of the turbulence kinetic energy. —: Turbulence kinetic energy,: u^2 , - - - - : v^2 , - - - : w^2

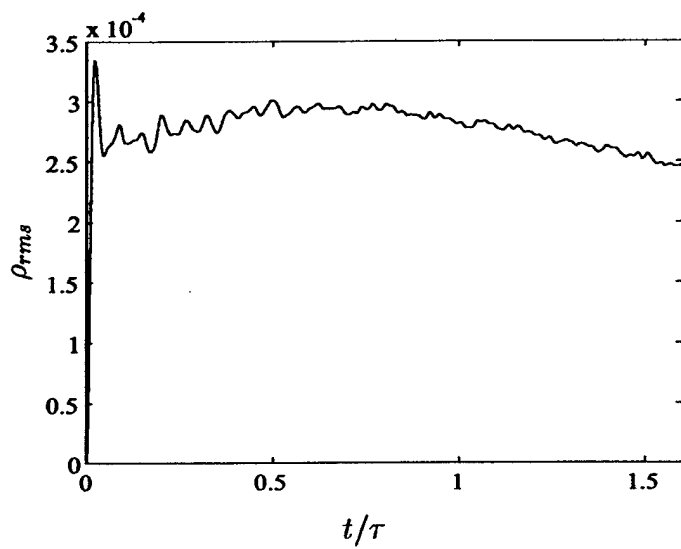


Figure 4.5: Time development of the density fluctuation.

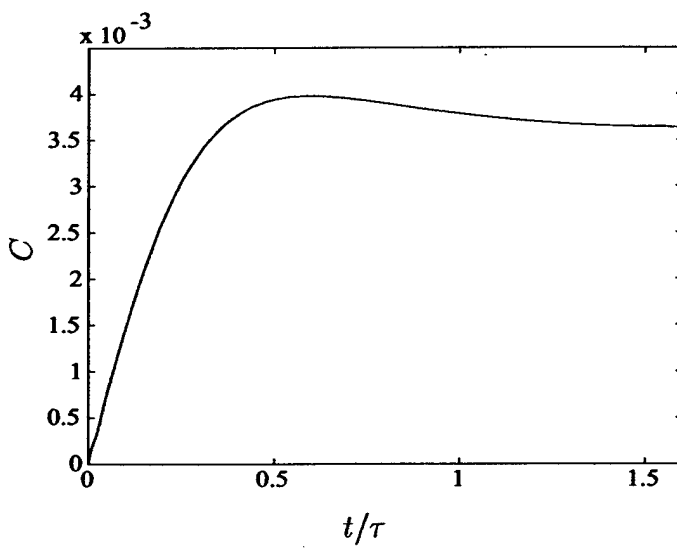


Figure 4.6: Time development of the dynamic SGS model coefficient C.

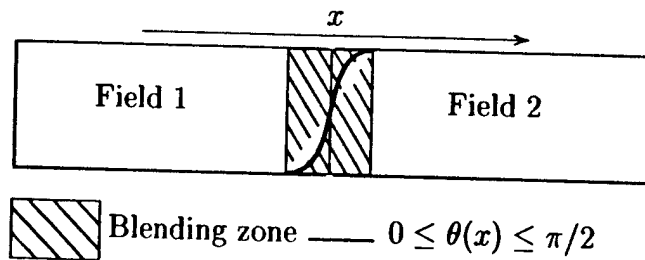


Figure 4.7: Blending function for joining two turbulence realizations.

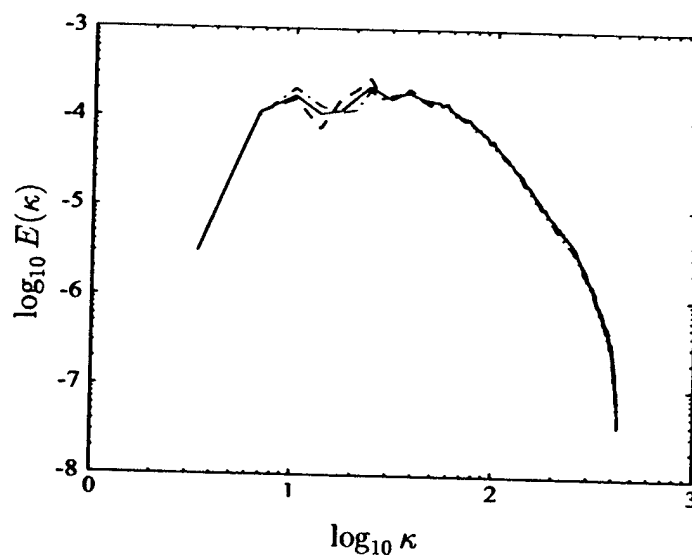


Figure 4.8: Energy spectra for the original and blended data sets. —·—: data 1, - - - : data 2, ———: blended

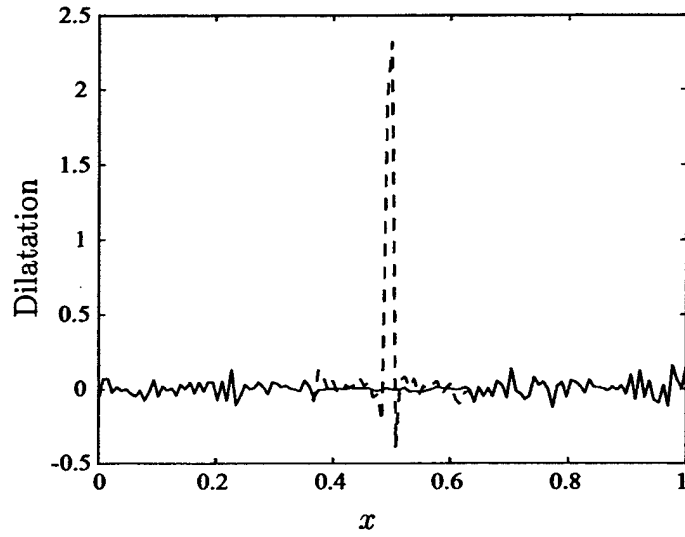


Figure 4.9: Divergence of blended compressible turbulence data before and after the removal of extra dilatation field. -----: original, ——, extra dilatation removed.

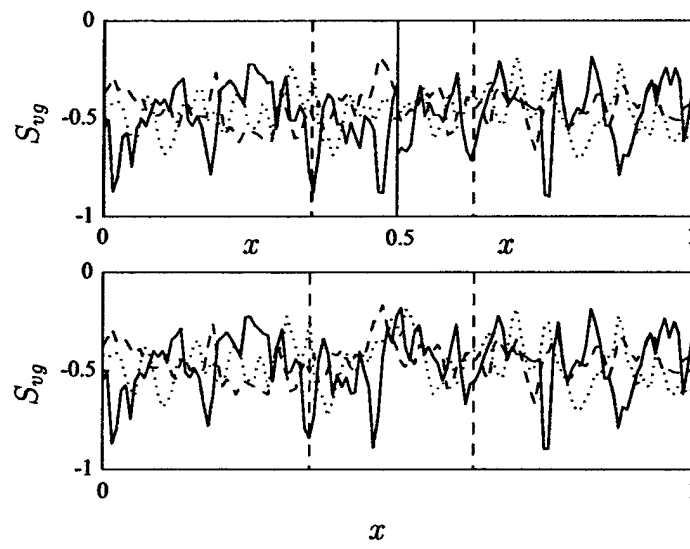


Figure 4.10: Velocity gradient skewness. The blending zone are marked between dashed lines. ——, -----, and ······ are S_{vg} in x , y , z directions.

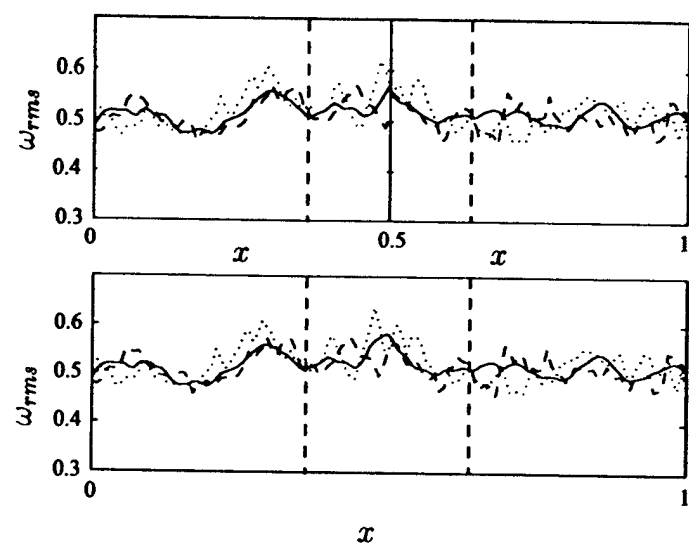


Figure 4.11: Vorticity fluctuation. The blending zone are marked between dashed lines. —, ----, and ······ are ω in x, y, z directions.

Chapter 5

Numerical Simulation Results

In this chapter, we present the numerical results of LES of free-stream turbulence impinging upon an elliptical leading edge and the related heat transfer enhancement. The problem set up is based on the experimental results of Van Fossen et al. (1995), and the LES results shows very good agreement with the experimental measurements. The interaction process between the free stream turbulence and leading edge is analyzed through the turbulence statistics. The characteristic vortical structures responsible for the heat transfer enhancement are identified.

5.1 Experimental Setup

In the wind tunnel experiments of Van Fossen et al. (1995), free-stream turbulence is generated by different grids with different length scale and intensity, see figure 5.1. The heat transfer is measured in the stagnation region of four elliptical leading edge models; the ratios of major to minor axes are 1:1, 1.5:1, 2.25:1, and 3:1. The Reynolds number based on diameter of curvature at leading edge and the mean streamwise velocity ranges from 37000 to 228000. Turbulence intensity (measured in the absence of the models) is in the range of 1.1 to 15.9 percent. The ratio of turbulence integral length scale to the leading edge diameter range from 0.05 to 0.30. In this section we describe the specification of turbulence intensity and length scale according to the experiments. We choose to use experimental data set No. 244, corresponding the leading edge with 3:1 major to minor axis ratio, as an example to describe the method. In our simulations, this corresponds to the case B

in table 5.2 where the flow conditions and computational parameters used in the present LES are summarized. The main simulation results that will be presented in this chapter are also from case B.

First, the Reynolds number Re in the simulation is defined as

$$Re_{\infty} = \frac{(\rho U)_{\infty} D}{\mu_{\infty}} = \frac{2(1-B)}{2-B} \frac{(\rho U)_{av} D}{\mu} = 0.8284 Re_{av} \quad (5.1)$$

where Re_{av} is the Reynolds number used in the experiments, and $(\rho U)_{av}$ is the average between the mass fluxes at far upstream and the location with maximum model blockage. The blockage coefficient B (Maximum model thickness / Wind Tunnel Height) is 0.293 for the 3:1 model. The experimental condition is corresponding to the data set No. 244 for this model and the measured turbulence data are:

$$Re_{av} = 50700 \quad Tu = 0.0352 \quad \Lambda_x/D = 0.121, \quad D = 6.6 \text{ cm} \quad (5.2)$$

Note the values of Tu and Λ_x/D are taken at the corresponding location of leading edge but in the absence of the model. The following experimental correlations are obtained for Tu (in percentage) and Λ_x as a function of the streamwise distance x from the turbulence generating grid:

$$Tu = a\left(\frac{x}{b}\right)^m \quad \frac{\Lambda_x}{b} = I\left(\frac{x}{b}\right)^{0.5} \quad (5.3)$$

where b is the bar width of the grid. For the grid used in this group of measurement, grid G3, the coefficients in equation (5.3) are

$$a = 149.4, \quad b = 0.318 \text{ cm}, \quad m = -0.830, \quad I = 0.264 \quad (5.4)$$

Thus, corresponding to the experimental value given in equation (5.2), we can obtain that the leading edge is located at

$$x_{LE} = 91.45 b = 4.4 D \quad (5.5)$$

downstream the grid. The corresponding values for Tu and Λ_x at the inflow boundary which is in current simulation located 1.5D upstream of the leading edge can then be obtained by setting

$$x_{IN} = x_{LE} - 1.5D = 2.9 D = 60.19 b \quad (5.6)$$

Thus the Reynolds number, turbulence intensity Tu and streamwise integral scale Λ_x are

$$Re_D = 42000, \quad Tu = 0.05, \quad \frac{\Lambda_x}{D} = 0.1 \quad (5.7)$$

Under the operation condition of the wind tunnel at $T \approx 300K$, the kinematic viscosity of air is $\nu = 1.60 \times 10^{-5} m^2/s$. For the Reynolds number $Re = 42,000$, the incoming upstream velocity is $U_\infty = 10.18 m/s$, which is roughly corresponding to $M_\infty = 0.03$. To make the compressible code run efficiently, we choose the upstream Mach number to be

$$M_\infty = 0.15 \quad (5.8)$$

5.2 Simulation procedure

To represent the experimental conditions accurately with the current flow configuration, the simulations are performed in a progressive way. We first generate the incompressible potential flow around the body with blockage effect taken into account. For this purpose, consider a point source placed midway between two parallel planes with a uniform incoming stream U_∞ , the blockage effect causes the flow field to differ, particularly in pressure distribution, from the open flow case where the walls are absent. Let a be the half height of the wind tunnel and b the half thickness of the plate (see appendix A), choose the stagnation point at the center line $y = 0$ as the origin $x = 0$, the downstream blockage can be realized by placing the point source S of strength $2\pi m$, where

$$m = \frac{ab}{\pi(a-b)} U_\infty \quad (5.9)$$

at location $x = c$, where

$$c = \frac{a}{\pi} \ln \left(1 + \frac{\pi m}{a U_\infty} \right) \quad (5.10)$$

The resulting velocity field may be expressed as

$$\begin{aligned} u &= \frac{b U_\infty}{2(a-b)} \left[\frac{\coth \frac{\pi(x-c)}{2a}}{\cos^2(\frac{\pi y}{2a}) + \sin^2(\frac{\pi y}{2a}) \coth^2 \frac{\pi(x-c)}{2a}} + \frac{2a}{b} - 1 \right] \\ v &= \frac{b U_\infty}{2(a-b)} \left[\frac{\tan(\frac{\pi y}{2a})}{\sinh^2 \frac{\pi(x-c)}{2a} + \tan^2(\frac{\pi y}{2a}) \cosh^2 \frac{\pi(x-c)}{2a}} \right] \end{aligned} \quad (5.11)$$

Although in leading edge region, the separating streamline in (5.11) represents a modified Rankin body instead of the exact elliptic shape of the model, it is a good approximation to the low Mach number flow far upstream and downstream. So (5.11) has been used as the initial condition for the compressible potential solution. The compressible potential flow is solved using the procedure described in Chapter 3 and the solution sought in two steps. First we solve the potential flow in a large domain which covers half of the ellipse downstream and extends vertically from the bottom to the top wind tunnel wall. On such a grid, the far field boundary conditions can be readily provided by the above incompressible solution. After the compressible solution is obtained on the large grid, a smaller grid which only surrounds the leading edge region is extracted for the subsequent viscous computations. Accordingly, the boundary conditions needed for viscous computation on this smaller, inner grid can now be provided through the whole solution at the boundary, see figure 5.2. This dual grid approach improves the resolution near the leading edge and reduces the computational cost for three dimensional turbulence simulation.

As aforementioned, four different models with the same leading edge diameter but different major to minor axes ratios, from 1:1, 1.5:1, 2.25:1 to 3:1, were used in the experiments to produce different leading edge velocity gradient. These cases have been duplicated in the compressible potential solution to test the numerical accuracy. Figure 5.4 shows the comparison of the velocity gradients at the leading from the present compressible potential solution at $M_\infty = 0.15$ with the results obtained by a panel method(Van Fossen et al., 1995). Note the leading edge velocity gradients are affected significantly by the blockage effect, and the excellent agreement shows that this important feature of the experiments has been captured accurately.

For the viscous calculation, the flow parameters are $Re_D = 42,000$, $M_\infty = 0.15$, $T_w/T_0 = 1.075$, where T_w and T_0 are the wall and total free stream temperature. The laminar solution for density ρ , velocity u and v and the temperature T are shown in Figure 5.5 to 5.8. The corresponding profiles along the stagnation streamline ($y = 0$) are shown in figure 5.9 to 5.11. It can be seen that while the ρ and T are only significantly changed inside the boundary layer, considerable gradient caused by the presence of the model exists in the mean streamwise velocity even at the inflow boundary.

The non-dimensional leading-edge heat transfer coefficient, or Frössling

number, is defined as

$$Fr = \frac{Nu}{Re_D^{1/2}} = -\frac{\kappa_w T_{n,w}}{\kappa_0 \Delta T Re_D^{1/2}} \quad (5.12)$$

where $T_{n,w}$ is the nondimensional wall normal temperature gradient, and κ_w and κ_0 is the thermal conductivity evaluated at the wall temperature and the free-stream total temperature. Following Rigby and VanFossen (1992), the characteristic temperature difference ΔT in (5.12) is chosen to be the difference between the wall temperature and the adiabatic wall temperature, i.e. $\Delta T = T_w - T_{aw}$. The adiabatic temperature can be approximated by

$$T_{aw} = \sqrt{Pr} (T_0 - T_{edge}) + T_{edge} \quad (5.13)$$

Here T_{edge} is the temperature at the edge of the boundary layer. Using the isentropic relation and assuming constant pressure across the boundary layer, the T_{edge} is obtained by

$$T_{edge} = T_0 \left(\frac{P_{wall}}{P_0} \right)^{(\gamma-1)/\gamma} \quad (5.14)$$

where P_0 is the free stream total pressure. The laminar computation of the Fr distribution along the leading edge surface is compared with experimental data obtained without the turbulence generating grids in figure 5.12 . Three groups of data at slightly different Reynolds numbers (based on U_{av}) are included, and the agreement is quite good. Note that in such cases, the background fluctuation in the wind tunnel is $Tu = 0.3\%$ and the length scale is $L/D = 2.308$.

The steady two dimensional viscous solution is then taken as the LES base flow to which free-stream turbulence, generated by the method described in Chapter 4, is introduced through the inflow boundary.

However, prior to the LES corresponding to case B, a preliminary simulation, Case A, was preformed at a lower Reynolds number to test the numerical method and optimize the computation configuration. Figure 5.13 shows the turbulence intensity along the the stagnation stream line. The root-mean-square values are obtained by averaging u' , v' and w' in time and in the spanwise direction. The turbulence is largely decaying until it reaches a distance of about D from the leading edge where the behavior of u' , v' and w' start to change. Notice that close to the body u' and w' are amplified while v' continues to decay. In Van Fossen's experiment, a power law curve of

Case	Ma	Re	Tu	L/D	Domain (x, y, z)	Grid
A	0.15	10,000	0.08	0.10	$7D \times 10D \times D$	$384 \times 192 \times 64$
B	0.15	42,000	0.05	0.10	$3.5D \times 5D \times 0.4D$	$192 \times 144 \times 48$
C	0.15	43,740	0.11	0.06	$3.5D \times 5D \times 0.4D$	$192 \times 144 \times 48$
D	0.60	42,000	0.04	0.06	$3.5D \times 5D \times 0.4D$	$192 \times 144 \times 48$

Table 5.1: Flow conditions and the parameters of numerical simulations.

the form $Tu \sim x^m$ was used to fit the decay of free-stream turbulence in the absence of the model, here x is the distance downstream of the turbulence-generating grid. The power-law-fitted curve is also plotted in Fig. 5.13 with the same exponent $m = -0.83$ used in the experiments. The fairly good agreement indicates that the initial decay rate of the free-stream turbulence has been captured correctly in the simulation.

Figure 5.14 uses a logarithmic scale on a slightly shifted x-axis to show the same data as in figure 5.13 with the leading edge region amplified for clarity. The transformation of the x-axis used here is $\tilde{x} = \log(4.02 - x)$. Note $x = 4$ corresponds to the location of the leading edge. It reveals that the free-stream turbulence goes through three different stages as it impinges upon the leading edge. The first is free decay of the turbulence, corresponding to the distance from the inflow to approximately $x = 3$, as the presence of the body has not been felt strongly by the incoming turbulence. The second stage is an inviscid rapid distortion process, approximately corresponding to the distance from $x = 3$ to $x = 3.95$, where the free-stream turbulence experiences large straining by the diverging mean streamlines. A direct, quantitative comparison between the present results and the compressible rapid distortion theory (RDT)(Goldstein, 1978) is not easily obtained due to the viscous effect and the relatively small scale of turbulence, but the increase of u'_{rms} and w'_{rms} , and decrease of v'_{rms} are qualitatively in agreement with the temporal prediction of RDT under plane strain(Batchelor and Proudman, 1954). The third stage occurs at a distance very close to the wall where the viscous

dissipation dominates and all the turbulence rapidly reduces to zero at the wall. Also notable is that the spanwise velocity w'_{rms} continues to increase significantly while u'_{rms} and v'_{rms} start decreasing due to the presence of the wall. This is due to inviscid wall-blocking or splatting effect (Hunt and Graham, 1978; Perot and Moin, 1995), in which the wall normal fluctuation is suppressed by the no penetration condition of the wall and has to transfer its energy to the other two components. As wall blocking is an inviscid process, it typically extends beyond the viscous dissipation range in the normal direction.

It is based on the results of this simulation that a dual mesh methodology is adopted for subsequent simulations as shown in figure 5.2. This allows the LES to focus on the rapid strain of the free-stream turbulence and the viscous interaction between the turbulence and wall. Hence in the LES of case B, C and D, the inflow boundary of the mesh is chosen to be roughly corresponding to the end of the free decaying process, in the present case at $1.5D$ upstream the leading edge. The domain size in the spanwise direction is chosen to be $0.4D$. Figure 5.3 shows four streamwise locations along the leading edge surface where profiles of various turbulence statistics at these location will be presented.

5.3 Inflow turbulence

Twelve independent realizations of homogeneous isotropic turbulence with intensity $Tu = 5\%$ and integral length scale $\mathcal{L}/D = 0.1$ are pre-computed using the large eddy simulation. The LES code for inflow turbulence generation uses the same dynamic SGS model and is adapted from a DNS code (Lui, 2003) which incorporates six-order compact finite differencing and fourth order R-K time marching scheme. To fit the aspect ratio of the main simulation, the LES of decaying turbulence is performed in a rectangular box of size $1.6D$, $1.6D$ and $0.4D$ in x , y and z direction, respectively. The number of grid points is $128 \times 128 \times 32$ to ensure the turbulence isotropy and initial velocity field is solenoidal. After the twelve independent turbulence fields are obtained, they are then lined up spatially and joined together by applying the blending procedure at the interface between adjacent fields, resulting in a box of turbulence twelve times longer than each individual realization, but having the same characteristics as each one. This long blended field then serves as the free-stream turbulence which is convected into the main com-

putational domain through the inflow boundary located $1.5D$ upstream the leading edge.

Figure 5.15 shows the visualization of instantaneous spanwise velocity within a slice of $z = 0$ and the temperature gradient at the blade surface near the stagnation point $s = 0$. It can be seen that the isotropic turbulence eddies are strongly stretched near the leading edge region. As a result, the vorticity in the free-stream in x direction ω_x is compressed and reduced, but the ω_y is greatly stretched and amplified. After the leading edge, these vortices wrap around the leading edge; the vortices originally in transverse direction tend to form strong streamwise vortices. The strong and relatively thinly stretched vortices impinging upon the leading edge and modifies the thermal boundary layer significantly. As a result, the surface heat transfer distribution develops into thin, streamwise elongated streaky structures as shown in figure 5.15.

The instantaneous temperature contour, corresponding to the flow field in figure 5.15 are shown in figure 5.16 through a series of wall normal sections at different streamwise locations. Clearly, the instantaneous temperature contours develops into various mushroom like structures under the influence of the incoming turbulence eddies. A sequence of visualizations show that these mushroom structures typically do not occupy a fixed spanwise location, but moves laterally over a significant distance during their lifetime. The characterization of this movement and its implication are discussed subsequently.

5.4 Turbulent mean flow and heat transfer

The turbulent mean density $\bar{\rho}$, streamwise velocity U , transverse velocity V and temperature \bar{T} are shown in figure 5.17, 5.18, 5.19 and 5.20. The contours of the turbulent mean fields show qualitatively similar patterns to the corresponding laminar quantities, particularly outside the boundary layer.

The profiles of turbulent mean streamwise velocity U (in local $s - n$ coordinates) and temperature $(T - 1)/(T_w - 1)$ are compared with the laminar profiles at $s = 0$ in figure 5.21, $0.2D$ in figure 5.22, $0.8D$ in figure 5.23 and $1.6D$ in figure 5.24. Of all the locations, the turbulent mean temperature profile has a greater slope at the wall while the mean velocity profile has almost identical slope at the wall. This means that the heat transfer is much more sensitive to the free-stream turbulence than the skin friction.

The time history of spanwise averaged Frössling number at the stagnation point is shown in figure 5.25. Notice that the significant increase in Fr around $t = 4$ is the time when the free-stream turbulence reaches the leading edge after entering the domain at $t = 0$. The turbulent mean Fr after $t = 4$ shows a clear increase over the laminar value, indicating the heat transfer enhancement by the free-stream turbulence. The distribution of the Fr on the surface is plotted in figure 5.26 along with the experimental measurements of Van Fossen et al. (1995) for comparison. Both the computation and experimental results show that while the surface distribution of the heat transfer coefficient is essentially the same as in the laminar case, its amplitude is significantly increased by the free-stream turbulence. Although the present LES result is slightly lower than the experimental measurements, as not all the turbulence scales are resolved in the computation, the overall agreement is quite good. It will be shown in Chapter 6 that except at very small scales, as the length scale of the turbulence decreases, its effect on heat transfer increases. So it is generally important to resolve the small scale turbulence for good numerical prediction of stagnation point heat transfer.

To quantify the effect of SGS modelling, a typical distribution of spanwise averaged SGS ν_T is shown in figure 5.27. The distribution of time averaged SGS ν_T is shown in 5.28. Both figures show that the maximum ν_T occurs in the leading edge region, where strong vortex stretching and amplification produces small scale turbulence. However, the value of ν_T is relatively small, about half of the molecular viscosity, indicating the grid resolution close to the wall is adequate.

5.5 Reynolds stress and turbulent transport

Of main interest in stagnation point turbulent flow is the distribution of turbulence statistics along the stagnation streamline. Figure 5.29 shows stagnation line distribution of RMS value of turbulence intensity. As mentioned before, the choice of the closer inflow boundary essentially eliminates the free decaying stage of the turbulence. After a relatively balanced, isotropic development stage before $x \sim 2.4$, the free-stream turbulence becomes strongly anisotropic due to the mean flow straining effect, i.e. u_{rms} , w_{rms} increase but v_{rms} decreases between $x \sim 2.4$ to $x \sim 2.7$. At this stage, the turbulence experiences the change of mean flow due to the presence of the leading edge, but it was not until within even a closer distance $x > 2.7$ that the leading

edge surface itself exerts a strong blocking effect upon the turbulence. The blocking effect causes a continuing, rapid increase in w_{rms} while u_{rms} already starts to decay. At the same time, because the high value of u_{rms} and w_{rms} in this case, the previously decreasing v_{rms} also start to increasing after $x \sim 2.7$ in an almost linear fashion. Within an extremely closer distance, viscous effect dominates and all the turbulence vanishes at the wall.

To understand the dynamics of turbulence Reynolds stress and heat transport, it is instructive to write their governing equations — the Reynolds averaged Navier-Stokes equations. Let \bar{f} denote the time average value of f , we can decompose turbulence fields into mean and the fluctuation

$$\rho = \bar{\rho} + \rho', \quad u_i = U_i + u'_i, \quad p = P + p', \quad T = \bar{T} + T' \quad (5.15)$$

and similarly for the transport coefficients

$$\lambda_T = \bar{\lambda} + \lambda', \quad \mu_T = \bar{\mu} + \mu', \quad \kappa_T = \bar{\kappa} + \kappa', \quad (5.16)$$

Then the steady transport equation for the Reynolds stress $\bar{u}_i u_j$ is

$$\begin{aligned} \bar{\rho} U_k \overline{(u'_i u'_j)}_{,k} &= -\overline{u'_j p'_{,i}} - \overline{u'_i p'_{,j}} \\ &\quad - U_{i,k} [\bar{\rho} \overline{(u'_k u'_j)} + U_k \overline{\rho' u'_j} + \overline{\rho' u'_k u'_j}] \\ &\quad - U_{j,k} [\bar{\rho} \overline{(u'_k u'_i)} + U_k \overline{\rho' u'_i} + \overline{\rho' u'_k u'_i}] \\ &\quad - \bar{\rho} \overline{u'_k (u'_i u'_j)_{,k}} - \overline{\rho' u'_k (u'_i u'_j)_{,k}} \\ &\quad + \Phi_R \end{aligned} \quad (5.17)$$

On the right hand side of (5.17), the first row is the velocity pressure gradient correlation; the second and the third rows are the Reynolds stress production; the fourth row is the turbulence transport. Φ_R in the last row is the turbulent dissipation

$$\begin{aligned} \Phi_R &= \frac{1}{Re} [(\bar{\lambda} \overline{D'_{,i} u'_j} + \overline{D_{,i} \lambda' u'_j} + \overline{\lambda' D'_{,i} u'_j}) + \\ &\quad (\bar{\lambda} \overline{D'_{,j} u'_i} + \overline{D_{,j} \lambda' u'_i} + \overline{\lambda' D'_{,j} u'_i})] \\ &+ \frac{2}{Re} [(\bar{\mu} \overline{S'_{ik,k} u'_j} + \overline{S_{ik,k} \mu' u'_j} + \overline{\mu' S'_{ik,k} u'_j}) + \\ &\quad (\bar{\mu} \overline{S'_{jk,k} u'_i} + \overline{S_{jk,k} \mu' u'_i} + \overline{\mu' S'_{jk,k} u'_i})] \end{aligned} \quad (5.18)$$

Where $D \equiv u_{i,i}$ denotes the divergence of the velocity field. Similarly, for the turbulence heat flux $\overline{u'_iT'}$, we have

$$\begin{aligned}
\bar{\rho}U_k\overline{(u'_iT')_k} &= -\bar{T}'p'_i \\
&- \bar{T}_{,k}[\bar{\rho}\overline{u'_ku'_i} + U_k\overline{\rho'u'_i} + \overline{\rho'u'_ku'_i}] \\
&- U_{i,k}[\bar{\rho}\overline{u'_kT'} + U_k\overline{\rho'T'} + \overline{\rho'u'_kT'}] \\
&- \bar{\rho}\overline{u'_k(u'_iT')_k} - U_k\overline{\rho'(u'_iT')_k} - \overline{\rho'u'_k(u'_iT')_k} \\
&+ \frac{\gamma}{PrRe}[\bar{\kappa}\overline{u'_iT'_{,kk}} + \bar{\kappa'}\overline{u'_iT_{,kk}} + \bar{\kappa'}\overline{u'_iT'_{,kk}}] \\
&+ \Phi_p + \Phi_H
\end{aligned} \tag{5.19}$$

On the right hand side of (5.19), the first row is the temperature pressure gradient correlation; the second and the third rows are the heat flux production; the fourth row is the turbulence transport and the fifth row is the turbulent heat conduction. In the last row Φ_p , and Φ_H are the pressure dilatation work and viscous dissipation. The expressions for Φ_p and Φ_H are omitted here; they are usually not importance in understanding the turbulence dynamics.

Figure 5.30 to 5.32 show the turbulence budget for $\overline{u'^2}$, $\overline{v'^2}$ and $\overline{w'^2}$ along the stagnation line. For $\overline{u'^2}$, there is a large production term corresponding to $-\overline{u'^2}\partial U/\partial x$ due to the mean flow straining. Conversely, the production for $\overline{v'^2}$ is $\overline{u'^2}\partial U/\partial x$ which has an opposite sign, and thus actually takes energy away from the vertical fluctuation. Since the turbulent mean flow is two dimensional, there is not production term for $\overline{w'^2}$.

The turbulent transport has the largest absolute value but is mostly confined only within near wall region. It also reverse sign as the wall is approached. This is characteristic of turbulent transport, i.e. when integrated along the stagnation line, its net contribution to turbulence energy is zero. Turbulent transport is not important for $\overline{v'^2}$ compared to other terms. For $\overline{w'^2}$, turbulent transport largely cancels with the mean convection term, and the summation of these two plotted in 5.32 shows it has a weak dissipative effect on the $\overline{w'^2}$.

The viscous dissipation term extends from the wall the largest distance for $\overline{u'^2}$ and smallest distance for $\overline{v'^2}$. It has the largest value $\overline{w'^2}$ yet smallest value for $\overline{u'^2}$. Except for $\overline{w'^2}$, the dissipation term do not play a significant role at the along the stagnation line unless within the extremely close distance to the wall for $\overline{v'^2}$.

Of particular interest is the redistribution term, i.e. the correlation between velocity and pressure gradient. It has comparable amplitude in all

three Reynolds normal stress and plays very a important role for each of them . Essentially, its overall effect is to induce large turbulence anisotropy in strongly strained mean flow. In figure 5.30, it appears largely negative for $\overline{u'^2}$ but positive for $\overline{v'^2}$ and $\overline{w'^2}$ as shown in figure 5.32 and 5.32. So it takes energy from $\overline{u'^2}$ and redistribute it to $\overline{v'^2}$ and $\overline{w'^2}$. For both of them, this appears to be the only major energy input. For $\overline{v'^2}$ it balances with the negative production term, while for $\overline{w'^2}$, it balances with the viscous dissipation and total convection. It should be pointed out that this particular feature of redistribution term is important for Reynolds stress modelling. The turbulence anisotropy induced by the redistribution is often the cause of the failure of using two equation models in strongly strained flows, since in these models the turbulence is usually assumed isotropic and only the kinetic energy k is modelled.

To more clearly show the vortex stretching effect, the fluctuation vorticity along the stagnation line is plotted in figure 5.33. It can be seen that the amplitude of turbulence vorticity ω'_y has increased by two order of magnitude from the inflow to the wall.

To better visualize the typical vortex structures and its effect on heat transfer, the temperature contour and the corresponding velocity field in the stagnation plane $y = 0$ is shown in figure 5.34 at a time interval of $\Delta t = 0.6$. The velocity fields show clearly the formation of these mushroom shapes in the thermal contour; the strong, amplified y -oriented vortices creates reverse flow ($u < 0$) in the stagnation region, which lifts up the hot fluid particle close to the wall and swaps them with those away from the wall at a lower temperature. In doing so, the mushroom structure for temperature contour forms. However, it should be noted that directly underneath these mushrooms structures, the thermal boundary layer is thicker than the undisturbed case — the heat transfer is in fact reduced. It is the region between these mushrooms, where the disturbed flow has a positive normal velocity towards the wall, the boundary layer become thinner, and consequently the heat transfer is increased. The overall or spanwise averaged Fr number apparently will depend on the distribution and intensity of these thickened and thinned regions.

From figure 5.34, it is observed that these mushrooms are moving along the spanwise direction. To quantify its average convection speed, the space-time correlation of the wall vorticity along the stagnation line (z -axis) is shown in figure 5.35. By following the slowest descent line on the contour, the expected value of the moving speed is found at ± 0.06 , the same order as

w_{rms} . The lateral movement of the wall vorticity can also be explained by the wall blocking effect. Considering a single vortex approaching a wall parallel to its axis, an inviscid image vortex with opposite sign will be generated at a equal distance on the other side of the wall in order to satisfy the no penetration boundary condition on the wall. Then the mutual induction of these two vortices generates a velocity along the wall whose magnitude is in general proportional to the intensity of the approaching vortex, and this cause the vortex moves laterally.

The probability density function of Fr at the leading edge is shown in figure 5.36. It deviates from a normal distribution and indicates that events associated with large positive heat transfer are less frequent than those with large negative variance.

Figure 5.37 to figure 5.46 show the distribution and profiles of $\overline{\rho^2}$, $\overline{u^2}$, $\overline{v^2}$, $\overline{w^2}$ and $\overline{T'^2}$. Figure 5.47 to figure 5.52 show the distribution and profiles of $\overline{u'v'}$, $\overline{u'w'}$, and $\overline{v'w'}$. Figure 5.53 to figure 5.58 show the distribution and profiles of $\overline{u'T'}$, $\overline{v'T'}$ and $\overline{w'T'}$.

The rest of the figures show the magnitude and distribution of various terms in the Reynolds stress transport equation, including the production, pressure strain and turbulent transport. These terms are typically important for turbulence modelling and the profiles at specific locations are intended to provide quantitative information. For brevity, the description of the characteristics of each figures is omitted here, but the specific information are mostly provided in the captions.

5.6 High intensity and High Mach Number cases

At the time of this writing, the post processing of the data from the LES of high turbulence intensity, case C, and high Ma number, case D, is still in progress. Only preliminary results will be presented here. Figure 5.83 shows the stagnation streamline distribution of turbulence intensity. It has essentially similar features as lower Tu case B except the turbulence decays after entering the domain. This is mainly because the smaller length scale for case C. The heat transfer coefficient on the surface is shown in figure 5.84. It shows good agreement with the experimental results but the simulation results is also lower than the measured data. Figure 5.85 shows the

Fr distribution on the surface for high Mach number case. Since in this case the intensity is relatively low, the heat transfer enhancement is modest. Qualitatively, the shape appears similar to the low Mach number cases.

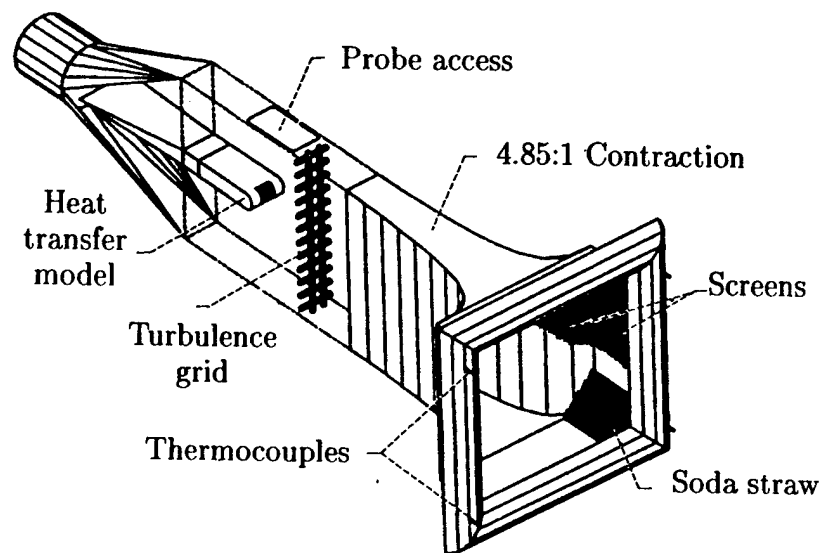


Figure 5.1: Wind tunnel measurements for leading edge heat transfer enhancement under free stream turbulence. (Van Fossen et al., 1995)

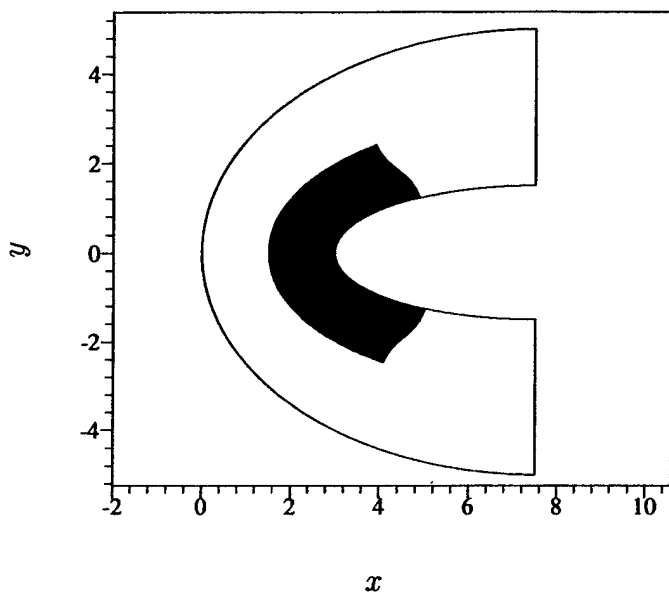


Figure 5.2: The inner grid of 192×144 near the leading edge and outer region in which potential solution are first obtained to provide the boundary conditions for the inner solution.

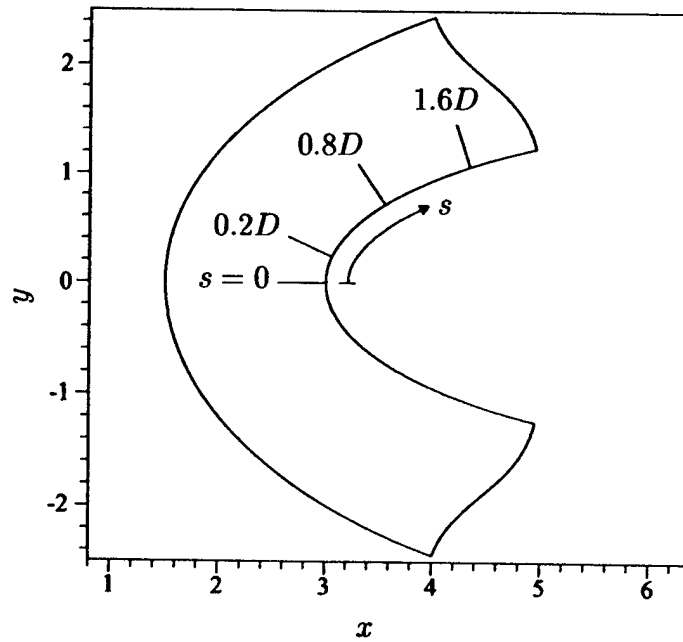


Figure 5.3: Locations of the cross sections along the surface.

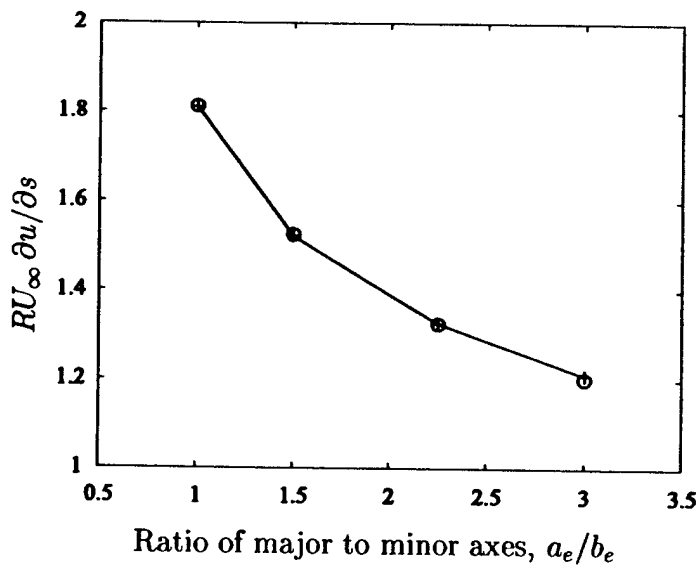


Figure 5.4: Leading edge velocity gradients. Solid line with plus sign is the present simulation, and the circles from Van Fossen et al. (1995).

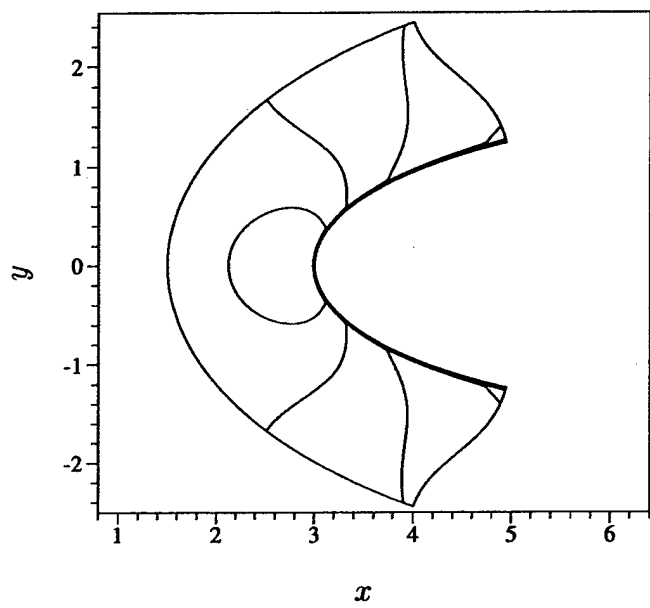


Figure 5.5: Contours of density ρ of the laminar flow at $Ma = 0.15$, $Re = 42,000$, $T_w/T_0 = 1.075$.

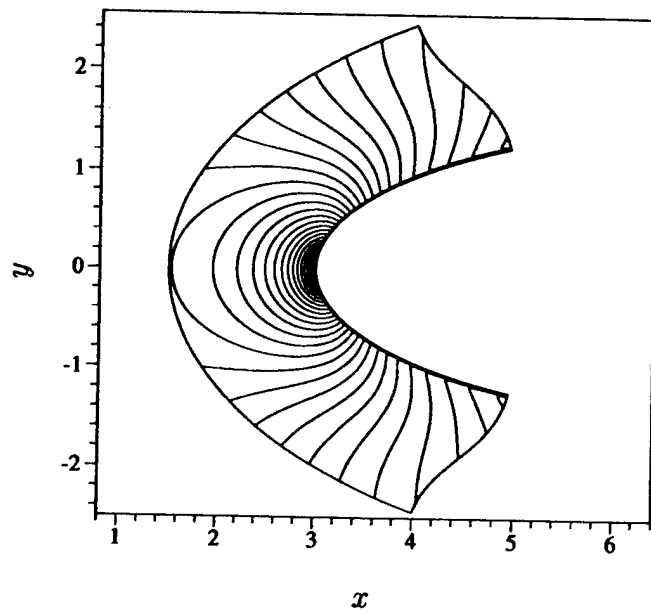


Figure 5.6: Contours of streamwise velocity u of the laminar flow at $Ma = 0.15$, $Re = 42,000$, $T_w/T_0 = 1.075$.

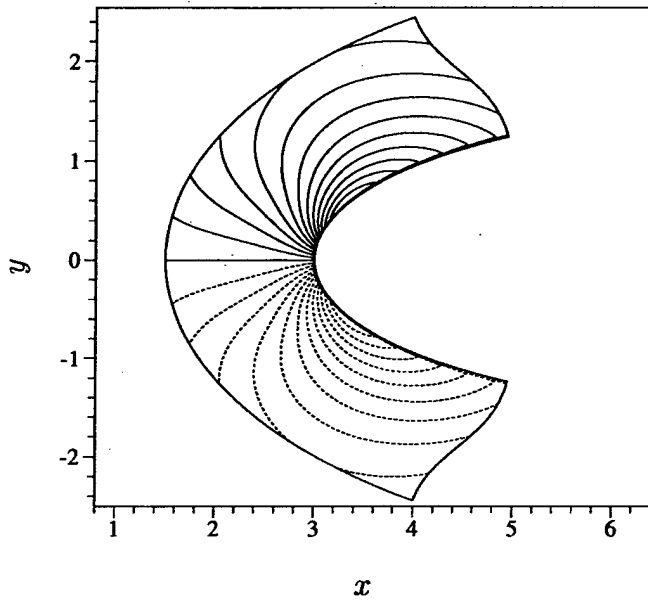


Figure 5.7: Contours of transverse velocity v of the laminar flow at $Ma = 0.15$, $Re = 42,000$, $T_w/T_0 = 1.075$.

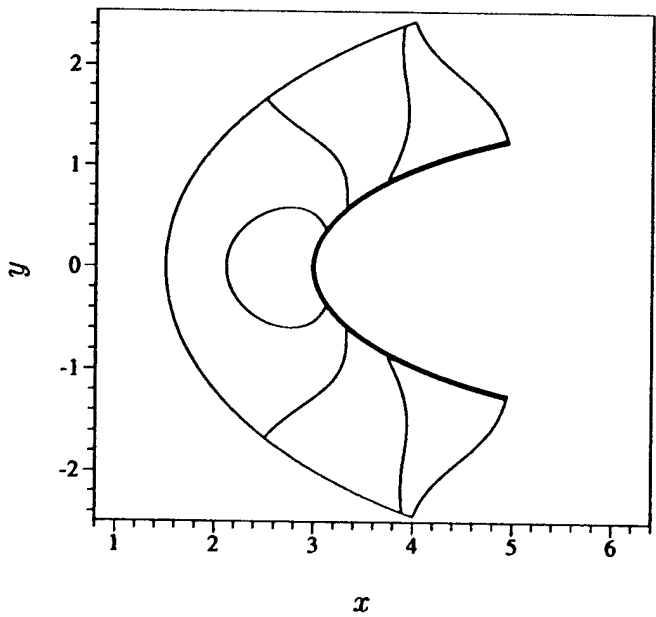


Figure 5.8: Contours of temperature T of the laminar flow at $Ma = 0.15$, $Re = 42,000$, $T_w/T_0 = 1.075$.

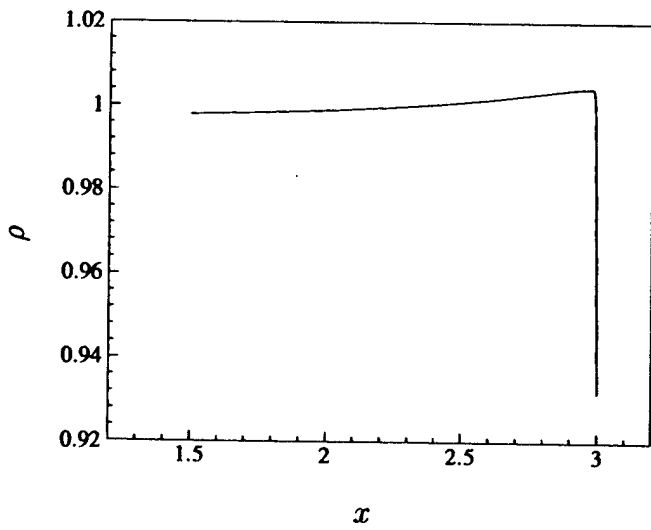


Figure 5.9: Density ρ along the stagnation line. $Ma = 0.15$, $Re = 42000$.

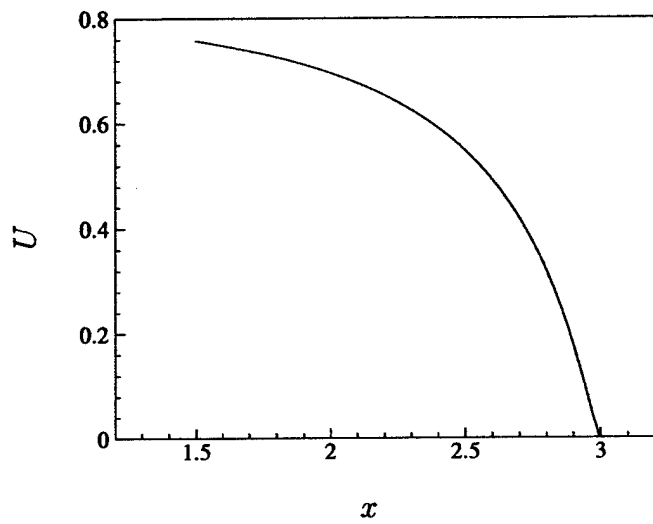


Figure 5.10: Streamwise velocity U along the stagnation line. $Ma = 0.15$, $Re = 42000$.

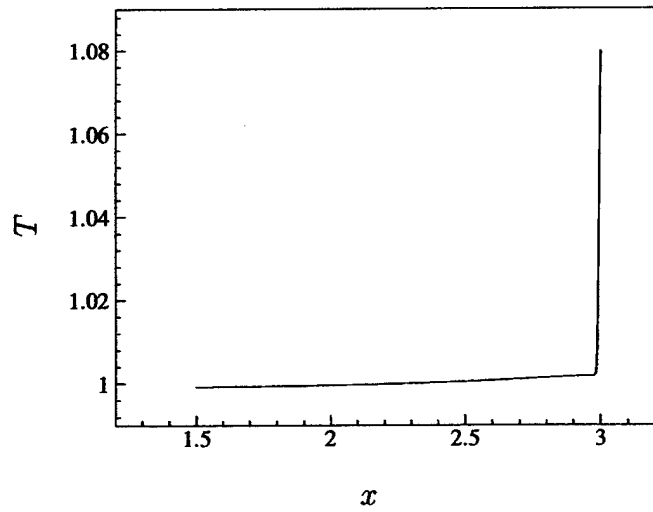


Figure 5.11: Temperature T along the stagnation line. $Ma = 0.15$, $Re = 42000$.

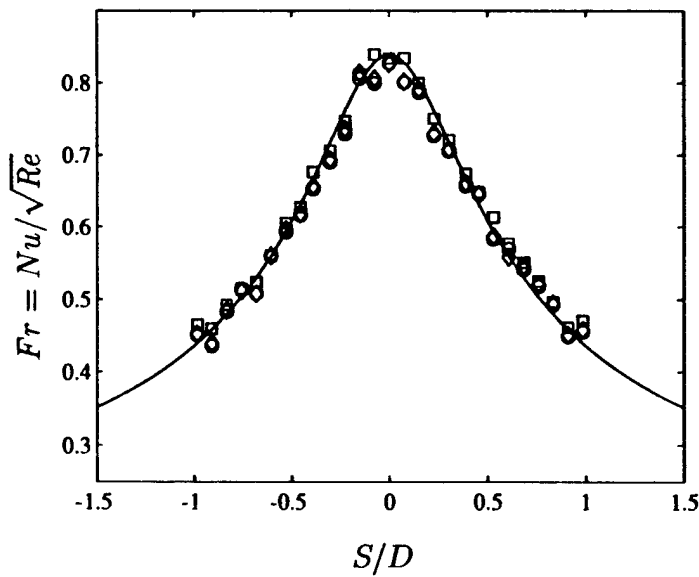


Figure 5.12: Frössling number distribution on the surface. —: laminar computation, Symbols: experimental measurements at $Tu = 0.3\%$, $L/D = 2.308$; \circ : $Re_{av} = 50100$, \triangle : $Re_{av} = 50200$, \square : $Re_{av} = 50700$.

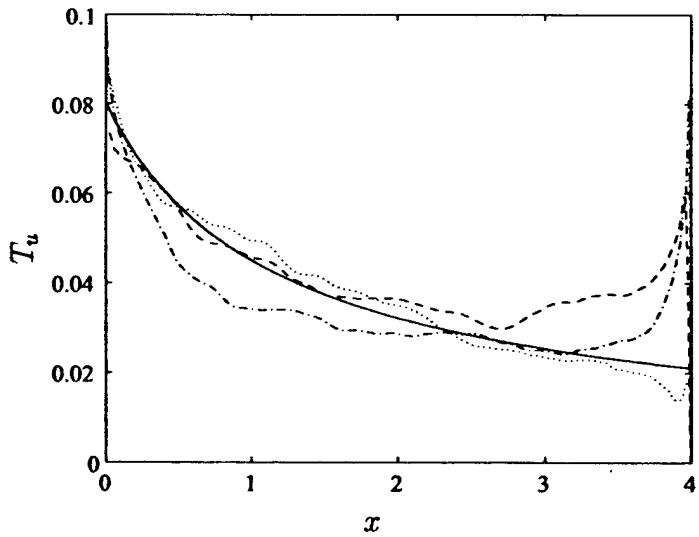


Figure 5.13: Turbulence intensity along the stagnation streamline. -----: u_{rms} ,: v_{rms} , -·-: w_{rms} , —: power law fit by $x^{-0.83}$. (Van Fossen et al., 1995).

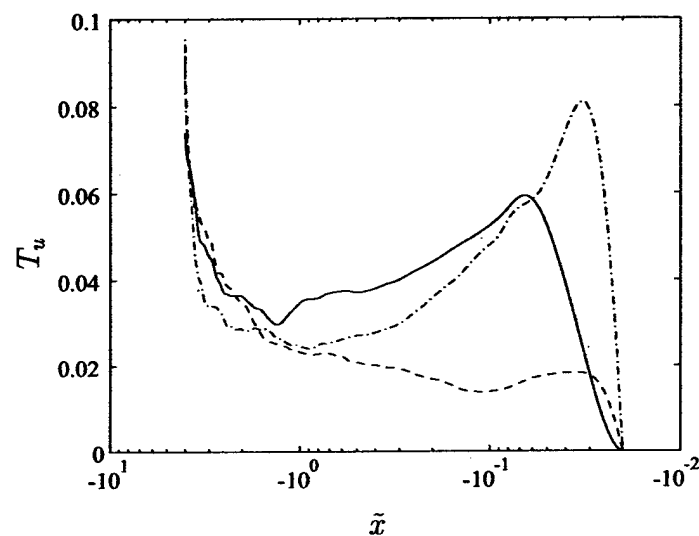


Figure 5.14: Turbulence intensity along the stagnation streamline in transformed coordinates \tilde{x} for clarity, where $\tilde{x} = \log(4.02 - x)$. —: u_{rms} , - - -: v_{rms} , - · - : w_{rms}

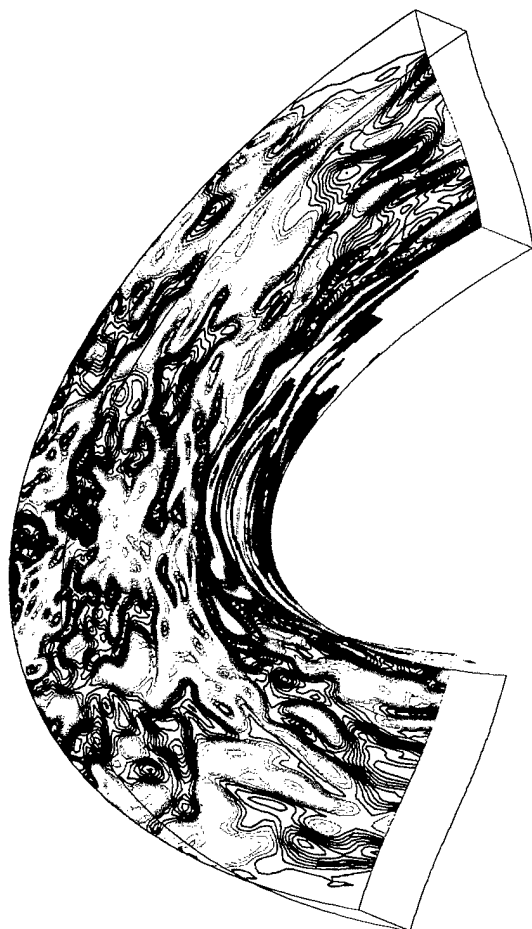


Figure 5.15: Instantaneous spanwise velocity in $x - y$ plane and temperature gradient on the body surface.

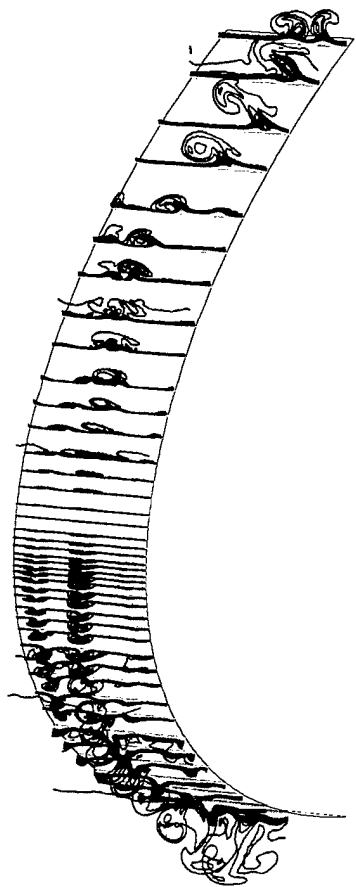


Figure 5.16: Instantaneous temperature contours at different locations on the body surface.

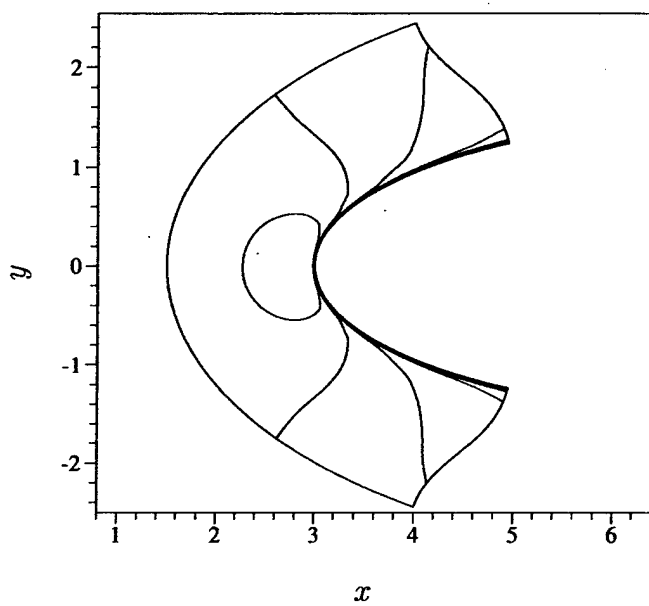


Figure 5.17: Mean density contours. $Re = 42,000$, $Ma = 0.15$, $Tu = 0.05$, $L/D = 0.1$. Contour minimum: 0.9076, maximum: 1.004, increment: 0.0048.

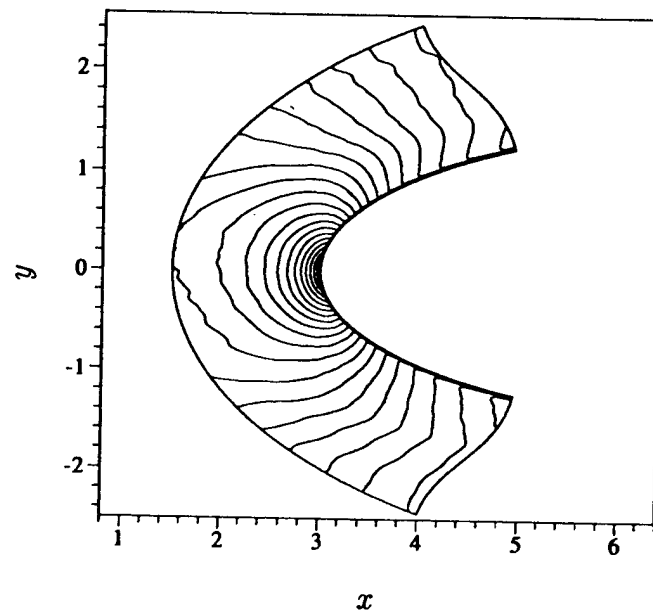


Figure 5.18: Mean streamwise velocity contours. $Re = 42,000$, $Ma = 0.15$, $Tu = 0.05$, $L/D = 0.1$. Contour minimum: 0.0 , maximum: 1.233, increment: 0.0615.

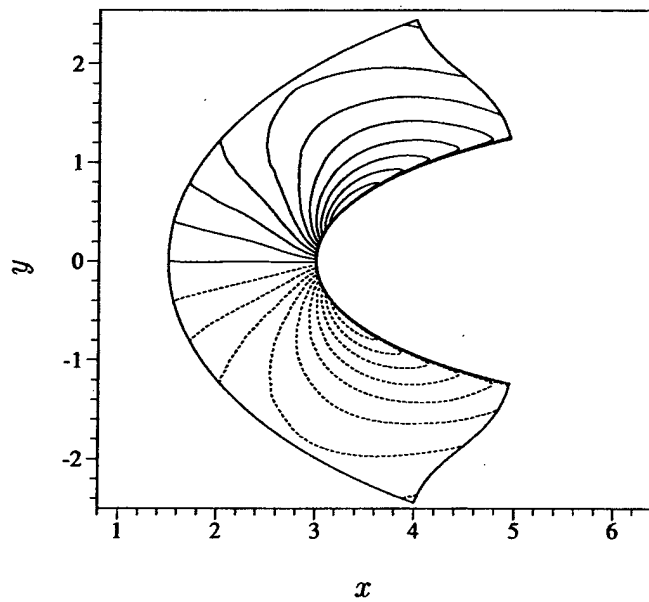


Figure 5.19: Mean vertical velocity contours. $Re = 42,000$, $Ma = 0.15$, $Tu = 0.05$, $L/D = 0.1$. Contour minimum: -0.5926, maximum: 0.5977, increment: 0.0567.

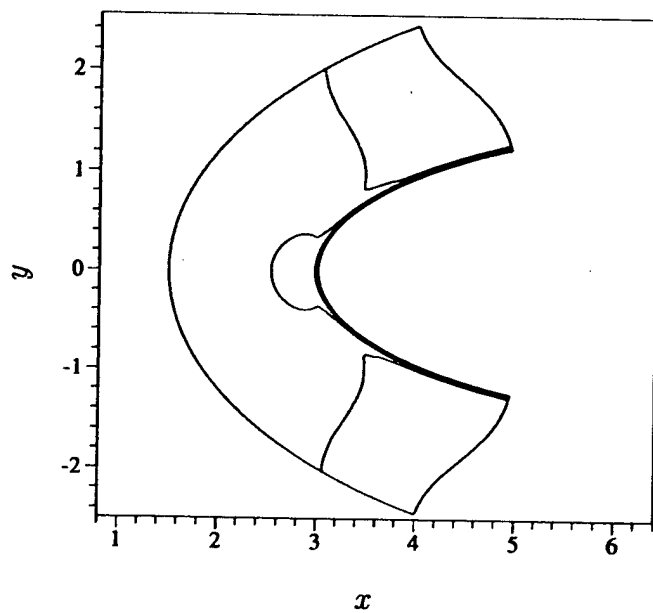


Figure 5.20: Mean temperature contours. $Re = 42,000$, $Ma = 0.15$, $Tu = 0.05$, $L/D = 0.1$. Contour minimum 0.995, maximum 1.075, increment: 0.0027.

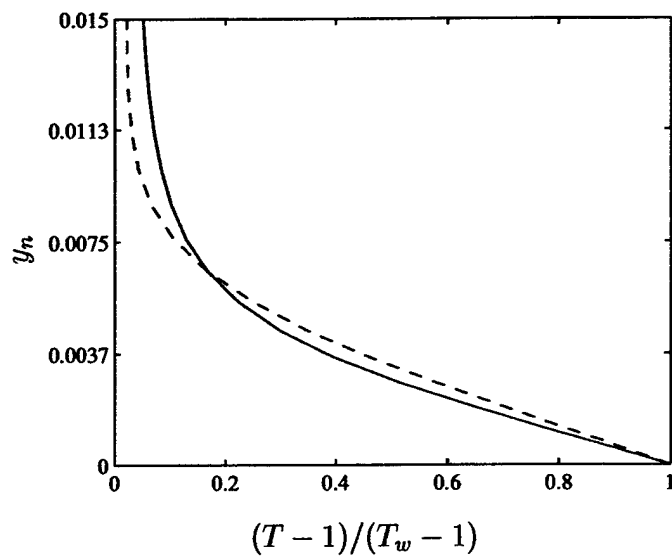


Figure 5.21: Comparison between turbulent mean and laminar temperature profile along stagnation streamline $s = 0$. ———: turbulent mean, -----: laminar.

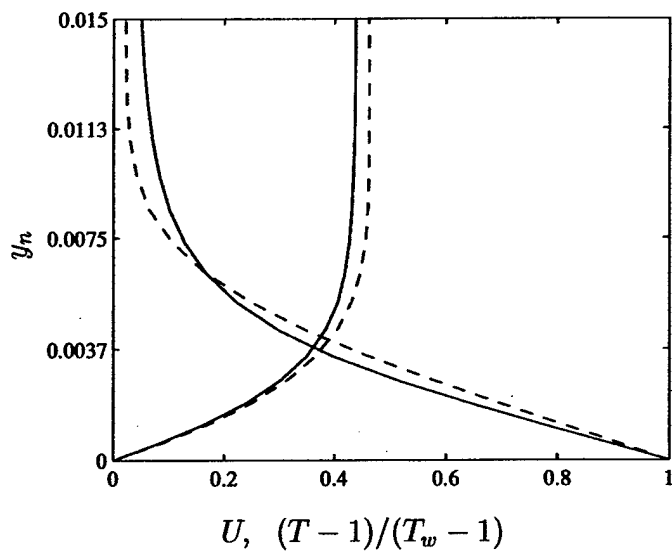


Figure 5.22: Comparison between profiles of turbulent mean velocity U , temperature $(T - 1)/(T_w - 1)$ at $s = 0.2D$ with laminar profiles, ———: turbulent mean, -----: laminar.

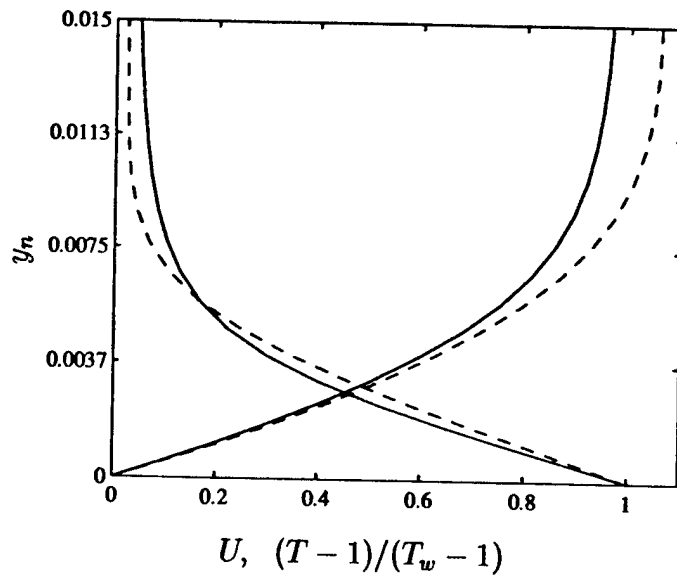


Figure 5.23: Comparison between profiles of turbulent mean velocity U , temperature $(T-1)/(T_w-1)$ at $s = 0.8D$ with laminar profiles, —: turbulent mean, - - -: laminar.

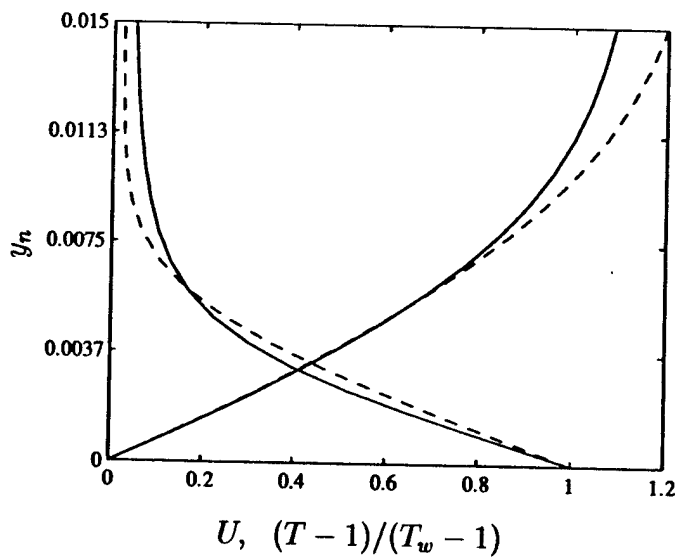


Figure 5.24: Comparison between profiles of turbulent mean velocity U , temperature $(T-1)/(T_w-1)$ at $s = 1.6D$ with laminar profiles, —: turbulent mean, - - -: laminar.

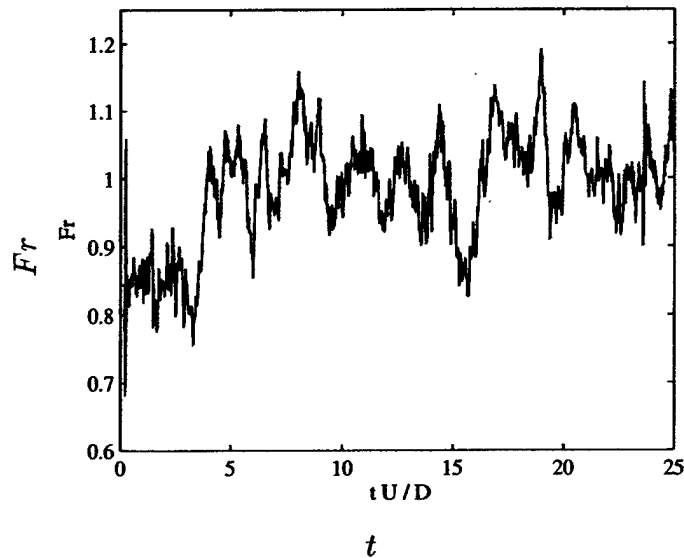


Figure 5.25: Time history of spanwise averaged Frössling number at the leading edge.

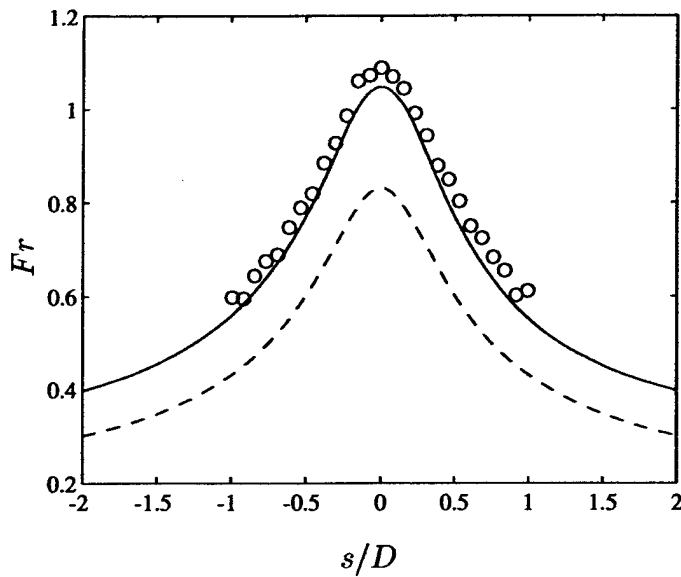


Figure 5.26: Averaged Frössling number distribution on the body surface.
 —: turbulent mean, -----: laminar, \circ : experimental data (Van Fossen et al., 1995).

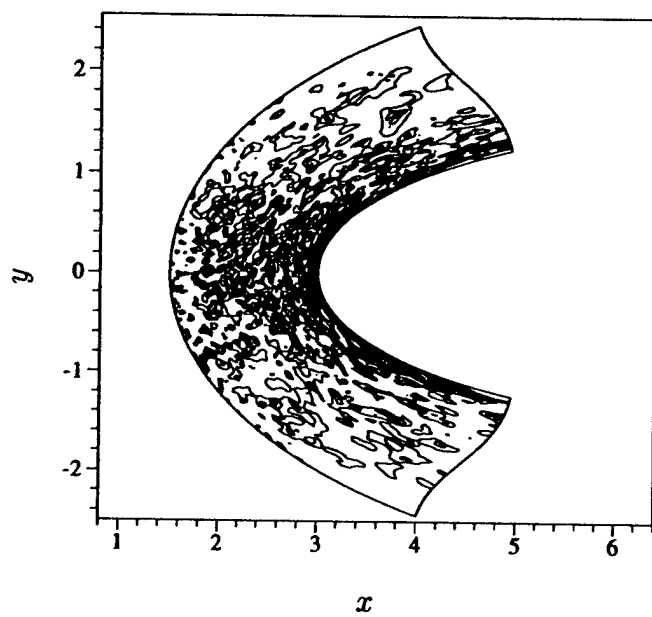


Figure 5.27: Instantaneous SGS eddy viscosity ν_T/ν (averaged in z) . $Re = 42,000$, $Ma = 0.15$, $Tu = 0.05$, $L/D = 0.1$. Contour minimum : 0.05, maximum: 0.75, increment: 0.014.

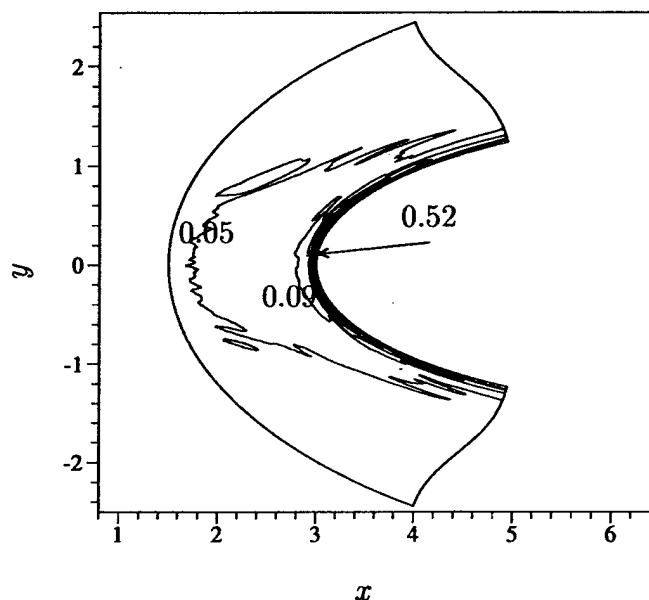


Figure 5.28: Turbulent mean SGS eddy viscosity ν_T/ν . $Re = 42,000$, $Ma = 0.15$, $Tu = 0.05$, $L/D = 0.1$. Contours: minimum : 0.05, maximum: 0.52, increment: 0.040.

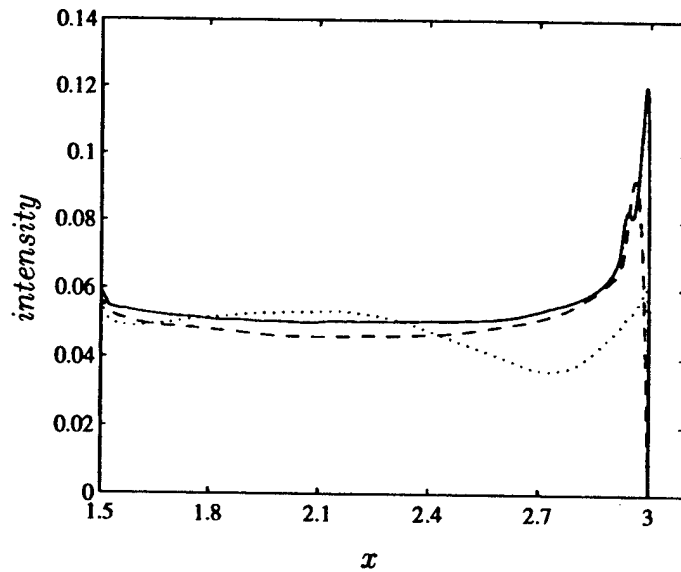


Figure 5.29: Turbulence intensity along the stagnation streamline. -----: u_{rms} ,: v_{rms} , ———: w_{rms}

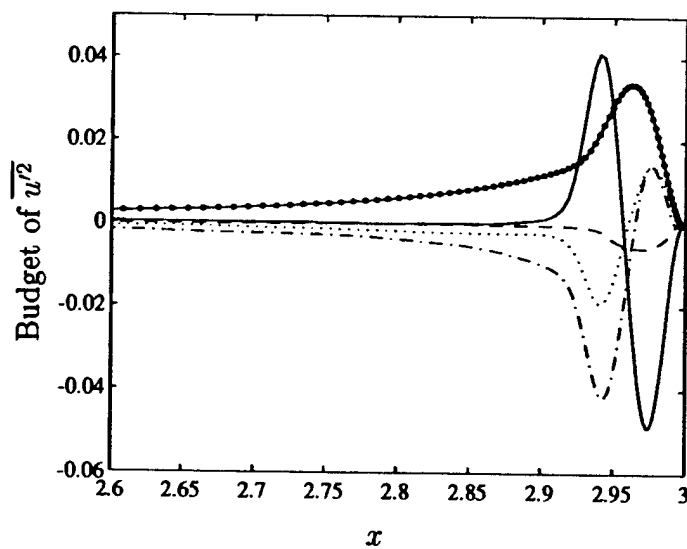


Figure 5.30: Turbulence budget of $\overline{u'^2}$ along the stagnation streamline.
 —○—: production, -----: dissipation,: mean convection, ———: turbulent transport, —···—: pressure gradient velocity correlation.

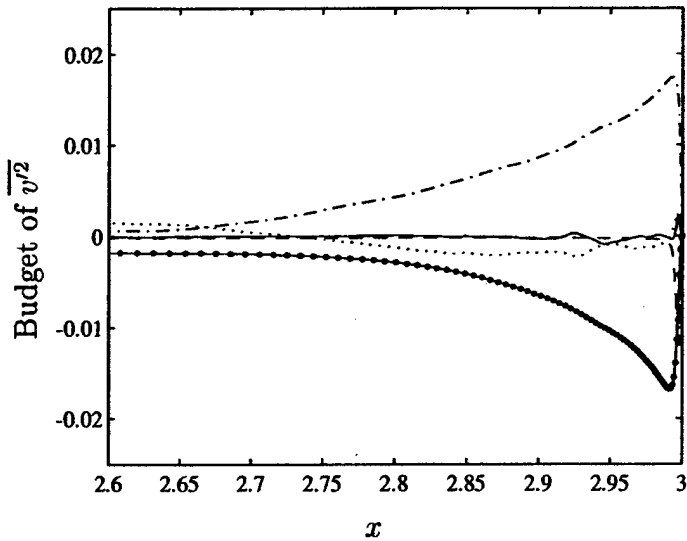


Figure 5.31: Turbulence budget of $\overline{v'^2}$ along the stagnation streamline.
 —○—: production, -----: dissipation, ······: mean convection, ———: turbulent transport, —·—: pressure gradient velocity correlation.

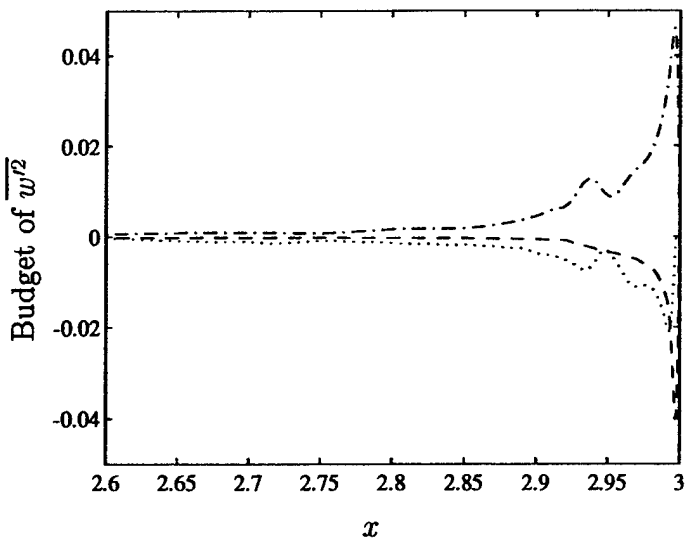


Figure 5.32: Turbulence budget of $\overline{w'^2}$ along the stagnation streamline.
 -----: dissipation, ······: mean convection + turbulent transport, —·—: pressure gradient velocity correlation

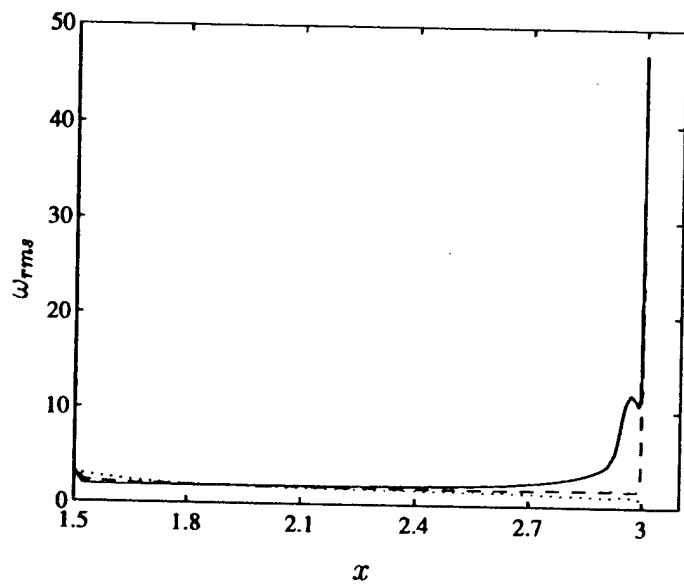


Figure 5.33: RMS value of turbulence vorticity along the stagnation streamline. -----: ω_z ,: ω_x ; ———: ω_y .

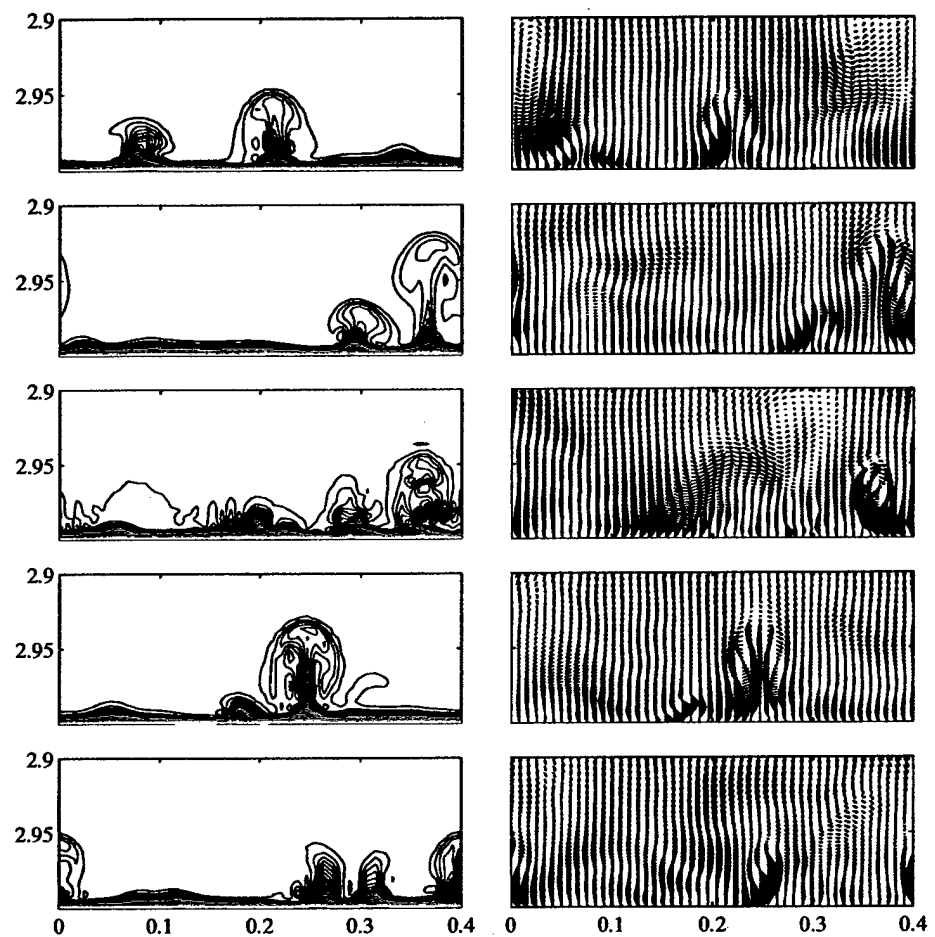


Figure 5.34: Temperature contour and the corresponding velocity field in the stagnation plane at different times. The mean flow direction is downward and the time interval is $\Delta t = 0.6$

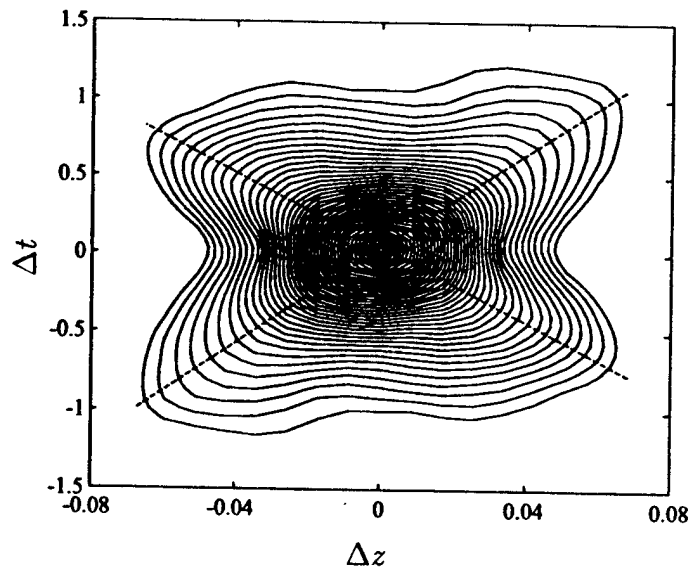


Figure 5.35: Space-time correlation of vorticity at the leading edge ($s = 0$). Contour minimum: 0.1, maximum: 1.0, increment: 0.002. The dash lines indicates that the most probable convection speed in spanwise direction is $\sim \pm 0.06$.

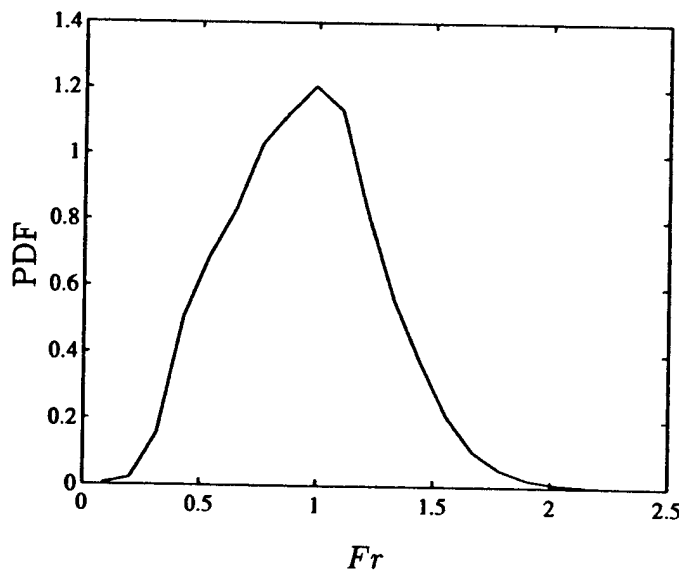


Figure 5.36: Probability density function of Frössling number at the leading edge

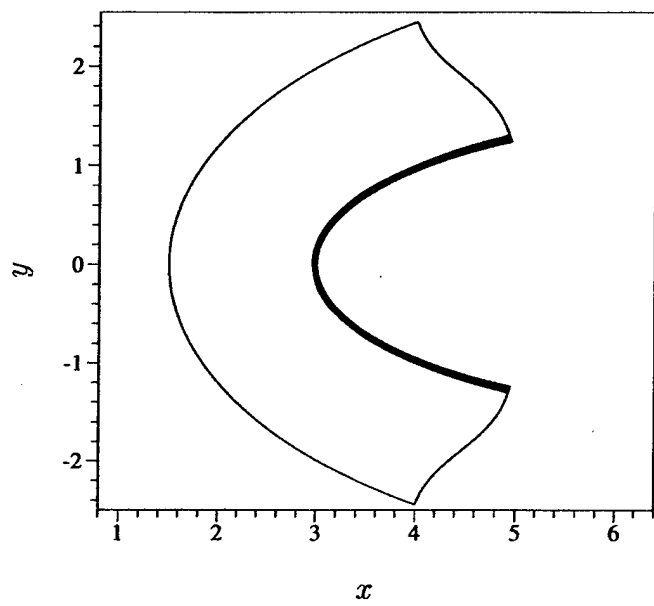


Figure 5.37: Turbulent density fluctuation $\overline{\rho^2}$, $Re = 42,000$, $Ma = 0.15$, $Tu = 0.05$, $L/D = 0.1$. Contour minimum : 0.00001, maximum: 0.00019, increment: 0.00001.

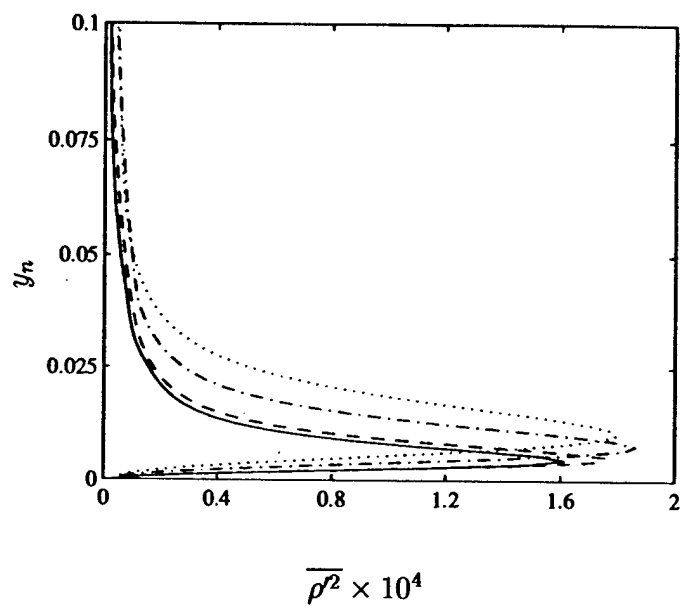


Figure 5.38: The profiles of turbulent density fluctuation along wall normal direction. —: $s = 0$, - - -: $s = 0.2D$, - · -: $s = 0.8D$, and · · ·: $s = 1.6D$.

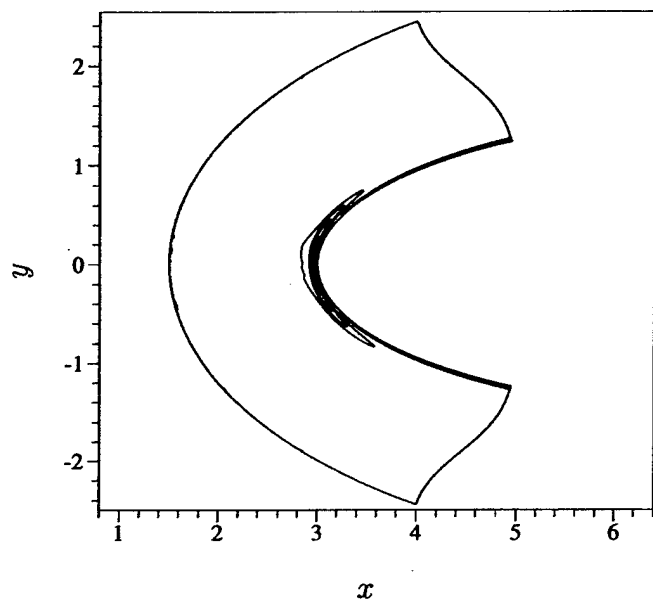


Figure 5.39: Turbulent velocity fluctuation $\overline{u'^2}$, $Re = 42,000$, $Ma = 0.15$, $Tu = 0.05$, $L/D = 0.1$. Contour minimum : 0.0035, maximum: 0.0233, increment: 0.001.

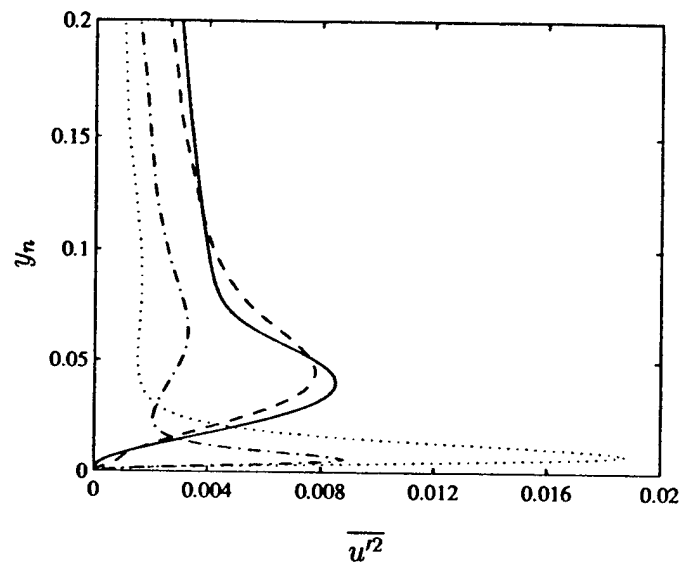


Figure 5.40: The profiles of turbulent velocity fluctuation $\overline{u'^2}$ along wall normal direction. —: $s = 0$, - - -: $s = 0.2D$, - · - : $s = 0.8D$, and · · · : $s = 1.6D$.

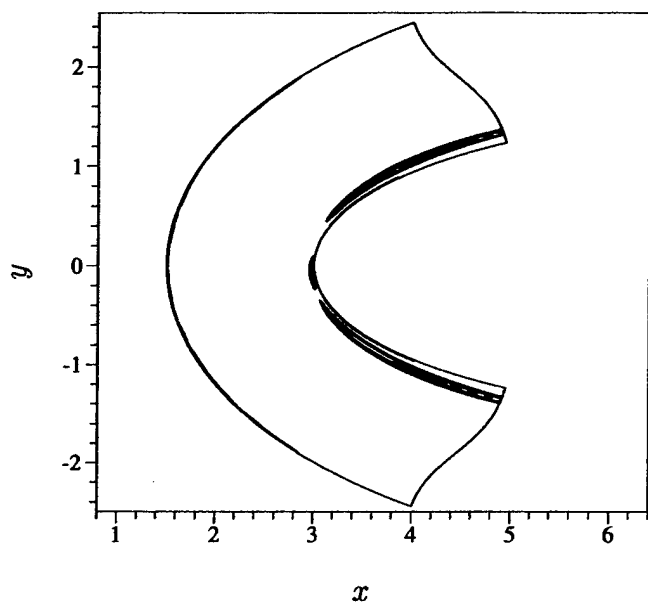


Figure 5.41: Turbulent velocity fluctuation $\overline{v'^2}$, $Re = 42,000$, $Ma = 0.15$, $Tu = 0.05$, $L/D = 0.1$. Contour minimum : 0.0030, maximum: 0.0045, increment: 0.00015.

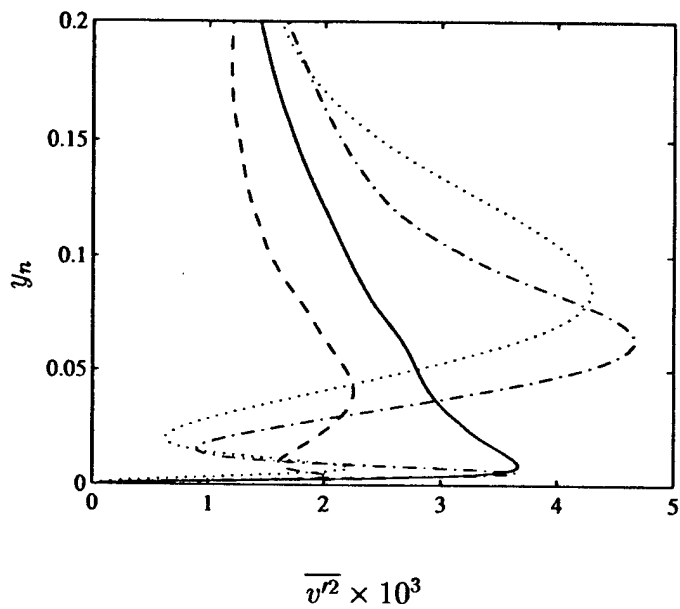


Figure 5.42: The profiles of turbulent velocity fluctuation $\overline{v^2}$ along wall normal direction. —: $s = 0$, - - -: $s = 0.2D$, - · -: $s = 0.8D$, and · · · · : $s = 1.6D$.

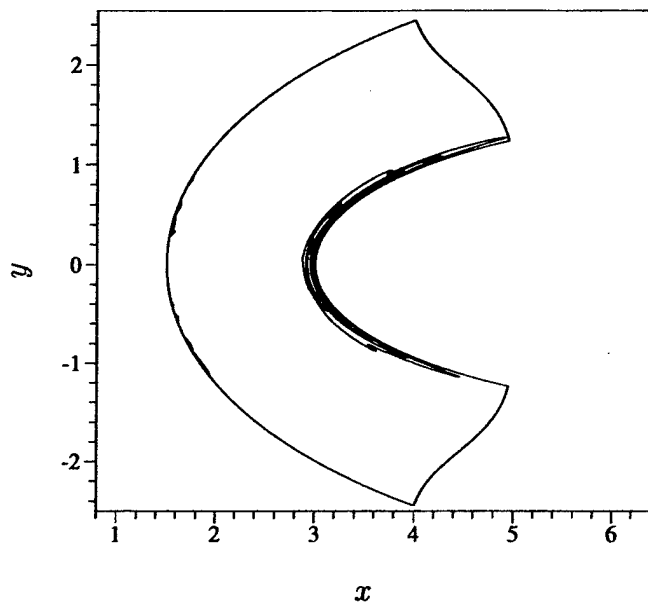


Figure 5.43: Turbulent velocity fluctuation $\overline{w^2}$, $Re = 42,000$, $Ma = 0.15$, $Tu = 0.05$, $L/D = 0.1$. Contour minimum : 0.0040, maximum: 0.0140, increment: 0.001.

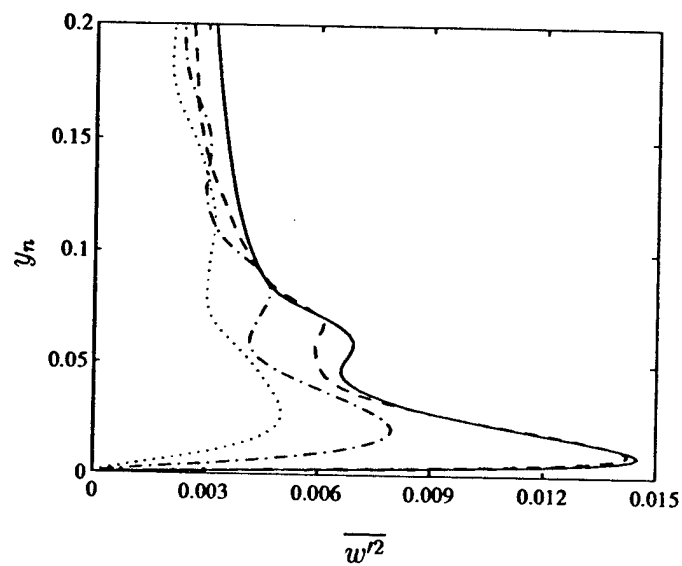


Figure 5.44: The profiles of turbulent velocity fluctuation $\overline{w'^2}$ along wall normal direction. —: $s = 0$, - - -: $s = 0.2D$, - · - : $s = 0.8D$, and · · · : $s = 1.6D$.

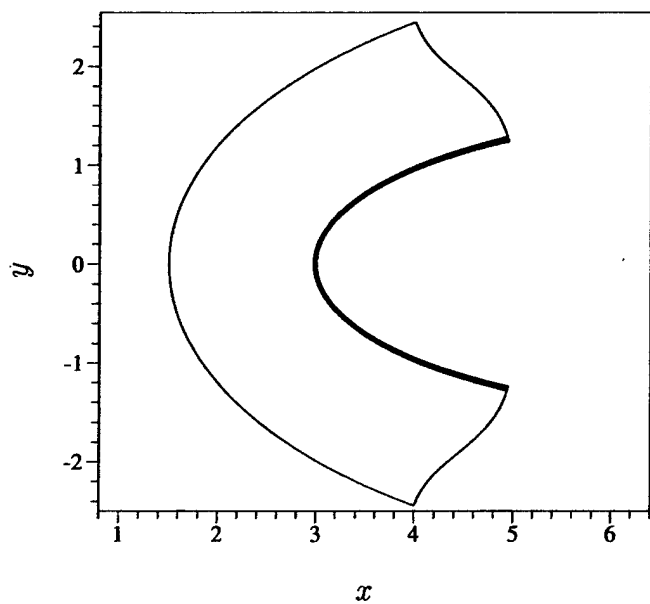
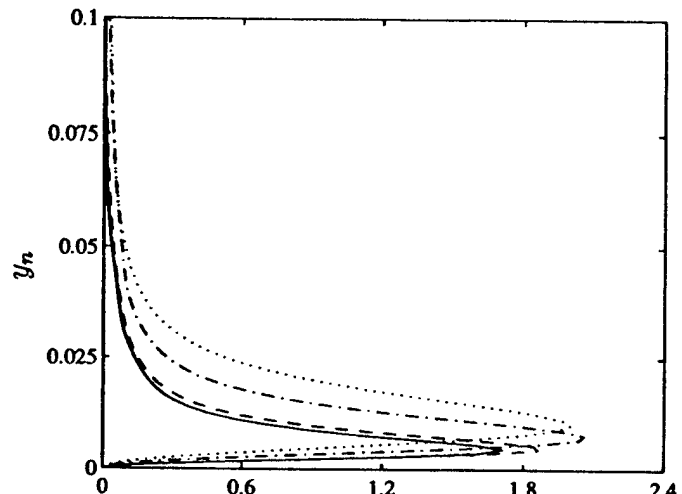


Figure 5.45: Turbulent temperature fluctuation $\overline{T^2}$, $Re = 42,000$, $Ma = 0.15$, $Tu = 0.05$, $L/D = 0.1$. Contour minimum : 0.00002, maximum: 0.0002, increment: 0.00002.



$$\overline{T^2} \times 10^4$$

Figure 5.46: The profiles of turbulent temperature fluctuation $\overline{T^2}$ along wall normal direction. —: $s = 0$, - - -: $s = 0.2D$, - · - : $s = 0.8D$, and · · · : $s = 1.6D$.

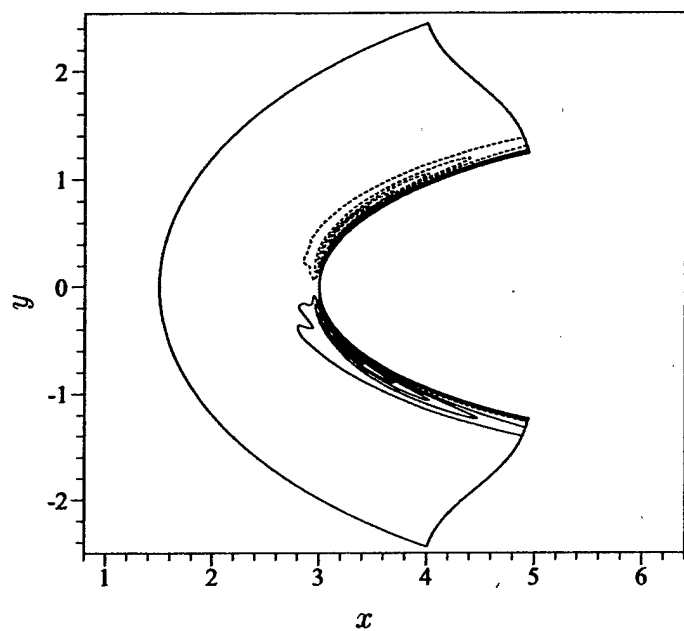


Figure 5.47: Turbulent Reynolds stress $\overline{u'v'}$, $Re = 42,000$, $Ma = 0.15$, $Tu = 0.05$, $L/D = 0.1$. Contour minimum : -0.006, maximum: 0.006, increment: 0.0006.

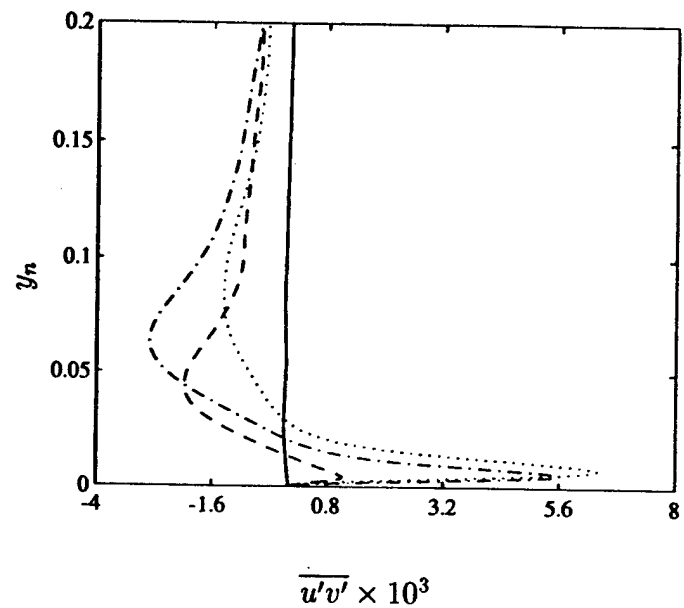


Figure 5.48: The profiles of turbulent Reynolds stress $\overline{u'v'}$ along wall normal direction. —: $s = 0$, - - -: $s = 0.2D$, - · - : $s = 0.8D$, and · · · · : $s = 1.6D$.

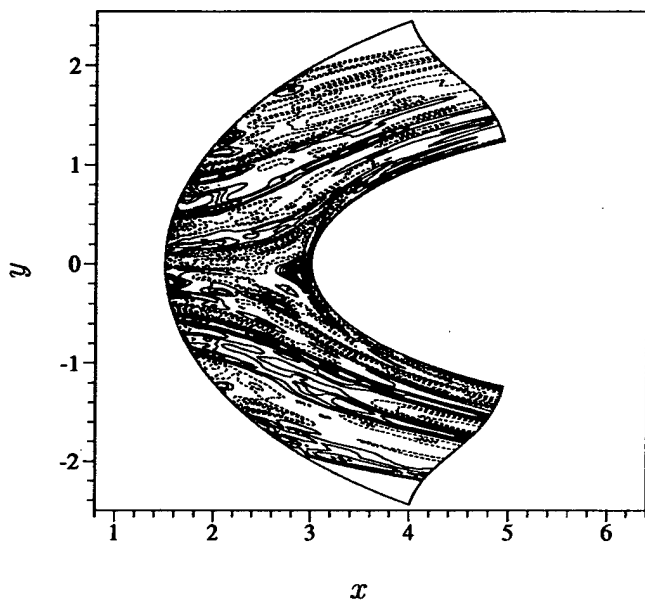


Figure 5.49: Turbulent Reynolds stress $\overline{u'w'}$, $Re = 42,000$, $Ma = 0.15$, $Tu = 0.05$, $L/D = 0.1$. Contour minimum : -0.0005, maximum: 0.0005, increment: 0.00005.

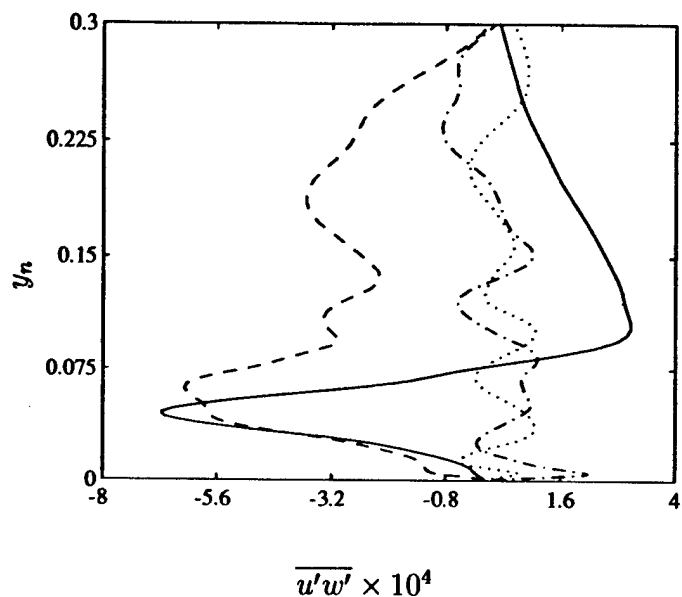


Figure 5.50: The profiles of turbulent Reynolds stress $\overline{u'w'}$ along wall normal direction. —: $s = 0$, - - -: $s = 0.2D$, - · - : $s = 0.8D$, and · · · · : $s = 1.6D$.

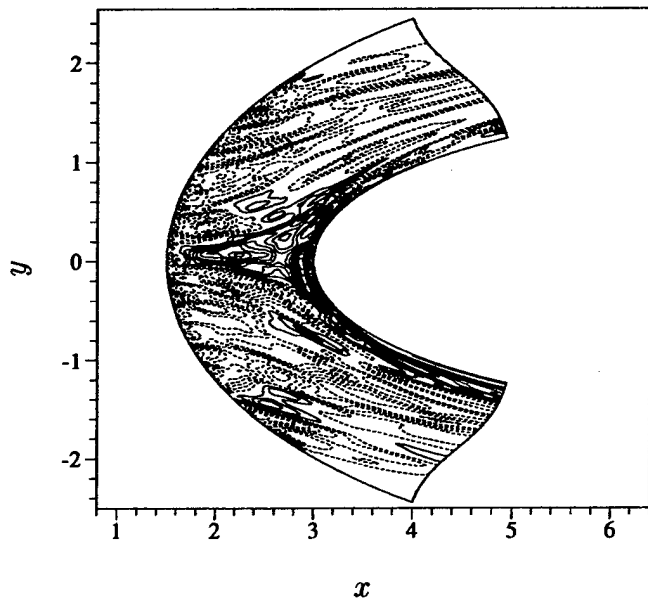


Figure 5.51: Turbulent Reynolds stress $\overline{v'w'}$, $Re = 42,000$, $Ma = 0.15$, $Tu = 0.05$, $L/D = 0.1$. Contour minimum : -0.0006, maximum: 0.0006, increment: 0.00005.

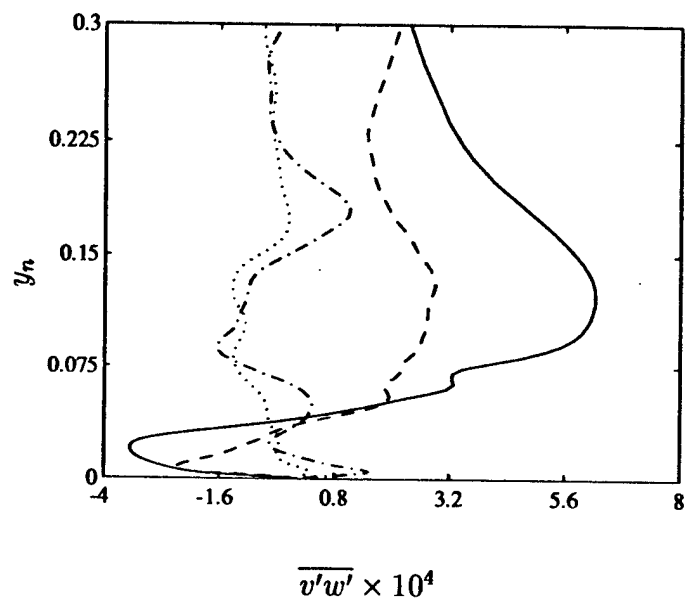


Figure 5.52: The profiles of turbulent Reynolds stress $\overline{v'w'}$ along wall normal direction. —: $s = 0$, - - -: $s = 0.2D$, - · - : $s = 0.8D$, and · · · · : $s = 1.6D$.

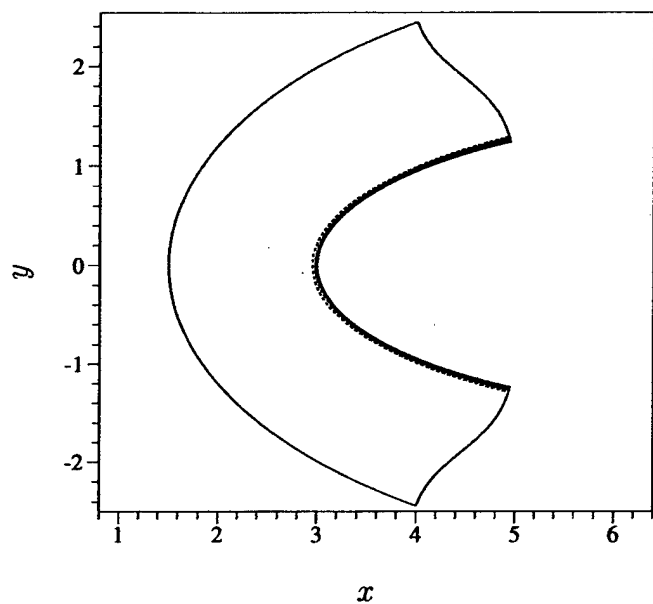
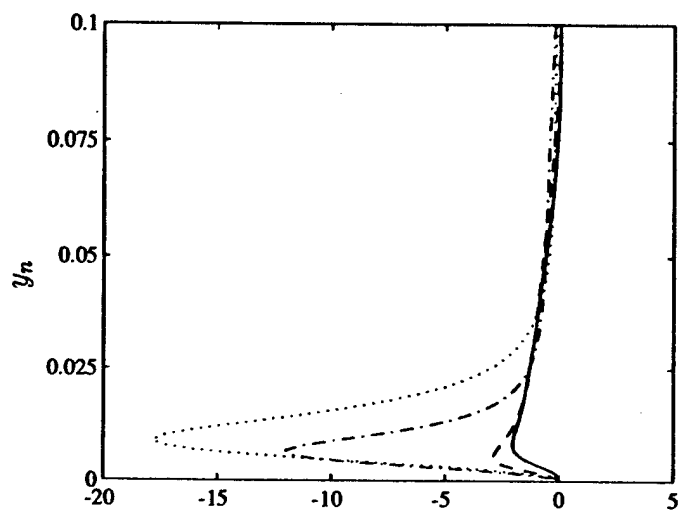


Figure 5.53: Turbulent heat flux $\overline{u'T'}$, $Re = 42,000$, $Ma = 0.15$, $Tu = 0.05$, $L/D = 0.1$. Contour minimum : -0.0019, maximum: -0.0001, increment: 0.0001.



$$\overline{u'T'} \times 10^4$$

Figure 5.54: The profiles of turbulent heat flux $\overline{u'T'}$ along wall normal direction. —: $s = 0$, - - -: $s = 0.2D$, - · - : $s = 0.8D$, and · · · · : $s = 1.6D$.

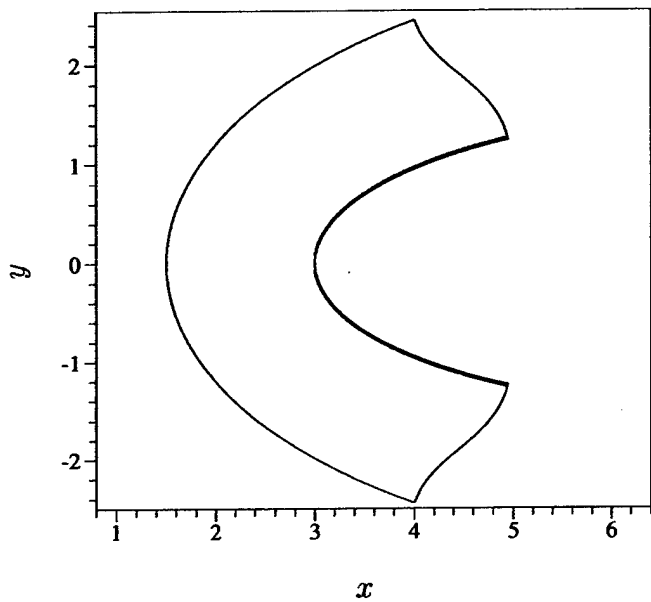


Figure 5.55: Turbulent heat flux $\overline{v'T'}$, $Re = 42,000$, $Ma = 0.15$, $Tu = 0.05$, $L/D = 0.1$. Contour minimum : -0.0007, maximum: -0.0007, increment: 0.0001.

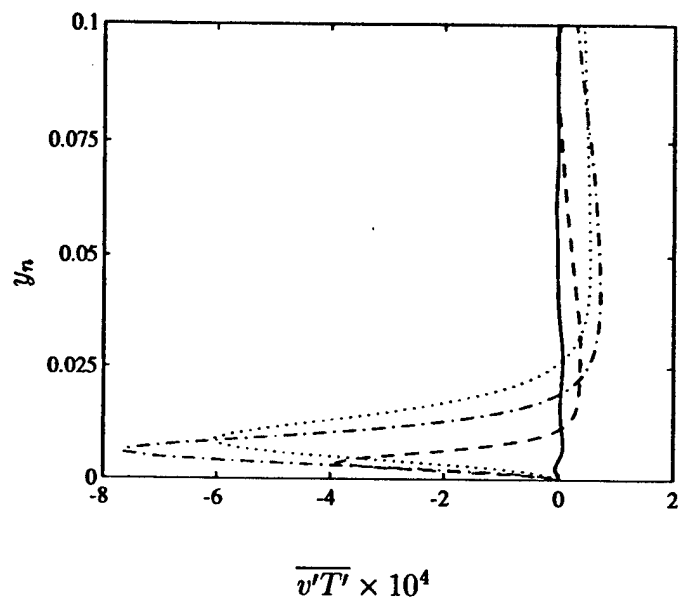


Figure 5.56: The profiles of turbulent heat flux $\overline{v'T'}$ along wall normal direction. —: $s = 0$, - - -: $s = 0.2D$, - · - : $s = 0.8D$, and · · · · : $s = 1.6D$.

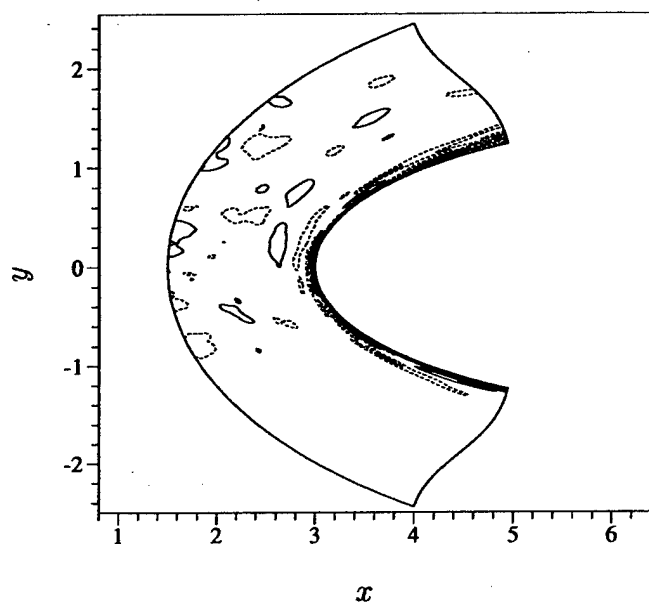


Figure 5.57: Turbulent heat flux $\overline{w'T'}$, $Re = 42,000$, $Ma = 0.15$, $Tu = 0.05$, $L/D = 0.1$. Contour minimum : -0.000065, maximum: -0.000044, increment: 0.00001.

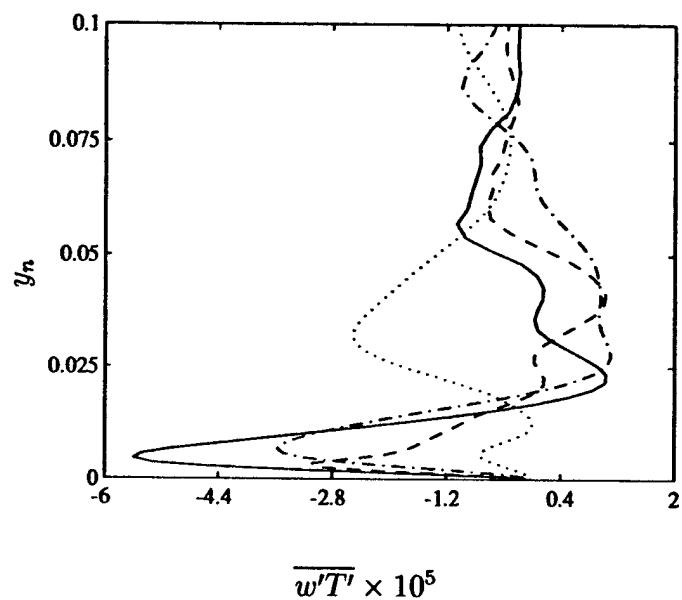


Figure 5.58: Profiles of turbulent heat flux $\overline{w'T'}$ along wall normal direction.
 —: $s = 0$, - - -: $s = 0.2D$, - · - : $s = 0.8D$, and · · - : $s = 1.6D$.

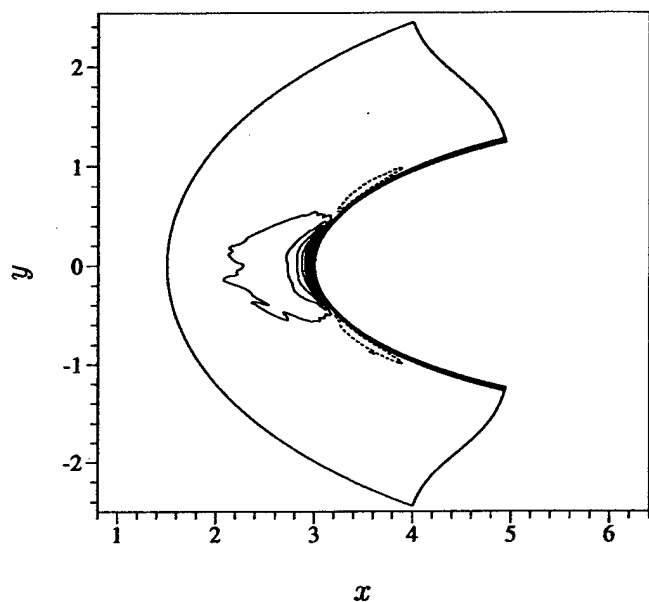


Figure 5.59: Turbulence production for $\overline{u'^2}$, $Re = 42,000$, $Ma = 0.15$, $Tu = 0.05$, $L/D = 0.1$. Contour minimum : -0.0018, maximum: -0.066, increment: 0.003.

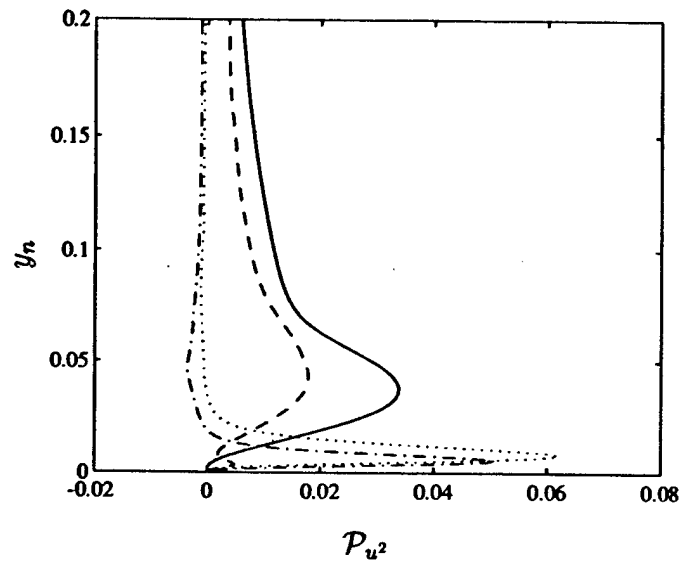


Figure 5.60: Profiles of turbulence production for $\bar{u'^2}$ along wall normal direction. —: $s = 0$, - - -: $s = 0.2D$, - · - : $s = 0.8D$, and · · · · : $s = 1.6D$.

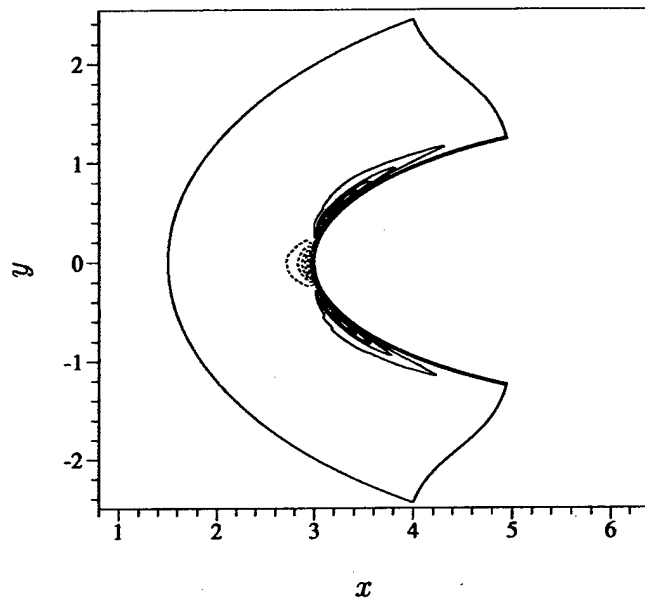


Figure 5.61: Turbulence production for $\bar{v^2}$, $Re = 42,000$, $Ma = 0.15$, $Tu = 0.05$, $L/D = 0.1$. Contour minimum : -0.0016, maximum: -0.036, increment: 0.002.

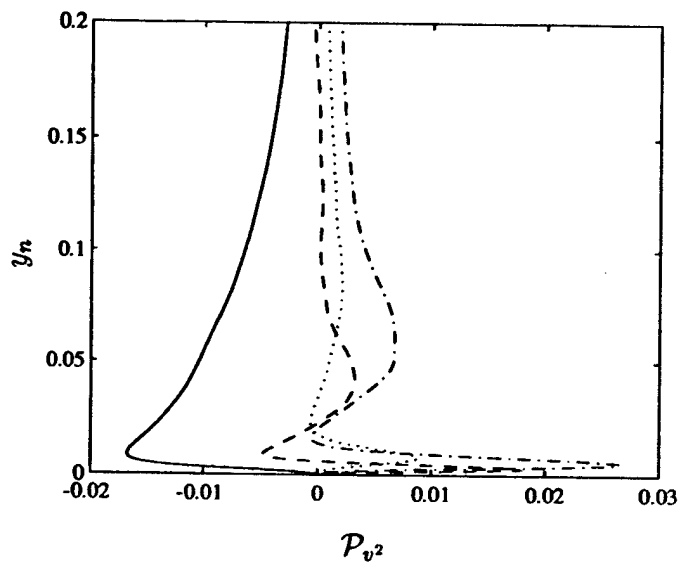


Figure 5.62: Profiles of turbulence production for $\overline{v'^2}$ along wall normal direction. —: $s = 0$, - - - : $s = 0.2D$, - · - : $s = 0.8D$, and · · · · : $s = 1.6D$.

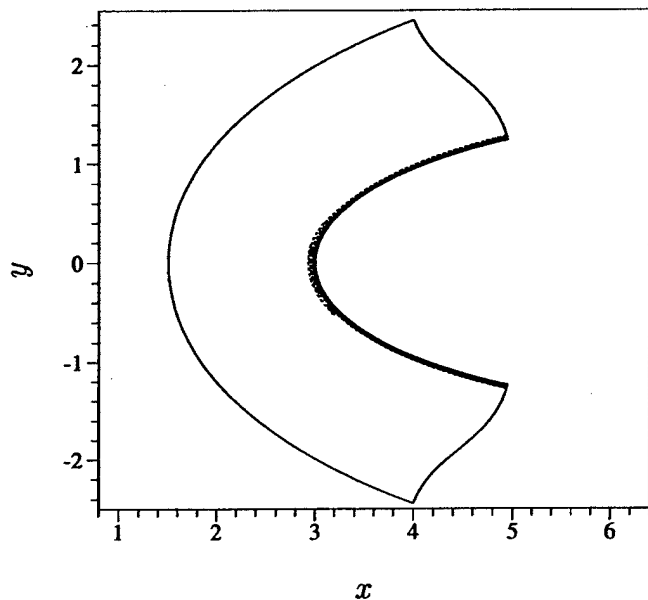
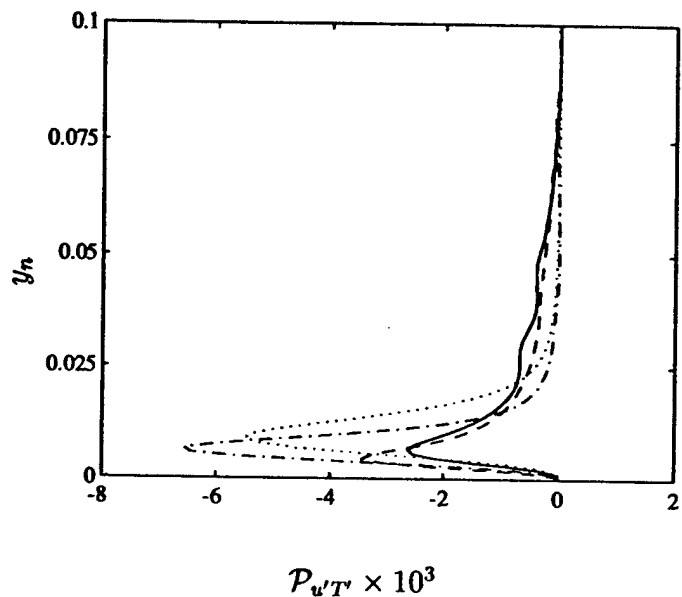


Figure 5.63: Turbulence production for $\overline{u'T'}$, $Re = 42,000$, $Ma = 0.15$, $Tu = 0.05$, $L/D = 0.1$. Contour minimum : -0.007, maximum: -0.0002, increment: 0.0002.



$$\mathcal{P}_{w'T'} \times 10^3$$

Figure 5.64: Profiles of turbulence production for $\bar{w'T'}$ along wall normal direction. —: $s = 0$, - - -: $s = 0.2D$, - · - : $s = 0.8D$, and · · · : $s = 1.6D$.

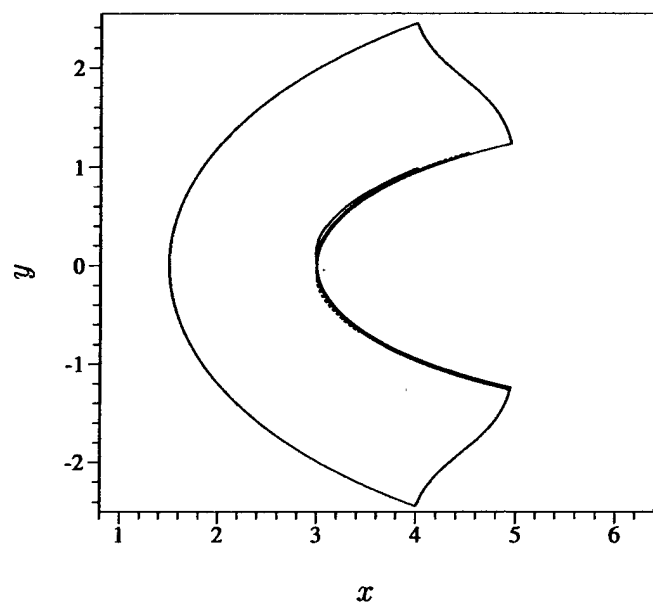


Figure 5.65: Turbulence production for $\overline{v'T'}$, $Re = 42,000$, $Ma = 0.15$, $Tu = 0.05$, $L/D = 0.1$. Contour minimum : -0.007, maximum: 0.01, increment: 0.0005.

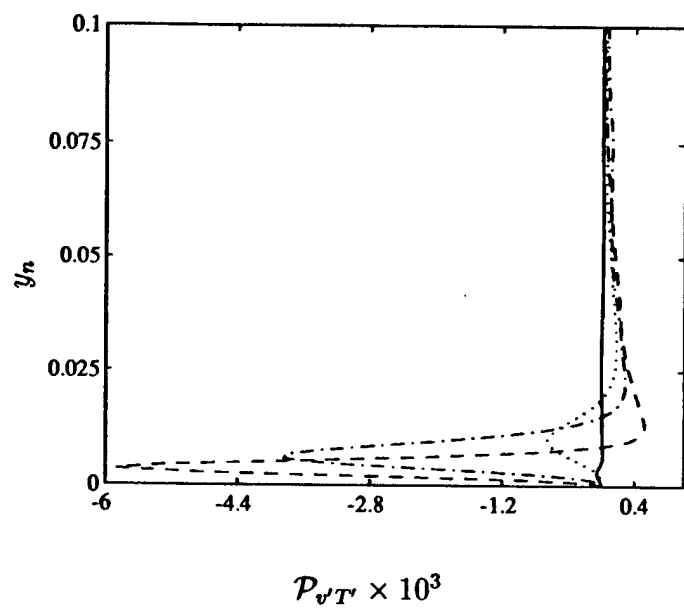


Figure 5.66: Profiles of turbulence production for $\overline{v'T'}$ along wall normal direction. —: $s = 0$, - - - : $s = 0.2D$, - · - : $s = 0.8D$, and · · - : $s = 1.6D$.

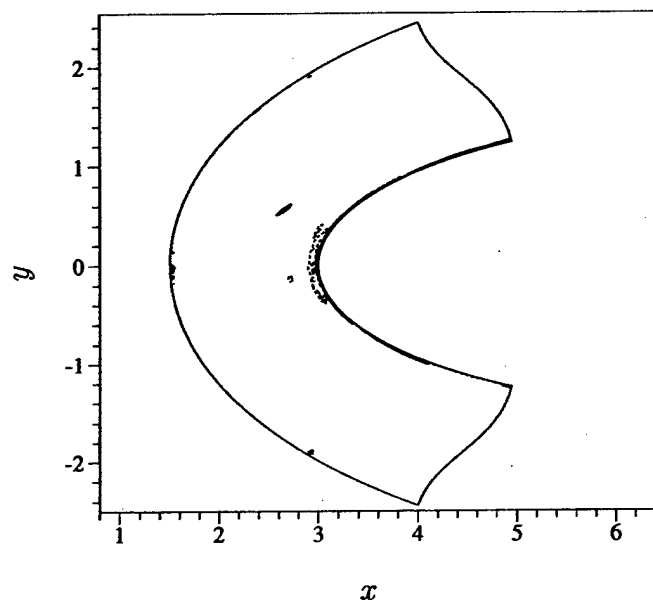


Figure 5.67: Pressure-strain correlation $\overline{p' S'_{11}}$, $Re = 42,000$, $Ma = 0.15$, $Tu = 0.05$, $L/D = 0.1$. Contour minimum : -0.115, maximum: 0.08, increment: 0.005.

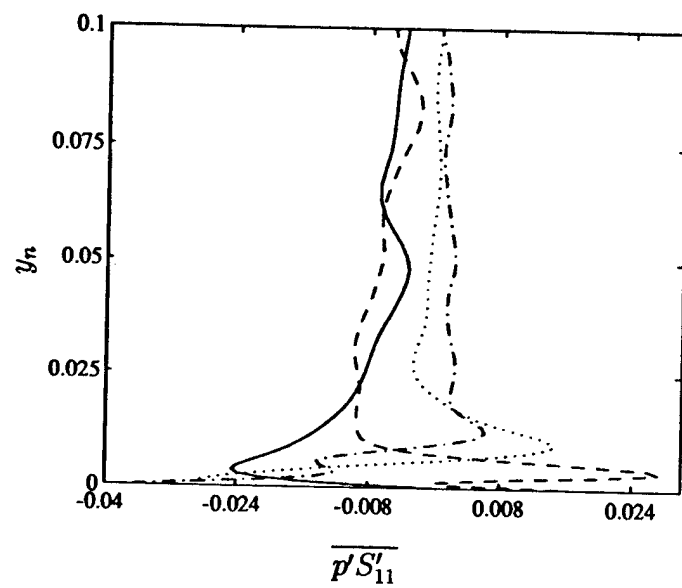


Figure 5.68: Profiles of pressure strain correlation $\overline{p' S'_{11}}$ along wall normal direction. —: $s = 0$, - - -: $s = 0.2D$, - · - : $s = 0.8D$, and · · · · : $s = 1.6D$.

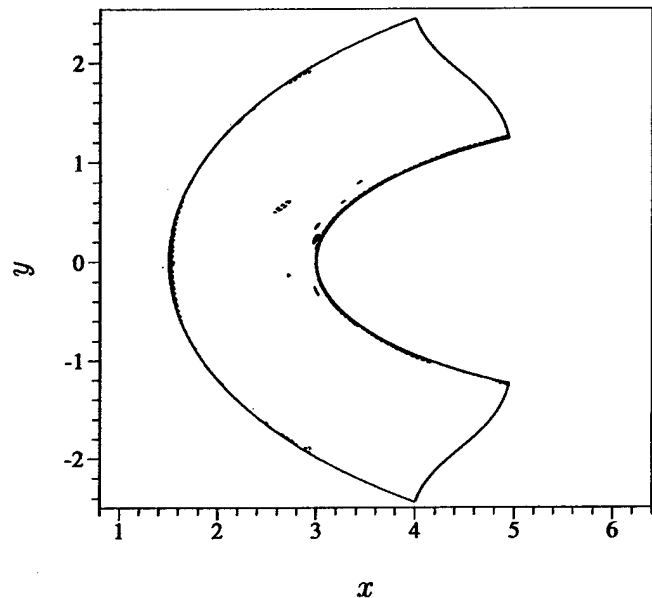


Figure 5.69: Pressure-strain correlation $\overline{p' S'_{22}}$, $Re = 42,000$, $Ma = 0.15$, $Tu = 0.05$, $L/D = 0.1$. Contour minimum : -0.08, maximum: 0.115, increment: 0.005.

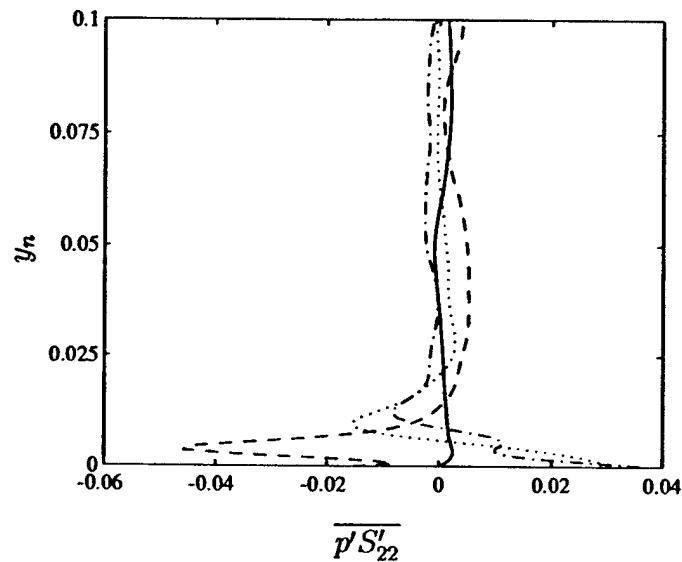


Figure 5.70: Profiles of pressure strain correlation $\overline{p' S'_{22}}$ along wall normal direction. —: $s = 0$, - - - : $s = 0.2D$, - · - : $s = 0.8D$, and · · · : $s = 1.6D$.

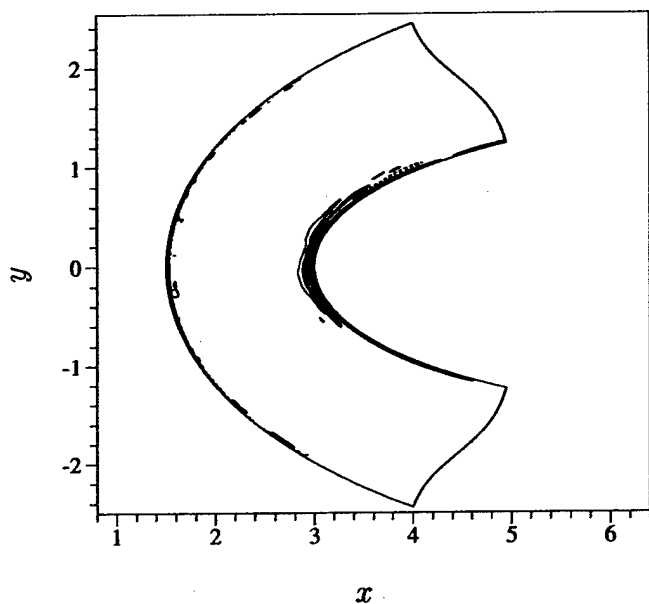


Figure 5.71: Pressure-strain correlation $\overline{p' S'_{33}}$, $Re = 42,000$, $Ma = 0.15$, $Tu = 0.05$, $L/D = 0.1$. Contour minimum : -0.016, maximum: 0.023, increment: 0.001.

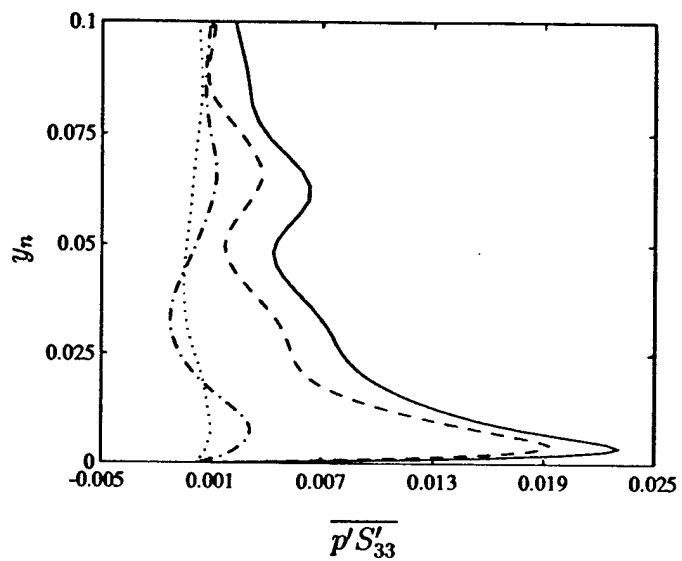


Figure 5.72: Profiles of pressure strain correlation $\overline{p' S'_{33}}$ along wall normal direction. —: $s = 0$, - - -: $s = 0.2D$, - · - : $s = 0.8D$, and · · · : $s = 1.6D$.

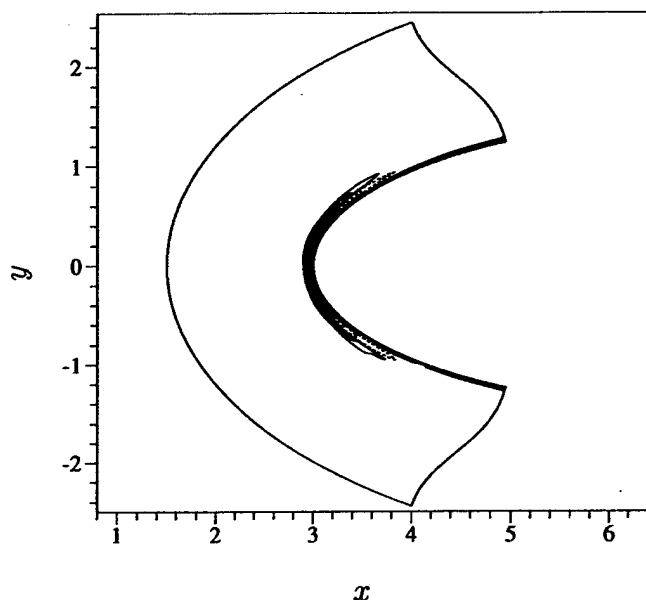


Figure 5.73: Turbulent transport for $\overline{u^2}$, $Re = 42,000$, $Ma = 0.15$, $Tu = 0.05$, $L/D = 0.1$. Contour minimum : -0.05, maximum: 0.04, increment: 0.004.

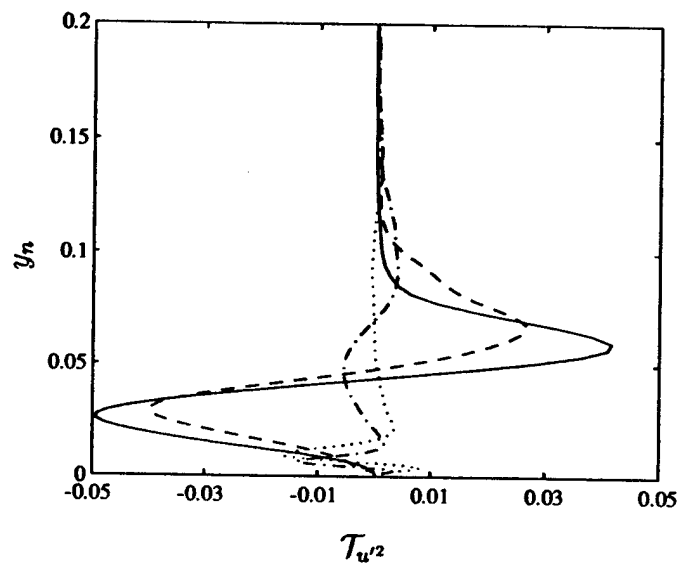


Figure 5.74: Profiles of turbulent transport for $\bar{u'^2}$ along wall normal direction. —: $s = 0$, - - -: $s = 0.2D$, - · - : $s = 0.8D$, and · · - : $s = 1.6D$.

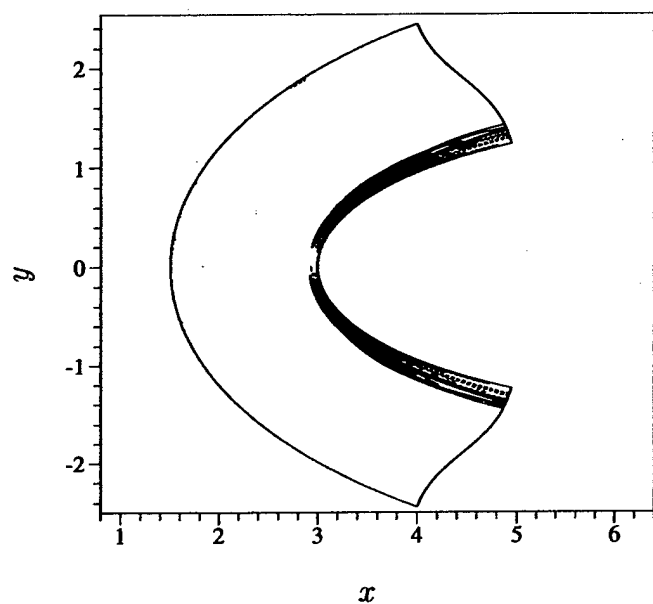


Figure 5.75: Turbulent transport for $\overline{v^2}$, $Re = 42,000$, $Ma = 0.15$, $Tu = 0.05$, $L/D = 0.1$. Contour minimum : -0.014, maximum: 0.014, increment: 0.001.

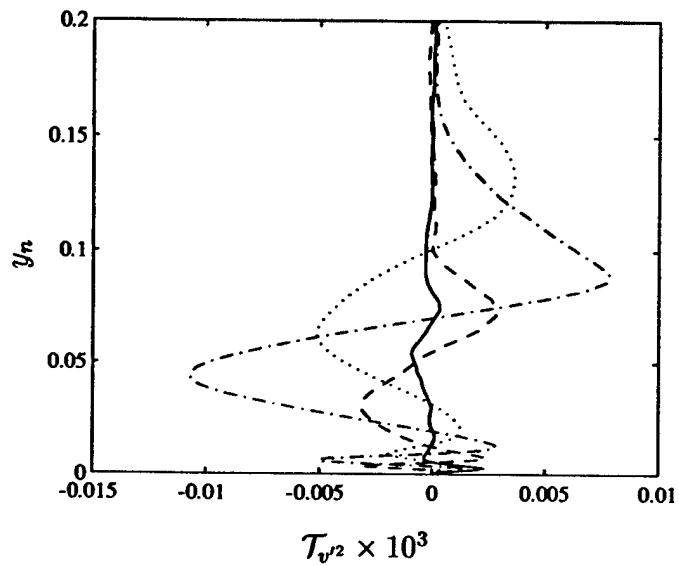


Figure 5.76: Profiles of turbulent transport for $\overline{v'^2}$ along wall normal direction. —: $s = 0$, - - -: $s = 0.2D$, - · - : $s = 0.8D$, and · · - : $s = 1.6D$.

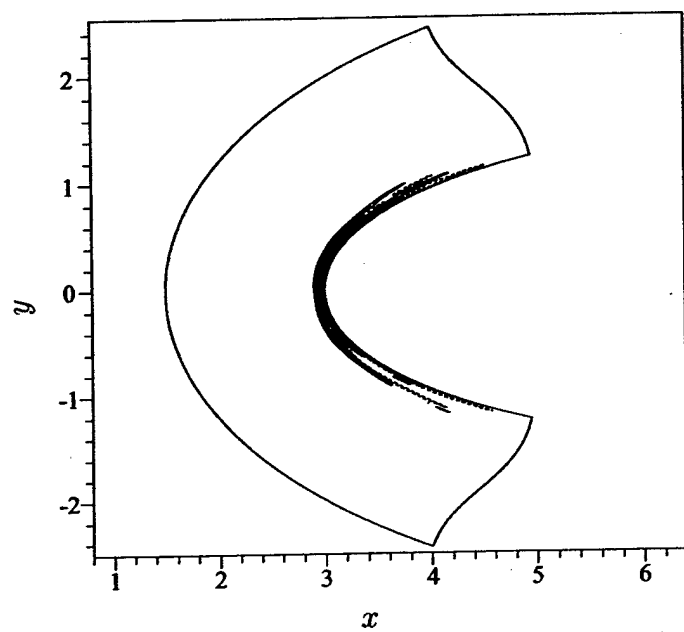


Figure 5.77: Turbulent transport for $\overline{w^2}$, $Re = 42,000$, $Ma = 0.15$, $Tu = 0.05$, $L/D = 0.1$. Contour minimum : -0.028, maximum: 0.012, increment: 0.002.

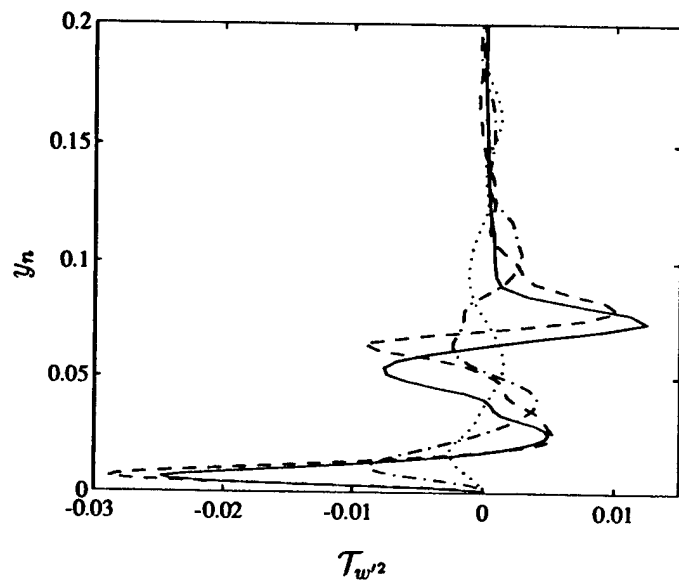


Figure 5.78: Profiles of turbulent transport for $\overline{w'^2}$ along wall normal direction. —: $s = 0$, - - -: $s = 0.2D$, - · - : $s = 0.8D$, and · · - : $s = 1.6D$.

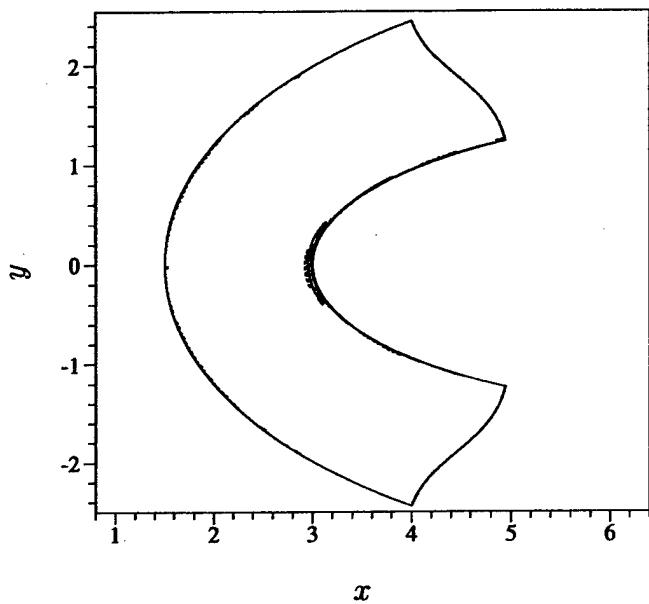


Figure 5.79: Turbulent transport for $\overline{2\partial(p'w')/\partial x}$, $Re = 42,000$, $Ma = 0.15$, $Tu = 0.05$, $L/D = 0.1$. Contour minimum : -0.16, maximum: 0.24, increment: 0.02.

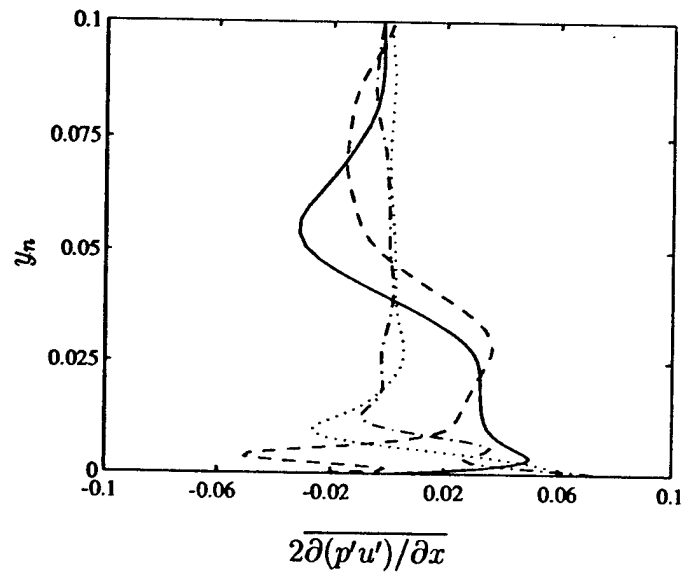


Figure 5.80: Profiles of pressure velocity correlation $2\overline{\partial(p'u')/\partial x}$ along wall normal direction. —: $s = 0$, - - -: $s = 0.2D$, - · - : $s = 0.8D$, and · · · : $s = 1.6D$.

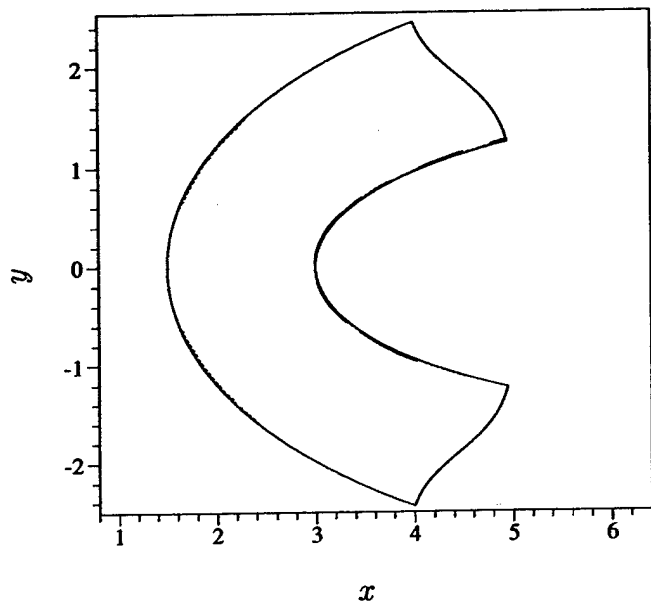


Figure 5.81: Turbulent transport for $2\overline{\partial(p'v')}/\overline{\partial y}$, $Re = 42,000$, $Ma = 0.15$, $Tu = 0.05$, $L/D = 0.1$. Contour minimum : -0.24, maximum: 0.16, increment: 0.02.

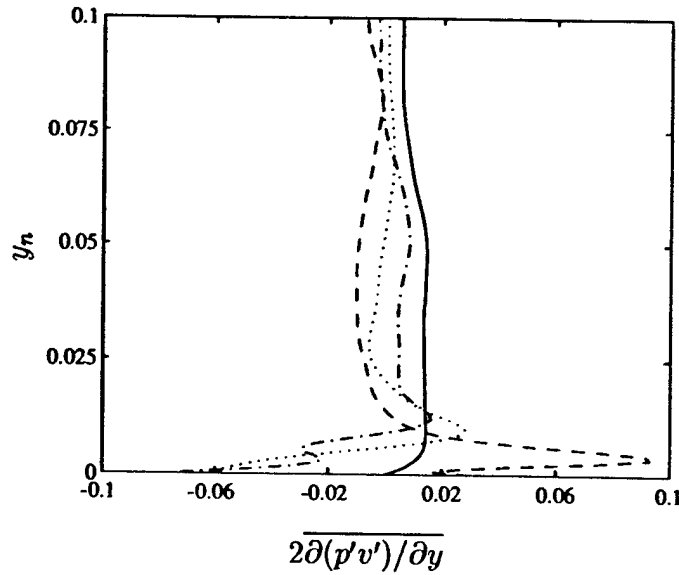


Figure 5.82: Profiles of pressure velocity correlation $\overline{2\partial(p'v')/\partial y}$ along wall normal direction. —: $s = 0$, - - -: $s = 0.2D$, - · - : $s = 0.8D$, and · · · : $s = 1.6D$.

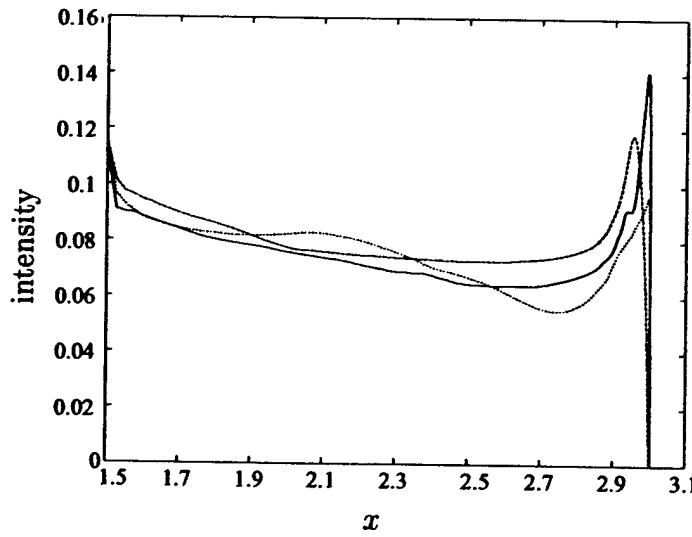


Figure 5.83: Turbulence intensity along the stagnation streamline. $Tu = 0.11$, $L/D = 0.06$, $Re = 43740$, - - -: u_{rms} , · · · : v_{rms} , —: w_{rms}

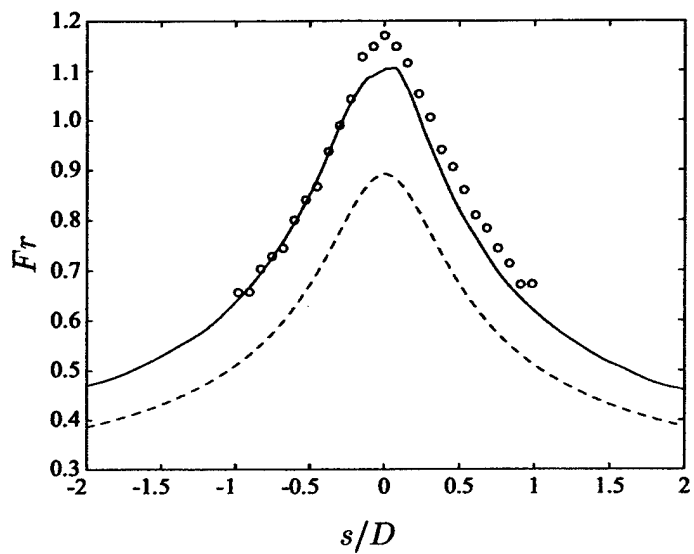


Figure 5.84: Averaged Frössling number distribution on the body surface.
 —: turbulent mean, -----: laminar, o : experimental data (Van Fossen et al., 1995).

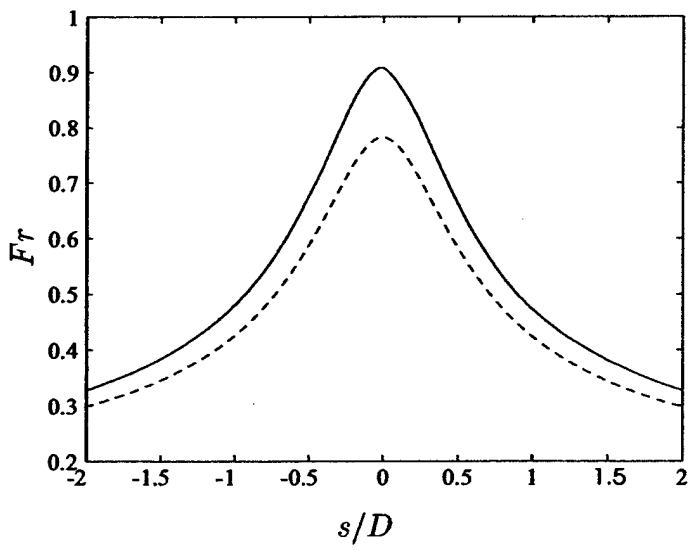


Figure 5.85: Averaged Frössling number distribution on the body surface at $Ma = 0.6$. —: turbulent mean, -----: laminar

Chapter 6

Theoretical Analysis

6.1 Introduction

The study of fluid flow and heat transfer at a perturbed two-dimensional forward stagnation point provides an improved understanding of the effects of free-stream turbulence in a wide range of engineering problems. In a modern gas turbine engine, for instance, the gas flow exiting the combustor contain high levels of turbulence which cause significant enhancement of heat transfer to the downstream turbine blades (Goldstein, 2001), the effect being most severe in the stagnation point region near blade leading edge. Efforts to improve the thermal efficiency and reliability of the blade cooling system hinges critically upon an accurate prediction of heat transfer in the presence of free-stream turbulence. Stagnation point flow also plays important roles in other industrial applications such as material processing and electronics cooling (Nakayama, 1995).

Over the years, a number of experiments have investigated the heat transfer enhancement over its laminar value in stagnation point flows in the presence of free-stream turbulence, see Kestin (1966); Sadeh and Brauer (1980); Van Fossen, Simoneau, and Ching (1995); and Ames (1997). The turbulence intensity, length scale and the mean flow Reynolds number were shown to be the most important parameters in determining the turbulent heat transfer rate. Typically, the heat transfer enhancement was found to increase with increased Reynolds number and turbulence intensity, but decrease with increased turbulence length scale. Semi-empirical correlations have been proposed to predict the heat transfer enhancement, see for example Smith and

Kuethe (1966); Van Fossen et al. (1995); and Ames (1997). Numerical simulations have also been performed to study the detailed interaction between free-stream turbulence and a stagnation point boundary layer. Spalart (1989) found that out of initial white-noise disturbances in a swept Hiemenz boundary layer, the most unstable disturbance-mode is the one that has the same similarity form as the mean Hiemenz flow, i.e. the streamwise velocity is a linear function of the streamwise coordinate x , and the wall normal velocity is independent of x . The flow structures induced by free-stream turbulence in a stagnation region are found to be qualitatively similar to those induced by upstream organized disturbances (Xiong and Lele, 2001). The importance of the disturbance length scale has been shown recently through direct numerical simulation of a turbulent stagnation point flow by Bae, Lele, and Sung (2003).

Theoretically, the effect of temporal modulation of free-stream velocity was first studied by Lighthill (1954) who obtained the Stokes-layer corrections for skin friction and heat transfer for a two-dimensional pulsating mean flow about a cylinder. The steady streaming (second order alteration to the mean flow owing to the Reynolds stresses) in an oscillatory Hiemenz boundary layer was further examined by Grosch and Salwen (1982) and Merchant and Davis (1989), but the emphasis is on finding similarity solutions and the modification to skin friction. The enhancement of heat transfer in a perturbed Hiemenz boundary layer was also conceived as a consequence of flow instability induced by the incoming disturbances. However, Kestin and Wood (1970) found, and later much clarified by Wilson and Gladwell (1978), that the two-dimensional Hiemenz boundary layer is always linearly stable to the incoming three dimensional disturbances. The nonlinear instability was studied by Lyell and Huerre (1985) who showed that if the level of the external disturbances exceeds certain threshold value, Hiemenz flow can be destabilized. Recently, the linear instability for the more general attachment-line boundary layer flow has also been investigated by Lin and Malik (1996) and Theofilis et al. (2003). Morkovin (1979), in a comprehensive review, argued that the enhancement of heat transfer is more likely a forced response to the upstream disturbances rather than a result of internal flow instability. The flow visualizations by Nagib and Hodson (1978) and Botcher and Wedemeyer (1989) strongly support this argument. This view point was advocated earlier by Sutera (1965) who analyzed the amplification effect of the mean flow on the incoming disturbances and linked them to the sensitivity of heat transfer to upstream vortical disturbances. By generalizing the classical

rapid distortion theory (RDT) (Batchelor and Proudman, 1954), Hunt (1973) analyzed the second order moment of the turbulent velocity field when the free-stream turbulence, of either very large or very small integral scales, impinges onto a circular cylinder, but the heat transfer between the fluid and the cylinder was not considered. Dhanak and Stuart (1995) showed that, in the forward stagnation region of any two-dimensional body, the viscous boundary layer can support a substructure of counter-rotating streamwise eddies when there exists weak cross-stream vorticity in the external flow. Kerr and Dold (1994) obtained a family of strained periodic vortex array embedded in an inviscid two-dimensional stagnation point flow. Andreotti, Douady, and Couder (2001) have recently used these vortices as a model to study experimentally the dynamics of interaction between strain and vorticity. Although much progress has occurred in understanding the heat transfer augmentation mechanism, there is however no, to the authors's knowledge, analytical solution to the impinging vortical disturbances in a viscous Hiemenz boundary layer. Theoretical analysis on the effects of length scale, intensity and frequency of the impinging disturbance and the associated heat transfer has been lacking. This is partly the reason that the prediction of stagnation point heat transfer in the presence of free-stream turbulence has largely remained empirical. In this paper, the distortion of unsteady three-dimensional disturbances in a two-dimensional stagnation point flow is investigated using theoretical analysis and numerical solutions. Its objective is to gain quantitative understanding of the heat transfer augmentation mechanism, particularly its dependence on disturbance parameters, e.g. length scale, intensity, and frequency, as a way to improve the prediction of turbulence effects in this technologically important flow.

The paper is organized as follows. The governing equations for the mean flow and the disturbances are formulated in §2, followed by a discussion of the length and velocity scales associated with the disturbances. The numerical solutions of the nonlinear disturbance equations, showing the characteristics of the disturbance development, are presented in §3. Analysis based on a linear vortex dynamics is pursued in §4 to derive the dependence of vorticity amplification on the disturbance length and time scales. In §5, the asymptotic behavior for large scale and low frequency disturbance is discussed, along with its implications for the wall heat transfer. By superposing different modes of upstream disturbance, the analysis is extended in §6 to treat the case of homogeneous isotropic free-stream turbulence. A new heat transfer scaling correlation based on the turbulence intensity, integral length scale

and Reynolds number is proposed and compared with recent experimental measurements. The conclusions of the present study and a discussion is given in §7.

6.2 Governing equations

We consider unsteady, incompressible, viscous flow with constant fluid properties in the forward stagnation region of an arbitrary two-dimensional bluff body shown in figure 6.1a. The coordinate axes are chosen as follows: x is parallel to the body and normal to the attachment line, y along the free-stream away from the body, and z along the attachment line. The mean flow around the bluff body is assumed to be steady and two-dimensional but the incoming disturbances are three-dimensional and may vary with time. The length scale of the disturbances is assumed to be large compared with the boundary layer thickness but much smaller than the diameter of curvature at the stagnation point, hence the mean flow in this region is well modelled by a plane Hiemenz boundary layer flow, see for example in Batchelor (1967). Indeed, Wilson and Gladwell (1978) showed that as Reynolds number $Re \rightarrow \infty$, the laminar flow in the stagnation region of any two-dimensional bluff body is reduced to a plane Hiemenz flow problem. Exploiting this reduction, the present analysis will be focused on the Hiemenz boundary layer flow in the presence of upstream disturbances as shown in figure 6.1b. By relating the strain rate in Hiemenz solution to the free-stream velocity and the diameter of curvature at the stagnation point, the present analysis applies to a general two-dimensional bluff body.

When the characteristic length scale l_0 and velocity scale v_0 of the Hiemenz boundary layer, defined as

$$l_0 = \sqrt{\nu^*/A^*}, \quad u_0 = \sqrt{\nu^* A^*} \quad (6.1)$$

are used to nondimensionalize the coordinates and the flow variables, we have

$$(\xi, \eta, \zeta) = \left(\frac{x^*}{l_0}, \frac{y^*}{l_0}, \frac{z^*}{l_0} \right) \quad (6.2a)$$

$$(\tilde{u}, \tilde{v}, \tilde{w}) = \left(\frac{u^*}{u_0}, \frac{v^*}{u_0}, \frac{w^*}{u_0} \right) \quad (6.2b)$$

$$\tilde{\rho} = \frac{\rho^*}{\rho_\infty^*} = 1, \quad \tilde{p} = \frac{p^*}{\rho_\infty^* u_0^2} \quad (6.2c)$$

$$\tilde{\theta} = \frac{T^* - T_w^*}{T_\infty^* - T_w^*} \quad (6.2d)$$

where the superscript * is used hereafter to denote the dimensional quantities, ν^* is the kinematic viscosity and A^* is the strain rate of the external potential flow in the Hiemenz solution. p^* and ρ^* are the pressure and density. The wall is assumed to be isothermal with temperature T_w^* and the upstream flow temperature is T_∞^* .

The flow field $\{\tilde{\mathbf{u}}, \tilde{p}, \tilde{\theta}\}$ is assumed to consist of a plane stagnation point flow $\{\mathbf{U}, P, \Theta\}$ and a unsteady disturbance field $\{\mathbf{u}, p, \theta\}$, i.e.

$$\tilde{\mathbf{u}} = \mathbf{U} + \mathbf{u}, \quad \tilde{p} = P + p, \quad \tilde{\theta} = \Theta + \theta \quad (6.3)$$

Following Batchelor (1967), the mean velocity \mathbf{U} of Hiemenz flow may be expressed as

$$\mathbf{U} = (U, V, W) = (\phi' \xi, -\phi, 0). \quad (6.4)$$

Together with the mean temperature Θ , they satisfy the following Hiemenz equations

$$\phi''' + \phi \phi'' + 1 - \phi'^2 = 0 \quad (6.5a)$$

$$\Theta'' + Pr\phi \Theta' = 0. \quad (6.5b)$$

where ϕ is only a function of η and ' denotes $d/d\eta$. Pr is the Prandtl number. The boundary conditions for ϕ and Θ are given by

$$\phi(0) = \phi'(0) = 0, \quad \phi'(\infty) = 1 \quad (6.6a)$$

$$\Theta(0) = 0, \quad \Theta(\infty) = 1 \quad (6.6b)$$

The general governing equations for the perturbation field, following from (6.1) and (6.3), can be written as

$$\nabla \cdot \mathbf{u} = 0 \quad (6.7a)$$

$$\partial_t \mathbf{u} + \mathbf{u} \cdot \nabla \mathbf{u} + \mathbf{U} \cdot \nabla \mathbf{u} + \mathbf{u} \cdot \nabla \mathbf{U} = -\nabla p + \nabla^2 \mathbf{u} \quad (6.7b)$$

$$\partial_t \theta + \mathbf{u} \cdot \nabla \theta + \mathbf{U} \cdot \nabla \theta + \mathbf{u} \cdot \nabla \Theta = \frac{1}{Pr} \nabla^2 \theta \quad (6.7c)$$

In this paper, perturbations of the form

$$\mathbf{u} = \{u(\eta, \zeta, t)\xi, v(\eta, \zeta, t), w(\eta, \zeta, t)\}, \quad p = p(\eta, \zeta, t), \quad \theta = \theta(\eta, \zeta, t) \quad (6.8)$$

are considered; the perturbation variables have no ξ dependence except the ξ -component of \mathbf{u} . As noted by Spalart (1989), this is a good approximation to the flow field in the neighborhood of the stagnation $\eta - \zeta$ plane. Steady perturbations of this form were also used by Sutera (1965). Substituting (6.8) into (6.7) yields the governing equations for the perturbation field:

$$u + v' + \partial_\zeta w = 0 \quad (6.9a)$$

$$\partial_t u + (u^2 + vu' + w\partial_\zeta u) - \phi u' + v\phi'' + 2u\phi' = u'' + \partial_\zeta^2 u \quad (6.9b)$$

$$\partial_t v + (vv' + w\partial_\zeta v) - (\phi v)' = -p' + (v'' + \partial_\zeta^2 v) \quad (6.9c)$$

$$\partial_t w + (vw' + w\partial_\zeta w) - \phi w' = -\partial_\zeta p + (w'' + \partial_\zeta^2 w) \quad (6.9d)$$

$$\partial_t \theta + (v\theta' + w\partial_\zeta \theta) + v\Theta' - \phi\theta' = \frac{1}{Pr}(\theta'' + \partial_\zeta^2 \theta) \quad (6.9e)$$

Note here the prime ' denotes the partial derivative $\frac{\partial}{\partial \eta}$. The disturbance vorticity may be conveniently found as

$$\omega_\xi = w' - \partial_\zeta v, \quad \omega_\eta = \xi \partial_\zeta u, \quad \omega_\zeta = -\xi u' \quad (6.10)$$

As will be seen in subsequent discussion, the disturbance vorticity in ξ direction ω_ξ , which is subject to stretching by the mean diverging flow, plays a central role in describing the disturbance evolution in this type of flow. Hence the governing equation for streamwise vorticity, hereafter denoted by ω , is written as

$$\partial_t \omega - (\omega'' + \partial_\zeta^2 \omega) - (\phi \omega)' = -(v\omega)' - \partial_\zeta(w\omega) \quad (6.11)$$

To seek solutions which are periodic in time t (or steady) and periodic in the spanwise direction ζ , we expand u, v, w, ω and θ in a double Fourier series:

$$u(\eta, \zeta, t) = A_p \sum_{m,n=1}^{\infty} u_{mn}(\eta) \exp\{i(m\sigma_0 t + nk_0 \zeta)\} + v'_0(\eta) \quad (6.12a)$$

$$v(\eta, \zeta, t) = A_p \sum_{m,n=1}^{\infty} v_{mn}(\eta) \exp\{i(m\sigma_0 t + nk_0 \zeta)\} - v_0(\eta) \quad (6.12b)$$

$$w(\eta, \zeta, t) = A_p \sum_{m,n=1}^{\infty} (nk_0)^{-1} w_{mn}(\eta) \exp\{i(m\sigma_0 t + nk_0 \zeta)\} \quad (6.12c)$$

$$\omega(\eta, \zeta, t) = A_p \sum_{m,n=1}^{\infty} \omega_{mn}(\eta) \exp\{i(m\sigma_0 t + nk_0 \zeta)\} \quad (6.12d)$$

$$\theta(\eta, \zeta, t) = A_p \sum_{m,n=1}^{\infty} \theta_{mn}(\eta) \exp\{i(m\sigma_0 t + nk_0 \zeta)\} + \theta_0(\eta) \quad (6.12e)$$

where A_p is the perturbation amplitude; $k_0 = k^* l_0$ is the fundamental wavenumber in spanwise direction and $\sigma_0 = \sigma^*/A^*$ the fundamental frequency. The functions $v_0(\eta)$ and $\theta_0(\eta)$ represent the nonzero spanwise averages of the perturbation velocity and temperature, i.e. the modification to the mean flow profiles due to the nonlinear interaction among the disturbance modes. Additionally, the normal derivative of $\theta_0(\eta)$ at the wall gives the spanwise averaged heat transfer enhancement.

Substituting the expansions (6.12) into the continuity equation (6.9a) yields

$$u_{mn} + v'_{mn} + i w_{mn} = 0, \quad (6.13)$$

and from the definition of ω_{mn} , it follows that

$$i n^2 k_0^2 v_{mn} - w'_{mn} + nk_0 \omega_{mn} = 0. \quad (6.14)$$

Similarly, the governing equations for streamwise velocity u_{mn} , vorticity ω_{mn} and temperature θ_{mn} reduce to

$$u''_{mn} - (2\phi' + n^2 k_0^2 + im\sigma_0) u_{mn} + \phi u'_{mn} - \phi'' v_{mn} = \mathcal{N}_0(u, v, w) \quad (6.15)$$

$$\omega''_{mn} - (n^2 k_0^2 + im\sigma_0) \omega_{mn} + (\phi \omega_{mn})' = \mathcal{N}_1(v, w, \omega) \quad (6.16)$$

$$\theta''_{mn} - (n^2 k_0^2 + imPr\sigma_0) \theta_{mn} + Pr\phi \theta'_{mn} - Prv_{mn}\Theta' = \mathcal{N}_2(v, w, \theta) \quad (6.17)$$

The equations for $v_0(\eta)$ and $\theta_0(\eta)$ can also be derived as

$$v'''_0 + \phi v''_0 - 2\phi' v'_0 + \phi'' v_0 = \mathcal{N}_3(u, v) \quad (6.18)$$

$$\theta''_0 + Pr\phi \theta'_0 = \mathcal{N}_4(v, w, \theta) \quad (6.19)$$

In the above equations, \mathcal{N}_i 's are the nonlinear terms given by the following expression:

$$\mathcal{N}_0 = \frac{A_p}{2} \sum_{p,q=1}^{\infty} \{ u_{pq} u_{m-p, n-q} + \hat{u}_{pq} u_{m+p, n+q} + v_{pq} u'_{m-p, n-q} + \hat{v}_{pq} u'_{m+p, n+q}$$

$$+\frac{i}{q}[(n-q)w_{pq}u_{m-p,n-q}+(n+q)\hat{w}_{pq}u_{m+p,n+q}]\} \quad (6.20a)$$

$$\begin{aligned} \mathcal{N}_1 = & \frac{A_p}{2} \sum_{p,q=1}^{\infty} \{ [v_{pq}\omega_{m-p,n-q} + \hat{v}_{pq}\omega_{m+p,n+q}]' \\ & + \frac{in}{q} [w_{pq}\omega_{m-p,n-q} + \hat{w}_{pq}\omega_{m+p,n+q}] \} \end{aligned} \quad (6.20b)$$

$$\begin{aligned} \mathcal{N}_2 = & \frac{A_p Pr}{2} \sum_{p,q=1}^{\infty} \{ v_{pq}\theta'_{m-p,n-q} + \hat{v}_{pq}\theta'_{m+p,n+q} \\ & + \frac{i}{q} [(n-q)w_{pq}\theta_{m-p,n-q} + (n+q)\hat{w}_{pq}\theta_{m+p,n+q}] \} \end{aligned} \quad (6.20c)$$

$$\mathcal{N}_3 = A_p^2 \sum_{p,q=1}^{\infty} [|u_{pq}|^2 + \frac{1}{2}(v_{pq}\hat{u}_{pq})'] \quad (6.20d)$$

$$\mathcal{N}_4 = \frac{A_p^2 Pr}{2} \sum_{p,q=1}^{\infty} \text{Re}\{\hat{v}_{pq}\theta'_{pq} + i\hat{w}_{pq}\theta_{pq}\} \quad (6.20e)$$

where $\hat{\cdot}$ stands for the complex conjugate. Suppose that unsteady disturbance vorticity is introduced upstream at $\eta = H_0 \gg 1$ by superimposing a simple sinusoidal variation with the amplitude A_p , at the fundamental spanwise wavenumber k_0 , and frequency σ_0 on the mean velocity $\phi(\eta)$. The disturbance boundary conditions at $\eta = H_0$ are

$$v_{11} = 1, \quad v_{mn} = 0 \quad \text{for } m, n \neq 1, \quad u_{mn} = w_{mn} = \theta_{mn} = 0 \quad (6.21)$$

At the wall $\eta = 0$, no slip and isothermal boundary conditions are enforced for the velocities and temperature, thus

$$u_{mn} = v_{mn} = w_{mn} = \theta_{mn} = 0 \quad (6.22)$$

Once the disturbance velocity v_{mn} , w_{mn} and temperature θ_{mn} are obtained, the relative heat transfer enhancement Δh over its undisturbed mean value h can be found by solving (6.19)

$$\frac{\Delta h}{h} = \frac{\theta'_0(0)}{\Theta'(0)} = - \int_0^{\infty} e^{-Pr \int_o^{\eta} \phi d\eta'} \int_0^{\eta} \mathcal{N}_4 e^{Pr \int_o^{\eta'} \phi d\eta''} d\eta' d\eta \quad (6.23)$$

It is convenient to introduce new length and velocity scales besides those in (6.1). By the assumed spanwise periodicity, a natural choice for the disturbance length and velocity scales are

$$l_d = 1/k^*, \quad u_d = \nu k^* \quad (6.24)$$

It is observed below that the square of the ratio between the disturbance length scale l_d and the Hiemenz boundary layer scale l_0 , represented by a dimensionless parameter λ see Kerr and Dold (1994),

$$\lambda = \left(\frac{l_d}{l_0}\right)^2 = \frac{A^*}{\nu^* k^{*2}} = \frac{1}{k_0^2} \quad (6.25)$$

is a critical parameter in determining the evolution of the disturbances. When λ is large, the distortion of the upstream disturbances is mainly due to the mean flow straining effect; the nonlinear interaction among the disturbance modes is of higher order. This is similar to the cases treated by the traditional linear RDT. But in the presence of viscosity, the nonslip wall introduces the viscous effect in its vicinity and must be included in the formulation both for the mean flow and the disturbances. Interestingly, λ can also be interpreted as the time scale ratio between the disturbance turn-over time l_d/u_d and the mean flow straining time $1/A^*$, i.e.

$$\lambda = \left(\frac{l_d}{u_d}\right) A^* \quad (6.26)$$

For different values of λ as well as A_p , the numerical solutions to the flow problem posed here are presented in the next section.

6.3 Numerical Results

The system of equations (6.13) - (6.19), with boundary conditions (6.21)-(6.22), forms a second order boundary-value problem driven by an inhomogeneous boundary condition away from the wall. Numerically, they can be readily solved using the over-relaxation method, described for example in Isaacson and Keller (1993). Fourth order finite difference scheme is adopted to approximate the spatial derivatives and different numbers of grid points are used to obtain the grid independent solutions. For the nonlinear calculations, a total number of modes resulting from a truncation at $m = 6, n = 6$ of the double Fourier series in (6.12) are found sufficient for the solutions to converge. The details of the numerical method and convergence study can be found in Xiong (2004).

The case of steady disturbance, i.e. $\sigma_0 = 0$, is discussed first; this will help clarify the dependence of the disturbance evolution on the length scale ratio λ . In all computations, the Prandtl number is taken as $Pr = 0.71$,

and the disturbance amplitude A_p is ten percent of the mean flow velocity ϕ at the inflow boundary $\eta = H_0$, i.e. $A_p = 0.1\phi(H_0)$ and $H_0 = 18$. Figure 6.2 shows the profiles of the base state velocity and temperature (without any free-stream disturbance). The velocity and temperature boundary layer thicknesses (defined as the location at which 99% of the external value is reached) are around $\eta = 2.4$ and $\eta = 4$, respectively. Figure 6.3 shows the streamline patterns of the perturbed flow in the stagnation plane for different values of λ . The horizontal axis spans one spanwise wavelength for each case.

As can be seen, initially at $\lambda = 1.1$, the perturbed streamlines converge toward a free stagnation point at the symmetry plane $z = 0$. At $\lambda \sim O(2)$, a pair of counter rotating vortices start to form at the edge of the boundary layer. The strength of these vortices increases rapidly with the increasing λ and attains its maximum at $\lambda = 4$. When λ increases further, the vortex strength slowly decreases. At $\lambda = 32$ the vortices disappear and are replaced again by a sink type free stagnation point. For even larger $\lambda = 64$, the mean flow dominates, and the free stagnation point also disappears. Qualitatively, these streamline patterns can be first classified into two groups depending whether a free stagnation point (FSP) is present. The stagnation point emerges when the disturbance wall normal velocity v exceeds the mean flow ϕ . Since at the wall, $\phi = \phi' = v = v' = 0$, this can occur when $|v''(0)| \geq |\phi''(0)|$. Furthermore, depending on the direction of the spanwise velocity in the neighborhood of FSP, the resulting FSP can be either a sink point — when the spanwise velocity w points inward, or a saddle point — when it points outward. Since by symmetry $w \equiv 0$ at $z = 0$, the direction of w is determined by $\frac{\partial w}{\partial z}$. From continuity equation, this is in turn determined by $\frac{\partial v}{\partial y}$, the rate at which the vertical velocity tends to zero at the free stagnation point. When $\frac{\partial v}{\partial y} < 0$, it becomes a saddle point and the streamlines emanating from the stagnation point eventually form the spiral vortices. For the present case with fixed A_p , the free stagnation point emerges for $\lambda > 1$, and transition from a sink point to a saddle point type occurs at $\lambda = 1.6$. At $\lambda = 30$, the saddle type stagnation point changes back to a sink point type, causing the vortices to disappear. At $\lambda \geq 60$, the free stagnation point also disappears, and the perturbed flow becomes unidirectional in wall normal direction.

In addition to the change of λ , the effect of the disturbance amplitude A_p on the vortex formation is shown in figure 6.4 where A_p varies from 2 to 15 percent of $\phi(H_0)$ for fixed $\lambda = 4$. In this case, the free stagnation

Amplitude $A_p / \phi(H_0)$	Velcoity $ v_{max} $	Vorticity $ \omega_w $	Heat transfer $\Delta h / h$
0.02	0.9321	1.4953	0.0100
0.05	2.5558	3.7457	0.0620
0.07	3.8928	5.2490	0.1206
0.10	6.4999	7.5256	0.2406
0.12	8.8094	9.0672	0.3368
0.15	13.729	11.410	0.4918

Table 6.1: The maximum wall normal disturbance velocity $|v_{max}|$, vorticity at the wall $|\omega_w|$ and the heat transfer enhancement $\Delta h/h$ for different A_p at $\lambda = 4, H_0 = 18$.

point first emerges at $A_p = 0.03\phi(H_0)$, and the transition from the sink type to the saddle type takes place at $A_p = 0.05\phi(H_0)$. The latter can be considered as a threshold for A_p since only beyond this value the counter-rotating vortices become possible in the streamline pattern. Moreover, figure 6.4 also reveals that although the strength of the vortices increases with the increasing A_p , the overall flow pattern remains qualitatively similar once the threshold is reached. The existence of a threshold in disturbance amplitude is also consistent with earlier observations by Nagib and Hodson (1978) on the formation of vortex pair at the stagnation region of a bluff body subject to the impingement of wakes. Similar flow patterns as those shown in figure 6.3 and 6.4 also emerge in aforementioned experiments (Nagib and Hodson, 1978; Botcher and Wedemeyer, 1989) as well as numerical simulations (Xiong and Lele, 2001; Bae et al., 2003). The quantitative characterization of the flow fields in figure 6.4 in terms of the maximum wall normal disturbance velocity $|v_{max}|$, wall vorticity $|\omega_w|$ and heat transfer enhancement $\Delta h/h$ are summarized in Table 6.1.

Figure 6.5 shows the profiles of the fundamental mode and higher harmonics at $\lambda = 4$ for the disturbance velocity, vorticity and temperature. The disturbance v velocity and vorticity are found to be amplified before reaching the boundary layer. Compared to the fundamental mode $m = 1, n = 1$, the amplitudes of the higher harmonics are typically small, except for temperature where the mean temperature modification θ_0 attains an amplitude similar to θ_{11} . Of the three components of the disturbance velocity, u_{mn} is found to be typically one order of magnitude smaller than v_{mn} and w_{mn} . The

corresponding contours for the vorticity and temperature are plotted in figure 6.6 and figure 6.7. The incoming vorticity is amplified by a factor greater than 5 due to stretching and thus large amplitude vorticity with opposite sign is induced within a thin near-wall region to satisfy the no slip boundary condition. The temperature contours are also significantly modified by the disturbance velocity. The upward velocity causes the local thermal boundary layer to become thicker, while the downward velocity makes it thinner. The net effect on the spanwise averaged heat transfer depends on the strength and distribution of these thickened and thinned regions.

In figure 6.8, the relative heat transfer enhancement $\Delta h/h$ is plotted as a function of λ . For small λ , or small disturbance wavelength, $\Delta h/h$ increases rapidly as λ increases. But for large λ , it decrease slowly with the increase of λ . A peak value is found around $\lambda = 4$, indicating that an optimum disturbance length scale exists at about five times the boundary layer thickness and produces maximum heat transfer enhancement. Also shown in figure 6.8 is the maximum value of the fundamental mode of the disturbance wall normal velocity v_{11} . It shows a similar trend with λ and optimum amplification at nearly the same value of λ . However, for large λ , $v_{max} \sim \lambda^{-1/2}$ while $\Delta h/h \sim \lambda^{-1}$. Finally, in figure 6.9 the amplitude of the vorticity at the wall is plotted as a function of λ . Besides a similar peak location around $\lambda = 4$, the striking feature of the wall vorticity is that it approaches a constant which depends only on H_0 and A_p as λ becomes large.

The dependence of flow characteristics on the length scale is due to the competition between the vortex stretching and the viscous dissipation. The convective heat transfer or more generally passive scalar transport is a direct consequence of the amplified velocity disturbances, and may in fact be regarded as an indication of how significantly the flow near the wall has been modified. Based on this point of view, the vorticity equation (6.16), comprising the mean flow stretching, viscous dissipation and nonlinear interaction effects, shall be the starting point for analyzing the disturbance evolution. From the profiles of ω_{mn} in figure 6.5, the nonlinear interaction is shown to be relatively weak, hence in the subsequent analysis the nonlinear terms in (6.16) will be neglected. A similar rationale is also the basis for the linear RDT which has been successfully applied to this type of flow. However, unlike the purely inviscid interaction considered in RDT, in the present problem viscosity exerts a significant influence upon the disturbance throughout the whole domain, even when the mean flow can be treated largely as inviscid in the region outside the boundary layer. Indeed, it is the balance between the

vortex stretching and viscous diffusion that produces the maximum vorticity near the edge of boundary layer. Therefore, analysis of the vorticity dynamics helps to understand the basic mechanism governing the flow and the associated scalar transport. This is carried out in detail in the subsequent sections.

6.4 Linear Vortex Dynamics

The primary goal of the analysis in this section is to find an asymptotic expression describing the evolution of the large scale, low frequency disturbances in the Hiemenz boundary layer. The solution is sought by first expressing the vorticity in a series expansion based on the large length scale ($\lambda \gg 1$) and low frequency($\sigma_0 \ll 1$). This solution is formally valid in the entire spatial domain, but insufficient to describe the vorticity evolution in an explicitly way owing to the lack of closed form expression for ϕ . On the other hand, by exploiting the particularly simple form taken by ϕ in the region outside the Hiemenz boundary layer, a closed form solution for the vorticity can be found for any arbitrary λ and σ_0 in that region. These two solutions are required to match in the region outside the Hiemenz boundary layer where they are both valid. Thus, an explicit composite asymptotic solution can be formulated which describes the evolution of the large scale, low frequency vortical disturbances, and forms the basis of further analysis.

6.4.1 Series expansion

As shown by the numerical results in figure 6.5, the disturbance typically reaches its maximum amplitude at the edge of the boundary layer before it decays . By (6.16) and (6.25), the linearized governing equation for ω_{mn} takes the form

$$\omega''_{mn} - \left(\frac{n^2}{\lambda} + i m \sigma_0 \right) \omega_{mn} + (\phi \omega_{mn})' = 0 \quad (6.27)$$

Here only the case of large $\lambda \gg 1$ and small $\sigma_0 \ll 1$ will be considered. These limits correspond to the situation where the upstream disturbance is of large scale and low frequency relative to the Hiemenz boundary layer scales. This regime is prototypical for the free stream turbulence impinging on gas turbine

blades. A small parameter ϵ may be defined as:

$$\epsilon = \frac{n^2}{\lambda} + i m \sigma_0, \quad |\epsilon| \ll 1 \quad (6.28)$$

and a series solution of ω_{mn} is sought in the powers of ϵ as a regular perturbation:

$$\omega_{mn} = \omega_{mn}^0 + \epsilon \omega_{mn}^1 + \dots \quad (6.29)$$

The equation at zeroth order becomes

$$(\omega_{mn}^0)'' + (\phi \omega_{mn}^0)' = 0 \quad (6.30)$$

whose general solution can be found as

$$\omega_{mn}^0(\eta) = E^0 e^{-\Phi} + F^0 e^{-\Phi} \int_0^\eta e^{\Phi(\eta')} d\eta'. \quad (6.31)$$

At first order the equation is

$$(\omega_{mn}^1)'' + (\phi \omega_{mn}^1)' = \omega_{mn}^0 \quad (6.32)$$

and the solution can be expressed using ω_{mn}^0 as

$$\omega_{mn}^1(\eta) = E^1 e^{-\Phi} + F^1 e^{-\Phi} \int_0^\eta e^{\Phi(\eta')} d\eta' + e^{-\Phi} \int_0^\eta e^{\Phi(\eta')} \int_0^{\eta'} \omega_{mn}^0(\eta'') d\eta'' d\eta' \quad (6.33)$$

where Φ is defined as

$$\Phi(\eta) = \int_0^\eta \phi(\eta') d\eta' \quad (6.34)$$

and E^0, E^1, F^0, F^1 are arbitrary constants. The higher order terms can be computed similarly. The series expansion (6.29) is valid in the entire spatial domain from the wall to the inflow but, as such, of limited use because it involves unknown constants. In next section, the exact solution of (6.27) in a region outside the Hiemenz boundary layer is obtained for arbitrary λ and σ_0 . By examining the characteristics of the exact solution for the case of $\lambda \gg 1$ and $\sigma_0 \ll 1$, the unknown constants in (6.31) can be determined.

6.4.2 Outside the boundary layer

Outside the Hiemenz boundary layer, the relevant length and velocity scales are determined by the incoming disturbance. To facilitate the subsequent analysis, the vorticity equation (6.27) is first rescaled by l_d and u_d defined in (6.24)

$$\omega_{mn}'' + \lambda \phi \omega_{mn}' + (\lambda \phi' - n^2 - i m \lambda \sigma_0) \omega_{mn} = 0. \quad (6.35)$$

Note here both the dependent and independent variables are rescaled, and the derivatives are now with respect to the new independent variable $s = y^*/l_d = \eta/\sqrt{\lambda}$. In particular, the mean velocity profile $\phi(s)$ in (6.35) is equal to the $\phi(\eta)$ multiplied by the factor $1/\sqrt{\lambda}$, i.e. $\phi(s) = \phi(\eta)/\sqrt{\lambda}$. The boundary conditions for the mean and disturbance flow remain unchanged under this rescaling.

As noted in figure 6.2, the mean velocity profile ϕ takes a simple irrotational form outside the Hiemenz boundary layer

$$\phi \sim s - s_d, \quad \phi' \sim 1. \quad (6.36)$$

where s_d represents the displacement thickness δ_d of the Hiemenz boundary layer, i.e. $s_d = \delta_d/\sqrt{\lambda}$. In this region, the main effect of ϕ on the disturbances, besides the convection, is to stretch the ξ -component of the incoming vorticity. When the disturbance scale is relatively large, viscosity plays a less important role and the straining effect leads to an increase of the vorticity.

Denoting ω_{mn} outside the boundary layer by ω_{mn}^p and using (6.36), (6.35) becomes

$$(\omega_{mn}^p)'' + \lambda (s - s_d) (\omega_{mn}^p)' + (\lambda - n^2 - i m \lambda \sigma_0) \omega_{mn}^p = 0 \quad (6.37)$$

On introducing a new independent variable τ

$$\tau = -\frac{1}{2} \lambda (s - s_d)^2 \quad (6.38)$$

the vorticity equation is further transformed into

$$\tau (\omega_{mn}^p)'' + \left(\frac{1}{2} - \tau \right) (\omega_{mn}^p)' - \frac{(\lambda - n^2 - i m \lambda \sigma_0)}{2\lambda} \omega_{mn}^p = 0 \quad (6.39)$$

where ' stands for $d/d\tau$. This is the confluent hypergeometric equation of the general form

$$xy'' + (c - x)y' - ay = 0 \quad (6.40)$$

whose solution may be expressed as

$$y = C_1 M(a; c; x) + C_2 U(c - a; c; -x) e^x$$

for $c \neq 0, \pm 1, \pm 2 \dots$. $M(a; c; x)$ and $U(a; c; x)$ are the first and second kind of confluent hypergeometric functions (Abramowitz and Stegun, 1970). In the present case, they correspond to

$$y = \omega_{mn}^p; \quad x = \tau; \quad c = \frac{1}{2}; \quad a = \frac{\lambda - n^2 - im\lambda\sigma_0}{2\lambda}, \quad (6.41)$$

An integral representation for $M(a; c; x)$ when $\operatorname{Re} c > \operatorname{Re} a > 0$ is

$$M(a; c; x) = \frac{\Gamma(c)}{\Gamma(a)\Gamma(c-a)} \int_0^1 t^{a-1} (1-t)^{c-a-1} e^{xt} dt$$

and $U(a; c; x)$ can be expressed by $M(a; c; x)$ through the following expression.

$$U(a; c; x) = \frac{\pi}{\sin(c\pi)} \left\{ \frac{M(a; c; x)}{\Gamma(1+a-c)\Gamma(c)} - x^{1-c} \frac{M(1+a-c; 2-b; x)}{\Gamma(a)\Gamma(2-c)} \right\} \quad (6.42)$$

Hence the general solution for the vorticity becomes

$$\omega_{mn}^p = C_1 M\left(\frac{\lambda - n^2}{2\lambda} - i\frac{m\sigma_0}{2}; \frac{1}{2}; \tau\right) + C_2 U\left(\frac{n^2}{2\lambda} + i\frac{m\sigma_0}{2}; \frac{1}{2}; -\tau\right) e^\tau \quad (6.43)$$

For $\lambda < 1$, the solution simply decays from its upstream value, and for $\lambda = 1$ it becomes a constant. So in what follows only the case of $\lambda > 1$ is considered. First writing s in terms of the original variable η , and by the definition of τ , it follows

$$\eta = \sqrt{\lambda}s, \quad \tau = -\frac{(\eta - \delta_d)^2}{2} = -\frac{\tilde{\eta}^2}{2} \quad (6.44)$$

where the shifted coordinate $\tilde{\eta}$ is defined as

$$\tilde{\eta} = \eta - \delta_d. \quad (6.45)$$

After some simplification, the general solution for the vorticity outside the boundary layer ω_{mn}^p may be expressed as

$$\omega_{mn}^p = C_{mn} M\left(\frac{\lambda - n^2}{2\lambda} - i\frac{m\sigma_0}{2}; \frac{1}{2}; -\frac{\tilde{\eta}^2}{2}\right) + D_{mn} M\left(\frac{2\lambda - n^2}{2\lambda} - i\frac{m\sigma_0}{2}; \frac{3}{2}; -\frac{\tilde{\eta}^2}{2}\right) \tilde{\eta}. \quad (6.46)$$

where C_{mn} , D_{mn} are arbitrary constants. A typical solution for $\lambda = 4$, $\sigma_0 = 0$ composed of two confluent hypergeometric functions (with C_{mn} , D_{mn} specified by (6.61) in section 6.4.4) is illustrated in figure 6.10.

6.4.3 Composite solution

To facilitate further analysis, the series solutions (6.29)-(6.33) is combined with the solution outside the boundary layer to derive a composite asymptotic solution. To do so, the unknown coefficients in the series expansion need to be determined first. Notice that as $\eta \rightarrow \infty$,

$$\phi \sim \tilde{\eta} \quad \text{and} \quad \Phi \sim \Phi_0 + \frac{\tilde{\eta}^2}{2} \quad (6.47)$$

where $\Phi_0 = \int_0^\infty (\phi - \tilde{\eta}) d\eta - \frac{\delta_d^2}{2}$ is an integral constant. This asymptotic representation is valid for $\tilde{\eta} > \tilde{\eta}_0$, where $\tilde{\eta}_0 \geq \delta_d$ is a location beyond which the irrotational flow applies. The zeroth order series solution (6.31) may be rewritten as

$$\omega_{mn}^0(\eta) = e^{-\Phi} [E^0 + F^0 \int_0^{\eta_0} e^{\Phi(\eta')} d\eta'] + F^0 e^{-\Phi} \int_{\eta_0}^\eta e^{\Phi(\eta')} d\eta'. \quad (6.48)$$

However when $\eta \rightarrow \infty$, the first term in (6.48) vanishes, so it follows

$$\omega_{mn}^0(\eta) \sim F^0 e^{-\Phi} \int_{\eta_0}^\eta e^{\Phi(\eta')} d\eta' \sim F^0 e^{-\frac{\tilde{\eta}^2}{2}} \int_0^{\tilde{\eta}} e^{\frac{\tilde{\eta}'^2}{2}} d\tilde{\eta}'. \quad (6.49)$$

where in the second expression, (6.47) has been used and the lower limit has been extended to zero using the same decomposition in (6.48). On the other hand, the corresponding zeroth order expansion of (6.46) in ϵ becomes

$$\omega_{mn}^{p0} = C_{mn} M\left(\frac{1}{2}; \frac{1}{2}; -\frac{\tilde{\eta}^2}{2}\right) + D_{mn} M\left(1; \frac{3}{2}; -\frac{\tilde{\eta}^2}{2}\right) \tilde{\eta}. \quad (6.50)$$

Noting the following identities

$$M(a; a; z) = e^z \quad \text{and} \quad e^{-\frac{z^2}{2}} \int_0^z e^{\frac{z'^2}{2}} dz' = z M\left(1; \frac{3}{2}; -\frac{z^2}{2}\right) \quad (6.51)$$

and comparing (6.49) and (6.50) for large η , we obtain

$$D_{mn} = F^0 \quad (6.52)$$

since the first term in (6.50) vanishes more rapidly than the second.

No appropriate matching condition for C_{mn} can be derived from the large η asymptotics. Hence, it is necessary to find the matching condition by

considering the behavior of the vorticity close to the wall. As shown in figure 6.9, the wall vorticity plays a key role in determining the interaction between the incoming disturbances and the Hiemenz boundary layer. An initial choice for matching C_{mn} and E^0 therefore seems to require the wall vorticity obtained from (6.46) and (6.31) to be equal. However, the vorticity at the wall obtained by setting $\eta = 0$ in (6.46) is not accurate, since (6.46) is only applicable outside the Hiemenz boundary layer. A more appropriate choice is to require the vorticity obtained from the two solutions to match at the edge of the Hiemenz boundary layer where both solutions apply. This results the following expression for C_{mn} ,

$$C_{mn} = [E^0 + F^0 \int_0^\delta e^\Phi d\eta] e^{-\Phi_\delta} - F^0 \int_0^{\delta-\delta_d} e^{\frac{\eta^2}{2}} d\eta \quad (6.53)$$

where $\Phi_\delta = \Phi(\delta) - (\delta - \delta_d)^2/2$. Further matching (6.46) to (6.33) at higher order requires evaluation of $M(a, c, z)$ subject to the perturbation of a and the asymptotic behavior of the last term in (6.33) for large η , for which the explicit expressions have not been obtained. Nevertheless, an approximate solution of ω_{mn} , more explicit than the series expansion, can still be constructed by a similar procedure to those in matched asymptotics (Van Dyke, 1975), i.e.

$$\omega_{mn} \sim \omega_{mn}^0 + \omega_{mn}^p - \omega_{mn}^{p0} \quad (6.54)$$

here the expressions for ω_{mn}^0 , ω_{mn}^p and ω_{mn}^{p0} are (6.31), (6.46) and (6.50), respectively. Using the matching condition (6.52) and (6.53), we obtain the following asymptotic expression for the incoming vorticity in the case of $\lambda \gg 1$ and $\sigma_0 \ll 1$ in the whole range of η

$$\begin{aligned} \omega_{mn}(\eta) &\sim C_{mn} \left[M\left(\frac{\lambda - n^2}{2\lambda} - i\frac{m\sigma_0}{2}; \frac{1}{2}; -\frac{(\eta - \delta_d)^2}{2}\right) + e^{(\Phi_\delta - \Phi)} - e^{-(\eta - \delta_d)^2/2} \right] \\ &+ D_{mn} \left[M\left(\frac{2\lambda - n^2}{2\lambda} - i\frac{m\sigma_0}{2}; \frac{3}{2}; -\frac{(\eta - \delta_d)^2}{2}\right)(\eta - \delta_d) + \right. \\ &\quad \left. e^{(\Phi_\delta - \Phi)} \int_0^{\delta-\delta_d} e^{\frac{\eta^2}{2}} d\eta + e^{-\Phi} \int_\delta^\eta e^{\Phi(\eta')} d\eta' - \right. \\ &\quad \left. M\left(1; \frac{3}{2}; -\frac{(\eta - \delta_d)^2}{2}\right)(\eta - \delta_d) \right] \end{aligned} \quad (6.55)$$

Here the dependence of ω_{mn} as an explicit function of λ and σ_0 , not readily obtained by the series expansion itself, has been retained in (6.55), and by

correcting the ω_{mn}^{p0} in the near wall region through ω_{mn}^0 , (6.55) also extends inside the Hiemenz boundary layer. In figure 6.11 and figure 6.12, the comparisons between the composite asymptotic solution (6.55) and the numerical solution are shown for $\lambda = 4$ and $\lambda = 36$, respectively. The vorticity profiles have been normalized by its value at the inflow boundary $\eta = H_0$. The numerical solution are obtained by solving both the linear equation (6.35) and the fully nonlinear equation (6.16). The asymptotic solution and the linear numerical solution agree well at $\lambda = 4$ and become indistinguishable at $\lambda = 36$. Recall that the disturbance amplitude is here taken as 10 percent of the mean free-stream velocity, $A_p = 0.1\phi(H_0)$, and the linear solution approaches the nonlinear solution quite well as λ increases. This indicates that the present linear analysis is adequate for describing the characteristics of disturbance development in a Hiemenz flow.

6.4.4 Boundary conditions for the vorticity

The general composite solution in (6.55) describes the evolution of disturbance vorticity in the whole domain from the inflow to the wall boundary. Now we set to specify the constants C_{mn} and D_{mn} by the inflow and wall boundary conditions. In fact, it will later become clear that both C_{mn} and D_{mn} bear clearly defined physical meanings. First, the initial disturbance vorticity is introduced at the inflow boundary far upstream, i.e.

$$\omega_{mn} = \omega_{mn}(H_0) \quad \text{at} \quad \eta = H_0 \quad (6.56)$$

Then, the value of vorticity at the wall needs be specified. However, there is no explicit expression for $\omega_{mn}(\eta = 0)$ because, as indicated by Sutera (1965), the vorticity equation is coupled, through the no-slip boundary condition, with the velocity equations. To obtain the correct value of vorticity on the wall, the equation for normal velocity v_{mn} must be solved first. By (6.13) and (6.14), it follows

$$v''_{mn} - n^2 k_0^2 v_{mn} = -ink_0 \omega_{mn} - u'_{mn}, \quad \text{with} \quad v_{mn}(0) = v'_{mn}(0) = 0. \quad (6.57)$$

Using the method of variation of parameters, the solution of v_{mn} satisfying the above boundary conditions is

$$v_{mn} = -\frac{e^{n k_0 \eta}}{2} \int_0^\eta (i \omega_{mn} + u_{mn}) e^{-n k_0 \eta'} d\eta' + \frac{e^{-n k_0 \eta}}{2} \int_0^\eta (i \omega_{mn} - u_{mn}) e^{n k_0 \eta'} d\eta' \quad (6.58)$$

But (6.58) contains u_{mn} which couples with v_{mn} through (6.15) and has not been solved. Nevertheless, by requiring that v_{mn} is bounded as $\eta \rightarrow \infty$, further analysis (see Appendix A) shows that the second boundary condition for ω_{mn} can be expressed as

$$\int_0^\infty \omega_{mn}^p e^{-nk_0\eta} d\eta = 0 \quad (6.59)$$

Together with (6.56), we now have

$$M_1 C_{mn} + M_2 D_{mn} = 1 \quad (6.60a)$$

$$I_1 C_{mn} + I_2 D_{mn} = 0. \quad (6.60b)$$

Solving (6.60) for C_{mn} and D_{mn} yields

$$C_{mn} = -\frac{I_2}{M_2 I_1 - M_1 I_2}, \quad D_{mn} = \frac{I_1}{M_2 I_1 - M_1 I_2} \quad (6.61)$$

where

$$M_1 = M\left(\frac{\lambda - n^2}{2\lambda} - i\frac{m\sigma_0}{2}; \frac{1}{2}; -\frac{(H_0 - \delta_d)^2}{2}\right) \quad (6.62a)$$

$$M_2 = M\left(\frac{2\lambda - n^2}{2\lambda} - i\frac{m\sigma_0}{2}; \frac{3}{2}; -\frac{(H_0 - \delta_d)^2}{2}\right)(H_0 - \delta_d) \quad (6.62b)$$

$$I_1 = \int_0^\infty M\left(\frac{\lambda - n^2}{2\lambda} - i\frac{m\sigma_0}{2}; \frac{1}{2}; -\frac{(\eta - \delta_d)^2}{2}\right) e^{-nk_0\eta} d\eta \quad (6.62c)$$

$$I_2 = \int_0^\infty M\left(\frac{2\lambda - n^2}{2\lambda} - i\frac{m\sigma_0}{2}; \frac{3}{2}; -\frac{(\eta - \delta_d)^2}{2}\right)(\eta - \delta_d) e^{-nk_0\eta} d\eta \quad (6.62d)$$

Notice that in (6.60) the vorticity at inflow has been chosen as $\omega_{mn}(H_0) = 1$ since the equation is linear. The value of ω_{mn} therefore represents the factor by which the initial vorticity is amplified or attenuated as it approaches the wall. Before we discuss the asymptotic behaviors of C_{mn} and D_{mn} , a few remarks on their significance and qualitative behavior are in order. First, (6.55) indicates that for a vortical disturbance specified upstream by λ and σ_0 , the induced vorticity on the wall is directly related to the value of C_{mn} and D_{mn} . In the case of $\lambda \gg n^2$, $|C_{mn}|$ represents the amplitude of vorticity at the wall, i.e. $|\omega_{mn}(0)| \sim |C_{mn}|$, and D_{mn} represents the amplitude of normal derivative of the vorticity at the wall, i.e. $|\omega'_{mn}(0)| \sim |D_{mn}|$. This can also be seen more clearly from figure 6.10. Consequently, the amplitude of

C_{mn} and D_{mn} indicates the effectiveness for the disturbance to penetrate the boundary layer and modify the mean flow structures near the wall. Second, the boundary condition (6.59) shows that for steady disturbance, ω^p must change sign in the flow domain; vorticity with sign opposite to the incoming vorticity needs be developed at the wall in order to satisfy the no slip boundary condition. This can be observed clearly from the vorticity contours in figure 6.6. Note that the amplitude of the induced vorticity at the wall $\omega_{mn}(0)$, as shown in figure 6.9, approaches a constant when λ becomes large. The origin and implications of this interesting behavior of $\omega_{mn}(0)$ can be understood through the asymptotic analysis for large λ and small σ_0 , and is presented in the next section.

6.5 Asymptotic Behavior

In this section, the asymptotic behavior of C_{mn} and D_{mn} in the vorticity expression is analyzed for the large scale $\lambda \gg 1$ and low frequency $\sigma_0 \ll 1$ disturbances. Based on this analysis, a scaling relation for the heat transfer enhancement in stagnation point flows in the presence of upstream disturbances is also derived.

6.5.1 Vorticity asymptotes

The asymptotic expression of C_{mn} for large λ and small σ_0 may be obtained as (see the Appendix B)

$$|C_{mn}| \sim H_0 \left[1 + (a_1 - \ln H_0) \frac{n^2}{\lambda} \right] \left[1 - \frac{\alpha_n m^2}{8} \sigma_0^2 \right] \quad (6.63)$$

where $a_1 = \frac{1}{2}(\ln 2 + \gamma)$ and $\gamma = 0.5772156\cdots$ is the Euler constant. The expression for $|D_{mn}|$ can be similarly obtained.

An important observation for (6.63) is that the amplitude of the vorticity induced at the wall, up to the leading order, is linearly dependent on the normal distance H_0 between the wall and the upstream location where the disturbance is introduced. This means that for large λ and small σ_0 , within the linear dynamics regime, the amplification factor due to the vortex stretching for the initial vortical disturbance has an upper limit set by H_0 . This explains the behavior seen in figure 6.9 as λ becomes large. From (6.63), one also finds that the unsteadiness of the disturbances tends to decrease the

induced vorticity amplitude at the wall compared with the steady case, but only to the second order in terms of frequency σ_0 . In figure 6.13, the vorticity profiles at different frequencies are computed numerically for $\lambda = 4$ to show the effect of the disturbance unsteadiness. Notice that although the numerical computation uses the full nonlinear equations, the vorticity value at the wall indeed follows the asymptotic behavior (6.63) and shows only modest changes relative to steady case for $\sigma_0 < 0.5$. From a viewpoint of time scale, $\sigma_0 \ll 1$ implies that the disturbance turn-over time is much longer than the time scale of mean flow distortion; vortex stretching is predominant, and hence generating flow structures similar to the steady case. For high frequency case $\sigma_0 \gg 1$, (6.28) is not valid, and in the course of disturbances being convected towards the wall, many cycles of oscillation have completed. The net vorticity induced at the wall is small due to the cancellation effect of the incoming disturbance vorticity with alternating signs. This effect, also known as ‘vortex piling’, has been analyzed by Hunt (1973). Our numerical results in figure 6.13 shows that indeed the induced vorticity at the wall decays monotonically with σ_0 and becomes rather small when $\sigma_0 > 2.5$.

6.5.2 Heat transfer scaling

With the amplitude of the velocity disturbance at the inflow $v_{mn}(H_0)$ kept constant, the vorticity ω_{mn} introduced at the inflow varies as a function of λ

$$\omega_{mn}(H_0, \lambda) = \omega_{mn}(H_0, 1) \lambda^{-\frac{1}{2}} \quad (6.64)$$

where $\omega_{mn}(H_0, 1)$ is a reference value of vorticity for $\lambda = 1$. Recall that, C_{mn} , D_{mn} , as functions of λ and σ_0 , represent the amplification factor for the wall vorticity value. The amplification factor increases with λ , initially at a large rate but eventually approaches a constant value determined by H_0 . Together with the $\lambda^{-\frac{1}{2}}$ factor, this gives rise to an overall optimum amplification for $\lambda \approx 4$

Once the vorticity is obtained, the corresponding velocity disturbance can be found by (6.58) as

$$v_{mn} = \frac{e^{-nk_0\eta}}{2} \int_0^\eta (i\omega_{mn} - u_{mn}) e^{nk_0\eta'} d\eta'. \quad (6.65)$$

As shown in appendix A, the second term of the integrand in (6.65) is expected to be much smaller than the first for $k_0 \ll 1$. Hence the dependence

of v_{mn} on λ directly follows that of ω_{mn} . When λ is large, the vorticity amplification factor C_{mn} approaches a constant. Accordingly, $|v|_{max} \sim \lambda^{-1/2}$, a trend noted in figure 6.8. Now from (6.23), it follows that

$$\frac{\Delta h}{h} = \frac{\theta'_0(0)}{\Theta'(0)} \sim \sum_{m,n} |v_{mn}| |\theta_{mn}| \quad (6.66)$$

For the temperature disturbance θ_{mn} , the linearized equation of (6.17) is

$$\theta''_{mn} + Pr\phi \theta'_{mn} - (n^2 k_0^2 + im Pr \sigma_0) \theta_{mn} = Pr v_{mn} \Theta' \quad (6.67)$$

The amplitude of the temperature fluctuation θ_{mn} can be deduced; *viz.* θ_{mn} will be proportional to the amplitude v_{mn} and follows the same asymptotic dependence on λ as ω_{mn} and v_{mn} . Hence, we have

$$|v_{mn}(\eta)| \sim |\theta_{mn}(\eta)| \sim |\omega_{mn}(\eta)| \sim |C_{mn}| \frac{|v_{mn}(H_0)|}{\sqrt{\lambda}} \quad (6.68)$$

For the low frequency case $\sigma_0 \ll 1$, the heat transfer enhancement scales with the disturbance parameters,

$$\frac{\Delta h}{h} \sim \frac{A_p^2 H_0^2}{\lambda} \sum_{m,n} [1 + (a_1 - \ln H_0) \frac{n^2}{\lambda}]^2 [1 - \frac{\alpha_n}{8} m^2 \sigma_0^2]^2 |v_{mn}(H_0)|^2. \quad (6.69)$$

When $\lambda \gg 1$, we have $\Delta h/h \sim \lambda^{-1}$ for fixed A_p , a behavior noted in figure 6.8. We can rewrite $\frac{1}{\lambda}$ in terms of the disturbance length scale l_d , and obtain the following scaling relation for the relative heat transfer enhancement at low disturbance frequency

$$\frac{\Delta h}{h} \sim \frac{A_p^2}{l_d^2} \sum_{m,n} (1 - \frac{\alpha_n}{8} m^2 \sigma_0^2)^2 |v_{mn}(H_0)|^2 \quad (6.70)$$

The above expression reveals different roles played by the various flow parameters in heat transfer enhancement. First, the enhancement is proportional to the square of the disturbance amplitude A_p due to the net convective flux by the disturbance modes. Second, the length scale of the disturbance has a critical effect upon the heat transfer enhancement. For large scale disturbances, the heat transfer enhancement decreases with increased length scale. The most effective disturbance will be those with length scales comparable

to the boundary layer thickness. Finally, the overall effect of the frequency of the disturbances is to reduce the heat transfer enhancement. The decrease is of the second order when the frequency is low, and at high frequencies the heat transfer enhancement approaches to zero owing to the rapid decay of the incoming disturbances. So far the Prandtl number has been kept at a constant in the analysis $Pr = 0.71$. For a different Prandtl number, both the mean thermal boundary layer thickness and the amplitude of the θ_{mn} 's will be affected. Nevertheless, the qualitative dependence on Prandtl number can be inferred from (6.23). For small Pr , the $\Delta h/h$ increases with the increase of Pr , but as Pr becomes very large, the effect diminishes due to the extremely thin thermal boundary layer. So there will be a optimal value of Prandtl number for each fixed value of λ which gives the maximum heat transfer enhancement. Numerical calculations show that this optimal Prandtl number decreases with increasing λ from $Pr = 7$ at $\lambda = 1.5$ to $Pr = 0.71$ at $\lambda = 12$. However, for a fixed Prandtl number, the optimal value of λ is still around $\lambda = 4$, and the overall maximum value of $\Delta h/h$ occurs around $\lambda = 4$ and $Pr = 1.5$ (Xiong, 2004).

6.6 Discussion of Free-Stream Turbulence

One of the primary goals of the preceding analysis is to provide an improved understanding on the free-stream turbulence effect in stagnation point flows. In this section, we extend the incoming disturbances from discrete harmonic modes to free-stream turbulence. The latter is assumed to be isotropic and homogeneous. This extension allows a comparison to experimental measurements. This also serves as a test of applicability of the analysis to relevant engineering problems. The formulation is analogous to that in RDT, i.e. the overall changes of the turbulence statistics are obtained by integrating over all the Fourier modes once the modal distortion for each of them is known. The goal is to derive a scaling relation between the characteristics of the free-stream turbulence and the relative heat transfer enhancement at the wall.

On expressing the velocity fluctuations as

$$\mathbf{u}(\xi, \eta, \zeta, t) = \int \int \int_{-\infty}^{\infty} \hat{\mathbf{u}}(\kappa_1, \kappa_2, \kappa_3) \exp[i(\kappa_1\xi + \kappa_2\eta + \kappa_3\zeta + \sigma t)] d\kappa_1 d\kappa_2 d\kappa_3 \quad (6.71)$$

and using Taylor's hypothesis, the free-stream turbulence is treated as 'frozen' while being convected into the domain through the inflow boundary with a time frequency $\sigma = -U\kappa_2$. Let $\eta = H_0$ be the location of the inflow boundary, then

$$\mathbf{u}(\xi, H_0 - Ut, \zeta) = \int \int \int_{-\infty}^{\infty} \hat{\mathbf{u}}_{in}(\kappa_1, \kappa_2, \kappa_3) e^{i(\kappa_1 \xi + \kappa_2(H_0 - Ut) + \kappa_3 \zeta)} d\kappa_1 d\kappa_2 d\kappa_3. \quad (6.72)$$

While being convected towards the stagnation point, the free-stream turbulence experiences an accumulated vortex stretching in ξ direction by the diverging mean flow. As a result, this leads to $k_1 \ll k_2, k_3$ in the stagnation point region. Thus the dependence of \mathbf{u} on ξ may be neglected in the above expression, and the inverse transformation of $\hat{\mathbf{u}}_{in}$ is now written as

$$\hat{\mathbf{u}}_{in}(\kappa_2, \kappa_3) = \frac{1}{(2\pi)^2} \int \int_{-\infty}^{\infty} \mathbf{u}(H_0 - Ut, \zeta) e^{-i(\kappa_2(H_0 - Ut) + \kappa_3 \zeta)} d\zeta dt \quad (6.73)$$

The heat transfer enhancement in the presence of free-stream turbulence can be computed in terms of the downstream velocity and temperature spectra $\hat{u}(\eta, \kappa_2, \kappa_3)$, $\hat{\theta}(\eta, \kappa_2, \kappa_3)$. Following the discussion in preceding sections, we assume that for the η -velocity \hat{v} and temperature $\hat{\theta}$

$$\hat{v}(\eta, \kappa_2, \kappa_3) = G(\eta) \hat{v}(H_0, \kappa_2, \kappa_3) \sim \hat{\theta}(\eta, \kappa_2, \kappa_3) \quad (6.74)$$

where function $G(\eta)$ represents the amplification ratio at downstream location η for mode $\hat{v}(\kappa_2, \kappa_3)$ due to mean flow straining and viscous dissipation. Taking the amplitude of $G(\eta)$ as $C(\kappa_2, \kappa_3)$, i.e.

$$|G(\eta, \kappa_2, \kappa_3)| \sim |C(\kappa_2, \kappa_3)| \quad (6.75)$$

The overall effect of free-stream turbulence on the heat transfer can be estimated by summing the contribution from all the modes of different wave numbers and frequencies. In view of (6.23), for a single mode disturbance specified at the inflow, the heat transfer enhancement mainly results from the second order interaction terms. Thus in the present linear analysis when (6.23) and (6.74) are used to find the contribution from mode \hat{v}_{mn} , the non-linear term \mathcal{N}_4 can be written as

$$\mathcal{N}_4(\kappa_2, \kappa_3) \sim |C(\kappa_2, \kappa_3)|^2 |\hat{v}(\kappa_2, \kappa_3)|^2 \sim |C(\kappa_2, \kappa_3)|^2 \Phi_{ii}(\kappa_2, \kappa_3) \quad (6.76)$$

where the $\Phi_{ii}(\kappa_2, \kappa_3)$ is the energy spectra density for the free stream turbulence. Since the free-stream turbulence is assumed to be isotropic and homogeneous, the energy spectrum $E(\kappa)$ is defined as:

$$E(\kappa) = 2\pi\Phi_{ii}(\kappa)\kappa^2 \quad (6.77)$$

The turbulence intensity T_u and the integral length scale L may be related to the amplitude and fundamental wavenumber of energy containing range by

$$A_p^2 \sim (UT_u)^2; \quad \kappa_0 \sim \frac{1}{L} \quad (6.78)$$

The total contribution from all wave number components is the integration of the turbulent energy spectrum, i.e.

$$A_p^2 \sum_{\kappa_2, \kappa_3} |\hat{v}(H_0, \kappa_2, \kappa_3)|^2 \sim \int \int \int_0^\infty \Phi_{ii}(\kappa) d^3\kappa \sim T_u^2 \int_0^\infty \frac{E(\kappa)}{q^2 L} d(\kappa L) \quad (6.79)$$

Substitute (6.76), (6.79) into the expression for heat transfer enhancement (6.23), it becomes

$$\frac{\Delta h_T}{h} \sim T_u^2 \int \tilde{E}(\kappa L) |C(kL)|^2 d(\kappa L) \quad (6.80)$$

where $\tilde{E}(\kappa L) = E(\kappa)/(q^2 L)$. In most of the engineering problems involving turbulence impinging on a stagnation point, the turbulent eddy turn-over time is typically much longer than the time scale associated with the mean flow straining. i.e. $\sigma_0 \ll 1$. In addition, the turbulence length scale is assumed much larger than the boundary layer thickness, i.e. $L \gg \delta$. By (6.68), for a fixed upstream location it follows

$$|C(kL)| \sim \frac{C_{mn}}{\sqrt{\lambda}} \sim \frac{D}{l_d} \sim (\kappa L) \left(\frac{D}{L} \right) \quad \text{for } 0 < \kappa < \kappa_{max} \quad (6.81)$$

Hence,

$$\frac{\Delta h_T}{h} \sim \left(\frac{DT_u}{L} \right)^2 \int_0^{\kappa_{max} L} \tilde{E}(\kappa L) (\kappa L)^2 d(\kappa L) \quad (6.82)$$

where κ_{max} represents the highest wavenumber component having contribution to the heat transfer augmentation. From the previous analysis, the heat transfer enhancement reaches its maximum value with the disturbance scale

similar to the the boundary layer thickness. At even smaller scales the disturbances decay rapidly because of the viscous dissipation and have little effect on the wall quantities.

For practical engineering problems, such as flows over a bluff body, the boundary layer thickness at the stagnation region scales

$$l_0 = \sqrt{\nu^*/A^*} \sim \delta \sim \frac{D}{\sqrt{Re}} \quad (6.83)$$

where the Reynolds number is based on the mean flow U and the diameter of curvature D , see figure 6.1a. For an effective strain rate A^* , e.g. $A^* = 4U/D$ for a circular cylinder, κ_{max} may be expressed as

$$\kappa_{max}L \sim \frac{L}{\delta} \sim \sqrt{Re} \frac{L}{D} \quad (6.84)$$

Furthermore, the energy spectrum of the free stream turbulence is assumed to follow the Kolmogoroff $-5/3$ law

$$\tilde{E}(\kappa L) \sim (\kappa L)^{-5/3} \quad (6.85)$$

Substituting (6.84) and (6.85) into (6.82), the heat transfer enhancement at stagnation point can now be correlated to the free-stream turbulence parameters by

$$\frac{\Delta h_T}{h} \sim \mathcal{H} = \frac{T_u^2 Re^{2/3}}{\left(\frac{L}{D}\right)^{2/3}} \quad (6.86)$$

Note that here the three-dimensional spectrum function is used. Following the form of organized disturbances in previous discussion, a one-dimensional spectra is probably more appropriate. However, at high Reynolds number, it also follows the same $-5/3$ law as the three dimensional spectrum.

In order to examine heat transfer scaling, (6.86) is compared against the experimental measurements for stagnation point flows in the presence of free-stream turbulence. A recent experiment was conducted by Ames, Wang, and Barbot (2002), in which the heat transfer to a model vane is measured for six different inlet turbulence conditions with turbulence intensity up to 14 percent. The different characteristics of the free-stream turbulence are generated using mesh biplanar grid and various mock combustion system configurations. The experimental set up is representative to modern dry low NOx and aeroderivative combustors. The downstream vane heat transfer

measurements can serve as a database for the validation of predictive methods. Another reason to choose this experiment is that the characteristics of free-stream turbulence i.e. intensity and length scale are measured with the model vane present in the flow. Thus the mean velocity follows the Hiemenz profile at the locations where the turbulence is measured. This is the same case as has been assumed in the present analysis. In some other experiments, e.g. Van Fossen et al. (1995), the free stream turbulence is first measured in the uniform flow without the model. When the model is present, the turbulence characteristics are obtained by extrapolation using a power law for decaying turbulence. At locations close to the stagnation point, the turbulence characteristics obtained by this method will be significantly different from those obtained with the presence of the model. Although the difference becomes smaller beyond a distance on the order of D away from the wall, the Hiemenz flow, as a good approximation at the stagnation point for bluff-body flows, is also only valid within the order of D away from the wall. Hence, in figure 6.14 the present heat transfer correlation is compared with the measurement of Ames et al. (2002) at four high turbulence levels generated by grid as well as by aero-derivative and dry low NOx mock combustor system. The Reynolds number based on the leading edge diameter ranges from 58,000 – 232,000; turbulence integral scale from $0.11D$ – $1.0D$ and the turbulence intensity from 8 – 14%. The collective experimental uncertainty is ± 5 percent for turbulence measurement and ± 3 percent for heat transfer data. Although some scatter is present, the correlation appears to agree reasonably well with the experimental data for the correlation parameter \mathcal{H} over the range 5 to 35. Notice that the turbulence levels in these experiments are quite high, but the analysis indicates that only small scale components contribute effectively to the heat transfer enhancement. So even the total turbulence level is high, the amplitude at the small scale, i.e. the scale of boundary layer thickness that affects the heat transfer most, would still be relatively small. For a single mode velocity disturbance at a level equivalent to 10 percent of the mean flow, the numerical results show that the disturbance evolution can still be largely described by linear vortex dynamics. This may explain why the correlation based on linear analysis seems to hold even for the case of high turbulence intensity. It is also interesting to notice that the present correlating parameter is close to the square of the empirical TLR parameter $TLR = T_u Re_D^{5/12} (D/L_u)^{1/3}$ proposed by Ames (1997), if the turbulence integral length scale were replaced by the ‘energy scale’ $L_u = 1.5|u'|^3/\epsilon_T$, where $|u'|$ is the r.m.s. streamwise fluctuation velocity and

ϵ_T is the turbulent dissipation rate.

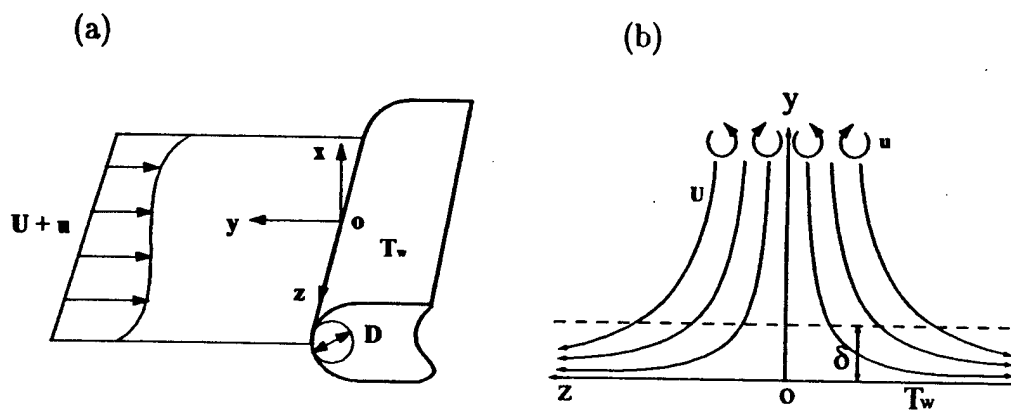


Figure 6.1: a) Disturbed stagnation point flow at the leading edge of a two-dimensional bluff body. b) Hiemenz boundary layer flow with upstream incoming disturbances.

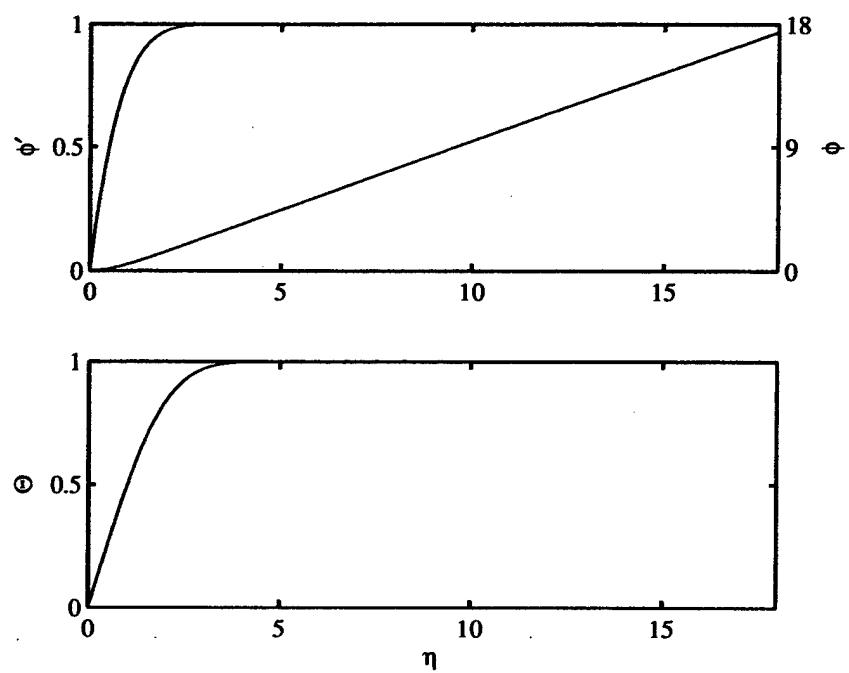


Figure 6.2: Profiles for the mean velocity ϕ , its derivative ϕ' and the mean temperature Θ .

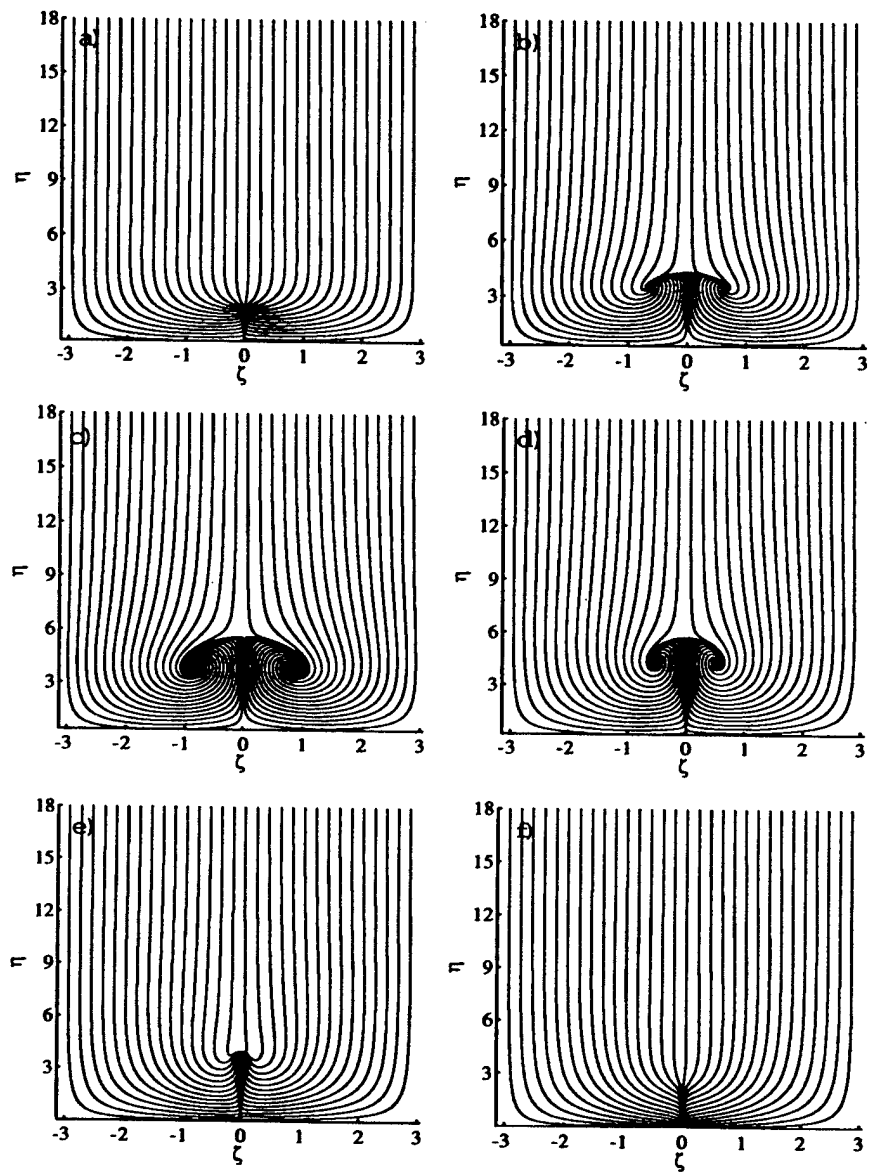


Figure 6.3: Streamline patterns in the stagnation plane for different values of λ . Flow is downward and the spanwise width is one disturbance wavelength. $\lambda = 1.1, 2, 4, 16, 32, 64$ from a to f.

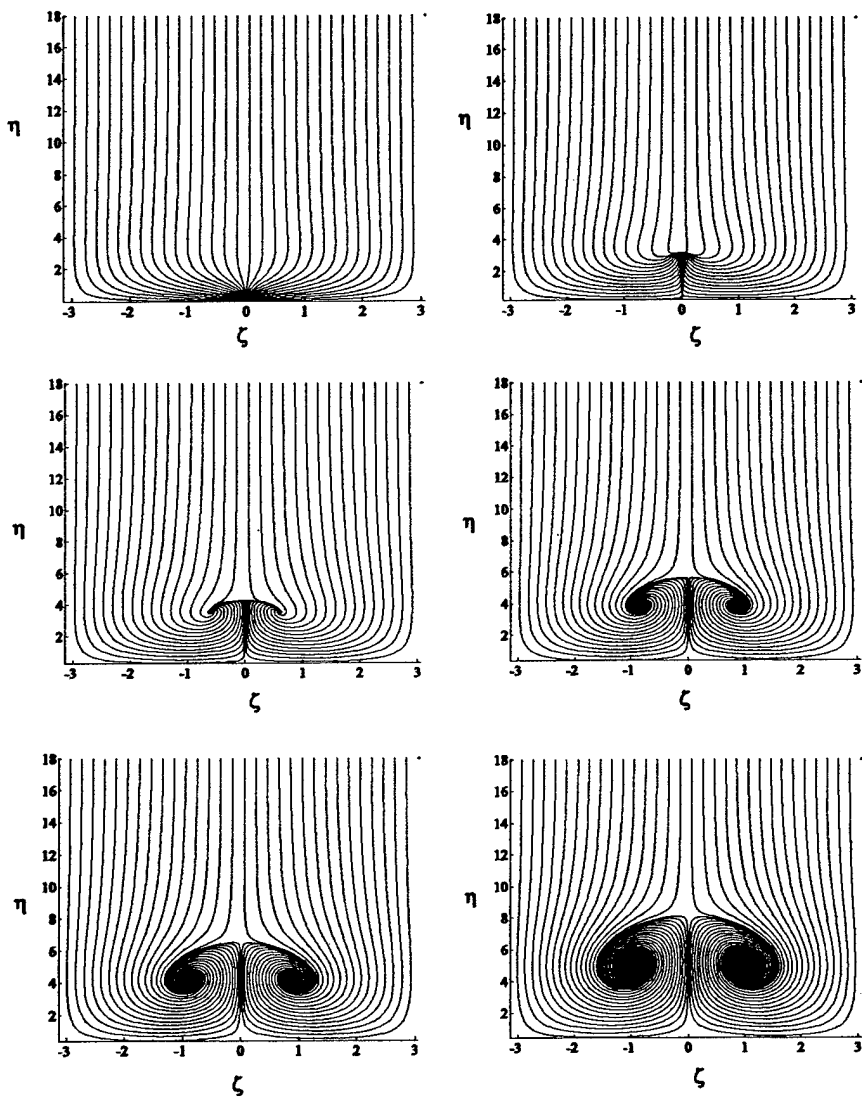


Figure 6.4: Streamline patterns in the stagnation plane for different values of A_p at $\lambda = 4$. Flow is downward and the spanwise width is one disturbance wavelength. $A_p = 0.02, 0.05, 0.07, 0.10, 0.12, 0.15$ from a to f.

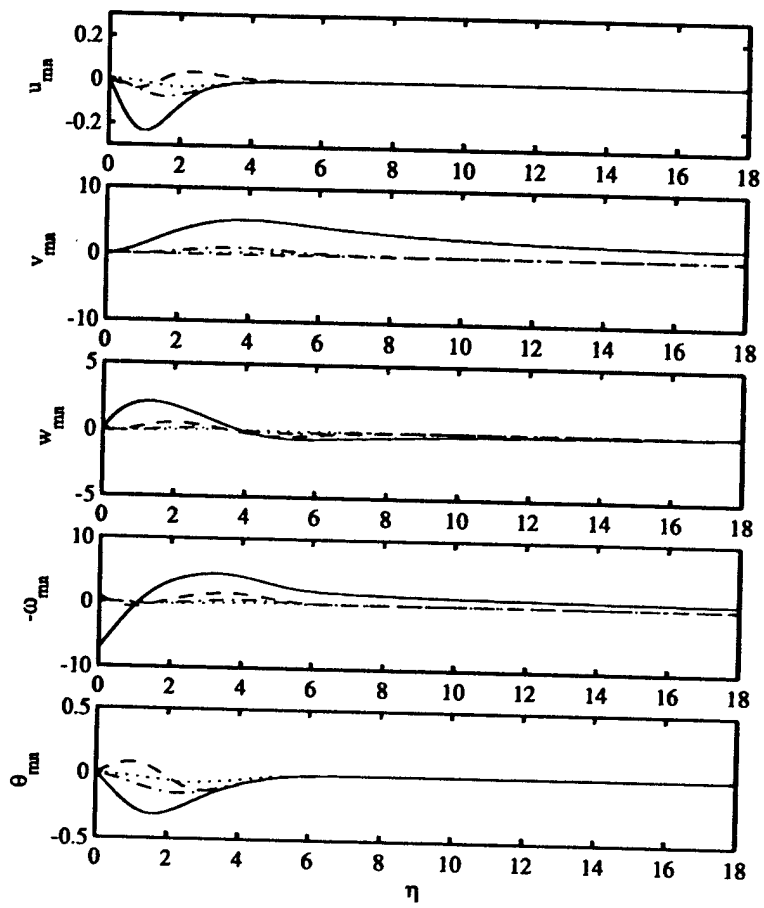


Figure 6.5: Profiles for steady ($\sigma = 0$) velocity and temperature disturbances at $\lambda = 4$. Solid line is the fundamental mode, The dash, dash dot and dotted line correspond to mean flow modification, second and third harmonics for u_{mn} , v_{mn} , θ_{mn} , and second, third and fourth harmonics for ω_{mn} and w_{mn} .

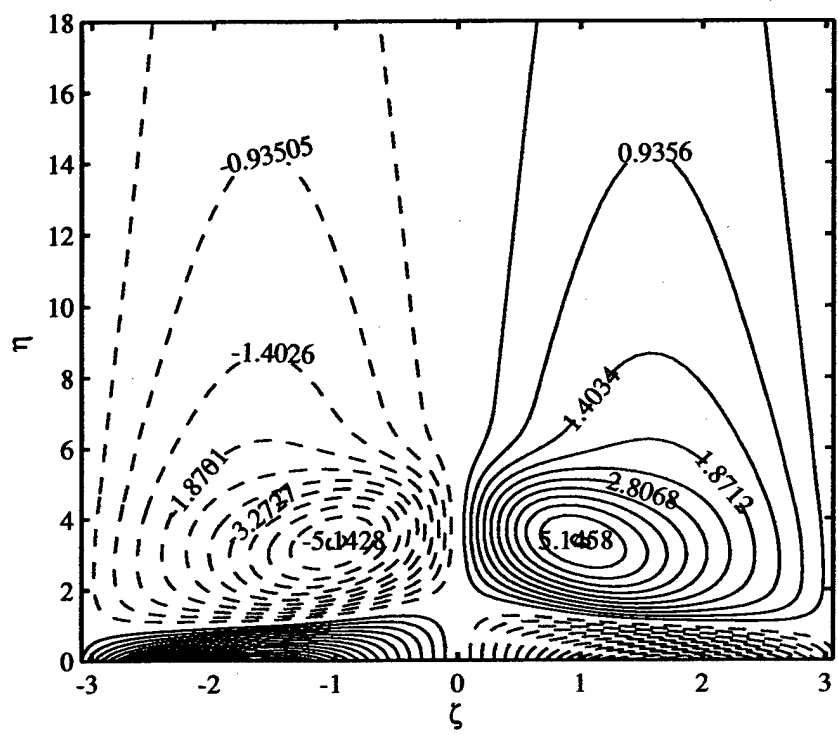


Figure 6.6: Vorticity contours in stagnation plane at $\lambda = 4$, Flow is downward and the spanwise width is 2π . Solid lines are for the positive values of ω and dash lines for the negative.

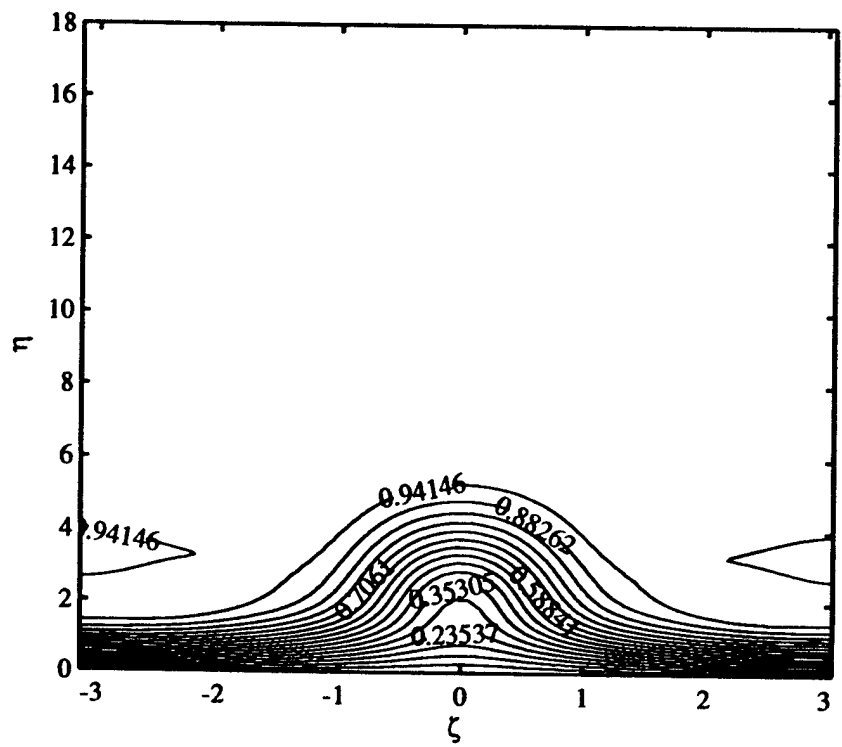


Figure 6.7: Temperature contours in stagnation plane at $\lambda = 4$. Flow is downward and the spanwise width is 2π .

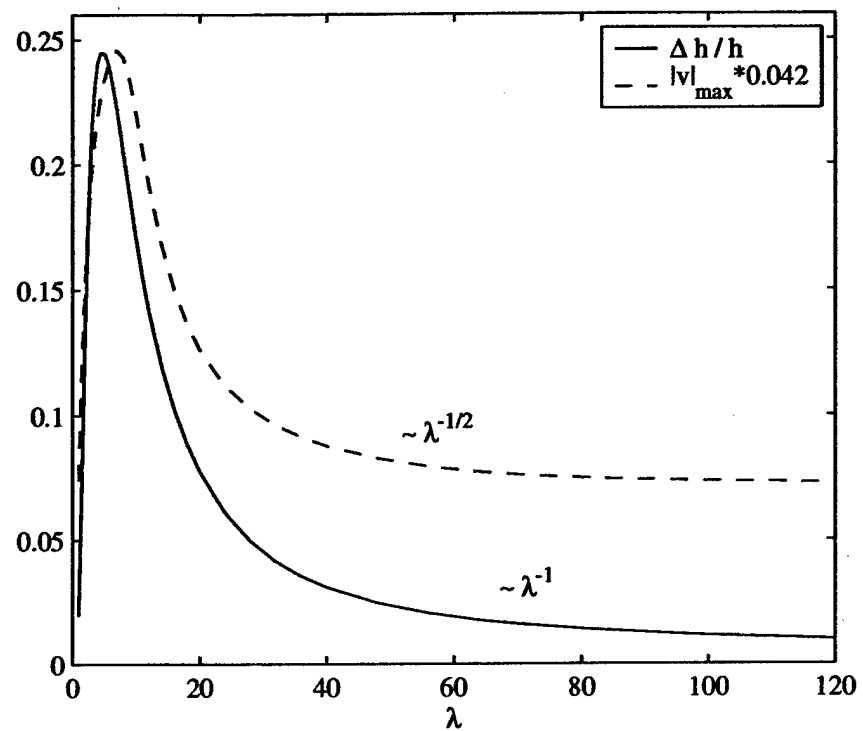


Figure 6.8: Relative heat transfer enhancement $\Delta h/h$ and the maximum amplitude of the fundamental v velocity (renormalized) as a function of λ .

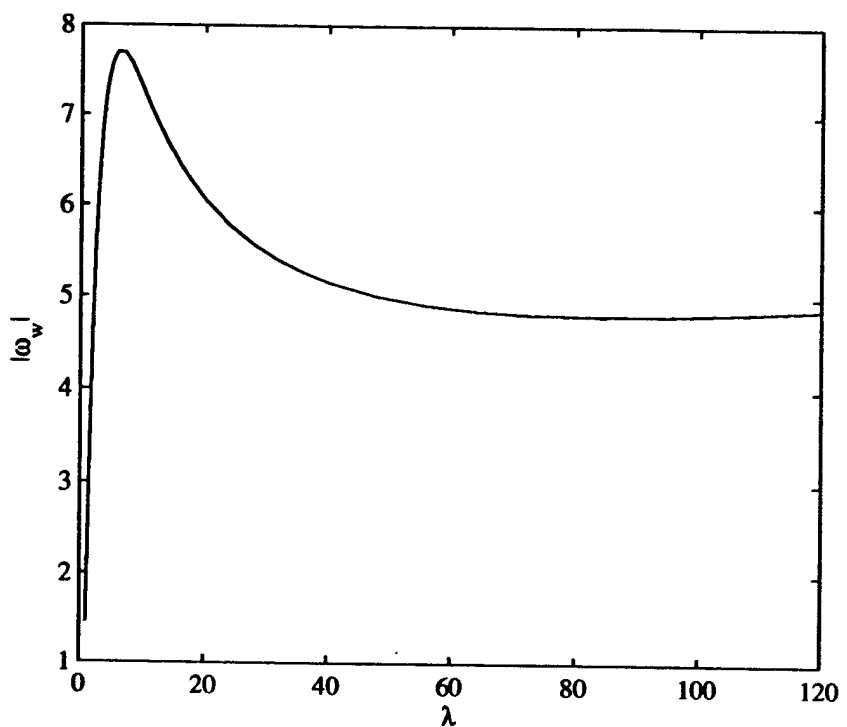


Figure 6.9: Vorticity magnitude at the wall as a function of λ for the steady fundamental mode.

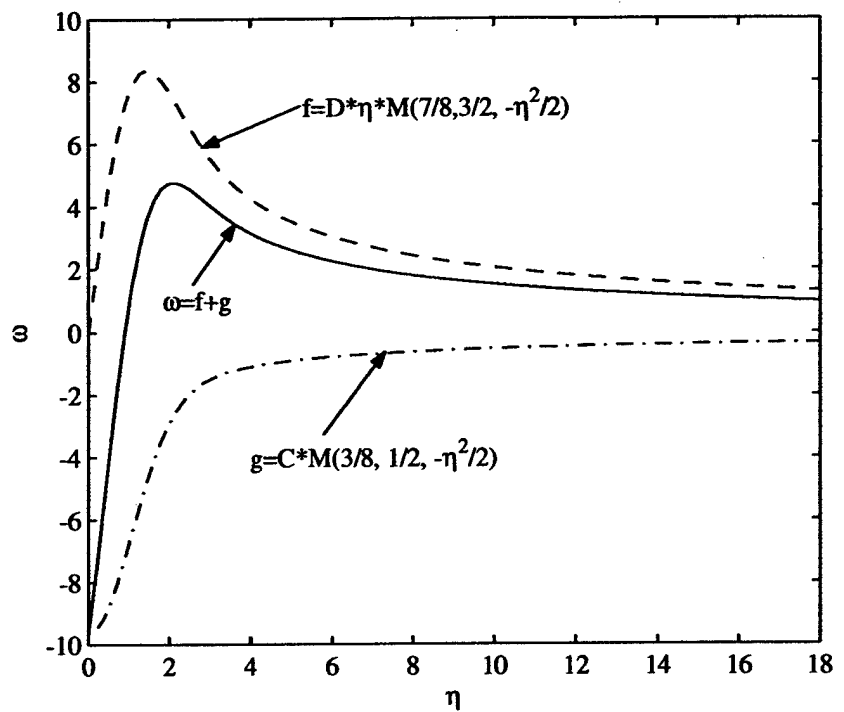


Figure 6.10: A typical vorticity profile composed of two confluent hypergeometric functions. $\lambda = 4$, $\sigma_0 = 0$

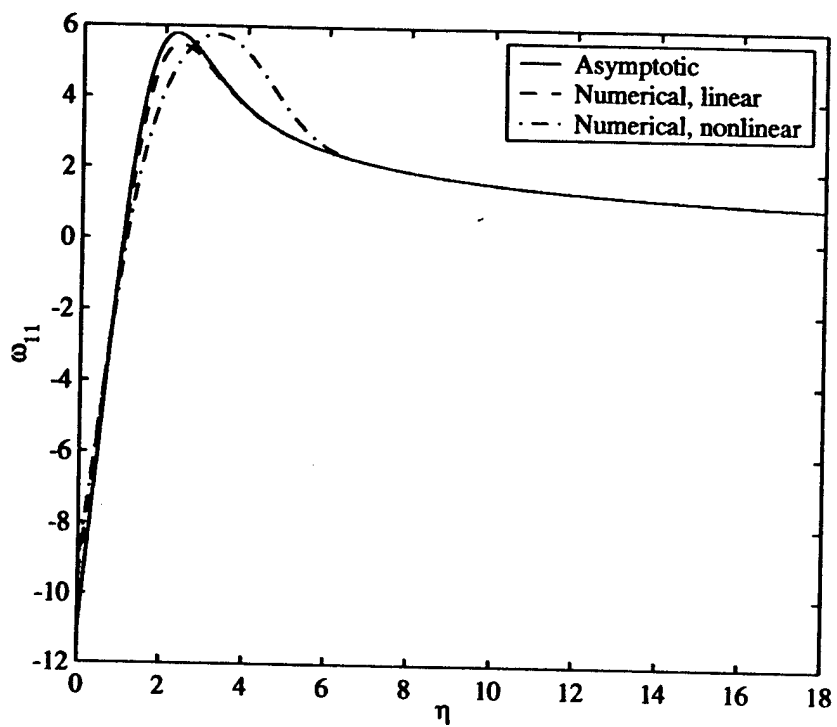


Figure 6.11: Comparison of vorticity profile between numerical and asymptotic solutions at $\lambda = 4$.

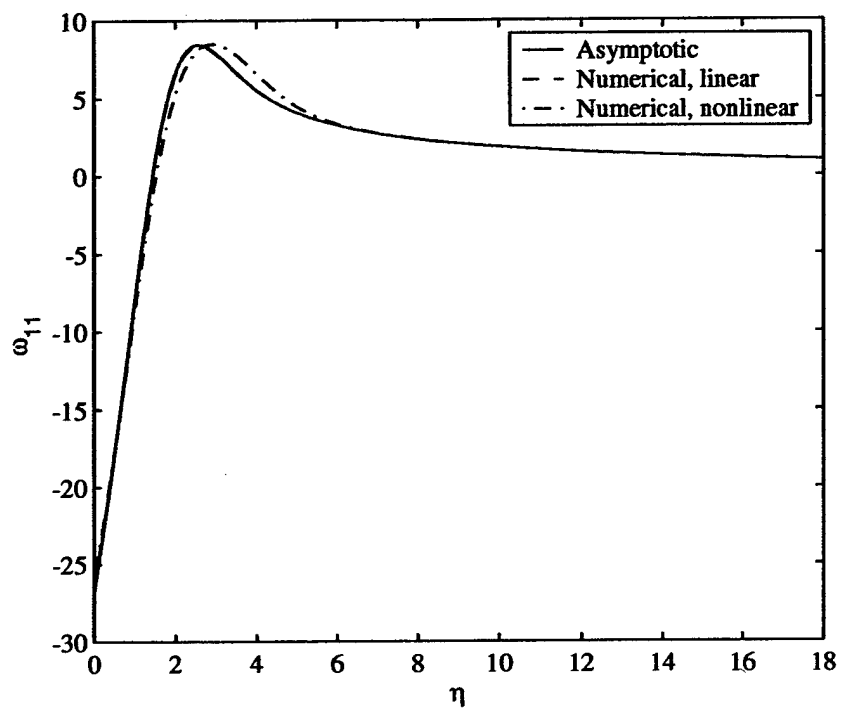


Figure 6.12: Comparison of vorticity profile between numerical and asymptotic solutions. $\lambda = 36$.

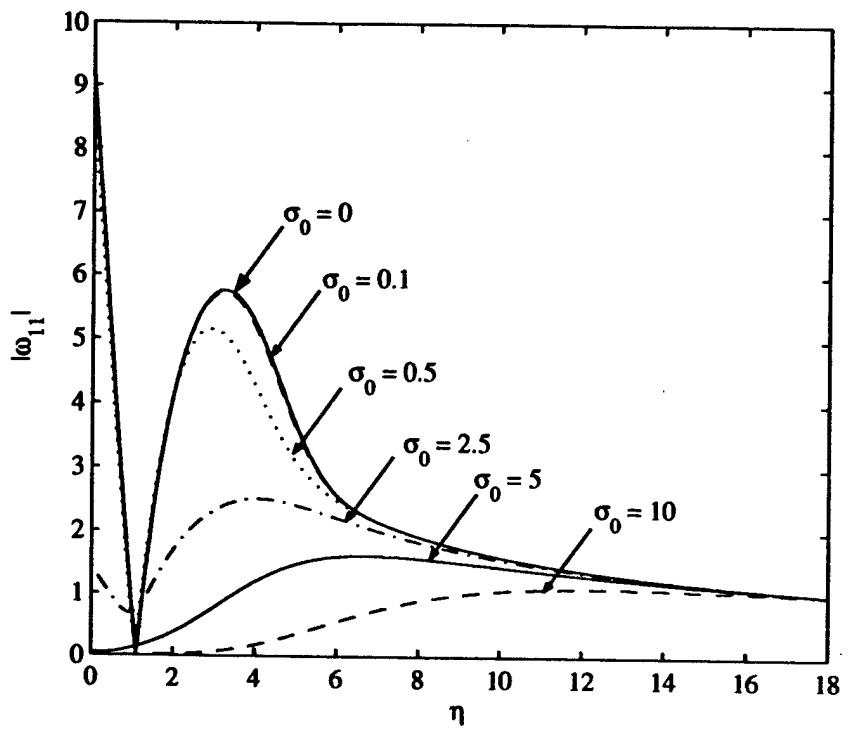


Figure 6.13: Vorticity profiles for different fundamental disturbance frequency σ_0 at $\lambda = 4$.

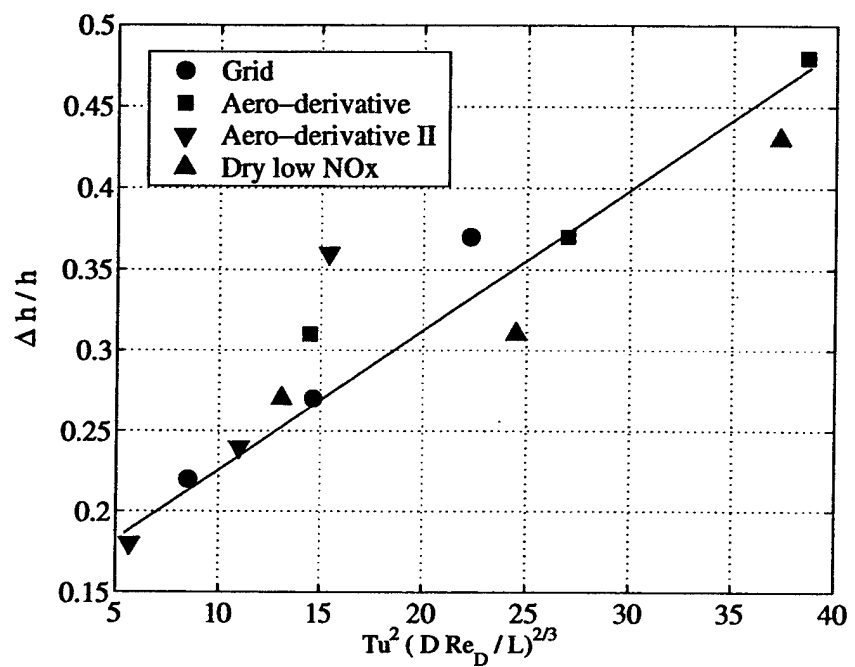


Figure 6.14: Experimental data of leading edge heat transfer enhancement under free-stream turbulence correlated by the present scaling parameter \mathcal{H} .

Chapter 7

Summary and Conclusion

We have developed a numerical method for three-dimensional compressible flow based on fourth order finite difference scheme in curvilinear coordinates, and a very efficient dual-time linearized subiteration scheme for fully implicit time marching. This method is suitable for numerically simulating turbulent flows around bluff bodies. It has been implemented, validated, and used to perform large eddy simulations of free-stream turbulence impinging on an elliptical leading edge and the resulting heat transfer enhancement.

A new blending procedure is developed by which independent but statistically identical realizations of homogeneous isotropic turbulence are combined into a unified field to represent free-stream turbulence realistically. The blending is performed over a blending zone at the interface between different realizations using a smooth varying function. Extra dilatation field within the blending zone is further removed using Helmholtz decomposition theorem. Outside the blending zone, the original turbulence fields remain unchanged. By construction, the combined field preserves the turbulence intensity, and the change to other statistical quantities are shown to be minimal. The method is simple yet effective and could be useful in other direct or large eddy simulations in which effects of sustained free-stream turbulence are important.

The large eddy simulation results characterize the anisotropy of turbulence due to the mean flow strain as it approaches the stagnation point. The turbulent budgets for the Reynolds stresses in such a strongly strained flow are presented, and different roles in the dynamics for different terms are discussed. These results provide guidelines for modelling strongly strained turbulent flows for Reynolds averaged Navier-Stokes equations, a subject which

has been proved difficult in the past. The numerical results also shows that free-stream turbulence significantly elevates the surface heat transfer coefficients, but the distribution of the heat transfer coefficient along the surface is essentially kept the same as in the laminar case. Both of these results show good agreement with the corresponding experimental measurements. The numerical simulation also reveals that small scale, intense vortical flow structures generated at the leading edge by vortex stretching induces significant changes in the thermal boundary layer thickness, and are the primary cause of the observed heat transfer enhancement.

In the theoretical study, we analyze the distortion of unsteady three dimensional organized disturbances in an incompressible Hiemenz boundary layer and its effect on the wall heat transfer. Based on linearized disturbance equations, it is found that the vorticity outside the boundary layer can be expressed analytically in terms of confluent hyper-geometrical functions, parameterized by the disturbance length scale and temporal frequency. When the scale of the disturbance is large and the frequency is low, an approximate asymptotic solution is obtained with explicit dependence on the disturbance length scale and frequency. This solution compares well with the full nonlinear numerical solutions over a wide range of disturbance parameters.

It is further shown that the ratio between the disturbance length scale and the boundary layer thickness is the critical parameter in determining the amplification factor of incoming vorticity. Essentially, it represents the interaction between the vortex stretching effect and viscous diffusion. The amplification factor is found to be inversely proportional to the length scale except at very small scales where it increases with increased length scale. The maximum amplification is found for the disturbances with a length scale about five times the Hiemenz boundary layer thickness. The associated heat transfer enhancement also strongly depends on the disturbance length scale and is analyzed through the induced vorticity at the wall. Compared to the steady case, the heat transfer enhancement is reduced by the unsteadiness of the disturbance but the effect is of second order when the frequency is low.

The analysis is further extended to the case of homogeneous and isotropic free-stream turbulence. The turbulence energy spectrum is assumed to follow the Kolmogoroff's $-5/3$ law and the integral scale is much larger than the boundary layer thickness. Under these conditions, a new scaling correlation is derived between the relative heat transfer enhancement and the turbulence intensity, integral length scale and the mean flow Reynolds number. In comparison to recent experimental data on turbine blade heat transfer

in the presence of free-stream turbulence, the present correlation provides a reasonable guide to the observed variations.

This technical report represents a status report at the time of writing. The post processing of the simulation data is continuing and the finalized version including all the results and discussions will be reported in the PhD thesis of Xiong (2004).

Acknowledgments

This work is supported by the Air Force Office of Scientific Research under grant No. F49620-01-1-0138 with Dr. Tom Beutner as the program manager. The computer resource was provided by the 48-node computer cluster under DoD DURIP grant No. F49620-01-1-0239 and the DoD MSRC centers at NAVO and ARL.

Appendix A

Incompressible Potential Flow

We derive the incompressible two dimensional potential flow solution of a point source placed midway between two parallel planes with a uniform incoming stream, see figure C.1. The configuration is prototypical to experiments where a blunt leading edge model with flat plate after-body placed in a wind tunnel test section, and due to the thickness of the model in comparison with the height of the test section, the flow passage is significantly blocked. The blockage causes the flow field to differ, particularly in pressure distribution, from the open flow case where the walls are absent. To make a direct comparison between computation and experiment, the blockage effect often needs to be accounted explicitly in the computational configuration.

Let U_∞ be the uniform incoming velocity at far upstream, a be the half height of the test section, and b the half thickness of the model. The coordinate is chosen such that the forward stagnation point is at the origin $x = 0$. The goal here is to find the strength $2\pi m$ and the location $x = c$ of a two dimensional point source S so that at far downstream, the required blockage ratio b/a can be reproduced.

Following Milne-Thomson (1960), the complex potential for a point source placed midway between two planes with a general uniform incoming stream U can be written as

$$W = \phi + i\psi = -Uz - m \ln \sinh \frac{\pi(z - c)}{2a} \quad (\text{A.1})$$

here ϕ and ψ are the velocity potential and stream function, and $z = x + iy$. By the definitions of complex function $\ln z$ and $\sinh z$

$$\ln z = \ln(\sqrt{x^2 + y^2}) + i \arctan \frac{y}{x} \quad (\text{A.2})$$

$$\sinh z = \cos y \sinh x + i \sin y \cosh x \quad (\text{A.3})$$

The stream function ψ in (A.1) is

$$\psi = -Uy - m \arctan \left[\tan \frac{\pi y}{2a} \coth \frac{\pi(x-c)}{2a} \right] \quad (\text{A.4})$$

The dividing streamline, which forms the boundary of the Rankine body, corresponds to $\phi = 0$. This requires

$$\tan \frac{Uy}{m} = -\tan \frac{\pi y}{2a} \coth \frac{\pi(x-c)}{2a} \quad (\text{A.5})$$

At far downstream $x \rightarrow \infty$, $\coth \frac{\pi(x-c)}{2a} \rightarrow 1$, thus

$$\tan \frac{Uy}{m} = -\tan \frac{\pi y}{2a} \quad (\text{A.6})$$

whose solution is

$$\frac{Uy}{m} = -\frac{\pi y}{2a} \pm n\pi, \quad n = 0, 1, 2, \dots \quad (\text{A.7})$$

Physical conditions indicate that only $n = 0$ and $n = 1$ are needed, so that at far downstream the y coordinates of the Rankine body are

$$y = 0; \quad y = \pm b = \pm \frac{2am\pi}{2aU + m\pi} \quad \text{as } x \rightarrow \infty \quad (\text{A.8})$$

Note that to ensure $|y| < a$ at $x \rightarrow \infty$, the incoming velocity U must satisfy

$$U > \frac{\pi m}{2a} \quad (\text{A.9})$$

Furthermore, the streamwise velocity u can be obtained from ψ by

$$u = -\frac{\partial \psi}{\partial y} = U + \frac{\pi m}{2a} \frac{\coth \frac{\pi(x-c)}{2a}}{\cos^2(\frac{\pi y}{2a}) + \sin^2(\frac{\pi y}{2a}) \coth^2 \frac{\pi(x-c)}{2a}} \quad (\text{A.10})$$

Setting $u(0, 0) = 0$, we obtain the location of the source c

$$c = \frac{a}{\pi} \ln \left(\frac{2aU + \pi m}{2aU - \pi m} \right) \quad (\text{A.11})$$

But, if we now let $x \rightarrow -\infty$, (A.10) leads

$$u = U - \frac{\pi m}{2a} \neq U \quad (\text{A.12})$$

That is, the resulting velocity at upstream differs from the value U which we initially imposed! This apparent contradiction stems from the fact that due to the presence of the planes, the velocity generated from the source, which would vanish as $1/r$ at $r \rightarrow \infty$ in open flows, does not vanish in the present case; instead, it reaches a constant value at $x = \pm\infty$. Indeed, by continuity equation and in the absence of imposed mean flow U , a point source of strength $2\pi m$ placed between two planes $y = \pm a$ generates velocity

$$u = \pm \frac{\pi m}{2a} \quad \text{at} \quad x = \pm\infty \quad (\text{A.13})$$

at $x = \pm\infty$. The incoming velocity at $x = -\infty$ is therefore a superposition of the imposed incoming mean flow U and the outgoing velocity $\frac{\pi m}{2a}$ from the source inside the domain. If the boundary condition is set $u = U_\infty$ at $x = -\infty$, then we need choose

$$U = U_\infty + \frac{\pi m}{2a} \quad (\text{A.14})$$

for the resulting velocity to be compatible. Hence, for given lengths a , b , and velocity U_∞ , substituting (A.14) into (A.8) and (A.11), we find the required downstream blockage can be realized by placing the point source S of strength $2\pi m$, where

$$m = \frac{ab}{\pi(a-b)} U_\infty \quad (\text{A.15})$$

at location $x = c$, where

$$c = \frac{a}{\pi} \ln \left(1 + \frac{\pi m}{a U_\infty} \right) \quad (\text{A.16})$$

An example of the streamline pattern for $a = 5$, $b = 1$ and $U_\infty = 1$ is shown in figure A.2. Note that obviously in the potential framework, the boundary layers developed along the model surface and the wind tunnel walls are neglected. Furthermore, in the near field, the generated Rankine body shape does not, in general, follow the specific geometry of the leading edge of a test model. The solution, however, can serve as an initial condition for numerical computations where specific leading edge geometry is incorporated, and, in low Mach number case, provides a reasonably good boundary condition at far field for the compressible flow in question.

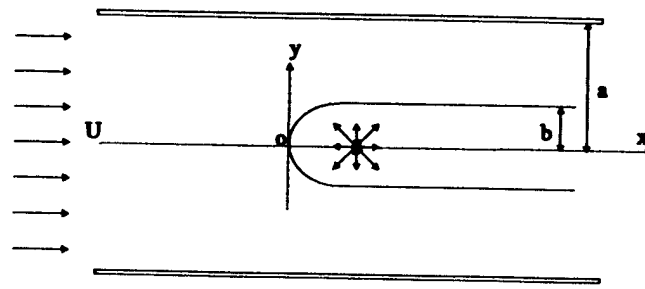


Figure A.1: A source with uniform incoming flow placed between two parallel plates

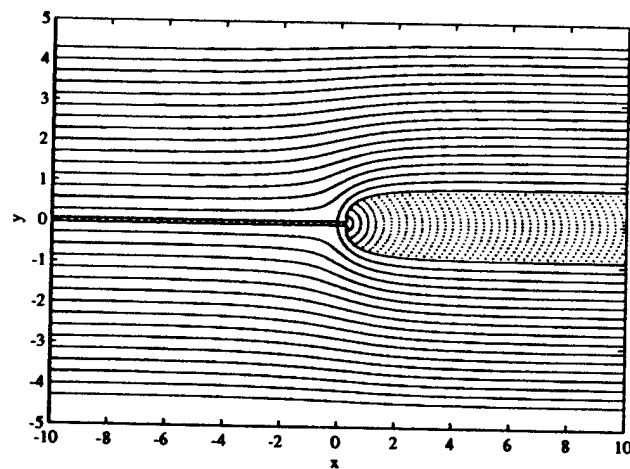


Figure A.2: Streamline pattern of a point source with uniform stream placed between two planes. $a = 5$, $b = 1$ and $U_\infty = 1$

Appendix B

On the Coefficient of Numerical Dissipation

Center differencing scheme (differencing scheme on a symmetric stencil) is dispersive but not dissipative. Owing to the stencil symmetry, the dissipation terms in the truncation error — the even order derivatives are completely canceled out. The discretization error in this case consists of only dispersion terms associated with the odd derivative terms. For a simple traveling wave computed using center differencing scheme, for instance, the wave will travel at a different speed due to the numerical dispersion, but the amplitude of the wave is maintained.

The inherent non-dissipative nature makes the center differencing scheme susceptible to numerical instability, particularly in the simulations of turbulence. Once some high wavenumber components are generated and can not be represented adequately by the underlying grid, they tend to persist in the course of computation and often eventually leads to numerical divergence. A common cure to this problem is to add controlled artificial dissipation terms to the governing equations to suppress the unwanted high wavenumber components. Another way of dealing it is to use numerical filtering, which will not be discussed here.

Specifically, consider a general one dimensional equation in its conservative form

$$f_t + F_x(f) = 0 \quad (\text{B.1})$$

where the subscripts denote temporal and spatial partial derivatives. Suppose in computational domain $[0, 1]$, a uniform grid consists of N points is used,

then $x_i = ih$, $1 \leq i \leq N$, where $h = 1/N$ is the grid spacing. A five point fourth order center differencing scheme

$$\tilde{f}_x = (\frac{\partial f}{\partial x})_i = \frac{f_{i-2} - f_{i+2} - 8(f_{i-1} - f_{i+1})}{12h} + O(h^4) \quad (B.2)$$

is chosen to approximate the spatial derivative. To enhance the robustness of difference equation resulting from (B.2), a numerical dissipation term of the form

$$-\sigma h^4 (\frac{\partial^4 f}{\partial x^4}) \quad (B.3)$$

may be added to the right hand side of (B.1). Here $\sigma > 0$ is the coefficient controlling the amount of numerical dissipation added, whereas the h^4 keeps the dissipation term, if σ is not excessively large, of the same order of the truncation error in (B.2). In this way, it is expected that the formal accuracy of the difference equation will not be ruined by the addition of (B.3). The fourth order derivative in (B.3) may be approximated by the following seven point 4th order scheme

$$\tilde{f}^{(4)} = (\frac{\partial^4 f}{\partial x^4})_i = \frac{1}{6h^4} [-(f_{i-3} + f_{i+3}) + 12(f_{i-2} + f_{i+2}) - 39(f_{i-1} + f_{i+1}) + 56f_i]. \quad (B.4)$$

Now the problem reduces to how to specify the value of σ so that the unresolved scales can be effectively damped while the resolved scales remain essentially unaffected. In practice, the value of σ is often chosen, to a large extent, empirically depending on the computations in question. Here, we analyze the proper bound of σ using modified wavenumber analysis; the purpose is to provide a guideline in determining the value of σ in practical computations.

To begin with modified wave number analysis, let f be a simple periodic function

$$f = e^{ikx} \quad \text{then} \quad f_x = ike^{ikx} \quad (B.5)$$

The relative error contained in the numerical differentiation \tilde{f}_x by (B.2) is

$$\frac{|f_x - \tilde{f}_x|}{|f_x|} = 1 - \frac{16 \sin(kh) - 2 \sin(2kh)}{12kh} \quad (B.6)$$

On the other hand, the relative error resulting from (B.3) can also be similarly expressed as

$$\frac{\sigma h^4 |\tilde{f}^{(4)}|}{|f_x|} = \sigma h \frac{-2 \cos(3kh) + 24 \cos(2kh) - 78 \cos(kh) + 56}{6kh} \quad (B.7)$$

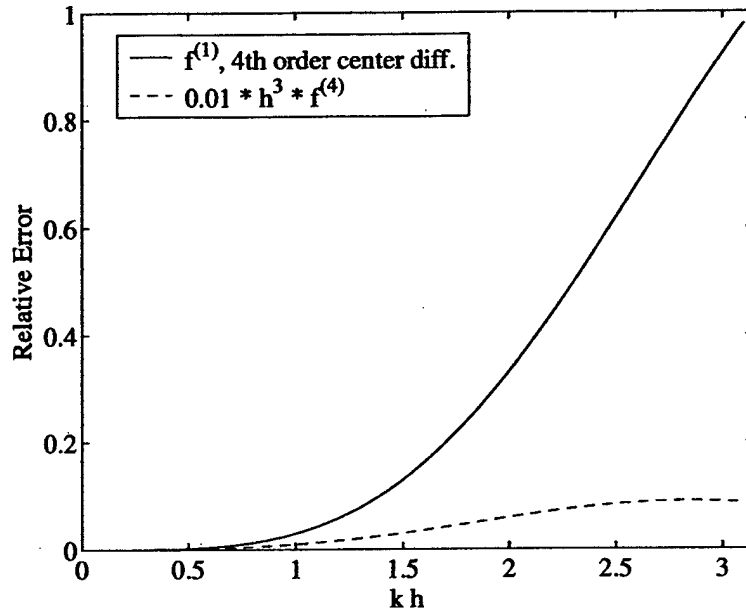


Figure B.1: Relative error of 4th order center differencing scheme and 4th order dissipation term (scaled) as a function of hk .

To maintain the formal accuracy of the numerical solution, we require that the maximum of the (B.7) is one order of magnitude smaller than maximum of (B.6), i.e.

$$\max \sigma h^4 |f^{(4)}| \leq 0.1 \max |f_x - \tilde{f}_x| \quad (\text{B.8})$$

For the particular choice of difference schemes used here, it is found that this can be achieved by setting

$$\sigma h \leq 0.01 \quad (\text{B.9})$$

For other differencing schemes, similar results can also be found. The comparison of (B.6) and (B.7) resulting from (B.9) is shown in the figure B.1 as a function of kh . As can be seen, the error in this case caused by the numerical dissipation term is negligible compared to the inherent difference truncation error. If we take (B.9) as an upper bound for σ for fixed $h = 1/N$, a useful estimation for σ can be derived as

$$\sigma \leq 0.01N \quad (\text{B.10})$$

In what follows, condition (B.10) is tested by solving the following one

dimensional convection equation with and without added numerical dissipation.

$$\begin{aligned} f_t + f_x &= -\sigma h^4 f^{(4)} \\ f(x, 0) &= e^{-100(x-0.5)^2} \end{aligned} \quad (\text{B.11})$$

The computational domain is $0 \leq x \leq 1$ with periodic boundary conditions at both ends. Although there are many choices for time marching scheme, we choose an implicit dual time stepping scheme with sub-iterations. While certainly not the simplest, this scheme is very representative to the time marching scheme often found in the unsteady wall bounded flow simulations. The derivation of this scheme is outlined as follows.

First, the semi-discrete form of (B.11) with implicit second order Euler scheme is

$$\frac{3f^{n+1} - 4f^n + f^{n-1}}{2\Delta t} + f_x^{n+1} = -\sigma h^4 f^{(4)n+1} \quad (\text{B.12})$$

After adding a pseudo time derivative f_τ to the left hand side, (B.12) becomes

$$f_\tau + \frac{3f^{n+1} - 4f^n + f^{n-1}}{2\Delta t} + f_x^{n+1} = -\sigma h^4 f^{(4)n+1} \quad (\text{B.13})$$

Now we approximate f_τ by first order Euler scheme $f_\tau = \frac{\delta f^k}{\Delta\tau}$, where $\delta f^k \equiv f^{k+1} - f^k$, and replace the index $n+1$ to $k+1$ in (B.13), the Δ form of the sub-iteration scheme becomes

$$\left(\frac{1}{\Delta\tau} + \frac{3}{2\Delta t} + \frac{\partial}{\partial x} + \sigma h^4 \frac{\partial^4}{\partial x^4} \right) \delta f^k = -\frac{3f^k - 4f^n + f^{n-1}}{2\Delta t} - \frac{\partial f^k}{\partial x} - \sigma h^4 \frac{\partial^4 f^k}{\partial x^4} \quad (\text{B.14})$$

When the sub-iteration converges, i.e. $\delta f^k = 0$, f^{k+1} is taken as f^{n+1} , and the right hand side of (B.14) recovers the (B.12). The pseudo time step $\Delta\tau$ can be properly chosen to accelerate the sub-iteration convergence. In the present computation, the first and fourth derivatives at the right hand side of (B.14) are approximated using (B.2) and (B.4). The fourth derivative at the left hand side of (B.14) is approximated by the following five point second order accurate scheme

$$\left(\frac{\partial^4 f}{\partial x^4} \right)_i = \frac{1}{h^4} [f_{i-2} + f_{i+2} - 4(f_{i-1} + f_{i+1}) + 6f_i]. \quad (\text{B.15})$$

which preserves the penta-diagonal structure of coefficient matrix at the left hand side of (B.14). The total number of grid points is taken $N = 50$, time

step $\Delta t = 0.001$, and the pseudo time step $\Delta\tau = 4\Delta t$. Five sub-iterations are used for each time step. The comparison of the numerical solutions with and without added dissipation term are shown in figure B.2 through B.5. Notice the small waves at the trailing edge of the numerical solution are the result of dispersion error in the center differencing scheme — the traveling speeds of these waves are different from their theoretical values. The decrease of the peak is also due to the dispersion of the constituent waves in an Gaussian function. Although we have used the maximum value of $\sigma = 0.5$ and a rather modest resolution $N = 50$, the comparison between the numerical solutions with and without the dissipation at four and eight flow through times is satisfactory. Only slight damping is observed on the side waves; the large structure of numerical solution is essentially unaffected by the addition of the dissipation term at $\sigma = 0.5$.

For different grid resolution, Table 1 summarizes the numerical error (in L_2 norm) with $\sigma = 0$ and $\sigma = 0.5$ after four flow through times. As can be seen, at $N \leq 50$, the error is smaller for $\sigma = 0.5$ compared to the no dissipation case because the unsolved scales are more damped by the dissipation term. Beyond $N = 50$, the dissipation term shows essentially no effect on the numerical accuracy. The corresponding solutions for $N = 100$ plotted in figure B.6 shows no discernible differences between $\sigma = 0$ and $\sigma = 0.5$. In addition, due to the increased resolution, the dispersion error is significantly reduced so that the numerical solutions are in good agreement with the exact solution.

In practical simulations, σ is typically set, often by trial and error, at the minimum value that can stabilize the computation. This criterion, while necessary, is not sufficient to maintain the formal accuracy of the original equation. To do so, σ should be further limited below its upper bound. The estimation of the upper bound of σ also offers a better assessment on the grid resolution: if the maximum σ is still insufficient to stabilize the computation, it suggests that the resolution is critically low and increasing the number of grid points is essential. Increased resolution, on the other hand, also increases the upper bound of σ according to (B.10), so on a refined mesh, σ can take a larger value and the numerical method can achieve, without sacrificing the accuracy, an improved robustness.

Number of grid points N	No Dissipation $\sigma = 0$	Dissipation at $\sigma = 0.5$
25	0.1362	0.1009
50	0.0214	0.0209
100	0.0025	0.0026
200	0.0015	0.0015

Table B.1: L_2 norm of the numerical error after four flow through times.

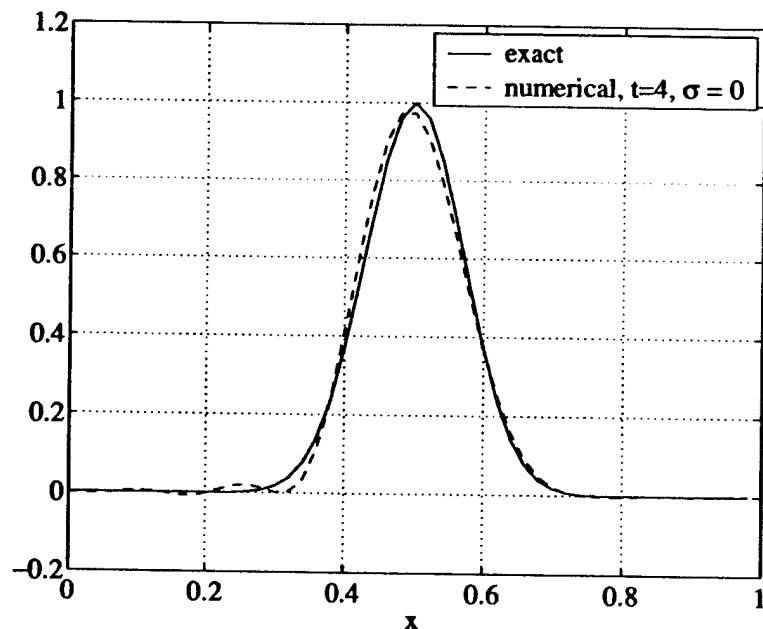


Figure B.2: Comparison between numerical and exact solutions of an initial Gaussian function, after 4 flow through time without numerical dissipation.

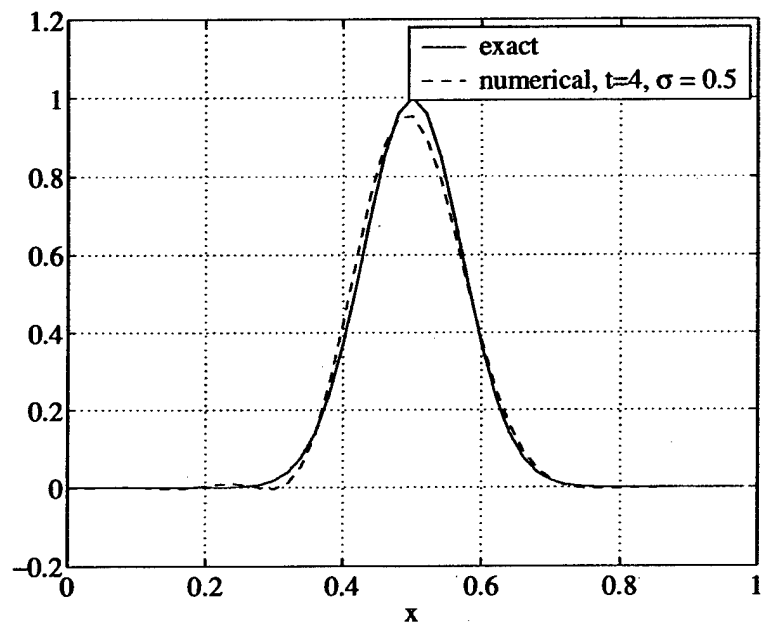


Figure B.3: Same as above, but with numerical dissipation $\sigma = 0.5$.

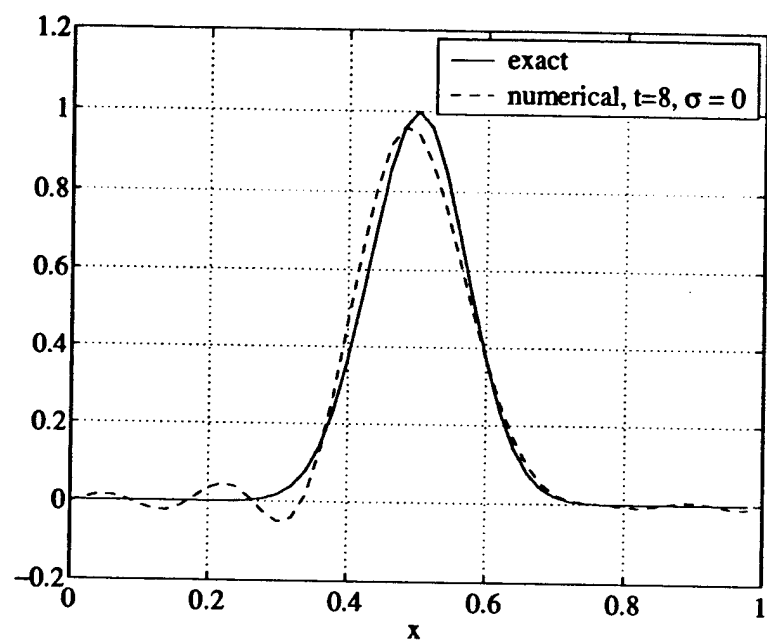


Figure B.4: Comparison between numerical and exact solutions of an initial Gaussian function, after 8 flow through time without numerical dissipation.

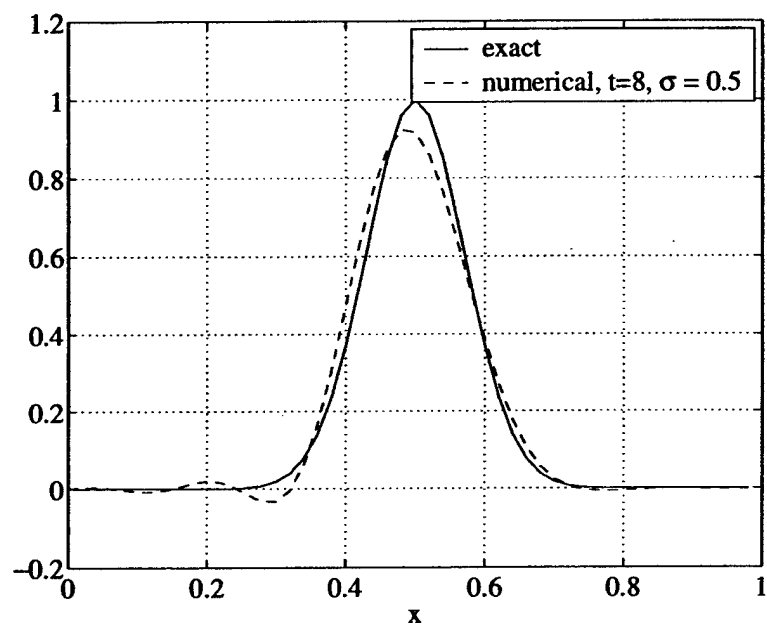


Figure B.5: Same as above, but with numerical dissipation $\sigma = 0.5$.

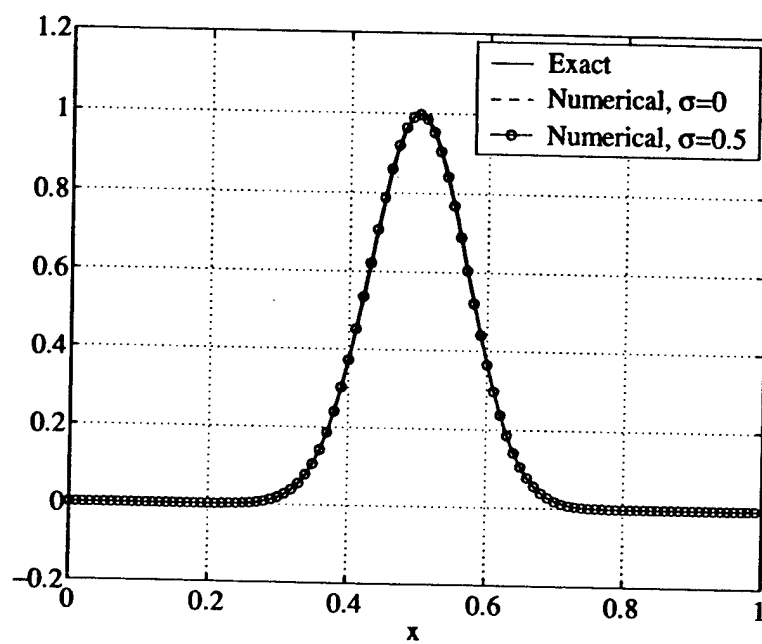


Figure B.6: Comparison between numerical and exact solutions of an initial Gaussian function, after 4 flow through time without numerical dissipation, $N = 100$.

Appendix C

Compressible Boundary Layer Over a Leading Edge

C.1 Introduction

The self-similar boundary layer momentum and energy equations in the region of the stagnation line of a swept cylinder in high speed compressible flows were first obtained by Roshko and Beckwith [1] using the Stewartson's transformation [2]. The solutions to these equations play the same role in a two dimensional stagnation point flow as the Blasius solution in a flat plate boundary layer. As exact solutions to the Navier-Stokes equations, they have been used in the present study to compare with numerical solutions to determine the accuracy of the numerical algorithm. The derivation of self-similar boundary layer equations, somehow unavailable in the literature, is provided in this note for completeness.

C.2 Boundary Layer Approximation

Consider compressible, viscous, and heat conducting gas moving at an uniform supersonic speed $M_\infty > 1$ towards an infinitely long cylinder placed at a swept angle θ , as sketched in figure C.1. We define the coordinates system such that the x -coordinate is the distance along the cylinder surface measured in chordwise direction from the leading edge stagnation line, y is the coordinate normal to the cylinder surface, and z is the spanwise direction. The subscripts ∞ , 1 , and e denote the flow quantities at upstream infinity,

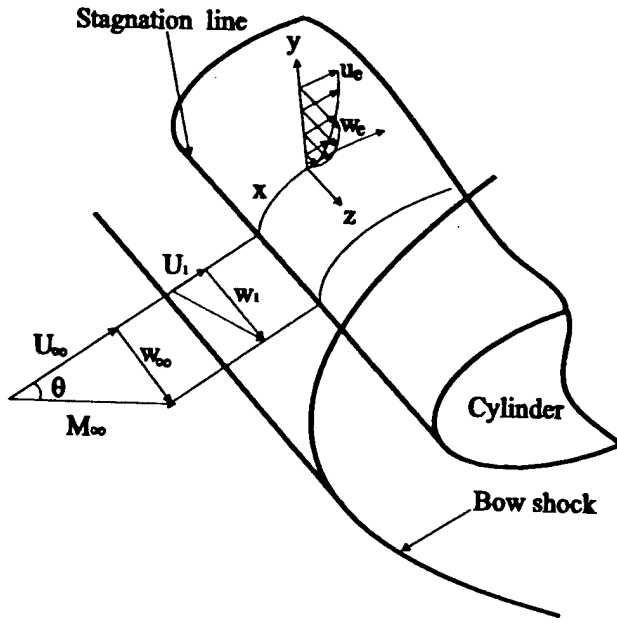


Figure C.1: Compressible boundary layer in the region of the stagnation line of a swept cylinder placed in a supersonic flow.

immediately downstream the bow shock, and the edge of the boundary layer. The boundary layer thickness is assumed to be small in the stagnation region compared with the local radius of curvature of the surface. Note that although the gas speed in the normal direction is reduced to subsonic after the bow shock, the velocity in spanwise direction w , not affected by the shock, may still be supersonic, i.e. $w_\infty = w_e$.

With the usual boundary layer approximation, and noting that all the spanwise derivatives are identically zero, i.e.

$$\frac{\partial}{\partial z} \equiv 0 \quad (\text{C.1})$$

the dimensional continuity, momentum, energy and state equations reduce to

Continuity:

$$\frac{\partial(\rho u)}{\partial x} + \frac{\partial(\rho v)}{\partial y} = 0 \quad (\text{C.2})$$

Momentum:

$$\rho u \frac{\partial u}{\partial x} + \rho v \frac{\partial u}{\partial y} = - \frac{\partial p}{\partial x} + \frac{\partial}{\partial y} \left(\mu \frac{\partial u}{\partial y} \right) \quad (\text{C.3})$$

$$\frac{\partial p}{\partial y} = 0 \quad (C.4)$$

$$\rho u \frac{\partial w}{\partial x} + \rho v \frac{\partial w}{\partial y} = \frac{\partial}{\partial y} (\mu \frac{\partial w}{\partial y}) \quad (C.5)$$

Energy:

$$\rho u \frac{\partial H}{\partial x} + \rho v \frac{\partial H}{\partial y} = \frac{\partial}{\partial y} \left[\frac{\mu}{Pr} \frac{\partial H}{\partial y} \right] - \frac{\partial}{\partial y} \left[\mu \left(\frac{1}{Pr} - 1 \right) \frac{\partial}{\partial y} \left(\frac{u^2 + w^2}{2} \right) \right] \quad (C.6)$$

State:

$$p = \rho RT \quad (C.7)$$

where ρ is density, u , v , and w are the velocity components in x , y , and z directions. p is pressure; μ is the dynamic viscosity, and Pr is the Prandtl number

$$Pr = \frac{\mu c_p}{\kappa} \quad (C.8)$$

The H in (C.6) is the total and stagnation enthalpy defined as

$$H = \frac{1}{2}(u^2 + v^2 + w^2) + E + \frac{p}{\rho} = \frac{1}{2}\mathbf{u}^2 + c_p T \quad (C.9)$$

where T is the temperature, E is the internal energy, κ is the heat conduction coefficient and $c_p = \frac{\gamma R}{\gamma - 1}$ is the specific heat at constant pressure.

The continuity and momentum equations follow directly from the boundary layer approximation and (C.1). The energy equation (C.6) is derived as follows. Following ? (p.158), the general energy equation is

$$\rho \frac{DH}{Dt} = \frac{\partial}{\partial x_j} \left\{ 2\mu u_i (e_{ij} - \frac{1}{3} \Delta \delta_{ij}) \right\} + \frac{\partial}{\partial x_i} \left(\kappa \frac{\partial T}{\partial x_i} \right) \quad (C.10)$$

where the strain e_{ij} and the dilatation e are

$$e_{ij} = \frac{1}{2} \left(\frac{\partial u_i}{\partial x_j} + \frac{\partial u_j}{\partial x_i} \right), \quad \Delta = e_{ii} \quad (C.11)$$

By the Einstein summation convention and (C.1), (C.10) becomes

$$\rho u \frac{\partial H}{\partial x} + \rho v \frac{\partial H}{\partial y} = \frac{\partial}{\partial x} \left\{ 2\mu \left[u \left(\frac{\partial u}{\partial x} - \frac{1}{3} \Delta \right) + \frac{v}{2} \left(\frac{\partial v}{\partial x} + \frac{\partial u}{\partial y} \right) + \frac{w}{2} \frac{\partial w}{\partial x} \right] \right\}$$

$$\begin{aligned}
& + \frac{\partial}{\partial y} \left\{ 2\mu \left[\frac{u}{2} \left(\frac{\partial u}{\partial y} + \frac{\partial v}{\partial x} \right) + v \left(\frac{\partial v}{\partial y} - \frac{1}{3} \Delta \right) + \frac{w}{2} \frac{\partial w}{\partial y} \right] \right\} \\
& + \frac{\partial}{\partial x} \left(\kappa \frac{\partial T}{\partial x} \right) + \frac{\partial}{\partial y} \left(\kappa \frac{\partial T}{\partial y} \right) \\
& = \frac{\partial}{\partial x} \left\{ \mu \left[\frac{\partial}{\partial x} \left(u^2 + \frac{v^2}{2} + \frac{w^2}{2} \right) + v \frac{\partial u}{\partial y} - \frac{2}{3} u \Delta \right] + \kappa \frac{\partial T}{\partial x} \right\} \\
& + \frac{\partial}{\partial y} \left\{ \mu \left[\frac{\partial}{\partial y} \left(\frac{u^2}{2} + v^2 + \frac{w^2}{2} \right) + u \frac{\partial v}{\partial x} - \frac{2}{3} v \Delta \right] + \kappa \frac{\partial T}{\partial y} \right\}
\end{aligned}$$

Apply the boundary layer approximation, i.e. neglecting terms of the form $\frac{\partial}{\partial x} \{ \mu [\frac{\partial}{\partial x} \dots] \}$ and $\frac{\partial}{\partial x} \{ \kappa [\frac{\partial}{\partial x} \dots] \}$, and all the high order terms of v , we obtain the energy equation as in (C.6)

$$\begin{aligned}
\rho u \frac{\partial H}{\partial x} + \rho v \frac{\partial H}{\partial y} &= \frac{\partial}{\partial y} \left[\mu \frac{\partial}{\partial y} \left(\frac{u^2}{2} + \frac{w^2}{2} \right) + \kappa \frac{\partial T}{\partial y} \right] \\
&= \frac{\partial}{\partial y} \left[\mu \frac{\partial}{\partial y} \left(\frac{u^2 + w^2}{2} \right) + \frac{\kappa}{c_p} \frac{\partial}{\partial y} \left(H - \frac{u^2 + w^2}{2} \right) \right] \\
&= \frac{\partial}{\partial y} \left[\frac{\mu}{Pr} \frac{\partial H}{\partial y} \right] - \frac{\partial}{\partial y} \left[\mu \left(\frac{1}{Pr} - 1 \right) \frac{\partial}{\partial y} \left(\frac{u^2 + w^2}{2} \right) \right]
\end{aligned}$$

The velocity and thermal boundary condition are

At $y = 0$

$$u = v = w = 0 \quad \text{and} \quad H = H_w \text{ or } \frac{\partial H}{\partial y} = 0 \quad (\text{C.12})$$

At $y \rightarrow \infty$

$$u = u_e, \quad w = w_e, \quad \text{and} \quad H = H_e \quad (\text{C.13})$$

The viscosity μ is assumed to be a linear function of temperature

$$\mu = \frac{\mu_w}{T_w} T \quad (\text{C.14})$$

where subscript w denotes the quantities at the surface. T_w is a known function of x , and μ_w may be taken as any desired function of T_w , such as the Sutherland law. Outside the boundary layer, the chordwise velocity satisfies the steady Euler equation

$$\rho_e u_e \frac{du_e}{dx} = - \frac{dp_e}{dx} = - \frac{\partial p}{\partial x} \quad (\text{C.15})$$

since p is a constant in the direction normal to the surface resulting from y -momentum equation.

C.3 Stewartson Transformation

Define stream function ψ such that

$$\psi_y \equiv \frac{\rho}{\rho_0} u, \quad \psi_x \equiv -\frac{\rho}{\rho_0} v \quad (\text{C.16})$$

The Stewartson transformation introduces the transformed coordinates X and Y by

$$X(x) = \int_0^x \frac{\mu_w}{T_w} \frac{T_0}{\mu_0} \frac{a_e}{a_0} \frac{p_e}{p_0} dx \quad (\text{C.17})$$

$$Y(x, y) = \frac{a_e}{a_0} \int_0^y \frac{\rho}{\rho_0} dy \quad (\text{C.18})$$

here the subscript 0 denotes the total or stagnation value of the corresponding quantity, and a is the speed of sound. From (C.17) and (C.18), we have

$$\frac{\partial}{\partial x} = X_x \frac{\partial}{\partial X} + Y_x \frac{\partial}{\partial Y} \quad (\text{C.19})$$

$$\frac{\partial}{\partial y} = Y_y \frac{\partial}{\partial Y} \quad (\text{C.20})$$

$$\frac{\partial^2}{\partial y^2} = Y_y^2 \frac{\partial^2}{\partial Y^2} + Y_{yy} \frac{\partial}{\partial Y} \quad (\text{C.21})$$

Furthermore, define the transformed velocities U and V as

$$U = \psi_Y, \quad V = -\psi_X \quad (\text{C.22})$$

Then, in terms of U and V , we have

$$u = \frac{a_e}{a_0} U \quad (\text{C.23})$$

$$v = -\frac{\rho_0}{\rho} (UY_x - VX_x) \quad (\text{C.24})$$

therefore

$$\begin{aligned} \rho u \frac{\partial u}{\partial x} + \rho v \frac{\partial u}{\partial y} &= \rho \frac{a_e}{a_0} U \frac{\partial}{\partial x} \left(\frac{a_e}{a_0} U \right) - \rho_0 (UY_x - VX_x) \frac{\partial}{\partial y} \left(\frac{a_e}{a_0} U \right) \\ &= \rho \left(\frac{a_e}{a_0} \right)^2 X_x \left[U_X U + U_Y V + \frac{a_e X}{a_e} U^2 \right] \end{aligned} \quad (\text{C.25})$$

$$\begin{aligned}\frac{\partial}{\partial y} \left(\mu \frac{\partial u}{\partial y} \right) &= \frac{a_e}{a_0} \frac{\rho}{\rho_0} \frac{\partial}{\partial Y} \left[\left(\frac{a_e}{a_0} \right)^2 \frac{\mu \rho}{\rho_0} \frac{\partial U}{\partial Y} \right] \\ &= \rho \left(\frac{a_e}{a_0} \right)^3 \frac{\mu_w p_e}{T_w \rho_0^2} U_{YY}\end{aligned}\quad (\text{C.26})$$

where in the last expression, (C.14) and (C.4) have been used. To derive the pressure gradient, we first note that in external flow, H is constant; thus

$$a_0^2 = a_e^2 + \frac{\gamma - 1}{2} (u_e^2 + w_e^2) \quad (\text{C.27})$$

Now introducing λ

$$\lambda = \frac{T_{N0}}{T_0} = \frac{1 + \frac{\gamma-1}{2} M_\infty^2 \cos^2 \theta}{1 + \frac{\gamma-1}{2} M_\infty^2} \quad (\text{C.28})$$

as the ratio between the total temperature in the streamwise direction and the total temperature upstream, we have

$$a_0^2 - \frac{\gamma - 1}{2} w_e^2 = a_0^2 \lambda = a_e^2 + \frac{\gamma - 1}{2} u_e^2. \quad (\text{C.29})$$

Differentiating it with respect to x yields,

$$\frac{1}{a_e} \frac{da_e}{dx} = - \frac{\gamma - 1}{2a_e^2} u_e \frac{du_e}{dx} \quad (\text{C.30})$$

Since $u_e = \frac{a_e}{a_0} U_e$, and U_e is only a function of X , we have

$$\begin{aligned}u_e \frac{du_e}{dx} &= \left(\frac{a_e}{a_0} \right) U_e \left[\frac{U_e}{a_0} \frac{da_e}{dx} + \frac{a_e}{a_0} U_{eX} X_x \right] \\ &= \left(\frac{a_e}{a_0} \right) U_e \left[-\frac{(\gamma - 1) U_e}{2a_e a_0} u_e \frac{du_e}{dx} + \frac{a_e}{a_0} U_{eX} X_x \right]\end{aligned}$$

that is

$$u_e \frac{du_e}{dx} = \frac{\left(\frac{a_e}{a_0} \right)^2}{1 + \frac{\gamma-1}{2} \left(\frac{U_e}{a_0} \right)^2} X_x U_e U_{eX} \quad (\text{C.31})$$

Combining (C.28), (C.29) and (C.32), the pressure gradient becomes

$$\frac{\partial p}{\partial x} = - \frac{\rho_e}{\lambda} \left(\frac{a_e}{a_0} \right)^4 X_x U_e U_{eX} \quad (\text{C.32})$$

Substituting (C.25), (C.26) and (C.32) into (C.3) yields the x -momentum equation

$$UU_X + VU_Y = \left[\frac{\rho_e}{\rho} \frac{1}{\lambda} \left(\frac{a_e}{a_0} \right)^2 U_e U_{eX} - \frac{a_{eX}}{a_e} U^2 \right] + \nu_0 U_{YY} \quad (\text{C.33})$$

where $\nu_0 = \mu_0/\rho_0$. However,

$$\begin{aligned} \frac{a_{eX}}{a_e} U^2 &= \frac{1}{a_e} \frac{da_e}{dx} \frac{1}{X_x} \left(\frac{a_0}{a_e} \right)^2 u^2 \\ &= -\frac{\gamma-1}{2a_e^2} u_e \frac{du_e}{dx} \frac{1}{X_x} \left(\frac{a_0}{a_e} \right)^2 u^2 \\ &= -\frac{\gamma-1}{2a_e^2} \left[\frac{1}{\lambda} \left(\frac{a_e}{a_0} \right)^4 U_e U_{eX} X_x \right] \frac{1}{X_x} \left(\frac{a_0}{a_e} \right)^2 u^2 \\ &= -\frac{\gamma-1}{2\lambda} \left(\frac{u}{a_0} \right)^2 U_e U_{eX} \end{aligned} \quad (\text{C.34})$$

and also noticing that $\rho_e T_e = \rho T$, so (C.33) becomes

$$UU_X + VU_Y = \left[\frac{T}{T_e} + \frac{\gamma-1}{2a_e^2} u^2 \right] \frac{1}{\lambda} \left(\frac{a_e}{a_0} \right)^2 U_e U_{eX} + \nu_0 U_{YY} \quad (\text{C.35})$$

Similarly, we have

$$\begin{aligned} \rho u \frac{\partial w}{\partial x} + \rho v \frac{\partial w}{\partial y} &= \rho \frac{a_e}{a_0} U (w_X X_x + w_Y Y_x) - \rho (UY_x - VX_x) \frac{\rho}{\rho_0} \frac{a_e}{a_0} w_Y \\ &= \rho \left(\frac{a_e}{a_0} \right) X_x (U w_X + V w_Y) \end{aligned} \quad (\text{C.36})$$

$$\frac{\partial}{\partial y} \left(\mu \frac{\partial w}{\partial y} \right) = \frac{a_e}{a_0} \frac{\rho}{\rho_0} \frac{\partial}{\partial Y} \left[\mu \left(\frac{a_e}{a_0} \right) \frac{\rho}{\rho_0} \frac{\partial w}{\partial Y} \right] \quad (\text{C.37})$$

$$= \rho \left(\frac{a_e}{a_0} \right)^2 \frac{\mu_w p_e}{T_w \rho_0^2} w_{YY} \quad (\text{C.38})$$

which leads the spanwise momentum equation (C.5) to (C.5)

$$U w_X + V w_Y = \nu_0 w_{YY} \quad (\text{C.39})$$

Since we can also write

$$\rho u \frac{\partial H}{\partial x} + \rho v \frac{\partial H}{\partial y} = \rho \frac{a_e}{a_0} U (H_X X_x + H_Y Y_x) - \rho (UY_x - VX_x) \frac{\rho}{\rho_0} \frac{a_e}{a_0} H_Y$$

$$= \rho \left(\frac{a_e}{a_0} \right) X_x (U H_X + V H_Y) \quad (C.40)$$

$$\begin{aligned} \frac{\partial}{\partial y} \left(\frac{\mu}{Pr} \frac{\partial H}{\partial y} \right) &= \frac{1}{Pr} \frac{a_e}{a_0} \frac{\rho}{\rho_0} \frac{\partial}{\partial Y} \left[\mu \left(\frac{a_e}{a_0} \right) \frac{\rho}{\rho_0} \frac{\partial H}{\partial Y} \right] \\ &= \frac{\rho}{Pr} \left(\frac{a_e}{a_0} \right)^2 \frac{\mu_w p_e}{T_w \rho_0^2} H_{YY} \end{aligned} \quad (C.41)$$

$$\begin{aligned} \frac{\partial}{\partial y} \left[\mu \left(\frac{1}{Pr} - 1 \right) \frac{\partial}{\partial y} \left(\frac{u^2 + w^2}{2} \right) \right] &= - \frac{Pr - 1}{Pr} \left[\frac{\partial}{\partial Y} \left(\frac{u^2 + w^2}{2} \right) \frac{\partial}{\partial y} (\mu Y_y) + \mu Y_y^2 \frac{\partial^2}{\partial Y^2} \left(\frac{u^2 + w^2}{2} \right) \right] \\ &= - \frac{\mu(Pr - 1)}{2Pr} Y_y^2 [(U^2)_{YY} + (w^2)_{YY}] \end{aligned} \quad (C.42)$$

where $\frac{\partial}{\partial y} (\mu Y_y) = 0$ has been used. Thus, the energy equation (C.6) now takes the form

$$U H_X + V H_Y = \frac{\nu_0 (Pr - 1)}{2Pr} [(U^2)_{YY} + (w^2)_{YY}] + \frac{\nu_0}{Pr} H_{YY} \quad (C.43)$$

Now, defining nondimensional functions g and θ as

$$g = \frac{w}{w_e} \quad (C.44)$$

$$\theta = \frac{H - H_w}{H_e - H_w} \quad (C.45)$$

$$(C.46)$$

and because of

$$H_0 = c_p T_0 = c_p T_e + \frac{1}{2} (u_e^2 + w_e^2) = H_e \quad (C.47)$$

we have

$$\begin{aligned} T_0 \left(1 - \frac{T_w}{T_0} \right) \theta &= (T_0 - T_w) \frac{H - H_w}{H_e - H_w} \\ &= T + \frac{u^2}{2c_p} + \frac{w_e^2}{2C_p} g^2 - T_w \\ &= T + \frac{u^2}{2c_p} + T_0 (1 - \lambda) g^2 - T_w \end{aligned} \quad (C.48)$$

This gives

$$T = T_0 \left[\left(1 - \frac{T_w}{T_0} \right) \theta - (1 - \lambda) g^2 + \frac{T_w}{T_0} - \frac{\gamma - 1}{2} \frac{u^2}{a_0^2} \right] \quad (C.49)$$

and further

$$\frac{T}{T_e} + \frac{\gamma - 1}{2a_e^2} u^2 = \frac{T_0}{T_e} \left[\left(1 - \frac{T_w}{T_0}\right) \theta - (1 - \lambda) g^2 + \frac{T_w}{T_0} \right] \quad (\text{C.50})$$

Substitute (C.50) into (C.35), the x-momentum equation becomes

$$UU_X + VU_Y = \left[\left(\frac{1}{\lambda} - \frac{T_w}{T_{N0}} \right) \theta - \left(\frac{1}{\lambda} - 1 \right) g^2 + \frac{T_w}{T_{N0}} \right] U_e U_{eX} + \nu_0 U_{YY} \quad (\text{C.51})$$

Substituting the definitions of λ into (C.28) and g and θ into (C.39), and (C.43), we thus obtain

x-momentum:

$$UU_X + VU_Y = U_e U_{eX} \left[1 + \left(\frac{T_0}{T_{N0}} - 1 \right) (1 - g^2) + \left(\frac{T_w}{T_0} - 1 \right) \left(\frac{T_0}{T_{N0}} \right) (1 - \theta) \right] + \nu_0 U_{YY} \quad (\text{C.52})$$

z-momentum:

$$Ug_X + Vg_Y = \nu_0 g_{YY} \quad (\text{C.53})$$

energy:

$$U\theta_X + V\theta_Y = \frac{\nu_0}{Pr} \left\{ \theta_{YY} - \left(\frac{\gamma - 1}{a_0^2} \right) \frac{1 - Pr}{1 - \left(\frac{T_w}{T_0} \right)} \left[\left(\frac{a_e}{a_0} \right)^2 (U^2)_{YY} + (w_e^2)(g^2)_{YY} \right] \right\} \quad (\text{C.54})$$

C.4 Similar Solutions

To obtain similar solutions, an external flow of the Falkner-Skan type

$$U_e = CX^m \quad (\text{C.55})$$

is assumed. Introduce the usual boundary layer transformation

$$\eta = Y \sqrt{\frac{m+1}{2} \frac{U_e}{\nu_0 X}} \quad (\text{C.56})$$

$$g = g(\eta) \quad (\text{C.57})$$

$$\theta = \theta(\eta) \quad (\text{C.58})$$

$$U = U_e f'(\eta) \quad (\text{C.59})$$

the momentum and energy equations in terms of f , g , and θ take the form

$$f''' + ff'' = \beta[f'^2 - 1 - (\frac{T_0}{T_{N0}} - 1)(1 - g^2) - \frac{T_0}{T_{N0}}(\frac{T_w}{T_0} - 1)(1 - \theta)] \quad (C.60)$$

$$g'' + fg' = 0 \quad (C.61)$$

$$\theta'' + Pr f \theta' = \frac{1 - Pr}{(1 - \frac{T_w}{T_0})} [\frac{\gamma - 1}{2} (\frac{u_e}{a_0})^2 (f'^2)'' + (1 - \frac{T_{N0}}{T_0})(g^2)''] \quad (C.62)$$

where

$$\beta = \frac{2m}{m + 1} \quad (C.63)$$

The boundary condition for the system equations are
at $\eta = 0$

$$f = f' = g = \theta = 0 \quad (C.64)$$

at $\eta \rightarrow \infty$

$$f' = g = \theta = 1 \quad (C.65)$$

Note the right hand side of the energy equation contains u_e which may in general depend on x . For similar solution to be permissible, this dependence must be identically vanish, i.e. the right hand can only be a function of η . For gas with $\gamma \neq 1$, this can be realized if one of the following conditions is satisfied.

- $Pr = 1$
- $u_e = \text{constant}$
- $[\frac{\gamma - 1}{2} (\frac{u_e}{a_0})^2] = \frac{T_{N0}}{T_0}$.

In such cases, the self-similar solutions can be found numerically. For the details of the numerical solutions, see ?.

Appendix D

Vorticity boundary conditions

Here we derive the second boundary condition (6.59) for the vorticity ω_{mn} . For simplicity, the subscript mn will be dropped from the disturbance quantities. Hence, the linearized governing equations for ω , u and v can be written in a general form as

$$\mathcal{L}_\omega(\phi, \omega) = 0, \quad \mathcal{L}_u(\phi, v, u) = 0, \quad \mathcal{L}_v(u, \omega, v) = 0 \quad (\text{D.1})$$

where the expressions for the \mathcal{L} s are those in (6.15), (6.16) and (6.57), respectively. Following a decomposition for the mean Hiemenz velocity ϕ

$$\phi(\eta) = \phi^p + \phi^b = (\eta - \delta_d) + \phi^b \quad (\text{D.2})$$

the operators \mathcal{L}_u and \mathcal{L}_ω can also be decomposed into

$$\begin{aligned} \mathcal{L}_\omega(\phi, \omega) &= \mathcal{L}_\omega^p(\phi^p, \omega) + \mathcal{L}_\omega^b(\phi^p, \phi^b, \omega) \\ \mathcal{L}_u(\phi, v, u) &= \mathcal{L}_u^p(\phi^p, v, u) + \mathcal{L}_u^b(\phi^p, \phi^b, v, u) \end{aligned} \quad (\text{D.3})$$

where the superscript p denotes the operator in which ϕ has been replaced by its potential form ϕ^p , and b denotes the complementary operator resulting from this decomposition; the effect of the Hiemenz boundary layer is thus incorporated in the \mathcal{L}^b operators. The disturbances ω , u and v can also be naturally decomposed as

$$\omega = \omega^p + \omega^b; \quad u = u^p + u^b; \quad v = v^p + v^b \quad (\text{D.4})$$

For the p quantities, the governing equations are

$$\mathcal{L}_\omega^p(\phi^p, \omega^p) = 0; \quad \mathcal{L}_u^p(\phi^p, v^p, u^p) = 0; \quad \mathcal{L}_v(u^p, \omega^p, v^p) = 0 \quad (\text{D.5})$$

The governing equations for the b quantities follow directly from the decompositions in (D.3) and (D.4). For velocities u^p and v^p , we enforce the same boundary conditions as those for the original u and v , i.e.

$$u^p = 0 \quad \text{at} \quad \eta = 0 \quad \text{and} \quad \eta \rightarrow \infty \quad (\text{D.6})$$

$$v^p = 0 \quad \text{and} \quad \frac{dv^p}{d\eta} = 0 \quad \text{at} \quad \eta = 0 \quad (\text{D.7})$$

For the ω^p , (6.56) leads to the first boundary condition

$$\omega^p \rightarrow \omega_\infty \quad \text{as} \quad \eta \rightarrow \infty \quad (\text{D.8})$$

where ω_∞ is the initial disturbance vorticity introduced far upstream. The second boundary condition for ω^p can be derived from the following fact that as $\eta \rightarrow \infty$

$$v^p \rightarrow \begin{cases} 1 & \text{for fundamental mode} \\ 0 & \text{else} \end{cases} \quad (\text{D.9})$$

which is implied by (6.21). To see this, solving the last equation in (D.5) subject to the boundary condition (D.7), we obtain

$$v^p = -\frac{e^{nk_0\eta}}{2} \int_0^\eta (i\omega^p + u^p) e^{-nk_0\eta'} d\eta' + \frac{e^{-nk_0\eta}}{2} \int_0^\eta (i\omega^p - u^p) e^{nk_0\eta'} d\eta' \quad (\text{D.10})$$

For (D.9) to be realizable, v^p must remain bounded as $\eta \rightarrow \infty$. So the coefficient of $e^{nk_0\eta}$ in (D.10) must go to zero as $\eta \rightarrow \infty$, i.e.

$$\int_0^\infty (i\omega^p + u^p) e^{-nk_0\eta'} d\eta' = 0 \quad (\text{D.11})$$

Moreover, notice that

$$u^p \equiv 0 \quad (\text{D.12})$$

as a result of $(\phi^p)'' \equiv 0$ in \mathcal{L}_u^p and the homogeneous boundary condition (D.6). Thus (D.11) reduces to

$$\int_0^\infty \omega^p e^{-nk_0\eta'} d\eta' = 0 \quad (\text{D.13})$$

which serves as the second boundary condition for ω^p . Since the general expression for ω^p has been obtained in (6.46), (D.8) and (D.13) can thus be used to specify the two arbitrary constants therein.

Once ω^p and v^p are known, the corresponding b quantities can be readily solved. Notice that, by construction, u^b and v^b satisfy homogeneous boundary conditions, and the boundary condition for ω^b for $\eta \rightarrow \infty$ is also homogeneous.

Appendix E

Vorticity asymptotes

The general asymptotic expression for the confluent hyper-geometric function with large real argument is (Abramowitz and Stegun, 1970)

$$M(a; c; -z) = \frac{\Gamma(c)}{\Gamma(c-a)} z^{-a} [1 + O(|z|^{-1})] \quad \text{as } z \rightarrow \infty; \quad ph(z) = 0 \quad (\text{E.1})$$

Since the inflow boundary is assumed to be far upstream, i.e. $H_0 \gg 1$, the asymptotic expressions for M_1 and M_2 in (6.60) are as follows.

$$M_1 \sim \frac{\Gamma(\frac{1}{2})}{\Gamma(\frac{n^2}{2\lambda} + i\frac{m\sigma_0}{2})} \left(\frac{H_0}{\sqrt{2}}\right)^{\frac{n^2}{\lambda}-1+im\sigma_0} \quad (\text{E.2a})$$

$$M_2 \sim \frac{\sqrt{2}\Gamma(\frac{3}{2})}{\Gamma(\frac{\lambda+n^2}{2\lambda} + i\frac{m\sigma_0}{2})} \left(\frac{H_0}{\sqrt{2}}\right)^{\frac{n^2}{\lambda}-1+im\sigma_0} \quad (\text{E.2b})$$

When $\lambda \rightarrow \infty$, by the nature of Γ function on complex plane, $|\Gamma(z)|$ decrease rapidly along the imaginary axis. So (E.2) shows that for large λ , $M_2 \gg M_1$. Moreover, $|I_1|$ and $|I_2|$ in (6.62) can be shown of the same order of magnitude, thus compared to $|I_1|/|I_2|M_2$, M_1 can be neglected. Substituting these relations into (6.61) yields the asymptotic expression for the amplitudes of C_{mn} and D_{mn} at large λ :

$$C_{mn} \sim -\frac{\Gamma(\frac{1}{2} + \frac{n^2}{2\sigma_0} + i\frac{m\sigma_0}{2})}{\sqrt{2}\Gamma(\frac{3}{2})} \frac{I_2}{I_1} \left(\frac{H_0}{\sqrt{2}}\right)^{1-\frac{n^2}{\lambda}-im\sigma_0} \quad (\text{E.3a})$$

$$D_{mn} \sim \frac{\Gamma(\frac{1}{2} + \frac{n^2}{2\lambda} + i\frac{m\sigma_0}{2})}{\sqrt{2}\Gamma(\frac{3}{2})} \left(\frac{H_0}{\sqrt{2}}\right)^{1-\frac{n^2}{\lambda}-im\sigma_0} \quad (\text{E.3b})$$

In order to evaluate ω_{mn} at the wall, the amplitudes of C_{mn} and D_{mn} may be estimated more explicitly if the fundamental frequency σ_0 is low. In fact, for the Γ function of a complex argument, it follows

$$|\Gamma(a + i b)| = \prod_{k=0}^{\infty} \frac{|a + k|}{|a + k + i b|} |\Gamma(a)| \quad (\text{E.4})$$

and as $\sigma_0 \ll 1$, it becomes

$$\Gamma\left(\frac{1}{2} + \frac{n^2}{2\lambda} + i \frac{m\sigma_0}{2}\right) \sim \frac{\Gamma\left(\frac{1}{2} + \frac{n^2}{2\lambda}\right)}{\sqrt{1 + \alpha_n \frac{m^2\sigma_0^2}{4}}} \quad (\text{E.5})$$

where

$$\alpha_n = \sum_{k=0}^{\infty} \frac{1}{(k + \frac{1}{2} + \frac{n^2}{2\lambda})^2}$$

Substitute these expressions into (E.3a), and expand the Γ function in terms of power series of $\frac{n^2}{\lambda}$ and $m^2\sigma_0^2$ up to the first order, we have

$$\begin{aligned} |C_{mn}| &\sim \frac{|I_2| \Gamma\left(\frac{1}{2} + \frac{n^2}{2\lambda}\right)}{|I_1| \sqrt{2} \Gamma\left(\frac{3}{2}\right) \sqrt{1 + \alpha_n \frac{m^2\sigma_0^2}{4}}} \left(\frac{H_0}{\sqrt{2}}\right)^{1 - \frac{n^2}{\lambda}} \\ &\sim \frac{|I_2|}{|I_1|} H_0^{1 - \frac{n^2}{\lambda}} [1 + a_1 \frac{n^2}{\lambda}] [1 - \frac{\alpha_n m^2}{8} \sigma_0^2] \\ &\sim H_0 [1 + (a_1 - \ln H_0) \frac{n^2}{\lambda}] [1 - \frac{\alpha_n m^2}{8} \sigma_0^2] \end{aligned} \quad (\text{E.6})$$

where $a_1 = \frac{1}{2}(\ln 2 + \gamma)$ and $\gamma = 0.5772156\cdots$ is the Euler constant. The expression for $|D_{mn}|$ can be similarly obtained. Notice that the value of $|I_1|/|I_2|$, as mentioned before, is slow-varying and of order one. For instance, in the limit of low frequency and large scale, i.e. $\sigma_0 \rightarrow 0$ and $\lambda \rightarrow \infty$,

$$I_1 \sim \sqrt{\frac{\pi e}{2}} [1 - \operatorname{erf}\left(\frac{\sqrt{2}}{2}\right)]; \quad I_2 \sim \frac{\sqrt{e}}{2} \operatorname{Ei}\left(1, \frac{1}{2}\right) \quad (\text{E.7})$$

where erf and Ei are the error function and exponential integral, we have therefore $|I_2|/|I_1| \rightarrow 0.70378178\cdots$. To simplify the discussion, the dependence of I_1/I_2 on λ and σ_0 will be neglected, i.e. $|I_1|/|I_2|$ is treated as a constant.

Bibliography

R. Abid and C. G. Speziale. The freestream matching condition for stagnation point turbulent flows - an alternative formulation. *Technical Report AM-94-001, Boston University*, 1994.

M. Abramowitz and I. A. Stegun, editors. *Handbook of Mathematical Functions with Formulas, Graphs, and Mathematical Tables*. Dover Publications, Inc., New York, 1970.

F. E. Ames. The influence of large-scale high-intensity turbulence on vane heat transfer. *ASME Journal of Turbomachinery*, 199:23–30, 1997.

F. E. Ames and R. J. Moffat. Heat transfer with high intensity, large scale turbulence: The flat plate turbulent boundary layer and the cylindrical stagnation point. In *Dept. of Mech. Engng. Report No. HMT-44*, Stanford University, Stanford, CA, 1990.

F. E. Ames, C. Wang, and P. A. Barbot. Measurement and prediction of the influence of catalytic and dry low NO_x combustor turbulence on vane surface heat transfer. In *Proceedings of ASME TURBO EXPO 2002*, GT-2002-30524, Amsterdam, The Netherlands, June 3-6 2002.

B. Andreotti, S. Douady, and Y. Couder. An experiment on two aspects of the interaction between strain and vorticity. *J. Fluid Mech.*, 444:151–174, 2001.

S. Bae, S. K. Lele, and H. J. Sung. Influence of inflow disturbances on stagnation-region heat transfer. *ASME Journal of Heat Transfer*, 122: 258–265, 2000.

S. Bae, S. K. Lele, and H. J. Sung. Direct numerical simulation of stagnation region flow and heat transfer with free-stream turbulence. *Physics of Fluids*, 15(6):1462–84, 2003.

J.E. Bardina, P. G. Huang, and T. J. Coakley. Turbulence modeling validation. *AIAA Paper 97-2121*, 1997.

G. K. Batchelor. *An introduction to fluid dynamics*. Cambridge university press, 1967.

G. K. Batchelor and I. Proudman. The effects of rapid distortion of a fluid in turbulent motion. *Q. J. Mech. Appl. Maths*, 7:83–103, 1954.

R. M. Beam and R.F. Warming. An implicit factored scheme for the compressible Navier-Stokes equations. *AIAA Journal*, 16(4):393–402, April 1978.

M. Behnia, S. Parneix, Y. Shabany, and P. A. Durbin. Numerical study of turbulent heat tranfer in confined and unconfined impinging jets. *Int. J. Heat Fluid Flow*, 20:1–9, 1999.

J. Botcher and E. Wedemeyer. The flow downstream of screen and its influence on the flow in the stagnation region of cylindrical bodies. *J. Fluid Mech.*, 204:501–522, 1989.

W. R. Briley and H. McDonald. Solution of the three-dimensional compressible Navier-Stokes equations by an implicit technique. In *Proceedings of the Fourth International Conference on Numerical Methods in Fluid Dynamics, Lecture Notes in Physics*, volume 35, pages 105–110. Springer-Verlag, Berlin, 1975.

M. Champion and P. A. Libby. Asymptotic analysis of stagnating turbulent flows. *AIAA J.*, 29(1):16–24, 1991.

S. Scott Collis. *A Computational Investigation of Receptivity in High-Speed Flow Near A Swept Leading-Edge*. PhD thesis, Stanford University, April 1997.

G. Comte-Bellot and S. Corrsin. Simple Eulerian time correlation of full and narrow-band velocity signals in grid generated ‘isotropic’ turbulences.eddy shocklets in decaying compressible turbulence. *J. Fluid Mech.*, 48:273–337, 1971.

T. J. Craft, L. J. W. Graham, and B. E. Launder. Impinging jet studies for turbulence model assessment-ii. an examination of the performance of four turbulence models. *Int. J. Heat Mass Transf.*, 36(10):2685–2697, 1993.

M. R. Dhanak and J. T. Stuart. Distortion of the stagnation-point flow due to cross-stream vorticity in the external flow. *Phil. Trans. R. Soc. Lond. A*, 352:443–452, 1995.

K. Dullenkopf and R. E. Mayle. An account of free-stream-turbulence length scale on laminar heat transfer. *ASME Journal of Turbomachinery*, 117: 401–406, 1995.

P. Durbin. On the $k - \epsilon$ stagnation point anomaly. *Int. J. Heat and Fluid Flow*, 17:89–90, 1996.

C. A. J. Fletcher. *Computational techniques for fluid dynamics*. Berlin ; New York : Springer-Verlag, 2nd edition, 1991.

N. Frössling. Evaporation heat transfer and velocity distribution in two-dimensional and rotationally symmetrical laminar boundary-layer flow. *Technical Report TM-1432, NACA*, 1940.

M. Germano. Averaging invariance of the turbulent equations and similar subgrid-scale modeling. Manuscript, 116, Center for Turbulence Research, 1990.

M. M. Gibson and B. E. Launder. Ground effects on pressure fluctuation in the atmospheric boundary layer. *J. Fluid Mech.*, 86:491–591, 1978.

W. H. Giedt. Investigation of variation of point unit heat transfer coefficient around a cylinder normal to an airstream. *Trans. ASME 71*, pages 375–381, 1949.

M. E. Goldstein. Unsteady vortical and entropic distortions of potential flows round arbitrary obstacles. *J. Fluid Mech.*, 89:433–468, 1978.

R. J. Goldstein, editor. *Heat transfer in gas turbine systems*, volume 934. Annals of the New York Academy of Sciences, 2001.

H. Görtler. Three dimensional instability of the plane stagnation flow with respect to vortical disturbance. In H. Görtler and W. Tollmien, editors,

Fifty years of boundary layer research, pages 304–314. Vieweg and Sohn, 1955. Braunschweig.

C. E. Grosch and H. Salwen. Oscillating stagnation point flow. *Proc. R. Soc. Lond. A*, 384:175–190, 1982.

G. Häammerlin. On instability theory of plane stagnation point flow. In H. Görtler and W. Tollmien, editors, *Fifty years of boundary layer research*, pages 315–327. Vieweg and Sohn, 1955. Braunschweig.

P. E. Hancock and P. Bradshaw. The effect of free-stream turbulence on turbulent boundary layers. *ASME Journal of Fluids Engineering*, 105:284–289, 1983.

B. G. Van Der Hegge-Zijnen. Heat transfer from horizontal cylinders to a turbulent air flow. *Appl. Sci. Res. A*, 7:205–223, 1957.

J. C. R. Hunt. A theory of turbulent flow round two-dimensional bluff bodies. *J. Fluid Mech.*, 61:625–706, 1973.

J. C. R. Hunt and J. M. R. Graham. Free-stream turbulence near plane boundaries. *J. Fluid Mech.*, 84:205–235, 1978.

Y. H. Im, K. Y. Huh, and K-Y. Kim. Analysis of impinging and counter-current stagnating flows by Reynolds stress model. *ASME J. Fluid Engineering*, 124:706–718, 2003.

E. Isaacson and H. B. Keller. *Analysis of numerical methods*. Dover publication, Inc., 1993.

M. Ishigaki. Periodic boundary layer near a two-dimensional stagnation point. *J. Fluid Mech.*, 43:477–486, 1970.

M. Kato and B. E. Launder. Modelling flow-induced oscillation in turbulent flow around a square cylinder. *ASME FED*, 157:189–199, 1993.

O. S. Kerr and J. W. Dold. Periodic steady vortices in a stagnation-point flow. *J. Fluid Mech.*, 276:307–325, 1994.

J. Kestin. The effect of free-stream turbulence on heat transfer rates. In T. F. Irvine and J. P. Hartnett, editors, *Advances in heat transfer*, volume 3. Academic Press, 1966.

J. Kestin, P. F. Maeder, and H. H. Sogin. The influence of turbulence on the transfer of heat to cylinders near the stagnation point. *ZAMP*, 12:115–132, 1961.

J. Kestin and R. T. Wood. On the stability of two-dimensional stagnation flow. *J. Fluid Mech.*, 44:461–479, 1970.

J. Kestin and R. T. Wood. The influence of turbulence on mass transfer from cylinders. *ASME J. Heat Transfer*, 93C:321–327, 1971.

S. Lee, S. K. Lele, and P. Moin. Eddy shocklets in decaying compressible turbulence. *Physics of Fluids*, A 3(4):657–664, 1991.

S. Lee, S. K. Lele, and P. Moin. Direct numerical simulation of isotropic turbulence interacting with a weak shock wave. *J. Fluid Mech.*, 251:533–562, 1993.

S. K. Lele. Compact finite difference schemes with spectral-like resolution. *Journal of Computational Physics*, 103(1):16–42, 1992.

M. J. Lighthill. The response of laminar skin friction and heat transfer to fluctuations in the stream velocity. *Proc. Roy. Soc. A*, 224:1–23, 1954.

N. Lin. *Receptivity of the boundary layer over a flat plate with different leading-edge geometries: Numerical simulations*. PhD thesis, Arizona State University, 1992.

R. S. Lin and M. R. Malik. On the stability of attachment-line boundary layers. Part 1. the incompressible swept Hitzeman flow. *J. Fluid Mech.*, 311:239–255, 1996.

G. W. Lowery and R. I. Vachon. Effect of turbulence on heat transfer from heated cylinders. *Int. J. Heat Mass Transfer*, 18(No. 11):1229–1242, 1975.

C. Lui. *A numerical investigation of shock associated noise*. PhD thesis, Stanford University, 2003.

C. Lui and S. K. Lele. Direct numerical simulation of spatially developing compressible turbulence mixing layers. *AIAA Paper 2001-0291*, 2001.

M. J. Lyell and P. Huerre. Linear and nonlinear stability of plane stagnation flow. *J. Fluid Mech.*, 161:295–312, 1985.

G. Medic and P. A. Durbin. Toward improved prediction of heat transfer on turbine blades. *ASME J. of Turbomachinery*, 124:187–192, 2002.

A. B. Mehendale, J. C. Han, and S. Ou. Influence of high mainstream turbulence on leading edge heat transfer. *ASME Journal of Heat Transfer*, 113:843–850, 1991.

G. J. Merchant and S. H. Davis. Modulated stagnation-point flow and steady streaming. *J. Fluid Mech.*, 198:543–555, 1989.

L. M. Milne-Thomson. *Theoretical hydrodynamics*. The Macmillan Company, New York, 4th edition, 1960.

P. Moin, K. Squires, W. Cabot, and S. Lee. A dynamic subgrid-scale model for compressible turbulence and scalar transport. *Physics of Fluids*, A3 (11), November 1991.

M. V. Morkovin. Bypass-transition research: issues and philosophy. Technical Report Tech. Rep. AFFDL-TR-68-149, Air Force Flight Dynamics laboratory, Wright-Paterson Air Force Base, 1969.

M. V. Morkovin. On the question of instabilities upstream of cylindrical bodies. *NASA Contractor Report*, 3231, 1979.

H. M. Nagib and P. R. Hodson. Vortices induced in a stagnation region by wakes. In L. S. Fletcher, editor, *Aerodynamic heating and thermal protection systems*, volume 59 of *Progress in astronautics and aeronautics*, 1978.

W. Nakayama. Heat-transfer engineering in systems integration: outlook for closer coupling of thermal and electrical designs of computers. *IEEE Transactions on Components, Packaging, and Manufacturing Technology, Part A*, 18(4):818–26, 1995.

A. N. Oo and C. Y. Ching. Effect of turbulence with different vortical structures on stagnation region heat transfer. *ASME Journal of Heat Transfer*, 123:665–674, 2001.

S. Parneix, M. Behnia, and P. A. Durbin. Predictions of turbulent heat transfer in an axisymmetric jet impinging on a heated pedestal. *ASME J. Heat Transfer*, 121:43–49, 1999.

T. J. Pedley. Two-dimensional boundary layers in a free stream which oscillates without reversing. *J. Fluid Mech.*, 55:359–383, 1972.

B. Perot and P. Moin. Shear-free turbulent boundary layers. part 1. physical insights. *J. Fluid Mech.*, 295:199–227, 1995.

N. A. V. Piercy and E. G. Richardson. The variation of velocity amplitude close to the surface of a cylinder moving through a viscous fluid. *Phil. Mag. Series 7*, 6:970–977, 1928.

N. A. V. Piercy and E. G. Richardson. The turbulence in front of a body moving through a viscous fluid. *Phil. Mag. Series 7*, 9:1038–1041, 1930.

T. H. Pulliam. Time accuracy and the use of implicit methods. *AIAA paper 93-3360*, 1993.

M. M. Rai. Navier-Stokes simulations of blade-vortex interaction using high-order accurate upwind schemes. *AIAA paper 87-0543*, 1987.

E. Reshotko and I. E. Beckwith. Compressible laminar boundary layer over a yawed infinite cylinder with heat transfer and arbitrary prandtl number. Report 1379, NACA, 1957.

D. L. Rigby and G. J. VanFossen. Increased heat transfer to elliptical leading edges due to spanwise variations in the free-stream momentum: Numerical and experimental results. *AIAA paper 92-3070*, 1992.

W. J. Sadeh and H. J. Brauer. A visual investigation of turbulence in stagnation flow about a circular cylinder. *J. Fluid Mech.*, 99:53–64, 1980.

M. C. Smith and A. M. Kuethe. Effects of turbulence on laminar skin friction and heat transfer. *Phys. Fluids*, 9(No. 12):2337–2344, 1966.

P. R. Spalart. Direct numerical study of leading-edge contamination. *AGARD C*, 438(5.1-5.13):457–468, 1989.

P. R. Spalart and S. R. Allmaras. A one-equation turbulence model for aerodynamic flows. *AIAA paper 92-0439*, 1992.

C. G. Speziale, S. Sarkar, and T. B. Gatski. Modelling the pressure-strain correlation of turbulence: an invariant dynamic systems approach. *J. Fluid Mech.*, 227:245–272, 1991.

S. P. Sutera. Vorticity amplification in stagnation-point flow and its effect on heat transfer. *J. Fluid Mech.*, 21:513–534, 1965.

D. B. Taulbee and L. Tran. Stagnation streamline turbulence. *AIAA J.*, 26(8):1011–1013, 1988.

V. Theofilis, A. Fedorov, D. Obrist, and U. Ch. Dallmann. The extended Görtler-Hämmerlin model for linear instability of three-dimensional incompressible swept attachment-line boundary layer flow. *J. Fluid Mech.*, 487:271–313, 2003.

K. A. Thole, R. W. Radomsky, M. B. Kang, and A Kohli. Elevated freestream turbulence effects on heat transfer for a gas turbine vane. *Int. J. Heat and Fluid Flow*, 23:137–147, 2002.

R. M. Traci and D. C. Wilcox. Freestream turbulence effects on stagnation point heat transfer. *AIAA J.*, 13(7):890–896, 1975.

G. I. Tsourakis, D. G. Koubogiannis, and K. C. Giannakoglou. Transition and heat transfer predictions in a turbine cascade at various free-stream turbulence intensities through a one-equation turbulence model. *Int. J. Numer. Meth. Fluids*, 38:1091–1110, 2002.

M. Van Dyke. *Perturbation methods in fluid mechanics*. The parabolic press, Stanford, California, 1975.

G. J. Van Fossen, R. J. Simoneau, and C. Y. Ching. Influence of turbulence parameters, Reynolds number and body shape on stagnation region heat transfer. *ASME Journal of Heat Transfer*, 117:593–603, 1995.

G. J. VanFossen and R. S. Bunker. Augmentation of stagnation region heat transfer due to turbulence from a DLN can combustor. *NASA/TM-200-210241*, 2000.

S. Venkateswaran, P. E. O. Buelow, and C. L. Merkle. Development of linearized preconditioning methods for enhancing robustness and efficiency of euler and navier-stokes computations. *AIAA Paper 97-2030*, 1997.

C. R. Wang and F. C. Yeh. Application of turbulence modeling to predict surface heat transfer in stagnation flow region of circular cylinder. *NASA, Technical Paper, 2758*, 1987.

D. C. Wilcox. Turbulence modeling: An overview. *AIAA Paper 2001-0724*, 2001.

S. D. R. Wilson and I. Gladwell. The stability of a two-dimensional stagnation flow to three-dimensional disturbances. *J. Fluid Mech.*, 84:517–527, 1978.

R. W. Wlezien. Measurement of acoustic receptivity. *25th AIAA Fluid Dynamics Conference, AIAA 94-2221*, 1994.

Z. Xiong. *Stagnation point flow and heat transfer under free-stream turbulence*. PhD thesis, Stanford University, 2004.

Z. Xiong and S. K. Lele. Numerical study of leading-edge heat transfer under free-stream turbulence. *AIAA Paper 2001-1016*, January 2001.

N. R. Yardi and S. P. Sukhatme. Effect of turbulence intensity and integral length scale of a turbulent free stream on forced convection heat transfer from a circular cylinder in cross-flow. In *Proceedings 6th international heat transfer conference*, number 5 in FC(b)-29, pages 347–352, Toronto, Canada, 1978.

F. C. Yeh, S. A. Hippensteele, G. J. Van Fossen, P. E. Poinsatte, and A. Ameri. High reynolds number and turbulence effect on aerodynamics and heat transfer in a turbine cascade. *AIAA-93-2252*, 1993.